CHARLES UNIVERSITY

FACULTY OF SCIENCE

Animal Physiology

Dissertation

Molecular consequences of electron transport chain deficiency in proliferating and quiescent cells

---

Molekulární důsledky deficience elektronového transportního řetězce v proliferujících a klidových buňkách

Sílvia Carina Magalhães Novais

Supervisor: Jakub Rohlena Ph.D.

Institute of Biotechnology, Czech Academy of Sciences

Prague 2022

I declare that I have prepared this thesis independently and that I have included all sources of information and literature. I also declare that I did not submit this thesis or a part of it, to obtain any other academic degree.

In Prague on: Signature:

Here, I would like to express my gratitude to my supervisor Dr. Jakub Rohlena for his guidance, encouragement, support, and advice.

My thanks go also to Dr. Katerina Rohlenova from Laboratory of Cellular Metabolism and Professor Jíří Neužil from the Laboratory of Molecular Therapy for all the support and the opportunity to work in their laboratories.

I am thankful to the Charles University, Faculty of Science for the opportunity to pursue my Ph.D. studies.

The study was supported by the **Charles University in Prague,** project **GAUK 1552218, Czech Science Foundation** and the **BIOCEV European Regional Development Fund CZ.1.05/1.1.00/02.0109**.

TABLE OF CONTENTS

ABSTRACT IN ENGLISH 7

ABSTRACT IN CZECH 8

LIST OF ABBREVIATIONS 9

1. INTRODUCTION 11

1.1. Cell proliferation and quiescence 12

1.2. Cell cycle regulation 12

1.3. Metabolism of proliferating and quiescent cells 14

1.3.1. Metabolism of quiescent endothelial cells 15

1.4. Mitochondria 16

1.4.1. Mitochondrial oxidative phosphorylation (OXPHOS) 18

1.4.2. Generation of ROS in mitochondria 20

1.4.2.1. ROS are not all the same 21

1.4.3. Mitochondria are essential for de novo synthesis of pyrimidines 22

1.4.4. Mitochondria-induced cell death 24

1.4.5. Mitochondria in cell proliferation and quiescence 26

1.5. Cell quality control systems 28

1.5.1. Antioxidant defense 28

1.5.2. Autophagy 30

1.5.2.1. Autophagy regulation 30

1.5.2.2. Autophagy pathway 33

1.5.2.3. Autophagy in cell proliferation and quiescence 36

2. AIMS 37

3. LIST OF METHODS 38

4. RESULTS 41

5. DISCUSSION 46

6. CONCLUSIONS 53

7. REFERENCES 55

8. PUBLICATIONS *IN EXTENSO* 63

ABSTRACT IN ENGLISH

Oxidative phosphorylation (OXPHOS) system is best known for producing ATP in mitochondria. As a major metabolic hub, OXPHOS also supports other biological functions that are unrelated to ATP synthesis. Are these additional roles of OXPHOS unique to different cell states, such as to proliferation and quiescence, two of the most contrasting states of a mammalian cell? In this thesis we used genetic models of OXPHOS deficiency to show that in proliferating cells and in tumors OXPHOS primarily supports biosynthesis of nucleotides, whereas in quiescent cells OXPHOS provides oxidative stress resistance. Mechanistically, in growing tumors OXPHOS drives dihydroorotate dehydrogenase (DHODH), an enzyme crucial for de novo synthesis of pyrimidines. Complex II of OXPHOS also acts as a sensor of mitochondrial dysfunction and regulates pyrimidine synthesis for energy conservation. In contrast, in quiescent cells OXPHOS maintains autophagy by continuous low level ROS generation and together with the antioxidant defense provides constitutive oxidative stress protection. In summary, beyond ATP production OXPHOS has additional vital roles tailored to the particular requirements of quiescence and proliferation, with relevance for pathophysiology in cancer and vascular biology.

KEYWORDS

OXPHOS, proliferating cells, quiescent cells, biosynthesis, oxidative stress, DHODH, CII, ROS, autophagy, ATG4B, cell death.

ABSTRACT IN CZECH

Oxidativní fosforylace (OXPHOS) produkuje ATP v mitochondriích. OXPHOS ovšem může podporovat i další biologické funkce, které se syntézou ATP přímo nesouvisí. Liší se tyto funkce v různých buněčných stavech jako jsou např. proliferace a quiescence, tedy dva největší kontrasty kterými savčí buňka prochází? V této práci jsme využili genetické modely deficience OXPHOS a ukázali, že v proliferujících buňkách a v nádorech OXPHOS zajišťuje především biosyntézu metabolitů, zatímco v klidových buňkách OXPHOS zajišťuje odolnost vůči oxidačnímu stresu. Z hlediska mechanismu je hlavní úlohou OXPHOS v rostoucím nádoru udržovat v chodu dihydroorotátdehydrogenázu (DHODH), klíčový enzym de novo syntézy pyrimidinů. Dále jsme ukázali, že respirační komplex II funguje jako senzor mitochondriální dysfunkce a reguluje syntézu pyrimidinů za účelem úspory energie. V klidových buňkách pak aktivnější antioxidační obrana spolu se zvýšenou autofagií stimulovanou ROS které jsou produkované mitochondriální respirací poskytuje základní ochranu před oxidačním stresem. Lze tedy shrnout, že OXPHOS nejenom produkuje ATP, ale má i další životně důležité funkce, které jsou přizpůsobeny konkrétním požadavkům klidového stavu a proliferace, což je důležité pro patofyziologii v rakovině a vaskulární biologii.

KEYWORDS

OXPHOS, proliferující buňky, klidové buňky, biosyntéza, oxidační stres, DHODH, CII, ROS, autofagie, ATG4B, buněčná smr.

LIST OF ABBREVIATIONS

AMPK	AMP-activated protein kinase
ATG	autophagy gene
ATG4B	autophagy related 4B cysteine peptidase
ATP	adenosine triphosphate
Bcl2	B cell lymphoma 2
$CoQH_2$/CoQ	coenzyme Q reduce and oxidized forms
cyt C	cytochrome c
DHODH	dihydroorotate dehydrogenase
ECs	endothelial cells
ETC	electron transport chain
FAO	fatty acid oxidation
GPX	glutathione peroxidases
H_20_2	hydrogen peroxide
HSCs	hematopoietic stem cells
IMM	inner mitochondrial membrane
LC3	light chain 3
mtDNA	mitochondrial DNA
mTOR	mammalian target of rapamycin
NAD^+	nicotinamide adenine dinucleotide
NADH	nicotinamide adenine dinucleotide reductase
OMM	outer mitochondrial membrane

OXPHOS	oxidative phosphorylation
PARP	poly (ADP-ribose) polymerase
ROS	reactive oxygen species
SCs	supercomplexes
SOD2	superoxide dismutase 2
TCA	citric acid cycle
TFAM	transcription factor A, mitochondrial
TFEB	transcription factor EB
ULK1	UNC-51–like kinase 1
ΔΨmi	mitochondrial inner membrane potential

1. INTRODUCTION

Proliferation vs. quiescence is one of the biggest contrasts for a mammalian cell. The metabolism of proliferating and quiescent cells is adapted to address their unique requirements. Proliferating cells (e.g., cancer cells) engage in biosynthesis to build up biomass for rapid cell division and feature fast nucleic acid and protein turnover. In contrast, quiescent cells rely primarily on quality control systems to provide stress resistance.

Mitochondrial oxidative phosphorylation (OXPHOS) is best known for its role in ATP generation, but it also supports other biological processes. These include biosynthesis of essential metabolites, NADH/NAD+ redox cycling by respiratory complex I (CI) and generation of reactive oxygen species (ROS) that arise when electrons transported through the electron transport chain (ETC) 'leak' and react prematurely with oxygen. However, the degree of importance of these various functions of OXPHOS in proliferating and quiescent cells and their precise contribution to physiology and disease are not yet fully understood. This is an important question, as aberrant proliferation and faulty stress resistance underly multiple diseases.

To understand the role of OXPHOS during specific proliferative states, we first asked if/how OXPHOS function supports growing tumors, followed by investigations into a possible role of OXPHOS components in the regulation of metabolism of proliferating tumor cells. Next, we addressed the issue of ETC-based anticancer therapy, focusing on factors that determine its specificity for growing tumors. Leading from that, we investigated if/how OXPHOS provides stress resistance in quiescent cells and tissues.

1.1. Cell proliferation and quiescence

Cell proliferation is a fundamental requirement for organism homeostasis. In mammalian cells, regulated proliferation occurs in a variety of contexts such as during embryonic development, regeneration, and immune response. Cell proliferation can become uncontrolled which can give rise to cancer. In all cases, proliferating cells have similar metabolic requirements, but the pathways that different cells use to meet these metabolic demands differ.

In contrast to a specific case of proliferation, most somatic cells in the adult organism are in a non-dividing state, so called quiescence. Quiescence allows cells to remain in a dormant state for long periods of time. Quiescence can be found in adult stem cells as well in differentiated cells like endothelial and epithelial cells, fibroblasts and hepatocytes [1]. Interestingly, quiescence can also be found in malignancy as some cancer cells can lie dormant in tissues for long periods of time and be responsible for tumor relapse [2]. All these quiescent cell types can differ starkly in their metabolism, which can range from dormancy to high metabolic activity. Although the concrete terminology of quiescence is still in debate, in this thesis we define quiescent cells as metabolically active non-dividing cells.

1.2. Cell cycle regulation

Balance between proliferation and quiescence is primarily regulated by the cell cycle. The cell cycle consists of four main phases and is controlled at multiple checkpoints (Figure 1). In mammalian cells, the primary control is maintained by conserved cyclin-dependent kinases

(CDKs), enzymes that exert control over proteins known as cyclins that steer the cells through the various cell cycle phases.

After mitotic division of the parental cell in the M phase, daughter cells pass several checkpoints and enter a long G_1 phase, the maturation and vegetative stage. Once they are well established in the G_1 phase and receive a signal to continue further, they double the DNA content during DNA replication in the S phase. After the cellular biomass has been accumulated, the cell can progress into the G_2 phase to grow into another mitotic division. At this point, the cycle is completed. As the cells leave the M phase, they can exit the cell cycle by not entering the G_1 phase but sidestepping into the G_0 phase associated with the quiescent state. Whether a cell enters G_0 or proceeds through G_1 to continue cycling is dictated by the regulation of several key factors, including cyclins and CDKs, CDK inhibitors, and the retinoblastoma protein (Rb). Cyclin-CDK complexes drive cell cycle progression through the phosphorylation of proteins involved in each of the cell cycle phases [3]. Cyclin D-CDK4/6 and cyclin E-CDK2 complexes promote G_1 progression [4]. Thus, high levels of cyclin D/E and CDK4/6 increase proliferation by driving passage through G_1. Conversely, stimuli that decrease the abundance and activity of these proteins induce quiescence [4]. Several other cellular pathways are known to regulate the quiescence–proliferation transition and are thus essential for tissue maintenance and regeneration. Quiescence regulators include Notch-HES1 [5, 6], p53 [7] stress and metabolic response pathways [8, 9] as well as epigenetic mechanisms [10, 11].

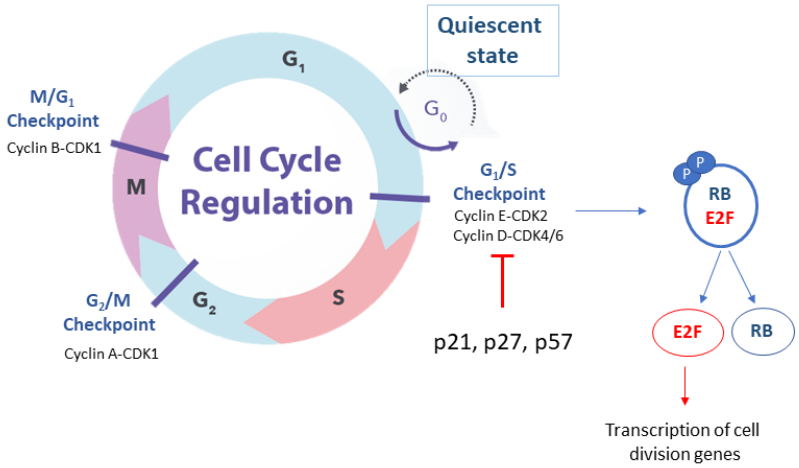

Figure 1: Cell cycle division and regulation. The cell cycle is divided into growth phase (G_1), DNA synthesis phase (S), waiting phase (G_2), and mitosis (M). Cells can exit this proliferative cycle by entering a quiescent state (G_0). Cell cycle checkpoints monitor and regulate the progress of the cell cycle. These checkpoints include expression of cyclins and cyclin-dependent kinases (CDKs) which can be regulated by its inhibitors such as p21, p27 and p57. Retinoblastoma protein (RB) is another important regulator of cell cycle. The phosphorylation of RB allows the activation of E2F1, a key transcriptional activator for cell cycle and cell division genes.

1.3. Metabolism of proliferating and quiescent cells

Proliferating and quiescent cells face distinct challenges. As a result, the metabolic needs of cell proliferation and quiescence are also different. All cells, irrespective of their proliferation status, require a source of energy and reducing power to maintain homeostasis and combat stress. However, how these individual needs are emphasized depends on the cellular state. Proliferating cells often display enhanced uptake of glucose which, besides providing ATP, is an important source of carbon to support lipid production and the biosynthesis of nucleotides and non-essential amino acids. Pyruvate to lactate conversion in glycolysis ensures the regeneration of

NAD^+ pool, allowing production of anabolic intermediates at a sufficiently fast rate. Proliferating cancer cells produce lactate even under conditions of ample oxygen, a phenomenon referred to as the 'Warburg effect'. However, contrary to what was believed, this does not mean that mitochondrial respiration is inactive or damaged in cancer cells, see below.

In contrast to proliferating cells, the need for biosynthesis in non-proliferating cells is expected to be reduced. However, most of the quiescent cells remain metabolically active and maintain considerable rate of glucose consumption [12]. These cells extract energy from glucose, but pyruvate is usually not converted to lactate. Instead, it is diverted into mitochondria to form acetyl-CoA that is oxidized in the citric acid cycle (TCA) cycle to produce NADH. NADH is then used by OXPHOS to produce energy [13]. Of note, some quiescent cell types like stem cell, immune cells or endothelial cells rely on glycolysis as their primary metabolic pathway [1]. Presumably, this is to reduce their production of ROS from the respiratory chain. This underscores that quiescent cells posse diverse metabolic adaptations depending on the unique functions and specific requirements of each cell type. Despite these metabolic differences, stress resistance is important for all quiescent cell types.

1.3.1. Metabolism of quiescent endothelial cells

Proliferation and quiescence are important aspects in the (patho-) biology of endothelial cells (ECs), which form the inner lining of blood vessels. During embryonic development ECs proliferate to promote formation of new vessel, so called angiogenesis. In contrast, later in adulthood vessels are mature and ECs are mostly in a quiescent state. Nevertheless, ECs can quickly become activated and proliferate to support angiogenesis during wound healing or in

tumors to help deliver oxygen and nutrients to (hypoxic) tissues. In this manner pathological angiogenesis/EC proliferation can promote cancer. Dysfunctional quiescent ECs also contribute to multiple diseases with high mortality, including atherosclerosis, stroke, and diabetes. Therefore, the prevention of ECs dysfunction is a therapeutic objective, and understanding how quiescent ECs are protected against stress is crucial for the clinic.

Studies on ECs metabolism have exploded in recent years, with cellular metabolic pathways emerging as key regulators of signaling and angiogenesis induction in both health and disease. ECs in the arterial, venous, lymphatic, and microvascular systems are all highly glycolytic, similarly to some cancer cells [14]. To minimize the oxygen consumption and formation of ROS, ECs do not rely on oxygen-dependent metabolism for energy production. Thus, even in healthy quiescent vasculature with abundant oxygen availability, ECs use mostly glycolysis for ATP production. For this reason, endothelial cells represent an interesting model to study ATP-unrelated functions of OXPHOS.

1.4. Mitochondria

Mitochondria are essential organelles that contribute to multiple cellular processes, including energy production in the form of ATP, generation of physiological levels of ROS, production of essential metabolites and initiation of cell death. Beyond its central role in cellular metabolism, mitochondria act as signaling organelles dictating the fate and function of the cell [15]. Given all these important functions, mitochondria provide a major contribution to the metabolism of proliferating and quiescent cells in health and disease.

Mitochondria are organelles that evolved from archeon ancestors' early symbiosis with prokaryotic species [16]. Mitochondria have evolved to retain some bacterial phenotypic

characteristics while gaining new roles such as regulation of energy generation, arrangement of intermediate metabolism, and, most significantly, control of cell growth and programmed cell death. Unlike other organelles of the mammalian cell, mitochondria contain their own mitochondrial DNA (mtDNA) which encodes essential subunits of respiratory complex I, III, IV and V (also known as ATP synthase) from the mitochondria ETC. However, mitochondria are not self-supporting entities as they also rely on imported nuclear gene products that for example fully encode respiratory complex II. Mitochondrial DNA is more vulnerable to intercalating agents than nucleic DNA. For this reason, chronical exposure of cells to low concertation of agents like ethidium bromide can cause selective mtDNA loss. The replication/transcription of mtDNA is ensured by the mitochondrial polymerase (POLG), mitochondrial DNA directed-RNA polymerase (POLMRT) and mitochondrial transcription factor A (TFAM). Knockdown of TFAM has been shown to cause mtDNA depletion in cultured cells [17, 18]. Therefore, removal of mtDNA or deletion of TFAM leads to impairment of enzymatic complexes of the oxidative phosphorylation system and thus respiratory deficiency.

Mitochondria are enclosed by two membranes that delineate two distinct mitochondria compartments: the mitochondrial matrix located within the inner mitochondrial membrane (IMM) and the intermembrane space (IMS) between the IMM and the outer mitochondrial membrane (OMM). OMM forms a border between the organelle and the cytoplasm, and contains many integral membrane proteins, transporters and conductance channels. These proteins mediate active transport of mitochondria-targeted proteins from cytoplasm, whereas ion channels such as voltage dependent anion channel (VDAC) contribute to the equilibration of ions such as Ca^{2+}, small metabolites from the TCA cycle and ROS between the IMS and cytoplasm. In contrast to OMM, which is similar to the cytoplasmic membrane, the composition

of the IMM is unique. The IMM forms folds referred to as mitochondrial cristae that significantly increase its surface to provide more space for integral membrane proteins. The IMM contains specific transporters, proteins that regulate metabolite and protein passage into and out of the mitochondrial matrix, proteins component responsible for mitochondrial dynamics, and especially the large protein complexes of the oxidative phosphorylation machinery.

1.4.1. Mitochondrial oxidative phosphorylation (OXPHOS)

The OXPHOS system, which is embedded in the IMM, plays a key function in the energy metabolism of the cell. OXPHOS generates ATP through five multi-subunit complexes and two mobile carriers. Electrons are received from nutritional components via respiratory complexes I or II and transferred through a series of oxidoreductase processes of the electron transport chain (ETC) to molecular oxygen, which is then reduced to water as the final electron acceptor. Complexes I (ubiquinone oxidoreductase), III (ubiquinol: ferricytochrome C oxidoreductase), and IV (cytochrome c oxidoreductase), but not complex II (succinyl dehydrogenase), function as proton pumps, transferring protons across the IMM and utilizing redox energy. This creates a proton gradient across the IMM, resulting in electrochemical potential. This membrane potential is used by Complex V (F1Fo-ATP synthase) to catalyze the condensation of ADP and inorganic phosphate into ATP. (Figure 2)

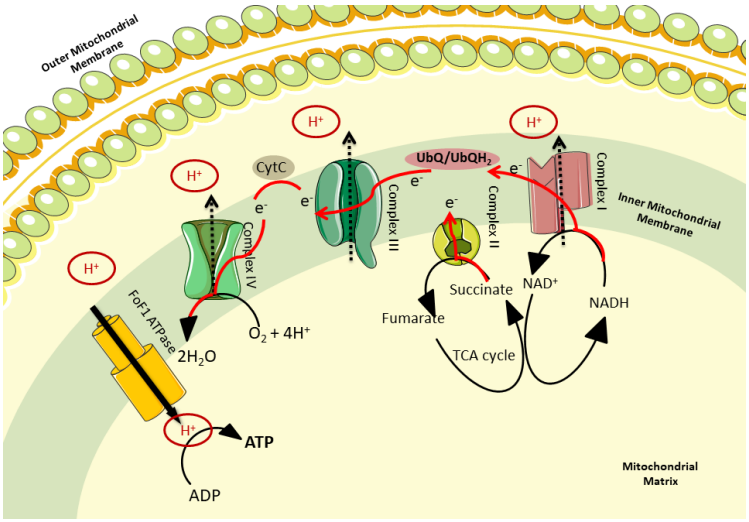

Figure 2. The OXPHOS system. Electrons transferred through the ETC (red arrows) originate at CI, which oxidize NADH coming from the TCA cycle, or at CII, which directly converts succinate to fumarate. Electrons are then transferred, via CIII and two mobile carriers CoQ and cyt c, to CIV, where they reduce molecular oxygen to form water. Proton pumping by CI, CIII and CIV is showed by the dashed black arrows. The resulting proton gradient is used by CV to generate ATP. Adapted from [19].

The first and biggest enzyme in the respiratory chain is Complex I (CI). CI accepts two electrons from oxidation of TCA-derived NADH and transfers them to flavin mononucleotide (FMN), the principal electron acceptor. Redox centers transport electrons to the final acceptor, ubiquinone (commonly known as coenzyme Q - CoQ), reducing it to ubiquinol (CoQH2). The movement of four protons through the IMM, from the negative matrix side to the positive intermembrane space side, is linked to this process. The second site of entry for electrons into the ETC is Complex II (CII - succinate dehydrogenase, SDH). In mitochondria, CII serves a dual purpose. It is a major enzyme in the TCA cycle as well as a component of the OXPHOS system. Within the TCA, CII catalyzes the oxidation of succinate to fumarate by using the succinate dehydrogenase activity. CII transports electrons from succinate to ubiquinone via the flavin

adenine dinucleotide and three [Fe-S] clusters [20]. This complex reaction is referred to as the succinate ubiquinone reductase (SQR) activity of the ETC [21]. CoQH2 generated by CI and CII is oxidized by CIII, and the electrons are transported from CoQH2 to cytochrome c. (cyt c). After that, electrons from cyt c are transferred to CIV, which then reduces oxygen into two molecules of H_2O. The trans-membrane proton gradient is then generated by CIV, which is utilized by CV as a proton-motive force to create ATP.

It has been documented that mitochondrial ETC complexes do not operate as separate entities but are mostly organized into so called supercomplexes (SCs) responsible for carrying out cellular respiration. SC assemblies react to the needs of cellular metabolism and may also respond to substrate availability [22]. While the role of SCs in substrate channeling is debated [23], they are important for the stability of ETC complexes and for reducing the production of ROS [24]. It is now widely accepted that SCs constitute functional assemblies of respiratory complexes, which is particularly apparent for CI [25]. The level of ETC organization in various subsets of cells is largely unexplored but could be associated with differences in sensitivity to ETC inhibition.

1.4.2. Generation of ROS in mitochondria

Mitochondrial metabolism is known to be the main source of ROS, but ROS can also be generated at other organelles like peroxisomes or by the activity of transmembrane NADPH oxidases. Within mitochondria, ROS can be produced at eleven different locations. The sites in the ETC at CI and CIII are considered the major sources of ROS [26-28] that can donate electrons to the oxygen molecule and form superoxide ($O_2^{\bullet}$) radicals. After $O_2^{\bullet}$ is released into mitochondria matrix or to cytoplasm it is rapidly converted to hydrogen peroxide (H_2O_2). The

inhibition of ETC results in ROS production [26, 29, 30] as compounds that bind to the downstream ETC components block the electron traffic. Before the point of inhibition, the electrons accumulate, increasing likelihood of leakage and ROS formation. ETC upstream of the blockade therefore becomes a source of ROS, while ROS formation downstream of the blockade is reduced due to shortage of electrons [30, 31]. At CI, the production of ROS can be pharmacologically induced by rotenone and piericidin A, whereas antimycin and myxothiazol induce ROS production by blocking CIII. CII has recently also been recognized as a significant source of ROS [26] and can be inhibited by atpenin 5, malonate or MitoVES. CIV and ATP synthase has not been reported to directly participate in ROS production. CIV was described to be particularly efficient in preventing premature electron leakage. It should be noted, however, that ATP synthase inhibition by oligomycin leads to increased mitochondria membrane potential and higher ROS production from the upstream sites in the ETC as a secondary effect. Increased ROS production may also result from an increase in respiration rate if the increase is caused by a larger substrate supply. When driven by ATP demand, increased respiratory rate, on the other hand, results in a decrease in ROS production, as the ETC redox centers become more oxidized [32].

1.4.2.1. ROS are not all the same

Although there is a tendency to consider ROS as a single entity, different ROS can have very different targets and activities. For instance, H_2O_2 plays an essential role in signaling through its ability to selectively modify and regulate the function of many proteins. The first example to be elucidated was the role of H_2O_2 as a second messenger in some cell types [33]. Multiple signaling

roles of H_2O_2 have been described [34, 35], including regulation of cellular functions such as growth, survival, proliferation [36, 37], hypoxia adaptation [38], and differentiation [36, 39]. Nevertheless, increased concentrations of H_2O_2 from internal or external stimuli can also trigger production of endogenous ROS leading to cell damage.

Other forms of ROS are more likely to lead to damage and toxicity. The highly reactive $O_2^{\bullet}$ can damage iron cluster proteins, and hydroxyl radicals can irreversibly damage proteins, DNA and lipids, leading to cell death [40].

The powerful and potentially dangerous functions of ROS play critical roles under many conditions that drive abnormal cell behavior, such as cancer. Cancer cells exhibit higher levels of ROS than normal cells [41]. The effects of this increase of ROS might vary, presumably they can both support and prevent malignant behavior. Whereas the damaging effects of ROS can be detrimental to cell survival, the acquisition of DNA damage and genomic instability can drive the accumulation of oncogenic alterations that promote cancer development [42, 43]. Moreover, the increased constitutive ROS levels in cancer cells lead to a dependency on antioxidant defense. Saturation of antioxidant defense with increased endogenous ROS makes cancer cells sensitive to exogenous ROS challenge or to inhibition of antioxidant defense components such as glutathione, which contributes to the specificity of ROS-based anticancer therapy [44, 45].

1.4.3. Mitochondria are essential for de novo synthesis of pyrimidines

In addition to ATP production and generation of ROS, mitochondria are a critical source of building blocks for biosynthesis of essential metabolites such as nucleotides, fatty acids, cholesterol, amino acids, glucose, and heme [46]. Of all these biosynthetic pathways, one of the

most intertwined with OXPHOS is the de novo synthesis of pyrimidines [42, 47] that provides building blocks of nucleic acids required for DNA/RNA replication and transcription [48, 49]. We know from in vitro evidence that OXPHOS promotes pyrimidine synthesis (depicted in Figure 3) for two reasons. First, ETC of OXPHOS enables biosynthesis of aspartate, a pyrimidine precursor, by maintaining NADH/NAD+ redox cycling at CI [50, 51]. Second, ETC supports the conversion of dihydroorotate (DHO) to orotate, catalyzed by the enzyme dihydroorotate dehydrogenase (DHODH) in the de novo pyrimidine synthesis pathway. Localized at the outer face of the IMM, DHODH is connected to the ETC through CoQ redox cycling, driven by CIII-CIV [52, 53]. For these reasons, we expected de novo pyrimidine synthesis might be affected by OXPHOS dysfunction in tumors in vivo.

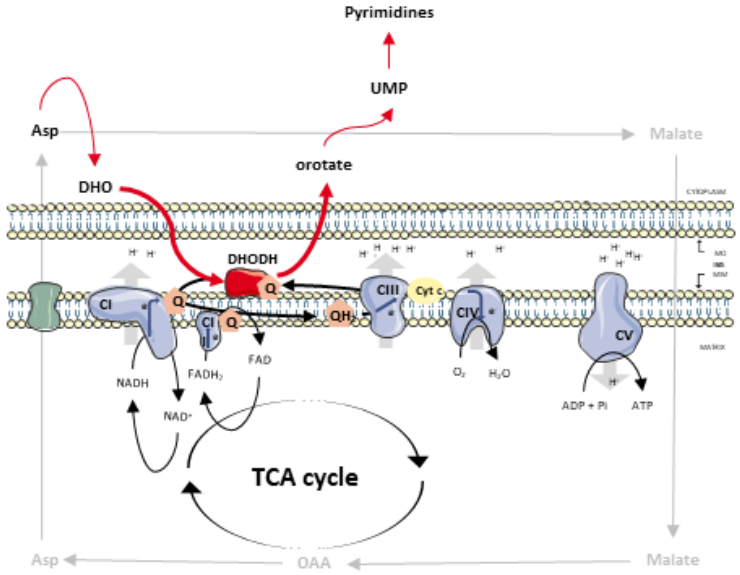

Figure 3: De novo pyrimidine synthesis pathway and OXPHOS. DHODH represents a crucial step in pyrimidine synthesis pathway (shown in red), where it catalyzes conversion of dihydroorotate (DHO) to orotate. CoQ acts as an electron acceptor that pools electrons obtained from DHODH with those from CI and CII and transports them to CIII. De novo pyrimidine synthesis is also limited by aspartate availability, which is dependent on the NADH/NAD+ redox cycling. Asp (aspartate); DHO (dihydroorotate); UMP

(uridine monophosphate); CoQ (coenzyme Q); cyt c (cytochrome c); OAA (oxaloacetate). Adapted from [53].

1.4.4. Mitochondria-induced cell death

Apoptosis, also known as programmed cell death, is a cellular self-destruction mechanism that plays a role in multiple biological processes. While apoptosis is crucial during normal development, aberrant apoptosis underlies conditions like cancer, ischemia, neurodegeneration, autoimmune diseases, and viral infections [54]. Apoptosis can be triggered either by extrinsic or intrinsic pathway, both of which converge on activating the executioner caspase-3 and -7, depending (Figure 4). In addition to caspase-mediated cleavage of numerous cellular proteins, the apoptotic cell exposes phosphatidylserine on the outer side of the plasma membrane and its DNA is fragmented and degraded by endonuclease G released from the IMS. These features are utilized for experimental detection of apoptosis by flow cytometry and TUNEL assays, respectively.

ROS derived from both CI and CII [26, 55] have been implicated in cell death induction. In case of CI, NDUFS1 subunit has been shown to be directly cleaved by effector caspase 3, leading to excessive ROS generation [56] causing oxidative damage to DNA. As mtDNA is very vulnerable to DNA damage, perturbations in mtDNA-encoded induce OXPHOS malfunction, resulting in amplification of ROS generation.

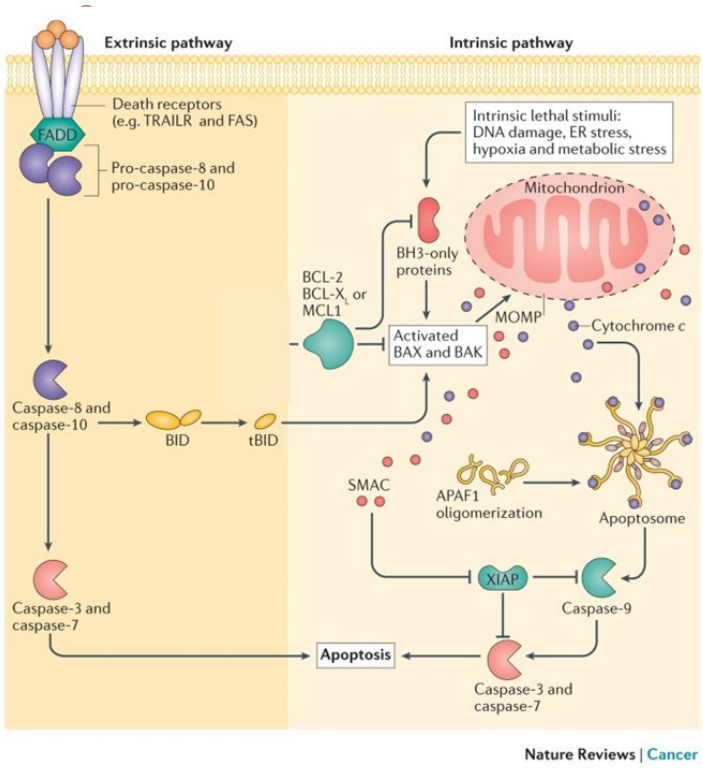

Figure 4: Extrinsic and intrinsic apoptotic signaling pathways. In the extrinsic apoptotic pathway, death receptors such as tumor necrosis factor (TNF)-related apoptosis-inducing ligand (TRAIL) receptor (TRAILR) and FAS can activate initiator caspases (caspase-8 and caspase-10) mediated by adaptor proteins such as FAS-associated death domain protein (FADD). Active caspase-8 and caspase-10 then cleave and activate the effector caspase-3 and caspase-7, leading to apoptosis. The intrinsic (or mitochondrial) pathway of apoptosis requires mitochondrial outer membrane permeabilization (MOMP). Cell stress engages BCL-2 homology domain 3 (BH3)-only protein activation, leading to BAX and BAK activity that triggers MOMP. Following MOMP, mitochondrial intermembrane space proteins such as second mitochondria-derived activator of caspases (SMAC) and cytochrome *c* are released into the cytosol. Cytochrome *c* interacts with apoptotic protease activating factor 1 (APAF1), triggering apoptosome assembly, which activates caspase-9. Active caspase-9, in turn, activates caspase-3 and caspase-7, leading to apoptosis. Mitochondrial release of SMAC facilitates apoptosis by blocking the caspase inhibitor X-linked inhibitor of apoptosis protein (XIAP). Caspase-8 cleavage of the BH3-only

protein BH3-interacting death domain agonist (BID) enables crosstalk between the extrinsic and intrinsic apoptotic pathways. ER, endoplasmic reticulum; MCL1, myeloid cell leukemia 1; tBID, truncated BID. Adapted from [57].

1.4.5. Mitochondria in cell proliferation and quiescence

Mitochondria play a vital role in bioenergetic and biosynthetic pathways and can rapidly adapt to meet the metabolic needs of the cell. The metabolic shift from OXPHOS to aerobic glycolysis in rapidly proliferating cells, including cancer cells, is controlled by cancer-associated proteins such as hypoxia-inducible factor 1α or Myc which are highly expressed in most solid cancers[58]. However, even in aerobic settings, many (but not all) cancer cells rely heavily on glycolysis to meet their energy needs – also known as the Warburg effect [59]. The aerobic glycolysis permits cancer cells to utilize glycolytic intermediates for anabolic processes while avoiding the high ROS levels produced as a consequence of using OXPHOS. However, except for cells that are unable to use OXPHOS due to a variety of mutations, this scenario has proven to be oversimplified. OXPHOS is still used by many cancer cells to boost their bioenergetic potential and create low quantities of ROS for signaling. In contrast to Warburg's deliberations that were interpreted as if mitochondria in cancer cells are dysfunctional, it is now clear that mitochondrial function is not affected in most malignancies [60]. Instead, the observed increase in aerobic glycolysis in proliferating cancer cells is due to elevated biosynthetic demands associated with fast growth and concomitant metabolic modulation [61]. Even though aerobic glycolysis is inefficient in terms of ATP yield, it can produce ATP at a significantly higher pace than respiration [62, 63]. Nonetheless, most cancer cells maintain active mitochondrial respiration in addition to aerobic glycolysis, implying that these two major sources of energy are

not interchangeable [13, 60]. A growing body of evidence indicates that functional OXPHOS is required for tumor initiation, progression, and metastasis [42, 47] and reliance on OXPHOS is one of the major characteristics of the treatment-resistant population of cancer cells [64-66]. Experimentally, the reliance of cancer cells on OXPHOS was demonstrated using mtDNA depleted (tumor) cells, also known as ρ^0 cells, which lack mitochondrially encoded OXPHOS components and are thus unable to engage in mitochondrial respiration. The ρ^0 cells showed delayed tumor growth when injected into experimental mice [47]. It has been shown that these cells could only form tumors in syngeneic animals after being repopulated with functional mitochondria from the host's surrounding tissue [47]. A model of TFAM deficiency was used in another study to demonstrate the critical function of OXPHOS in carcinogenesis [42]. However, it remains unclear why are mitochondria needed for cancer progression and which of their functions (ATP production, ROS generation, biosynthesis or other) are critical in oncogenesis.

Several studies have shown that mitochondria affect the fate of quiescent cells. For example, the mitochondrial fatty acid transport and b-oxidation in quiescent cells has been described as essential for ATP production as well as for redox homeostasis [67-69]. On contrary, quiescent endothelial cells rely on FAO to sustain TCA cycle for redox homeostasis through the NADPH regeneration [68, 69]. Mitochondrial ROS production has also been reported important in homeostasis, function, and long-term survival of quiescent cells.

Overall, a better understanding of mitochondrial significance in proliferating/quiescent cells, especially on how it can maintain their viability during oxidative stress or in low nutrient environments, may result in novel targeted therapeutic strategies.

1.5. Cell quality control systems

All the cells in an organism are exposed to oxidative stress and for this reason they need control systems to protect themselves. This is particularly important for quiescent cells, as they may stay in the non-proliferating state for a prolonged time under suboptimal conditions, and they need to cope with accumulated cellular stresses and metabolic changes. Prime examples of stress response pathways and quality control systems employed by quiescent cells are antioxidant defense and macroautophagy/autophagy.

1.5.1. Antioxidant defense

Under physiological conditions, ROS act as second messengers participating in regulation of various cellular functions. Their levels in cells therefore need to be tightly controlled and excessive ROS need to be effectively scavenged to protect the cell from oxidative damage. This is ensured by the antioxidant systems that significantly expedite inactivation of reactive radicals.

ROS are scavenged at several levels (Figure 5). First in the antioxidant cascade is superoxide dismutase (SOD), one of the most important antioxidant enzymes. SOD catalyzes the dismutation of $O_2^{\bullet}$ to H_2O_2 and oxygen, which is then inactivated by next-step antioxidant systems [70]. H_2O_2 in mitochondria is decomposed to water by mitochondria-specific glutathione peroxidases (GPX) [71], or by peroxiredoxins (PRX) in the thioredoxin system [72]. Both GPXs and PRXs inactivate H_2O_2 using reducing equivalents from NADPH. In addition, catalase inactivates the remaining H_2O_2 that escapes from mitochondria [73]. Because catalase has a significantly lower affinity for H_2O_2 than GPXs, GPXs were long thought to be the primary antioxidant enzyme responsible for H_2O_2 detoxification. However, catalase has been shown to be critical for cell survival [74].

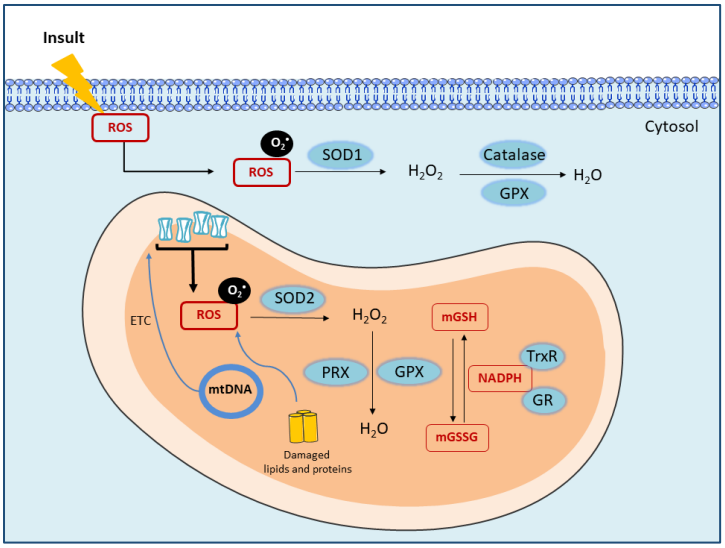

Figure 5: Antioxidant system (simplified). ROS can be triggered by external insults, ETC electron leak or from damaged lipids and proteins. The dismutation of superoxide ($O_2^{\bullet -}$) to generate H_2O_2 can be catalyzed by superoxide dismutase 2 (SOD2) in mitochondria or by SOD1 in cytosol. In cytosol, H_2O_2 can be detoxified to water by antioxidants such as catalase and glutathione peroxidase (GPX). In mitochondria, H_2O_2 is detoxified by GPXs and by peroxiredoxins (PRX). Glutathione reductase (GR) recycles oxidized glutathione (GSSG) to generate reduced glutathione (GSH) needed for GPX activity, while thioredoxin reductase (TrxR) directly regenerates oxidized PRX. Both GR and TrxR depend on NADPH for activity.

As discussed above, quiescent cells are geared for stress protection and they upregulate antioxidant defense to protect themselves from ROS-induced damage [75]. In contrast, proliferating cells are known to be more sensitive to ROS-induced damage but whether this is a general property of proliferating cells and whether antioxidants play a role here is still unknow.

1.5.2. Autophagy

To survive in sub-optimal conditions, cells can degrade and recycle their components in a process known as autophagy/macroautophagy. This includes degradation of damaged organelles and microbial invaders or breakdown products to support metabolism. Autophagy is an evolutionarily conserved system for engulfing cytoplasmic proteins and organelles in autophagosomes and degrading them in lysosomes. In the absence of stress, basal autophagy serves a housekeeping function. It provides a routine "garbage disposal" service to cells, eliminating damaged components that could otherwise become toxic. During starvation, autophagy can provide a nutrient source and thereby promote survival [76-78]. Autophagy is known to be involved in tumor suppression and antigen presentation [79] and is essential for the development of the embryo immediately after oocyte fertilization before it can absorb maternal nutrition [80]. Moreover, it was shown that autophagy-deficient mice have reduced amino acid levels in their tissues and plasma [81] suggesting that autophagy is not just a mechanism for the destruction of biomolecules, but also a mean of cell renewal [82].

The process of autophagy is divided into five phases: (i) initiation/regulation; (ii) phagophore nucleation; (iii) elongation and autophagosome formation; (iv) autophagosome-lysosome fusion and (v) cargo degradation.

1.5.2.1. Autophagy regulation

The first step of the autophagic pathway is the initiation phase, where cellular stresses induce signaling cascades culminating in the inhibition or induction of autophagy (Figure 6). In ample nutrient conditions, autophagy is inhibited by a nutrient sensor mTORC1. mTORC1 is activated

by growth factors and other factors that stimulate the class I phosphatidylinositol 3-kinase-threonine protein kinase (PI3K-AKT) signaling pathway. In contrast, stress stimuli, such as depletion of amino acids, induce autophagy through inhibition of mTORC1. mTORC1 inhibition allows the activation of the complex consisting of UNC-51–like kinase 1 (ULK1) and ATG13, which are crucial for autophagy initiation. Once activated, the ULK1 complex regulates the PI3K complex, which includes BECLIN-1, the class III phosphatidylinositol 3-kinase (VPS34), and ATG14L [82]. Stimulation of this complex generates phosphatidylinositol-3-phosphate (PI3P), which promotes vesicle nucleation and serves as signal to the recruitment of proteins required for vesicle elongation [83].

Another key regulator of autophagy is TFEB (transcription factor EB), which is a master transcription factor controlling cellular clearance. Similar to ATG13 and ULK1, TFEB is negatively regulated by mTORC1 and released following starvation to affect the expression of genes involved in lysosomal biogenesis and lipid catabolism [84]. TFEB family members control autophagy by directly regulating the expression of the mTOR-activating Rag GTPase complex, which provides a feedback circuit to balance the cellular metabolic state [85].

Autophagy can also be induced upon declining cellular energy levels. Deregulation of ATP/AMP ratio upon glucose deprivation activates regulatory kinases like 5′ AMP-activated protein kinase (AMPK) and serine/threonine-protein kinase STK11 (LKB1) [86]. LKB1 activates autophagy through AMPK by inhibition of mTORC1 either indirectly via activation of the TSC2 (tuberous sclerosis 2) complex or directly by phosphorylation of Raptor [87].

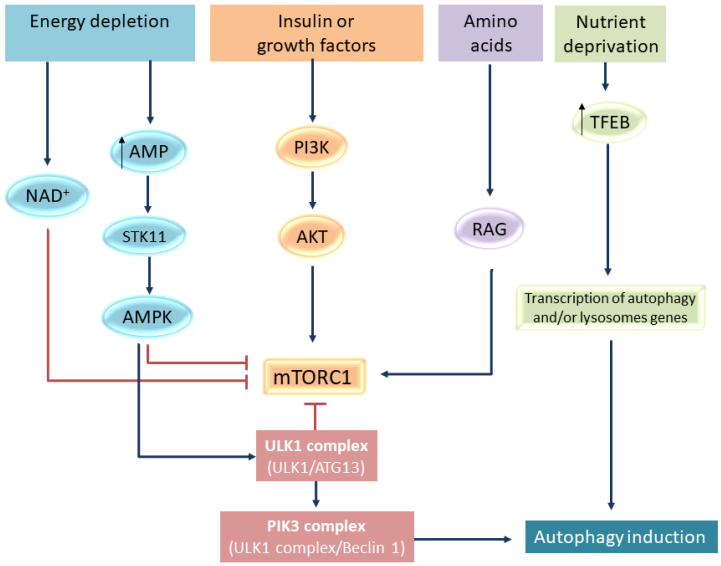

Figure 6: Canonical signaling networks for the regulation of autophagy. Mammalian target of rapamycin complex 1 (mTORC1) is the major negative regulator of autophagy, whereas AMP-activated protein kinase (AMPK) is a positive regulator. mTOR is activated by amino acids via the RAG family of GTPases or by growth factors through PI3K-AKT. AMPK is phosphorylated and activated by several upstream kinases, including serine/threonine protein kinase 11 (STK11). Once activated, AMPK can directly phosphorylate serine/ threonine protein kinase ULK1 (UNC-51–like kinase 1) and inhibit mTORC1 to promote autophagy. Depletion of cellular energy stores increases NAD+ levels and activates sirtuins which inhibit mTOR. mTOR inhibition allows the activation of the complex consisting of ULK1 and ATG13. Once activated, the ULK1 complex regulates the PI3K complex, which includes BECLIN-1. In addition, starvation stimulates the nuclear translocation of transcription factor EB (TFEB) to transactivate the expression of genes involved in autophagosome formation, lysosome biogenesis and lysosome function. PI3K, phosphoinositide 3-kinase

Autophagy can be directly regulated by ROS via ROS-responsive TFEB [88, 89], or post-transcriptionally via BECLIN-1 [90], or via ATG4B [91, 92]. ATG4B plays an important role in

ROS-regulated autophagy. Elezar and collaborates showed for the first time that ROS promote autophagy during starvation, suggesting they can act as signaling molecules [91]. Under starvation conditions, the production of ROS, specifically H_2O_2, was essential for autophagosome formation and autophagic degradation.

Finally, autophagy can respond to altered NADH levels that are controlled by the ETC [93, 94]. It was shown in proliferating cells that upon complex I defect, the increased NADH/NAD ratio suppress autophagy induced by mTOR inhibitors. In contrast, autophagy is enhanced by strategies that increase mitochondrial metabolism [94] with implications in cancer progression [93]. However, these findings come predominantly from proliferating cells and the mechanisms that modulate stress resistance and autophagy during quiescence have not been fully resolved.

1.5.2.2. Autophagy pathway

The autophagy pathway starts with the process of nucleation, i.e. formation of the phagophore, and is followed by elongation and maturation of autophagosomes (Figure 7). These phases of autophagy are concerted by a set of highly conserved autophagy genes (ATGs) and proteins such as microtubule-associated protein light chain 3B (LC3B). Autophagosome elongation requires two ubiquitin-like conjugation pathways, the ATG5-ATG12-ATG16L and the LC3 conjugation system. In the LC3 conjugation system, pre-LC3 is first proteolyzed to LC3B-I. Proteolysis of pre-LC3 on its C-terminus is in mammals preferentially done by the cysteine protease autophagy-related protein 4 B (ATG4B) [95]. Preprocessed LC3B-I is then activated by the E1 ubiquitin-like enzyme ATG7 and transferred to the E2 ubiquitin-like enzyme ATG3 that attaches phosphatidyl ethanolamine (PE) to LC3B-I. The resulting active, PE-conjugated form of LC3B

that stably associates with the autophagosome membrane is called LC3-II [96]. In the next step autophagosome fuses with lysosomes, forming autophagolysosomes, where the autophagic cargo is degraded by lysosomal proteases. After fusion with lysosomes, both autophagosome cargo and inner limiting membrane are degraded and the resulting monomeric structures are exported to cytosol for reuse in biosynthesis or energy production [97].

Although autophagy, as a quality control process may occur in a non-selective manner, increasing evidence indicates selectivity in the recognition of the structures that are to be degraded by autophagy. Selective autophagy requires not only molecular tag(s) such as ubiquitin chains but also the presence cargo receptors or adaptors such as p62/SQSTM1 (sequestosome 1) and neighbor of BRCA1 (NBR1). These proteins can on one hand recognize (ubiquitinated) cargo destined for autophagic degradation and on the other hand can bind to a component of the forming autophagosomes [98].

The activity of the autophagy pathway can be followed by chemical inhibitors that target distinct stages of the autophagy process. These include early and late-stage inhibitors. Early-stage inhibitors, such as 3- methyladenine, wortmannin, and LY294002, interfere with nucleation of the phagophore [99]. Late-stage inhibitors, such as chloroquine, hydroxychloroquine, monensin, and bafilomycin A1, prevent acidification of lysosomes impairing cargo degradation by digestive hydrolases [99, 100]. Treatment with late-stage inhibitors results in an accumulation of the active form of LC3, LC3-II (see above), which can be detected by western blot and provide information about the autophagic flux in the cell. As an

example, detection of more LC3B protein upon bafilomycin A1 treatment indicates increased autophagic flux.

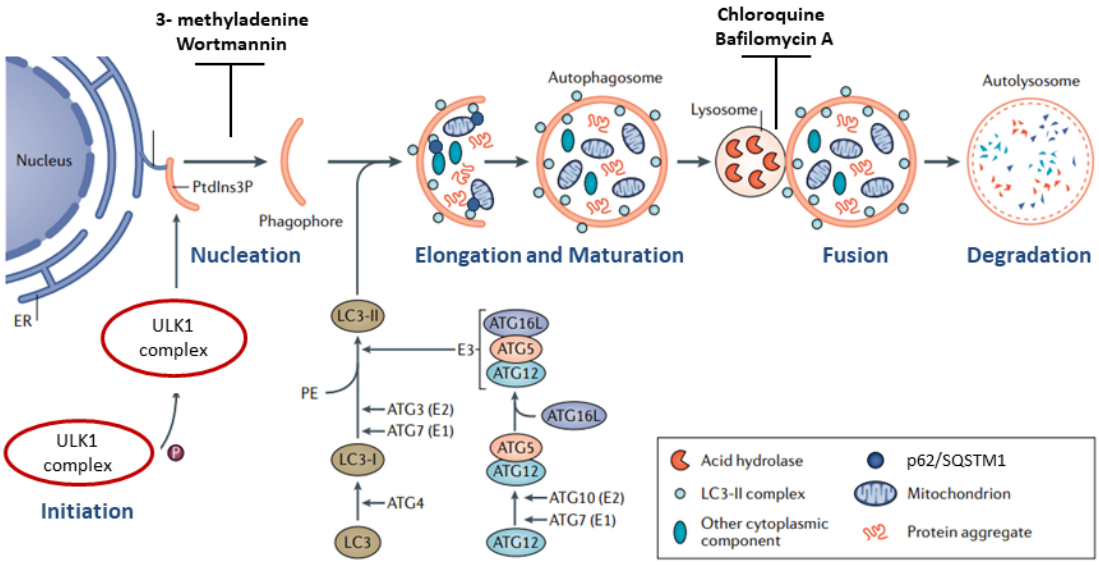

Figure 7: Core autophagic machinery. Autophagy is a multistep process involving initiation, nucleation of the phagophore, elongation and maturation of the autophagosome, fusion and degradation. Upon induction, the ULK1 complex phosphorylates multiple substrates, including components of the phosphoinositide 3-kinase (PI3K) III nucleation complex to promote the nucleation of a double membrane structure known as phagophore. This complex produces phosphatidylinositol-3-phosphate (PtdIns3P) which recruits PtdIns3P-binding proteins for phagophore expansion. The levels of these proteins can be depleted by inhibition of PI3K by 3-methyladenine or wortmannin. There are two ubiquitin-like conjugation systems participate in autophagosome elongation and completion, the ATG12–ATG5–ATG16L system and the microtubule-associated protein 1 light chain 3 (LC3) system. The completed autophagosome then fuses with a lysosome to form an autolysosome, in which the autophagosome inner membrane and cargos (delivered by p62/SQSTM1) are degraded by lysosomal hydrolases and eventually released for recycling. The fusion process is regulated by a large set of molecules, including cytoskeleton components and related motor proteins and can be inhibited by

chloroquine and bafilomycin A1. E1, ubiquitin-activating enzyme; E2, ubiquitin-conjugating enzyme; E3, ubiquitin ligase; ER, endoplasmic reticulum; PE, phosphatidylethanolamine. Adapted from [101].

1.5.2.3. Autophagy in cell proliferation and quiescence

As mentioned above, quality control systems such as autophagy play a critical role in quiescent cells which need to stay in the non-proliferating state for a prolonged time. Indeed, impaired autophagy by depletion of autophagic genes ATG7 and ATG5 in vivo results in a lethal loss of normal function of quiescent cells [102-104]. Autophagy deficiency increased the abundance of mitochondria, stimulating mitochondrial ROS production and enhancing ROS-derived oxidative damage of cellular components, resulting in cell death [102, 104]. Moreover, maintenance of a high basal autophagy flux can attenuate toxicity in quiescent satellite cells [105]. Similarly to healthy tissue, autophagy also plays a role in proliferating cancer cells and thus in tumor progression. However, the effects of autophagy in cancer are paradoxical as autophagy can prevent tumor initiation, but also support growth of established tumors [106].

Considering the significance of autophagy in proliferating and quiescent cells, better understanding how this process is regulated will have relevance for mammalian physiology and pathology.

2. AIMS

In this project we aim to reveal the function of OXPHOS in proliferating and quiescent cells and how these cells react to OXPHOS inhibition/dysfunction. This general goal is divided into specific aims:

1. Investigate why functional OXPHOS is crucial for tumorigenesis.

   a. Which aspect of OXPHOS activity is limiting for tumor growth?

   b. Does OXPHOS have a signaling role with respect to biosynthesis?

2. Investigate the specificity of ETC inhibitors in tumor suppression.

   a. What determines the specificity of ETC inhibitors for proliferating (cancer) cells, while sparing cells of quiescent healthy tissue?

   b. Does the antioxidant defense provide resistance to ETC inhibitors in quiescent cells and what are the key antioxidant components responsible for this resistance?

3. Investigate the role of OXPHOS in quiescent cells.

   a. Is it linked to stress resistance, such as antioxidant defense or autophagy?

   b. Which aspects of OXPHOS function are important in quiescent cells and what are the pathways/system that OXPHOS regulates?

3. LIST OF METHODS

Below is a list of methods used by the author while preparing the publications included in the thesis.

Cell culture

- Cancer cells
- Non-malignant cells: endothelial and epithelial cells and mouse embryonic fibroblasts (MEFs)

Cell fractionation

- Isolation of mitochondrial, nuclear, and cytosolic fractions

Cloning

Preparation of cellular sublines

- Transfection with expressing vectors
- RNA interference (shRNA, siRNA)

Electrophoretic methods and western blotting

- SDS-PAGE
- Blue native-PAGE

Microscopy

- Fluorescent microscopy
- Confocal microscopy

- Transmission electron microscopy

Flow cytometry

- Detection of cell death
- Cell cycle analysis
- Fluorescent probes (ROS, Autophagy)
- Immunodetection

Activity assays

- ATG4B activity
- DHODH activity
- In gel enzymatic activity of antioxidant enzymes
- Cytochrome C Oxidase / Succinate Dehydrogenase (COX/SDH) activity in situ

Colorimetric assays

- ATP levels
- Lactate formation
- $NADH/NAD^+$ ratio

Respiration and glycolysis evaluation

- Oroboros oxygraph measurement (DHODH respiration)
- Seahorse

High throughput methodology

- RNAseq
- Metabolomics
- Proteomics

Mice work

- Intra-peritoneal, intra-vein and sub-cutaneous administrations,
- Monitoring of subcutaneous tumor growth
- Dissections, collection of tissues
- EdU-based detection of proliferating cells
- In situ cell death and ROS measurements

4. RESULTS

The presented thesis consists of a total of four publications. Below is a summary of results achieved in each publication.

1. Bajzikova, M., Kovarova, J., Coelho, A. R., Boukalova, S., Oh, S., Rohlenova, K., Svec, D., Hubackova, S., Endaya, B., Judasova, K., Bezawork-Geleta, A., Kluckova, K., Chatre, L., Zobalova, R., Novakova, A., Vanova, K., Ezrova, Z., Maghzal, G. J., **Magalhaes-Novais, S**., Olsinova, M., Krobova, L., An, Y. J., Davidova, E., Nahacka, Z., Sobol, M., Cunha-Oliveira, T., Sandoval-Acuna, C., Strnad, H., Zhang, T., Huynh, T., Serafim, T. L., Hozak, P., Sardao, V. A., Koopman, W. J. H., Ricchetti, M., Oliveira, P. J., Kolar, F., Kubista, M., Truksa, J., Dvorakova-Hortova, K., Pacak, K., Gurlich, R., Stocker, R., Zhou, Y., Berridge, M. V., Park, S., Dong, L., Rohlena, J. and Neuzil, J. (2018). "**Reactivation of Dihydroorotate Dehydrogenase-Driven Pyrimidine Biosynthesis Restores Tumor Growth of Respiration-Deficient Cancer Cells.**" Cell Metab. 29(2): 399-416 e310.

Impactor factor = 22.78

Proliferating cancer cells without mitochondrial mtDNA do not form tumors unless they highjack mitochondria from the host. In this study, we showed that the acquired mitochondrial electron transport chain is necessary to drive de novo pyrimidine synthesis to overcome cell-cycle arrest. Surprisingly, ATP generation is dispensable for tumorigenesis in this context. We highlighted the role of DHODH and CoQ redox cycling as a bottleneck for pyrimidine synthesis in non-respiring cells.

Contribution to the publication: Experimental work (cell culture, stable transfections and mice experiments).

2. Bezawork-Geleta, A., Wen, H., Dong, L., Yan, B., Vider, J., Boukalova, S., Krobova, L., Vanova, K., Zobalova, R., Sobol, M., Hozak, P., **Magalhaes-Novais, S**., Caisova, V., Abaffy, P., Naraine, R., Pang, Y., Zaw, T., Zhang, P., Sindelka, R., Kubista, M., Zuryn, S., Molloy, M. P., Berridge, M. V., Pacak, K., Rohlena, J., Park, S. and Neuzil, J. (2018). "**Alternative assembly of respiratory complex II connects energy stress to metabolic checkpoints**." Nat Commun 9(1): 2221.

Impactor Factor = 12.35

Cancer cell growth and survival depend on a delicate balance between energy production and synthesis of metabolites. Here, we provide evidence that an alternative mitochondrial complex II (CII) assembly species, designated as CII_{low}, serves as a checkpoint for metabolite biosynthesis under bioenergetic stress in proliferating cancer cells. We observed that depletion of CII_{low} leads to an imbalance in energy utilization and metabolite synthesis, as the presence of CII_{low} mediates suppression of energetically demanding de novo pyrimidine synthesis. Analysis of paraganglioma tissues from patients with sporadic, SDHA and SDHB mutations further corroborated the in vitro findings. These results suggest that CII_{low} is a core complex inside mitochondria that provides homeostatic control of cellular metabolism depending on the availability of energy in proliferating cells.

Contribution to the publication: Experimental part (cell culture, RNA isolation and Blue native-PAGE).

3. Blecha, J., **Magalhaes-Novais, S.**, Rohlenova, K., Novotna, E., Lettlova, S., Schmitt, S., Zischka, H., Neuzil, J., and Rohlena, J. (2017). "**Antioxidant defense in quiescent cells determines selectivity of electron transport chain inhibition-induced cell death**." Free Radic Biol Med **112**: 253-266.

Impact factor = 6.02

Mitochondrial electron transport chain (ETC) targeting has shown great promise in cancer therapy. However, why modern ETC-targeted compounds are tolerated on the organismal level remains unclear**.** We showed that quiescent cells, despite increased utilization of the ETC and enhanced supercomplex assembly, are less susceptible to cell death induced by ETC disruption when glucose is not limiting compared with proliferating cells. In this settings, increased detoxification of ETC-derived ROS by mitochondrial antioxidant defense, mainly by the superoxide dismutase 2 – thioredoxin axis, explained the resilience of OXPHOS inhibitors in quiescent cells. In contrast, we showed that in conditions of limited glucose, e.g. in poorly perfused tumors, ETC disruption causes rapid depletion of cellular ATP, optimizing impact towards tumor-associated dormant cells. All together we suggested that antioxidant defense in quiescent cells is aided by local glucose limitations to ensure selectivity of ETC inhibition-induced cell death.

Contribution to the publication: Experimental part (cell culture, preparation of expression plasmids, transient transfections and selection of sublines, cell death and ROS measurements by flow cytometry).

4. **Magalhaes-Novais, S**., Blecha, J., Naraine, R., Mikesova, J., Abaffy, P., Pecinova, A., Milosevic, M., Bohuslavova, R., Prochazka, J., Khan, S., Novotna, E., Sindelka, R., Machan, R., Dewerchin, M., Vlcak, E., Kalucka, J., Stemberkova Hubackova, S., Benda, A., Goveia, J., Mracek, T., Barinka, C., Carmeliet, P., Neuzil, J., Rohlenova, K., and Rohlena, J. (2022). **"Mitochondrial respiration supports autophagy to provide stress resistance during quiescence**." Autophagy: 1-18, published online ahead of print

Impactor factor = 16.02

We have shown before that OXPHOS supports biosynthesis during proliferation. However, the role of OXPHOS during quiescence, beyond ATP production, is not well understood. In this study, using two transgenic mouse models of OXPHOS-deficiency: (i) Inducible whole-body *Tfam* knock-out mice ($TFAM^{KO}$), (ii) inducible endothelial-specific *Tfam* knock-out mice ($TFAM^{ECKO}$) mice, we observed that in quiescent cells and tissues, OXPHOS actively initiates an autophagy-based mechanism to maintain oxidative stress resistance and counter ROS-induced damage inherently linked to OXPHOS function.

Autophagy and ROS resistance are suppressed in OXPHOS-deficient quiescent cells and mouse tissues, but not in OXPHOS-deficient proliferating cells. Mechanistically, ROS generated in the ETC attenuate the activity of ATG4B, a modulator of autophagy. OXPHOS-deficiency during quiescence leads to reduced baseline ROS levels and over-active ATG4B.

We further explored the physiological relevance of our findings. Using tumor-bearing $TFAM^{KO}$ mice treated with ROS-inducing anti-cancer agents (PEITC and doxorubicin) we showed that OXPHOS-deficiency or autophagy inhibition results in an increase in cell death specifically in healthy tissue, demonstrating that functional OXPHOS limits toxicity of ROS-based cancer

therapy and opens the therapeutic window. Moreover, by selectively ablating OXPHOS in mouse endothelium ($TFAM^{ECKO}$ mice) we demonstrate that LPS-induced systemic inflammation increased oxidative stress in OXPHOS-deficient (but not wild type) endothelium in vivo, which led to increased vessel permeability and severe leukocyte extravasation. Similarly, $TFAM^{ECKO}$ were highly susceptible to inflammatory bowel disease induced by dextran sodium sulphate administration, a condition associated with increased oxidative stress in the endothelium. $TFAM^{ECKO}$ mice suffered from extensive vascular leakage and leukocyte extravasation in the colon and showed more pronounced signs of colitis. Hence, OXPHOS-mediated oxidative stress resistance in the endothelium provides protection from inflammatory disorders.

Contribution to the publication: Study design. Experimental part (cell culture, RNA interference, stable and transient transfections and selection of sublines, apoptosis and ROS measurements, flow cytometry, confocal microscopy, enzymatic assays, western blotting, oxygraph measurements and mice experiments). Data analysis, manuscript writing, preparation of figures.

5. DISCUSSION

Mitochondrial respiration sustained by the OXPHOS system is crucial for most living organisms. OXPHOS, best known for its role in energy production, is also responsible for ROS generation and biosynthesis of metabolites. However, the relevance of these latter functions in proliferating and quiescent cells was unclear. The key finding of our studies therefore is that OXPHOS switches its function from supporting biosynthesis in proliferating cells to providing stress resistance (via ROS-stimulated autophagy) in quiescent cells.

The importance of mitochondria for the initiation and progression of tumorigenesis has been thoroughly documented. Indeed, tumors have active mitochondrial bioenergetic metabolism despite the well-known upregulation of glycolysis also known as the Warburg effect [107, 108]. Disruption of the ETC inhibits cancer cell proliferation and induces cell death [66, 109-111]. In fact, also mtDNA mutations or genetic ablation of OXPHOS were shown to restrain tumorigenesis [42, 47]. Disruption of the ETC thus seems to be a promising strategy for cancer therapy, but more insight is required before it becomes a new treatment option for patients. For instance, the previous studies did not identify which aspect of OXPHOS function is essential in this context. Here, using proliferating cancer cells deficient in ATP synthase, we made a surprising finding that these cells readily form tumors, suggesting that mitochondrial ATP production is not limiting for tumor growth. Instead, we found that the important OXPHOS-related feature that promotes tumorigenesis is de novo pyrimidine synthesis, directly driven by respiration via DHODH (an enzyme associated with OXPHOS) which converts dihydroorotate (DHO) to orotate, a pyrimidine precursor. This was clearly demonstrated by the failure of DHODH-deficient cells to form tumors, despite the fact that these cells show fully functional

OXPHOS and normal ATP levels. The central role for DHODH in tumorigenesis is consistent with a recent report demonstrating upregulation of DHODH during the course of UV-induced skin tumorigenesis and its functional role therein [112].

The link between OXPHOS and DHODH is maintained by CoQ redox cycling because electrons removed from DHO by DHODH are transferred to CoQ yielding CoQH2, which is then re-oxidized at CIII/CIV [52, 53] (Figure 3). Indeed, OXPHOS-deficient cancer cells showed higher ratio of reduced to oxidized ubiquinone (CoQH2/CoQ). The reactivation of DHODH-driven respiration by AOX expression, an alternative oxidase which can reconstitute CIII/CIV activity, was sufficient to normalize CoQH2/CoQ and restore tumorigenicity in the absence of mtDNA. These results suggest that CoQ redox cycling that propels DHODH is essential for tumorigenicity, a finding recently confirmed by an independent study [113]. DHODH may thus be a promising target for broad-spectrum cancer therapy, and its inhibition has shown efficacy in cancer settings either alone or in combination with other anti-cancer agents [114-116]. Furthermore, blocking CIII might be an even better anti-tumor strategy. CIII inhibition would increase the CoQH2/CoQ ratio, which would not only interfere with DHODH-driven pyrimidine synthesis, but also increase ROS generation from the redox centers upstream in the ETC [30, 31, 117]. In such a scenario the cancer cell would be hit by cell death induced by excessive oxidative stress [109] in combination with the cytostatic effect of DHODH inhibition.

The balance between energy production and synthesis of metabolites is essential for cell growth and survival. Here, we pointed out the regulatory role of CII of OXPHOS with respect to energy conservation in proliferative cancer cells. Besides its role in OXPHOS, CII converts succinate to fumarate in the TCA cycle, and is thus at the crossroad of the TCA cycle and OXPHOS. CII contains nuclear-encoded SDHA, SDHB, SDHC, and SDHD subunits and for

that reason the effects of mtDNA mutations in cancer on CII have not been in focus. Here, we provide evidence that following mtDNA depletion or SDHB deficiency, an alternative CII with different activity is formed. This alternative assembly of CII (CII_{low}) modulates metabolism in response to compromised mitochondrial bioenergetics in proliferating tumor cells. We suggest that the existence of CII_{low} in patients with SDHB-mutated paragangliomas may contribute to a cellular mechanism resulting in severe pathological outcomes, including enhanced migration and invasiveness as previous described [118, 119].

Apart from observations presented here, independent studies have reported that compromised OXPHOS activity due to CI inhibition suppresses tumor growth by limiting aspartate biosynthesis [120, 121]. Combined with our findings we can thus conclude that OXPHOS plays a major role in maintaining and regulating biosynthesis during proliferation, in particular de novo synthesis of pyrimidine nucleotides. For this reason, targeting OXPHOS by inhibitors in proliferating cancer cells might be a very plausible anticancer strategy, as has been suggested by previous studies [110, 122]

In contrast to proliferating cells, quiescent cells require increased protection from oxidative damage to maintain their long-lived components and support their extended life span. Here, we provide evidence that quiescent cells, under ample glucose supply, upregulate their antioxidant defense to cope with increased ROS levels. The enhanced antioxidant defense makes quiescent cells more resilient to effect of OXPHOS inhibitors that produce ROS. This is in line with previous findings demonstrating increased resistance of quiescent cells to oxidative challenge [13, 123, 124]. We also found that this ROS protection was provided specifically by the SOD2 - thioredoxin axis. The situation changes dramatically when glucose becomes limiting. Under these condition quiescent cells became highly sensitized to ETC inhibitors and the

increased cell death was largely ROS-independent and was due to severe depletion of ATP instead. This extreme sensitivity to combined glucose limitation/ETC inhibition seemed to result from the inability of quiescent cells to efficiently upregulate glucose transporters to efficiently scavenge the residual extracellular glucose to maintain some residual ATP level.

In normal healthy tissues where perfusion is intact, glucose does not present a limiting factor. It is thus expected that effective inactivation of ETC blockade-induced ROS by antioxidant defense will play the primary role in governing sensitivity, and quiescent tissues will remain resistant to pharmacological ETC inhibition. In contrast, in poorly perfused regions, such as hypoxic areas of tumors where the availability of nutrients is low, the application of ETC inhibitors may significantly accelerate cell death in a ROS-independent manner as demonstrated previously [125]. This will supplement the ROS-related effects and optimize impact towards cancer, including cancer cells with a dormant-like phenotype.

Pharmacological inhibition of OXPHOS by specific inhibitors blocks the electron transfer/ATP generation and at the same time increases ROS production. However, ROS production, along with ATP generation and biosynthesis, is a major consequence of OXPHOS activity. To establish the role of OXPHOS during quiescence, we thus sought a better model system where production of ROS is abolished. Hence, we eliminated OXPHOS completely in vitro and in vivo by removing mtDNA or by blocking its transcription in quiescent cells and in mice. Using this approach, we provide evidence that during quiescence OXPHOS maintains stress resistance by continuously generating low levels of ROS, which supports basal autophagic flux and provides constitutive level of ROS protection during quiescence.

We show that the OXPHOS/autophagy-mediated oxidative stress resistance is relevant in several patho-physiological scenarios. First, we document that OXPHOS/autophagy ensure

specificity of anti-cancer therapy by protecting normal non-proliferative tissues when tumors are treated with ROS-inducing anticancer agents, providing a therapeutic window. Hence, while many investigations focused on why tumors are sensitive to therapy, here we addressed an equally important, yet understudied question of why normal tissues are resistant. Our findings warrant caution when using autophagy inhibitors (chloroquine is in clinical trials in cancer) with ROS-inducing agents. Such a combination has the potential to compromise selectivity and thereby increase toxicity of cancer therapy. Second, by selectively ablating OXPHOS in adult quiescent endothelium, which is relatively independent of ATP production via OXPHOS, we document increased susceptibility of mice to systemic as well as local inflammation, conditions associated with oxidative stress in endothelial cells. OXPHOS ablation exacerbated oxidative stress in endothelial cells during inflammation, leading to increased vessel permeability and leukocyte extravasation. A similar phenotype was observed when resistance of endothelial cells to oxidative stress was reduced by alternative manipulations [68]. This demonstrates that OXPHOS/autophagy protect endothelial cells during inflammatory conditions such as colitis associated with IBD, documenting a new role for OXPHOS as a guardian against oxidative stress in quiescent endothelium. Others have shown that OXPHOS-mediated biosynthesis is crucial for biomass buildup in proliferating endothelial cells during angiogenesis [126], demonstrating that distinct functions of OXPHOS during proliferation and quiescence (i.e., biomass buildup versus stress protection) are maintained in vivo.

Our findings point to stark differences in regulation of stress resistance/autophagy in proliferating and quiescent cells. While in quiescent cells OXPHOS deficiency abrogated autophagy and resistance to stress, it had no effect in proliferating cells. Furthermore, our results indicate that during quiescence ETC signals to autophagy via ROS, but not via NADH. In

contrast, NADH has been found to regulate autophagy in proliferating cells [93, 94], pointing to distinct autophagy regulation during proliferation and quiescence. Consequently, NADH may be the dominant regulator of autophagy in proliferating cells which require biosynthesis (NADH:NAD^+ ratio is crucial for biosynthesis), while ROS become important in quiescent cells that accentuate stress resistance (ROS are important stressors). This is consistent with the dual role of OXPHOS which provides biosynthesis during proliferation and stress resistance during quiescence, reflecting the distinct needs of these two states.

How does OXPHOS, the main producer of intracellular ROS, induce protection against oxidative stress in quiescent cells? We propose that this is an active process where continuous low-level generation of endogenous ROS from the ETC attenuates the activity of ATG4B, a redox-regulated member of the autophagy cascade [91]. Such ROS-mediated ATG4B modulation sustains the basal, protective autophagy. The absence of ETC-produced ROS in OXPHOS-deficient cells is amplified by the quiescence-induced elevation of antioxidant defense, leading to unrestrained ATG4B activity that suppresses autophagy. Supplementation of OXPHOS-deficient quiescent cells with ROS normalized ATG4B activity and rescued autophagy as well as ROS resistance, which was phenocopied by direct attenuation of ATG4B activity by specific inhibitors or by RNA silencing. These findings favor a model where OXPHOS supports autophagy during quiescence by maintaining the optimal intracellular redox balance. In this way, OXPHOS/autophagy, along with the antioxidant defense, represent a basal, constitutive layer of ROS resistance in quiescent cells.

OXPHOS-mediated resistance to oxidative stress is conserved over multiple tissues and cell types, suggesting its ancient origin. This may have interesting evolutionary connotations. Eukaryotic cells acquired mitochondria to benefit from oxygen through oxidative metabolism

for efficient ATP production and biosynthesis, making complex life possible. At the same time, they apparently built in an autophagy-based mechanism to protect against oxygen levels that rose throughout the evolution of multicellular life forms [127] and that predispose to oxidative stress. In addition, by coupling OXPHOS to autophagy evolution would devise a safety measure against ROS-induced damage inherent to energy generation by mitochondria. The OXPHOS system thus features unexpected plasticity and readily adapts to specific requirements of cellular proliferation and quiescence with prominent functional consequences for pathology.

6. CONCLUSIONS

Far from being a simple purveyor of ATP, OXPHOS shows considerable plasticity and generates specific metabolic signatures during proliferation and quiescence.

In proliferating cancer cells OXPHOS is essential for pyrimidine biosynthesis, rather than OXPHOS-mediated ATP production. OXPHOS drives the activity of DHODH enzyme via CoQ redox cycling to enable proliferation of cancer cells within tumors. These findings establish an important link between de novo pyrimidine synthesis and respiration, which may contribute to development of broad-spectrum cancer therapy.

OXPHOS component CII in proliferating cancer cells can sense respiratory insufficiency and alter its assembly to downregulate de novo pyrimidine biosynthesis pathway to conserve cellular energy and increase invasiveness. Hence, CII can regulate biosynthesis.

In contrast, during quiescence OXPHOS does not contribute to biosynthesis. Instead, it provides oxidative stress resistance by maintaining basal autophagy flux. Mechanistically, OXPHOS constitutively generates low levels of ROS that suppress activity of ATG4B, a regulator of autophagy. The OXPHOS-mediated stress resistance in the endothelium is required to combat inflammation, and functional OXPHOS in normal tissues ensures selectivity of ROS-based anticancer therapy. Indeed, under physiological glucose levels, the ETC-directed anticancer compounds (and other ROS-inducing agents) are well tolerated by normal tissues, partially because of the mechanisms above (these compounds induce, not abolish ROS production from the ETC) and due to increased antioxidant defense in quiescent cells (in particular the SOD2-thioredoxin axis).

In summary, we present a concept that OXPHOS has additional vital roles beyond ATP production, and these roles fulfil the unique requirements of proliferating and quiescent cells. (Figure 8).

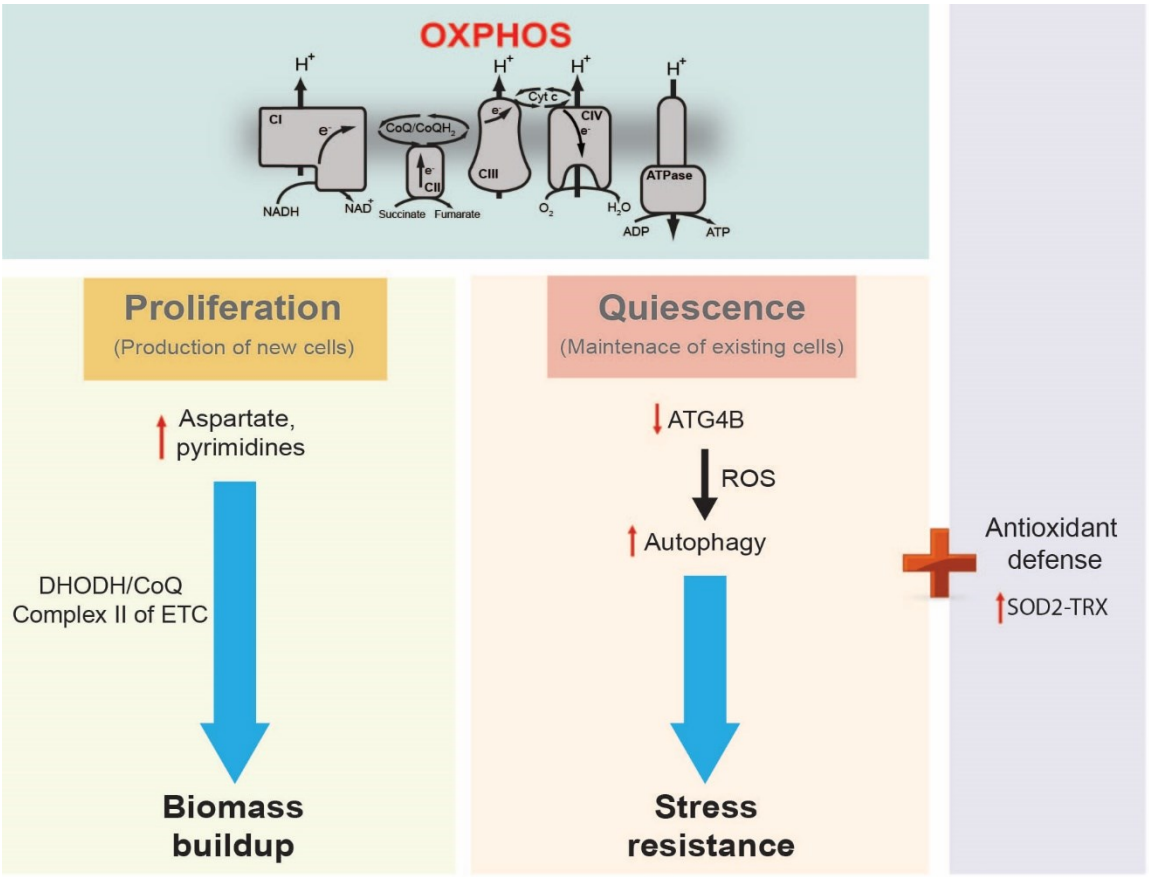

Figure 8: Distinct roles of OXPHOS during proliferation and quiescence. The proposed model depicts specific roles of OXPHOS in proliferating and quiescent cells. In proliferating cells OXPHOS supports biosynthesis, whereas in quiescent cells it provides stress resistance.

7. REFERENCES

1. Marescal, O. and I.M. Cheeseman, *Cellular Mechanisms and Regulation of Quiescence.* Dev Cell, 2020. **55**(3): p. 259-271.

2. Goddard, E.T., et al., *Dormant tumour cells, their niches and the influence of immunity.* Nat Cell Biol, 2018. **20**(11): p. 1240-1249.

3. Malumbres, M., *Cyclin-dependent kinases.* Genome Biol, 2014. **15**(6): p. 122.

4. Aktas, H., H. Cai, and G.M. Cooper, *Ras links growth factor signaling to the cell cycle machinery via regulation of cyclin D1 and the Cdk inhibitor p27KIP1.* Mol Cell Biol, 1997. **17**(7): p. 3850-7.

5. Bjornson, C.R., et al., *Notch signaling is necessary to maintain quiescence in adult muscle stem cells.* Stem Cells, 2012. **30**(2): p. 232-42.

6. Artavanis-Tsakonas, S., M.D. Rand, and R.J. Lake, *Notch signaling: cell fate control and signal integration in development.* Science, 1999. **284**(5415): p. 770-6.

7. Itahana, K., et al., *A role for p53 in maintaining and establishing the quiescence growth arrest in human cells.* J Biol Chem, 2002. **277**(20): p. 18206-14.

8. Kops, G.J., et al., *Forkhead transcription factor FOXO3a protects quiescent cells from oxidative stress.* Nature, 2002. **419**(6904): p. 316-21.

9. Tothova, Z., et al., *FoxOs are critical mediators of hematopoietic stem cell resistance to physiologic oxidative stress.* Cell, 2007. **128**(2): p. 325-39.

10. Kamminga, L.M., et al., *The Polycomb group gene Ezh2 prevents hematopoietic stem cell exhaustion.* Blood, 2006. **107**(5): p. 2170-9.

11. Evertts, A.G., et al., *H4K20 methylation regulates quiescence and chromatin compaction.* Mol Biol Cell, 2013. **24**(19): p. 3025-37.

12. Lemons, J.M., et al., *Quiescent fibroblasts exhibit high metabolic activity.* PLoS Biol, 2010. **8**(10): p. e1000514.

13. Hubackova, S., et al., *Mitochondria-driven elimination of cancer and senescent cells.* Biol Chem, 2019. **400**(2): p. 141-148.

14. De Bock, K., et al., *Role of PFKFB3-driven glycolysis in vessel sprouting.* Cell, 2013. **154**(3): p. 651-63.

15. Chakrabarty, R.P. and N.S. Chandel, *Mitochondria as Signaling Organelles Control Mammalian Stem Cell Fate.* Cell Stem Cell, 2021. **28**(3): p. 394-408.

16. Green, D.R. and J.C. Reed, *Mitochondria and apoptosis.* Science, 1998. **281**(5381): p. 1309-12.

17. Larsson, N.G., et al., *Mitochondrial transcription factor A is necessary for mtDNA maintenance and embryogenesis in mice.* Nat Genet, 1998. **18**(3): p. 231-6.

18. Pohjoismaki, J.L., et al., *Alterations to the expression level of mitochondrial transcription factor A, TFAM, modify the mode of mitochondrial DNA replication in cultured human cells.* Nucleic Acids Res, 2006. **34**(20): p. 5815-28.

19. Moreno, A.J., et al., *Measuring Mitochondrial Membrane Potential with a Tetraphenylphosphonium-Selective Electrode.* Curr Protoc Toxicol, 2015. **65**: p. 25 5 1-16.

20. Sun, F., et al., *Crystal structure of mitochondrial respiratory membrane protein complex II.* Cell, 2005. **121**(7): p. 1043-57.

21. Cecchini, G., *Function and structure of complex II of the respiratory chain.* Annu Rev Biochem, 2003. **72**: p. 77-109.

22. Ikeda, K., et al., *A stabilizing factor for mitochondrial respiratory supercomplex assembly regulates energy metabolism in muscle.* Nat Commun, 2013. **4**: p. 2147.

23. Blaza, J.N., et al., *Kinetic evidence against partitioning of the ubiquinone pool and the catalytic relevance of respiratory-chain supercomplexes.* Proc Natl Acad Sci U S A, 2014. **111**(44): p. 15735-40.

24. Maranzana, E., et al., *Mitochondrial respiratory supercomplex association limits production of reactive oxygen species from complex I.* Antioxid Redox Signal, 2013. **19**(13): p. 1469-80.

25. Acin-Perez, R. and J.A. Enriquez, *The function of the respiratory supercomplexes: the plasticity model.* Biochim Biophys Acta, 2014. **1837**(4): p. 444-50.

26. Kluckova, K., et al., *Ubiquinone-binding site mutagenesis reveals the role of mitochondrial complex II in cell death initiation.* Cell Death Dis, 2015. **6**: p. e1749.

27. Moreno-Sanchez, R., et al., *Reactive oxygen species are generated by the respiratory complex II--evidence for lack of contribution of the reverse electron flow in complex I.* FEBS J, 2013. **280**(3): p. 927-38.

28. Chen, Q., et al., *Production of reactive oxygen species by mitochondria: central role of complex III.* J Biol Chem, 2003. **278**(38): p. 36027-31.

29. Dong, L.F., et al., *Mitochondrial targeting of vitamin E succinate enhances its pro-apoptotic and anti-cancer activity via mitochondrial complex II.* J Biol Chem, 2011. **286**(5): p. 3717-28.

30. Quinlan, C.L., et al., *Sites of reactive oxygen species generation by mitochondria oxidizing different substrates.* Redox Biol, 2013. **1**: p. 304-12.

31. Murphy, M.P., *How mitochondria produce reactive oxygen species.* Biochem J, 2009. **417**(1): p. 1-13.

32. Brand, M.D., *Mitochondrial generation of superoxide and hydrogen peroxide as the source of mitochondrial redox signaling.* Free Radic Biol Med, 2016. **100**: p. 14-31.

33. Schreck, R., P. Rieber, and P.A. Baeuerle, *Reactive oxygen intermediates as apparently widely used messengers in the activation of the NF-kappa B transcription factor and HIV-1.* EMBO J, 1991. **10**(8): p. 2247-58.

34. Wang, X., et al., *The cellular response to oxidative stress: influences of mitogen-activated protein kinase signalling pathways on cell survival.* Biochem J, 1998. **333 (Pt 2)**: p. 291-300.

35. Schreck, R. and P.A. Baeuerle, *A role for oxygen radicals as second messengers.* Trends Cell Biol, 1991. **1**(2-3): p. 39-42.

36. Holmstrom, K.M. and T. Finkel, *Cellular mechanisms and physiological consequences of redox-dependent signalling.* Nat Rev Mol Cell Biol, 2014. **15**(6): p. 411-21.

37. Sundaresan, M., et al., *Requirement for generation of H2O2 for platelet-derived growth factor signal transduction.* Science, 1995. **270**(5234): p. 296-9.

38. Chandel, N.S., et al., *Reactive oxygen species generated at mitochondrial complex III stabilize hypoxia-inducible factor-1alpha during hypoxia: a mechanism of O2 sensing.* J Biol Chem, 2000. **275**(33): p. 25130-8.

39. Tormos, K.V., et al., *Mitochondrial complex III ROS regulate adipocyte differentiation.* Cell Metab, 2011. **14**(4): p. 537-44.

40. Hampton, M.B. and S. Orrenius, *Dual regulation of caspase activity by hydrogen peroxide: implications for apoptosis.* FEBS Lett, 1997. **414**(3): p. 552-6.

41. Szatrowski, T.P. and C.F. Nathan, *Production of large amounts of hydrogen peroxide by human tumor cells.* Cancer Res, 1991. **51**(3): p. 794-8.

42. Weinberg, F., et al., *Mitochondrial metabolism and ROS generation are essential for Kras-mediated tumorigenicity.* Proc Natl Acad Sci U S A, 2010. **107**(19): p. 8788-93.

43. Nieborowska-Skorska, M., et al., *Rac2-MRC-cIII-generated ROS cause genomic instability in chronic myeloid leukemia stem cells and primitive progenitors.* Blood, 2012. **119**(18): p. 4253-63.

44. Gorrini, C., I.S. Harris, and T.W. Mak, *Modulation of oxidative stress as an anticancer strategy.* Nat Rev Drug Discov, 2013. **12**(12): p. 931-47.

45. Schieber, M. and N.S. Chandel, *ROS function in redox signaling and oxidative stress.* Curr Biol, 2014. **24**(10): p. R453-62.

46. Spinelli, J.B. and M.C. Haigis, *The multifaceted contributions of mitochondria to cellular metabolism.* Nat Cell Biol, 2018. **20**(7): p. 745-754.

47. Tan, A.S., et al., *Mitochondrial genome acquisition restores respiratory function and tumorigenic potential of cancer cells without mitochondrial DNA.* Cell Metab, 2015. **21**(1): p. 81-94.

48. Lane, A.N. and T.W. Fan, *Regulation of mammalian nucleotide metabolism and biosynthesis.* Nucleic Acids Res, 2015. **43**(4): p. 2466-85.

49. Loffler, M., et al., *Pyrimidine pathways in health and disease.* Trends Mol Med, 2005. **11**(9): p. 430-7.

50. Birsoy, K., et al., *An Essential Role of the Mitochondrial Electron Transport Chain in Cell Proliferation Is to Enable Aspartate Synthesis.* Cell, 2015. **162**(3): p. 540-51.

51. Sullivan, L.B., et al., *Supporting Aspartate Biosynthesis Is an Essential Function of Respiration in Proliferating Cells.* Cell, 2015. **162**(3): p. 552-63.

52. Ayer, A., P. Macdonald, and R. Stocker, *CoQ(1)(0) Function and Role in Heart Failure and Ischemic Heart Disease.* Annu Rev Nutr, 2015. **35**: p. 175-213.

53. Boukalova, S., et al., *Dihydroorotate dehydrogenase in oxidative phosphorylation and cancer.* Biochim Biophys Acta Mol Basis Dis, 2020. **1866**(6): p. 165759.

54. Elmore, S., *Apoptosis: a review of programmed cell death.* Toxicol Pathol, 2007. **35**(4): p. 495-516.

55. Lemarie, A., et al., *Specific disintegration of complex II succinate:ubiquinone oxidoreductase links pH changes to oxidative stress for apoptosis induction.* Cell Death Differ, 2011. **18**(2): p. 338-49.

56. Ricci, J.E., et al., *Disruption of mitochondrial function during apoptosis is mediated by caspase cleavage of the p75 subunit of complex I of the electron transport chain.* Cell, 2004. **117**(6): p. 773-86.

57. Ichim, G. and S.W. Tait, *A fate worse than death: apoptosis as an oncogenic process.* Nat Rev Cancer, 2016. **16**(8): p. 539-48.

58. Jun, J.C., et al., *Hypoxia-Inducible Factors and Cancer.* Curr Sleep Med Rep, 2017. **3**(1): p. 1-10.

59. Warburg, O., F. Wind, and E. Negelein, *The Metabolism of Tumors in the Body.* J Gen Physiol, 1927. **8**(6): p. 519-30.

60. Zu, X.L. and M. Guppy, *Cancer metabolism: facts, fantasy, and fiction.* Biochem Biophys Res Commun, 2004. **313**(3): p. 459-65.

61. Ward, P.S. and C.B. Thompson, *Metabolic reprogramming: a cancer hallmark even warburg did not anticipate.* Cancer Cell, 2012. **21**(3): p. 297-308.

62. Koppenol, W.H., P.L. Bounds, and C.V. Dang, *Otto Warburg's contributions to current concepts of cancer metabolism.* Nat Rev Cancer, 2011. **11**(5): p. 325-37.

63. Pfeiffer, T., S. Schuster, and S. Bonhoeffer, *Cooperation and competition in the evolution of ATP-producing pathways.* Science, 2001. **292**(5516): p. 504-7.

64. Roesch, A., et al., *Overcoming intrinsic multidrug resistance in melanoma by blocking the mitochondrial respiratory chain of slow-cycling JARID1B(high) cells.* Cancer Cell, 2013. **23**(6): p. 811-25.

65. Viale, A., et al., *Oncogene ablation-resistant pancreatic cancer cells depend on mitochondrial function.* Nature, 2014. **514**(7524): p. 628-32.

66. Zhang, X., et al., *Induction of mitochondrial dysfunction as a strategy for targeting tumour cells in metabolically compromised microenvironments.* Nat Commun, 2014. **5**: p. 3295.

67. Shyh-Chang, N. and H.H. Ng, *The metabolic programming of stem cells.* Genes Dev, 2017. **31**(4): p. 336-346.

68. Kalucka, J., et al., *Quiescent Endothelial Cells Upregulate Fatty Acid beta-Oxidation for Vasculoprotection via Redox Homeostasis.* Cell Metab, 2018. **28**(6): p. 881-894 e13.

69. Ito, K., et al., *A PML-PPAR-delta pathway for fatty acid oxidation regulates hematopoietic stem cell maintenance.* Nat Med, 2012. **18**(9): p. 1350-8.

70. Turrens, J.F., *Mitochondrial formation of reactive oxygen species.* J Physiol, 2003. **552**(Pt 2): p. 335-44.

71. Esworthy, R.S., Y.S. Ho, and F.F. Chu, *The Gpx1 gene encodes mitochondrial glutathione peroxidase in the mouse liver.* Arch Biochem Biophys, 1997. **340**(1): p. 59-63.

72. Oberley, T.D., et al., *Localization of the thioredoxin system in normal rat kidney.* Free Radic Biol Med, 2001. **30**(4): p. 412-24.

73. Nohl, H. and W. Jordan, *The metabolic fate of mitochondrial hydrogen peroxide.* Eur J Biochem, 1980. **111**(1): p. 203-10.

74. Yu, L., et al., *Autophagic programmed cell death by selective catalase degradation.* Proc Natl Acad Sci U S A, 2006. **103**(13): p. 4952-7.

75. Coller, H.A., L. Sang, and J.M. Roberts, *A new description of cellular quiescence.* PLoS Biol, 2006. **4**(3): p. e83.

76. Rabinowitz, J.D. and E. White, *Autophagy and metabolism.* Science, 2010. **330**(6009): p. 1344-8.

77. Dunn, W.A., Jr., *Autophagy and related mechanisms of lysosome-mediated protein degradation.* Trends Cell Biol, 1994. **4**(4): p. 139-43.

78. Klionsky, D.J. and S.D. Emr, *Autophagy as a regulated pathway of cellular degradation.* Science, 2000. **290**(5497): p. 1717-21.

79. Yang, Z. and D.J. Klionsky, *Eaten alive: a history of macroautophagy.* Nat Cell Biol, 2010. **12**(9): p. 814-22.

80. Tsukamoto, S., et al., *Autophagy is essential for preimplantation development of mouse embryos.* Science, 2008. **321**(5885): p. 117-20.

81. Sou, Y.S., et al., *The Atg8 conjugation system is indispensable for proper development of autophagic isolation membranes in mice.* Mol Biol Cell, 2008. **19**(11): p. 4762-75.

82. Mizushima, N. and M. Komatsu, *Autophagy: renovation of cells and tissues.* Cell, 2011. **147**(4): p. 728-41.

83. Sinha, S. and B. Levine, *The autophagy effector Beclin 1: a novel BH3-only protein.* Oncogene, 2008. **27 Suppl 1**: p. S137-48.

84. Settembre, C., et al., *TFEB controls cellular lipid metabolism through a starvation-induced autoregulatory loop.* Nat Cell Biol, 2013. **15**(6): p. 647-58.

85. Doronzo, G., E. Astanina, and F. Bussolino, *The Oncogene Transcription Factor EB Regulates Vascular Functions.* Front Physiol, 2021. **12**: p. 640061.

86. Shaw, R.J., et al., *The tumor suppressor LKB1 kinase directly activates AMP-activated kinase and regulates apoptosis in response to energy stress.* Proc Natl Acad Sci U S A, 2004. **101**(10): p. 3329-35.

87. Shaw, R.J., *LKB1 and AMP-activated protein kinase control of mTOR signalling and growth.* Acta Physiol (Oxf), 2009. **196**(1): p. 65-80.

88. Settembre, C., et al., *TFEB links autophagy to lysosomal biogenesis.* Science, 2011. **332**(6036): p. 1429-33.

89. Zhang, X., et al., *MCOLN1 is a ROS sensor in lysosomes that regulates autophagy.* Nat Commun, 2016. **7**: p. 12109.

90. Guo, Q.Q., et al., *ATM-CHK2-Beclin 1 axis promotes autophagy to maintain ROS homeostasis under oxidative stress.* EMBO J, 2020. **39**(10): p. e103111.

91. Scherz-Shouval, R., et al., *Reactive oxygen species are essential for autophagy and specifically regulate the activity of Atg4.* EMBO J, 2007. **26**(7): p. 1749-60.

92. Zheng, X., et al., *The protease activity of human ATG4B is regulated by reversible oxidative modification.* Autophagy, 2020. **16**(10): p. 1838-1850.

93. Santidrian, A.F., et al., *Mitochondrial complex I activity and NAD+/NADH balance regulate breast cancer progression.* J Clin Invest, 2013. **123**(3): p. 1068-81.

94. Thomas, H.E., et al., *Mitochondrial Complex I Activity Is Required for Maximal Autophagy.* Cell Rep, 2018. **24**(9): p. 2404-2417 e8.

95. Yang, Z., et al., *ATG4B (Autophagin-1) phosphorylation modulates autophagy.* J Biol Chem, 2015. **290**(44): p. 26549-61.

96. Tanida, I., T. Ueno, and E. Kominami, *LC3 conjugation system in mammalian autophagy.* Int J Biochem Cell Biol, 2004. **36**(12): p. 2503-18.

97. Eskelinen, E.L. and P. Saftig, *Autophagy: a lysosomal degradation pathway with a central role in health and disease.* Biochim Biophys Acta, 2009. **1793**(4): p. 664-73.

98. Lamark, T., et al., *NBR1 and p62 as cargo receptors for selective autophagy of ubiquitinated targets.* Cell Cycle, 2009. **8**(13): p. 1986-90.

99. Yang, Z.J., et al., *The role of autophagy in cancer: therapeutic implications.* Mol Cancer Ther, 2011. **10**(9): p. 1533-41.

100. Yamamoto, A., et al., *Bafilomycin A1 prevents maturation of autophagic vacuoles by inhibiting fusion between autophagosomes and lysosomes in rat hepatoma cell line, H-4-II-E cells.* Cell Struct Funct, 1998. **23**(1): p. 33-42.

101. Tang, C., et al., *Autophagy in kidney homeostasis and disease.* Nat Rev Nephrol, 2020. **16**(9): p. 489-508.

102. Mortensen, M., et al., *The autophagy protein Atg7 is essential for hematopoietic stem cell maintenance.* J Exp Med, 2011. **208**(3): p. 455-67.

103. Oliver, L., et al., *Basal autophagy decreased during the differentiation of human adult mesenchymal stem cells.* Stem Cells Dev, 2012. **21**(15): p. 2779-88.

104. Ho, T.T., et al., *Autophagy maintains the metabolism and function of young and old stem cells.* Nature, 2017. **543**(7644): p. 205-210.

105. Garcia-Prat, L., et al., *Autophagy maintains stemness by preventing senescence.* Nature, 2016. **529**(7584): p. 37-42.

106. White, E. and R.S. DiPaola, *The double-edged sword of autophagy modulation in cancer.* Clin Cancer Res, 2009. **15**(17): p. 5308-16.

107. Marin-Valencia, I., et al., *Analysis of tumor metabolism reveals mitochondrial glucose oxidation in genetically diverse human glioblastomas in the mouse brain in vivo.* Cell Metab, 2012. **15**(6): p. 827-37.

108. Hensley, C.T., et al., *Metabolic Heterogeneity in Human Lung Tumors.* Cell, 2016. **164**(4): p. 681-94.

109. Rohlena, J., et al., *Mitochondrially targeted alpha-tocopheryl succinate is antiangiogenic: potential benefit against tumor angiogenesis but caution against wound healing.* Antioxid Redox Signal, 2011. **15**(12): p. 2923-35.

110. Rohlenova, K., et al., *Selective Disruption of Respiratory Supercomplexes as a New Strategy to Suppress Her2high Breast Cancer.* Antioxid Redox Signal, 2017. **26**(2): p. 84-103.

111. Blecha, J., et al., *Antioxidant defense in quiescent cells determines selectivity of electron transport chain inhibition-induced cell death.* Free Radic Biol Med, 2017. **112**: p. 253-266.

112. Hosseini, M., et al., *Energy Metabolism Rewiring Precedes UVB-Induced Primary Skin Tumor Formation.* Cell Rep, 2018. **23**(12): p. 3621-3634.

113. Martinez-Reyes, I., et al., *Mitochondrial ubiquinol oxidation is necessary for tumour growth.* Nature, 2020. **585**(7824): p. 288-292.

114. Brown, K.K., et al., *Adaptive Reprogramming of De Novo Pyrimidine Synthesis Is a Metabolic Vulnerability in Triple-Negative Breast Cancer.* Cancer Discov, 2017. **7**(4): p. 391-399.

115. Mathur, D., et al., *PTEN Regulates Glutamine Flux to Pyrimidine Synthesis and Sensitivity to Dihydroorotate Dehydrogenase Inhibition.* Cancer Discov, 2017. **7**(4): p. 380-390.

116. Sykes, D.B., et al., *Inhibition of Dihydroorotate Dehydrogenase Overcomes Differentiation Blockade in Acute Myeloid Leukemia.* Cell, 2016. **167**(1): p. 171-186 e15.

117. Adam-Vizi, V. and C. Chinopoulos, *Bioenergetics and the formation of mitochondrial reactive oxygen species.* Trends Pharmacol Sci, 2006. **27**(12): p. 639-45.

118. Benn, D.E., et al., *Clinical presentation and penetrance of pheochromocytoma/paraganglioma syndromes.* J Clin Endocrinol Metab, 2006. **91**(3): p. 827-36.

119. Fishbein, L., et al., *Comprehensive Molecular Characterization of Pheochromocytoma and Paraganglioma.* Cancer Cell, 2017. **31**(2): p. 181-193.

120. Garcia-Bermudez, J., et al., *Aspartate is a limiting metabolite for cancer cell proliferation under hypoxia and in tumours.* Nat Cell Biol, 2018. **20**(7): p. 775-781.

121. Sullivan, L.B., et al., *Aspartate is an endogenous metabolic limitation for tumour growth.* Nat Cell Biol, 2018. **20**(7): p. 782-788.

122. Molina, J.R., et al., *An inhibitor of oxidative phosphorylation exploits cancer vulnerability.* Nat Med, 2018. **24**(7): p. 1036-1046.

123. Naderi, J., M. Hung, and S. Pandey, *Oxidative stress-induced apoptosis in dividing fibroblasts involves activation of p38 MAP kinase and over-expression of Bax: resistance of quiescent cells to oxidative stress.* Apoptosis, 2003. **8**(1): p. 91-100.

124. Sarsour, E.H., et al., *Manganese superoxide dismutase activity regulates transitions between quiescent and proliferative growth.* Aging Cell, 2008. **7**(3): p. 405-17.

125. Galluzzi, L., et al., *Regulated cell death and adaptive stress responses.* Cell Mol Life Sci, 2016. **73**(11-12): p. 2405-10.

126. Diebold, L.P., et al., *Mitochondrial complex III is necessary for endothelial cell proliferation during angiogenesis.* Nat Metab, 2019. **1**(1): p. 158-171.

127. Planavsky, N.J., et al., *Earth history. Low mid-Proterozoic atmospheric oxygen levels and the delayed rise of animals.* Science, 2014. **346**(6209): p. 635-8.

8. PUBLICATIONS *IN EXTENSO*

Article

Cell Metabolism

Reactivation of Dihydroorotate Dehydrogenase-Driven Pyrimidine Biosynthesis Restores Tumor Growth of Respiration-Deficient Cancer Cells

Graphical Abstract

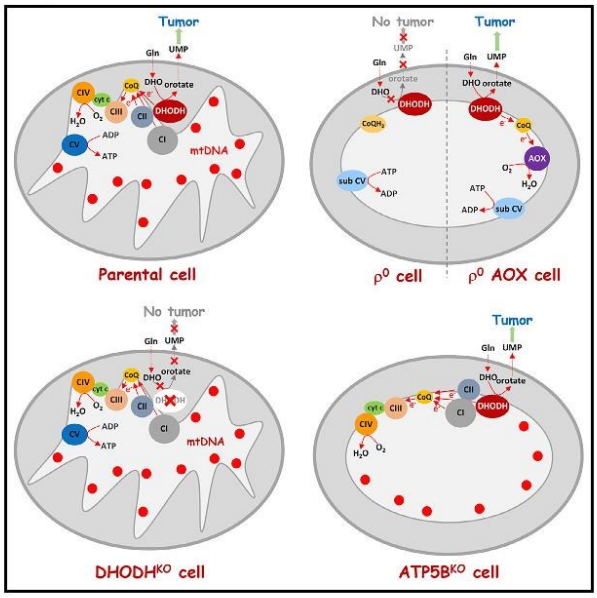

Highlights

- Tumorigenesis depends on functional OXPHOS
- OXPHOS-derived ATP is not required for tumor formation
- DHODH-driven pyrimidine biosynthesis requires CoQ redox-cycling
- CoQ redox-cycling via OXPHOS drives tumorigenesis through pyrimidine biosynthesis

Authors

Martina Bajzikova, Jaromira Kovarova, Ana R. Coelho, ..., Lanfeng Dong, Jakub Rohlena, Jiri Neuzil

Correspondence

jaromira.kovarova@ibt.cas.cz (J.K.), psh@snu.ac.kr (S.P.), l.dong@griffith.edu.au (L.D.), rohlenaj@ibt.cas.cz (J.R.), j.neuzil@griffith.edu.au (J.N.)

In Brief

Cancer cells without mitochondrial DNA (mtDNA) do not form tumors unless they can highjack host mitochondria. Bajzikova et al. show that the acquired mitochondrial electron transport is necessary to drive de novo pyrimidine synthesis to overcome cell-cycle arrest. Surprisingly, ATP generation is dispensable for tumorigenesis in this context.

Bajzikova et al., 2019, Cell Metabolism 29, 1–18
March 5, 2019 © 2018 Elsevier Inc.
https://doi.org/10.1016/j.cmet.2018.10.014

CellPress

Please cite this article in press as: Bajzikova et al., Reactivation of Dihydroorotate Dehydrogenase-Driven Pyrimidine Biosynthesis Restores Tumor Growth of Respiration-Deficient Cancer Cells, Cell Metabolism (2018), https://doi.org/10.1016/j.cmet.2018.10.014

Cell Metabolism
Article

Reactivation of Dihydroorotate Dehydrogenase-Driven Pyrimidine Biosynthesis Restores Tumor Growth of Respiration-Deficient Cancer Cells

Martina Bajzikova,[1,2,17] Jaromira Kovarova,[1,17,*] Ana R. Coelho,[1,3,17] Stepana Boukalova,[1,17] Sehyun Oh,[4,17] Katerina Rohlenova,[1,18] David Svec,[1] Sona Hubackova,[1] Berwini Endaya,[5] Kristyna Judasova,[1] Ayenachew Bezawork-Geleta,[5] Katarina Kluckova,[1,19] Laurent Chatre,[6,7] Renata Zobalova,[1] Anna Novakova,[1] Katerina Vanova,[1] Zuzana Ezrova,[1,2] Ghassan J. Maghzal,[8,16] Silvia Magalhaes Novais,[1,2] Marie Olsinova,[2] Linda Krobova,[1] Yong Jin An,[4] Eliska Davidova,[1,2] Zuzana Nahacka,[1] Margarita Sobol,[9] Teresa Cunha-Oliveira,[3] Cristian Sandoval-Acuña,[1] Hynek Strnad,[9] Tongchuan Zhang,[10] Thanh Huynh,[11] Teresa L. Serafim,[3] Pavel Hozak,[9] Vilma A. Sardao,[3] Werner J.H. Koopman,[12] Miria Ricchetti,[6,7] Paulo J. Oliveira,[3] Frantisek Kolar,[13] Mikael Kubista,[1] Jaroslav Truksa,[1] Katerina Dvorakova-Hortova,[1,2] Karel Pacak,[11] Robert Gurlich,[14] Roland Stocker,[8,16] Yaoqi Zhou,[10] Michael V. Berridge,[15] Sunghyouk Park,[4,*] Lanfeng Dong,[5,*] Jakub Rohlena,[1,*] and Jiri Neuzil[1,5,20,*]

[1]Institute of Biotechnology, Czech Academy of Sciences, 252 50, Vestec, Prague-West, Czech Republic
[2]Faculty of Science, Charles University, 128 44 Prague, Czech Republic
[3]CNC - Center for Neuroscience and Cell Biology, University of Coimbra, UC-Biotech, Biocant Park, 3060-197 Cantanhede, Portugal
[4]College of Pharmacy, Natural Product Research Institute, Seoul National University, Seoul 08826, Korea
[5]School of Medical Science, Griffith University, Southport, QLD 4222, Australia
[6]Department of Developmental and Stem Cell Biology, Institut Pasteur, 75015 Paris, France
[7]CNRS UMR 3738, Team Stability of Nuclear and Mitochondrial DNA, 75015 Paris, France
[8]Victor Chang Cardiac Research Institute, Darlinghurst, NSW 2010, Australia
[9]Institute of Molecular Genetics, Czech Academy of Sciences, 142 20 Prague, Czech Republic
[10]Institute for Glycomics, Griffith University, Southport, 4222 QLD, Australia
[11]Eunice Kennedy Shriver Child Health and Human Development, National Institutes of Health, Bethesda, MD, USA
[12]Department of Biochemistry (286), Radboud Institute for Molecular Life Sciences, Radboud University Medical Centre, 6525 Nijmegen, the Netherlands
[13]Institute of Physiology, Czech Academy of Sciences, 142 20 Prague, Czech Republic
[14]Third Faculty Hospital, Charles University, Prague, Czech Republic
[15]Malaghan Institute of Medical Research, Wellington 6242, New Zealand
[16]St Vincent's Clinical School, UNSW Medicine, University of New South Wales, Sydney, NSW 2052, Australia
[17]These authors contributed equally
[18]Present address: Laboratory of Angiogenesis and Vascular Metabolism, VIB-KU Leuven Center for Cancer Biology, Department of Oncology, KU Leuven, Leuven 3000, Belgium
[19]Present address: Institute of Metabolism and Systems Research, College of Medical and Dental Sciences, University of Birmingham, Birmingham, UK
[20]Lead Contact
*Correspondence: jaromira.kovarova@ibt.cas.cz (J.K.), psh@snu.ac.kr (S.P.), l.dong@griffith.edu.au (L.D.), rohlenaj@ibt.cas.cz (J.R.), j.neuzil@griffith.edu.au (J.N.)
https://doi.org/10.1016/j.cmet.2018.10.014

SUMMARY

Cancer cells without mitochondrial DNA (mtDNA) do not form tumors unless they reconstitute oxidative phosphorylation (OXPHOS) by mitochondria acquired from host stroma. To understand why functional respiration is crucial for tumorigenesis, we used time-resolved analysis of tumor formation by mtDNA-depleted cells and genetic manipulations of OXPHOS. We show that pyrimidine biosynthesis dependent on respiration-linked dihydroorotate dehydrogenase (DHODH) is required to overcome cell-cycle arrest, while mitochondrial ATP generation is dispensable for tumorigenesis. Latent DHODH in mtDNA-deficient cells is fully activated with restoration of complex III/IV activity and coenzyme Q redox-cycling after mitochondrial transfer, or by introduction of an alternative oxidase. Further, deletion of DHODH interferes with tumor formation in cells with fully functional OXPHOS, while disruption of mitochondrial ATP synthase has little effect. Our results show that DHODH-driven pyrimidine biosynthesis is an essential pathway linking respiration to tumorigenesis, pointing to inhibitors of DHODH as potential anti-cancer agents.

INTRODUCTION

Mitochondria are vital organelles for most eukaryotic cells (Karnkowska et al., 2016). They carry their own DNA (mtDNA) and are involved in a number of essential processes. The signature

feature of mitochondria is oxidative phosphorylation (OXPHOS), responsible for respiration and ATP formation. Respiration is performed by four respiratory complexes (RCs; i.e., CI-IV) that associate into supercomplexes (SCs) and generate a proton gradient across the inner mitochondrial membrane (IMM) that is used by ATP synthase (CV) to produce ATP (Acin-Perez et al., 2008; Althoff et al., 2011; Moreno-Lastres et al., 2012; Gu et al., 2016; Letts et al., 2016; Wu et al., 2016). Respiration also drives biosynthetic pathways directly or via the tricarboxylic acid cycle (Bezawork-Geleta et al., 2018).

Essential protein subunits of OXPHOS complexes are encoded by nuclear DNA and mtDNA. Therefore, when mtDNA is absent or damaged, OXPHOS is severely compromised (Brandon et al., 2006; Wallace, 2012). Recently we showed that cancer cells deficient in OXPHOS due to mtDNA depletion (ρ^0 cells) cannot form tumors unless they acquire functional mtDNA from host stroma (Tan et al., 2015) by transfer of whole mitochondria (Dong et al., 2017). Other researchers support our findings (Osswald et al., 2015; Lei and Spradling, 2016; Moschoi et al., 2016; Strakova et al., 2016). These observations suggest that functional OXPHOS is essential for tumorigenesis, a concept consistent with other reports (LeBleu et al., 2014; Viale et al., 2014). Furthermore, they conform to the notion that the Warburg effect is associated with altered biosynthetic needs of cancer cells rather than with cancer-linked mitochondrial damage (Vander Heiden et al., 2009; Vander Heiden and DeBerardinis, 2017).

However, important questions remain unresolved. Foremost, it is unclear which aspect of OXPHOS activity is limiting for tumor growth. ATP production is the best known function of OXPHOS, but proliferating cells also require respiration for its oxidizing power and to produce aspartate for pyrimidine biosynthesis (Birsoy et al., 2015; Sullivan et al., 2015; Titov et al., 2016). Further, OXPHOS directly drives the respiration-coupled mitochondrial enzyme dihydroorotate dehydrogenase (DHODH) that converts dihydroorotate (DHO) to orotate in the *de novo* pyrimidine synthesis pathway (Loffler et al., 2005).

Here we analyzed temporal events preceding tumor formation in ρ^0 cancer cells in the context of horizontal transfer of mtDNA *in vivo* and linked this to genetic manipulations of the OXPHOS system. Our results indicate that a key event facilitating tumor growth upon respiration recovery is reactivation of DHODH-driven pyrimidine synthesis.

RESULTS

mtDNA Is Replenished and Respiration Recovers Prior to Tumor Formation

Mouse breast cancer 4T1ρ^0 cells form tumors with a 3-week lag compared with parental cells, with palpable tumors appearing on day 20–25 (Figures 1A and S1A). To understand the sequence of events leading to tumor growth, 4T1ρ^0 cells (referred to as day 0, D0 cells) were grafted into BALB/c mice, tissue at the injection site was excised at various time points post injection (Figures 1B and 1C) and cancer cells were selected using 6-thioguanine (6TG) (Aslakson and Miller, 1992). Individual lines established in medium supplemented with pyruvate/uridine were stable over a long time in culture, maintaining their mtDNA status and growth properties. Analysis of the lines for respiration revealed its recovery prior to tumor formation (Figure 1D), pointing to an association between respiration recovery and tumor growth.

We next assessed the mtDNA content in the lines using single-cell PCR (sc/qPCR) and probes that discriminate between the 16S rRNA polymorphism of host cells and that of 4T1 cells (Bayona-Bafaluy et al., 2003; Tan et al., 2015). We observed a progressive increase in the homoplasmic mtDNA of host origin in D5–D15 cells as well as absence of 4T1 mtDNA polymorphism in these cells (Figure 1E). The distribution profile of mtDNA was normalized in D15 cells (Figure 1F). The relative mtDNA copy number was verified by qPCR (Figure S1B), and the host origin of homoplasmic polymorphism was confirmed by DNA sequencing (Table S1).

To test whether the acquired mtDNA was functional, we assessed replication (mREP) and transcription (mTRANS) of mtDNA in single cells by the mTRIP method (Chatre and Ricchetti, 2013). Figure 1G shows relatively high mREP and mTRANS signal already in D5 cells. We also set up a specific mitochondrial "chromatin" immunoprecipitation (mitoChIP) assay (Figure 1H) that revealed a gradual increase in mtDNA binding of mitochondrial transcription factor TFAM and DNA polymerase-γ (POLG). The binding was very low in D5 cells, increased in D10 cells, and normalized in D15 and D20 cells. The protein levels of TFAM, POLG, and the mitochondrial single strand-binding protein (mtSSB) fully recovered in D15 cells that contain substantial mtDNA (Figures S1C and 1I).

Transcripts of mitochondrial genes encoding subunits of RCs were detectable in D5 cells and approached parental values in D15–D20 cells (Figures 1J and S1D). Protein subunits of RCs recovered in D15 cells (Figure 1K), where also fully assembled RCs and SCs appeared, and a switch from sub-CV to CV occurred (Figure 1L). Finally, we assessed the lines for mitochondrial morphology by transmission electron microscopy (TEM) (Figure S2) and for the presence of mitochondrial nucleoids using stimulated emission depletion microscopy (STED) (Figure S3). TEM detected mitochondria with cristae in D15 cells, consistent with the link between cristae formation and respiration (Cogliati et al., 2013), while STED microscopy revealed high numbers of TFAM-containing nucleoids in D15 cell mitochondria (Kukat et al., 2015).

In conclusion, mtDNA is acquired and amplified, and OXHPOS machinery is reconstituted in ρ^0 cancer cells during the long dormant period prior to tumor appearance.

Mitochondrial Function and Bioenergetics Are Normalized Early in Tumorigenesis and Are Unrelated to ATP Generated by OXPHOS

We investigated whether replenishment of mtDNA/reconstitution of OXPHOS components are reflected by normalization of the mitochondrial function. Figure 2A shows that mitochondrial membrane potential ($\Delta\Psi_{m,i}$), low in D0 to D10 cells, increased in D15 cells to parental cell level. Similarly, mitochondrial superoxide increased in D15 cells (Figure 2B), consistent with active electron transport through assembled RCs/SCs.

We next assessed the bioenergetics of D0–D60 lines, evaluating their basal respiration. Figure 2C shows little or no respiration in D0–D10 cells, with an increase to 50%–60% of the parental cell values in D15 cells and normalization in D20 cells. This was similar for CI- and CII-dependent respiration

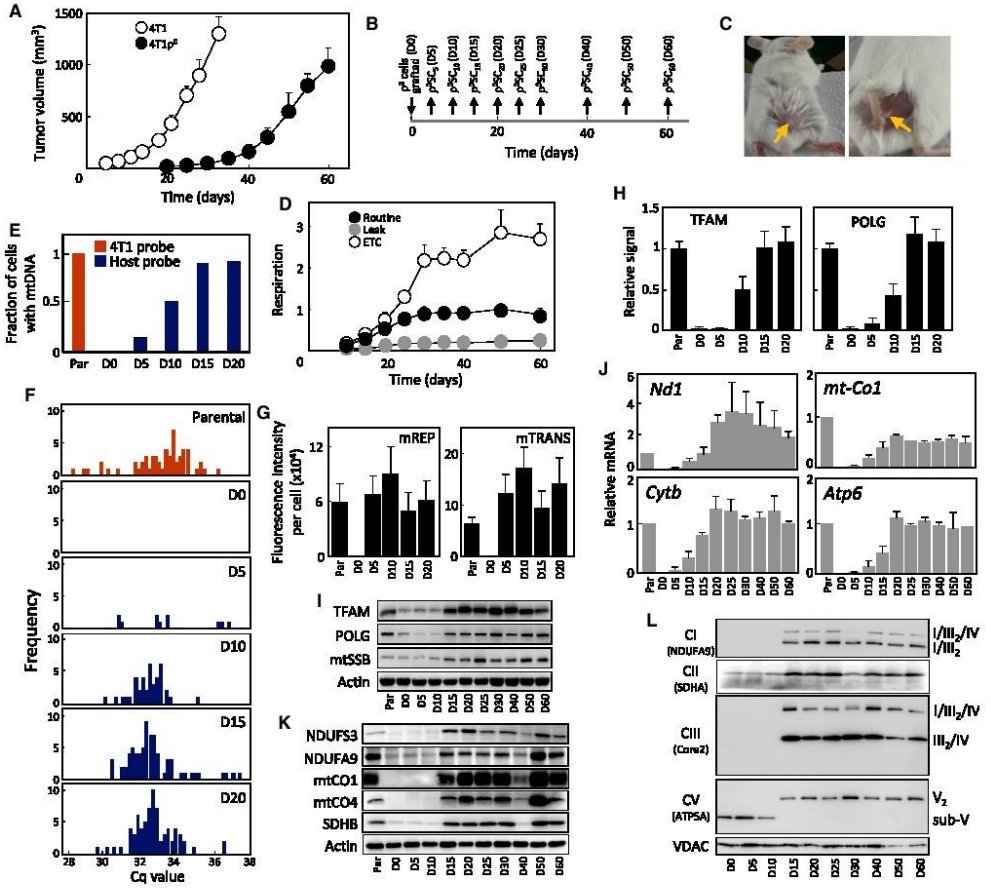

Figure 1. mtDNA Is Replenished and Respiration Recovers Early in Tumor Formation by 4T1ρ⁰ Cells

(A) BALB/c mice were grafted subcutaneously (s.c.) with 4T1 or 4T1ρ⁰ cells at 10^6 per animal, and tumor volume was assessed by ultrasound imaging (USI) (n = 6).

(B and C) Time schedule of retrieval of pre-tumor plaques and tumors from BALB/c mice is shown in (B), as indicated in (C) for D5 tissue.

(D) Individual lines retrieved from mice according to the schedule in (B) were assessed for uncoupled (ETC), routine, and leak respiration using the Oxygraph (n = 3).

(E) Cell lines were evaluated for the presence of mtDNA using probes against a polymorphism in either 4T1 or host 16S rRNA by sc/qPCR; 92 cells per line were assessed.

(F) Distribution of mtDNA polymorphism in 16S rRNA in single cells of lines shown in (E).

(G) mTRIP assay in the presence of proteinase K was used to detect the mtDNA initiation of replication marker (mREP) and global mitochondrial transcripts (mTRANS) unmasked from proteins, in single cells (n = 3; 100 cells were assessed per condition).

(H) Cell lines were assessed for binding of TFAM and POLG1 to the *D LOOP* region of mtDNA using a mitoChIP assay (n = 3).

(I) Individual lines were probed for the level of mtDNA-processing proteins using WB.

(J–L) qRT-PCR was used to assess the level of transcripts of selected subunits of mitochondrially encoded transcripts of RCs (n = 3) (J). Selected subunits of mitochondrial RCs were evaluated using WB in individual lines (K), which were then assessed by NBGE for the assembly of RCs and SCs using antibodies to relevant subunits, as shown (L).

Data in (A), (D), (G), (H), and (J) are mean values ± SD. Representative images of three biological replicates are shown for (I), (K), and (L).

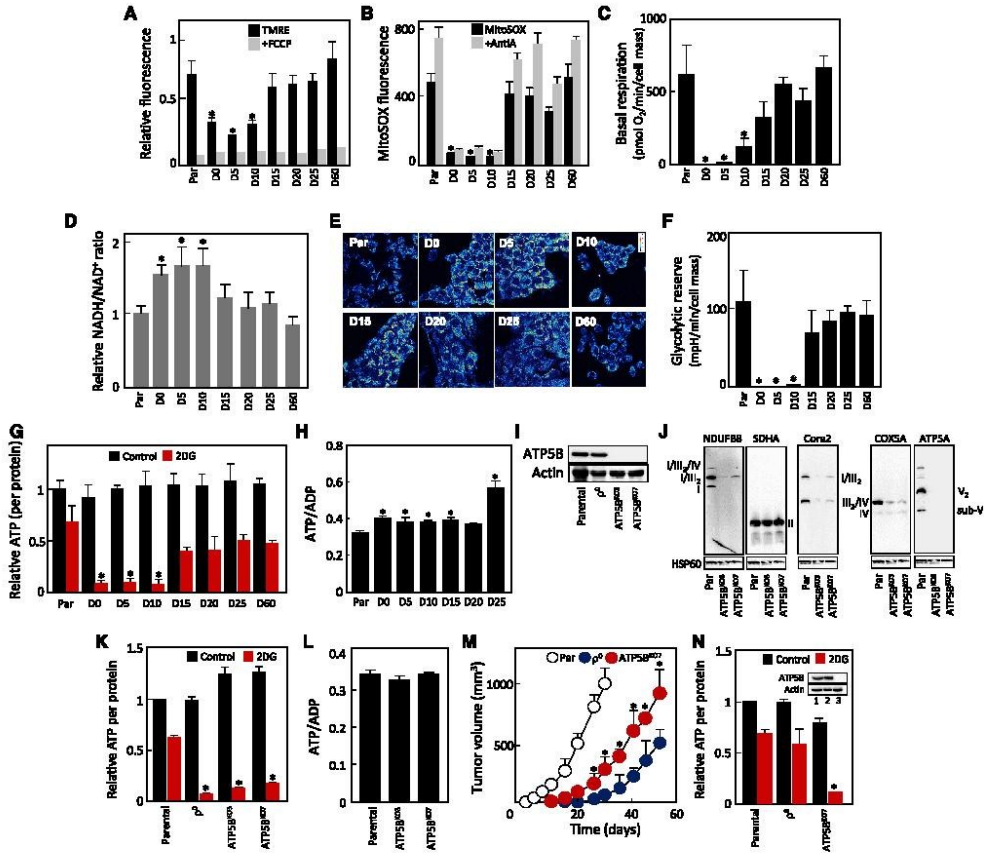

Figure 2. Mitochondrial Function and Bioenergetics Are Normalized Early in 4T1ρ^0 Cell Tumorigenesis and Are Unrelated to OXPHOS-Generated ATP

(A–C) Individual lines derived from 4T1ρ^0 cells were assessed for $\Delta\Psi_{m,i}$ using TMRE in the absence and presence of the uncoupler FCCP (A), for generation of mitochondrial superoxide using MitoSOX in the absence and presence of antimycin A (AntiA) (B), and for basal respiration using a Seahorse XF96 (C).

(D) NADH/NAD^+ ratio was assessed in cell lines using a luminescence kit.

(E) Two-photon microscopy was used to visualize the level of mitochondrial NAD(P)H in individual lines.

(F) Cell lines were assessed for glycolytic reserve using a Seahorse XF96.

(G) Individual lines were evaluated for ATP levels in the absence and presence of 50 mM 2DG at 4.5 g/L glucose and 1 mM pyruvate, and the results were expressed relative to total ATP in parental cells.

(H) The lines as shown were assessed for the ATP/ADP ratio using liquid chromatography-mass spectrometry.

(I) Parental and ρ^0 cells and two clones of $ATP5B^{KO}$ cells were probed for the level of ATP5B using WB.

(J–L) Parental, ρ^0, and $ATP5B^{KO}$ cells were assessed by NBGE for assembly of RCs and SCs (J). Parental, ρ^0, and $ATP5B^{KO}$ cells were tested for the level of ATP at 4.5 g/L glucose in the absence or presence of 50 mM 2DG (K) and for the ATP/ADP ratio (L).

(M) BALB/c mice were injected s.c. with 10^6 cells per animal, and tumor volume was quantified by USI.

(N) Cell lines derived on day 20 from tumors grown from parental, ρ^0, and $ATP5B^{KO}$ 4T1 cells were assessed for ATP as described in (G). The insert documents the level of ATP5B protein in the tumor-derived cell lines; 1, parental; 2, ρ^0; 3, $ATP5B^{KO7}$ cells.

Data in (A)–(D), (F)–(H), (K), (L), and (N) are mean values ± SD (n = 3); those in (M) are mean values ± SED (n = 5). The symbol "*" in (A)–(D), (F)–(H), (K), and (N) indicates statistically significant differences from parental cells; in (M), statistically significant differences from tumors grown from ρ^0 cells; and in (L), statistically different from tumors grown from parental cells, with $p < 0.05$. (E), (I), (J), and (N) (insert) show representative images of three biological replicates.

(Figure S4A), with reserve respiratory capacity absent in D0–D10 cells (Figure S4B). Compromised respiration was confirmed by increased NADH/NAD$^+$ ratio in D0–D15 cells evaluated by a luminescence kit (Figure 2D) and elevated mitochondrial NAD(P)H assessed by two-photon microscopy (Figures 2E and S4C). D0–D10 cells had no glycolytic reserve (Figure 2F), consistent with increased lactate production and glucose uptake compensating for the loss of OXPHOS-derived ATP (Figures S4D and S4E). Indeed, we found that glycolysis contributed to ATP generation by ≈30% in parental and 90% in D0–D10 cells (Figure 2G). Total ATP was comparable in all cell lines and the ATP/ADP ratio was not reduced in respiration-deficient cells, suggesting that ATP availability is not the limiting factor (Figure 2H).

To test directly whether the onset of tumor formation is dissociated from ATP generation by OXPHOS, we prepared cells that cannot assemble CV by knocking out ATP5B (Figure 2I). Native blue gel electrophoresis (NBGE) followed by western blotting (WB) revealed that ATP5B^{KO} cells failed to assemble CV (Figure 2J), with other RCs/SCs also decreased. ATP5B^{KO} cells predominantly used glycolysis for ATP formation, their ATP content was comparable to that of parental cells (Figure 2K), and the ATP/ADP ratio was maintained (Figure 2L). When grafted into BALB/c mice, ATP5B^{KO} cells produced tumors somewhat slower than parental cells, but significantly faster than 4T1ρ^0 cells (Figure 2M). To exclude the possibility that ATP5B^{KO}-derived tumors "acquire" ATP synthase and re-establish OXPHOS-dependent ATP production, we assessed ATP5B expression and ATP levels in lines isolated from tumors grown from 4T1, 4T1ρ^0, and 4T1 ATP5B^{KO} cells. We observed that ATP5B^{KO} tumor-derived cells were deficient in both OXPHOS-derived ATP and in ATP5B, whereas 4T1 ρ^0 cells re-established ATP production by mitochondrial transfer (Figure 2N).

To see whether these results are more broadly applicable, we deleted ATP5B in B16 cells. When grafted into C57BL/6 mice, B16 ρ^0 cells acquire mtDNA (Tan et al., 2015) via transfer of whole mitochondria, yielding B16 DP cells (Dong et al., 2017). We first assessed B16, B16ρ^0, B16 DP, and B16 ATP5B^{KO} cells by SDS-PAGE and NBGE for the level of subunits of RCs (Figure S5A) and their assembly (Figure S5B), and for ATP production (Figure S5C). These lines behaved similarly to their 4T1 counterparts. Also, B16 ATP5B^{KO} cells were more efficient in tumor formation than B16ρ^0 cells (Figure S5D). These results indicate that OXPHOS-derived ATP is not essential for tumorigenesis.

Respiration Recovery Is Associated with Reactivation of Dihydroorotate Dehydrogenase

Cells devoid of mtDNA are auxotrophic for uridine and pyruvate (King and Attardi, 1988, 1989). OXPHOS defects may also increase the dependence of cells on otherwise non-essential nutrients such as pyruvate (Sullivan et al., 2015; Birsoy et al., 2015; Cardaci et al., 2015; Lussey-Lepoutre et al., 2015). We therefore tested the auxothrophy profile of 4T1 lines and observed that uridine and/or pyruvate are needed for proliferation of non-/low-respiring cells (D0–D10), while the dependence is lost in D15–D20 cells (Figures 3A and S4F).

We next investigated whether auxotrophy for uridine could explain the association between recovery of respiration and the onset of tumor growth. Since uridine auxotrophy is related to the dysfunction of DHODH (King and Attardi, 1988; He et al., 2014), we investigated its role in D0–D60 lines and its link to the initiation of tumorigenesis. We found little difference in DHODH mRNA and protein contents in D0–D60 cells (Figure 3B). DHODH converts DHO to orotate, with the resulting two electrons transferred to the respiratory chain (Loffler et al., 2005). Figure 3C shows the extent of DHODH-dependent respiration in parental 4T1 cells and its suppression by leflunomide, a selective inhibitor of the enzyme (Greene et al., 1995). DHODH-dependent respiration was absent in D0–D10 cells and recovered in D15 cells (Figure 3D). We then assessed the orotate-to-DHO ratio, reflecting native DHODH activity. Figure 3E reveals low orotate/DHO ratio in D0–D10 cells, indicating little DHODH function in these cells, while its function recovered in D15 cells.

To link the level of respiration to the kinetics of tumor initiation, we grafted D0–D20 lines into BALB/c mice. D5 and D10 cells formed tumors with considerable lag, while D15 and D20 cells formed tumors with kinetics similar to parental cells (Figure 3F). We next evaluated tumors grown from parental and D0 cells for CI-, CII-, and DHODH-dependent respiration and found no significant difference (Figure 3G).

Finally, we tested whether respiration including the DHODH-dependent component was associated with proliferation of malignant cells after grafting 4T1ρ^0 (D0) cells into BALB/c mice (*cf.* Figures 1B and 1C). The tissue excised from the grafted region was sectioned and assessed for proliferation using Ki67 staining. Figure 3H shows low proliferation in D5 tissue, with some increase in D10 and with parental tumor levels in D15 tissue, consistent with the delay in tumor formation shown in Figure 3F. These results suggest an important role for DHODH in tumorigenesis.

DHODH Is Essential for Tumor Growth

To directly examine whether DHODH is important for tumor formation/progression, we deleted the gene for DHODH in 4T1 cells using CRISPR/Cas9. WB in Figure 4A shows the absence of DHODH in two clones of DHODH^{KO} cells and its presence in DHODH-reconstituted (DHODH^{rec}) cells. Consistent with this, DHODH-dependent respiration was undetectable in DHODH^{KO} cells and recovered in DHODH^{rec} cells, while routine respiration was identical in all lines (Figure 4B). We also found no difference in mitochondrial superoxide in these cells (Figure S4G). In contrast, DHODH^{KO} cells showed stalled proliferation in the absence of uridine, which was restored by DHODH reconstitution (Figure 4C). No significant difference in the NADH/NAD$^+$ ratio was detected in these lines (Figure 4D). NBGE revealed no discernible difference in the assembly of any of the five RCs or SCs in the cells, regardless of their DHODH status (Figure 4E), and also showed that DHODH does not associate with any of the complexes (Figure 4E, right panel). We then investigated DHODH^{KO} and DHODH^{rec} cells for ATP generation as well as for the role of glycolysis. Figure 4F shows that there was virtually no difference when DHODH-manipulated cells were compared with parental cells. Further, DHODH^{KO} cells contain mitochondria with cristae, unlike ρ^0 cells (Figure 4G).

We next assessed the activity of DHODH in parental, DHODH^{KO}, and DHODH^{rec} cells using an *in vitro* enzymatic assay independent of CIII/CIV. This revealed a similar pattern of DHODH activity to that of DHODH-dependent respiration

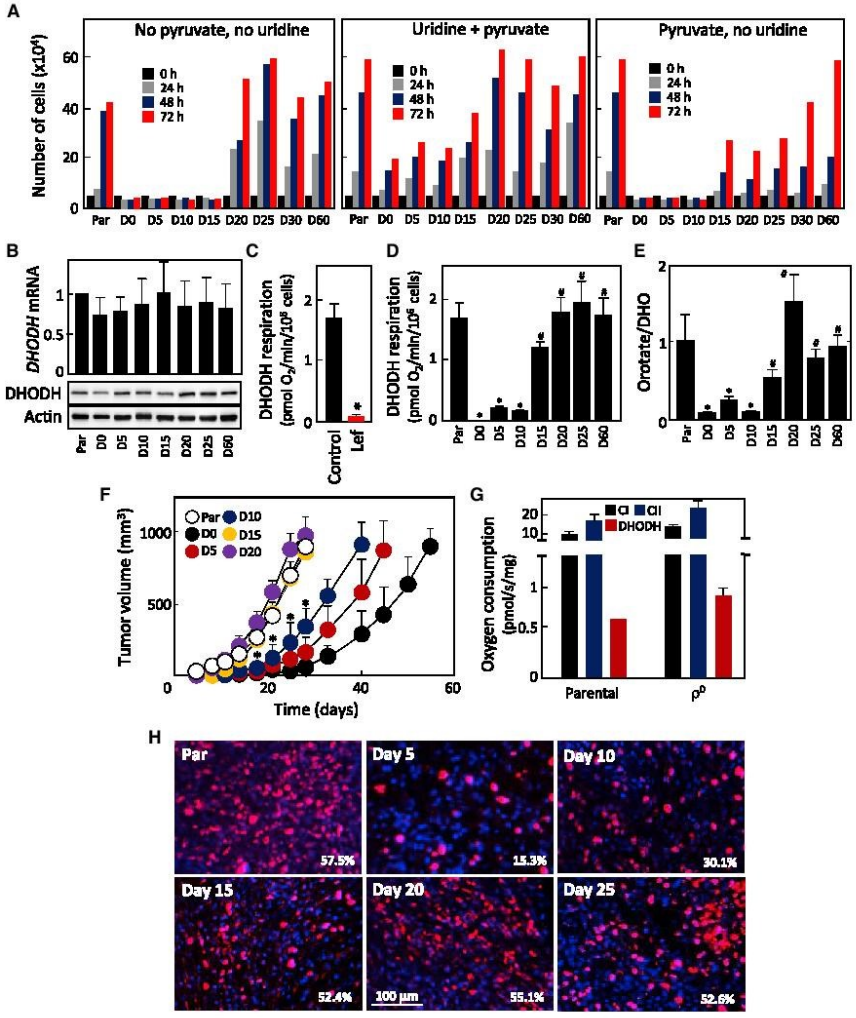

Figure 3. Respiration Recovery Is Associated with Reactivation of DHODH

(A) Cell lines as shown were evaluated for growth in the presence of uridine and pyruvate, or with pyruvate or uridine removed.

(B) Cell lines were assessed for DHODH expression by qRT-PCR and WB.

(C–E) DHODH-dependent respiration was assessed in parental 4T1 cells in the absence and presence of 30 μM leflunomide (Lef) (C). Individual lines were assessed for DHODH-dependent respiration (D) and for the orotate-to-DHO ratio (E).

(F) Parental, D0, D5, D10, D15, D20, D25, and D60 cells (10^6) were grafted s.c. into BALB/c mice, and tumor growth was evaluated by USI.

(G) Tumors grown from parental or 4T1ρ^0 cells were excised and processed in a dedicated tissue shredder, and the homogenates were assessed for CI-, CII-, and DHODH-dependent respiration using an Oxygraph.

(H) BALB/c mice were grafted s.c. with 10^6 D0 cells. On the days indicated, animals were sacrificed and tissue from the grafted region excised, sectioned, and assessed by immunohistochemistry for proliferation using anti-Ki67 IgG followed by confocal microscopy. The numbers indicate percentage of Ki67-positive cells.

Data in (A) are mean values derived from two biological replicates with differences less than 10%; data in (B) are mean values ±SD ($n \geq 3$); data in (C–G) are mean values ± SEM ($n \geq 3$); images in (B) and (H) are representative of three independent experiments. The symbol "*" indicates statistically significant differences from parental cells, and the symbol "#" indicates statistically significant difference from D0 cells, with $p < 0.05$.

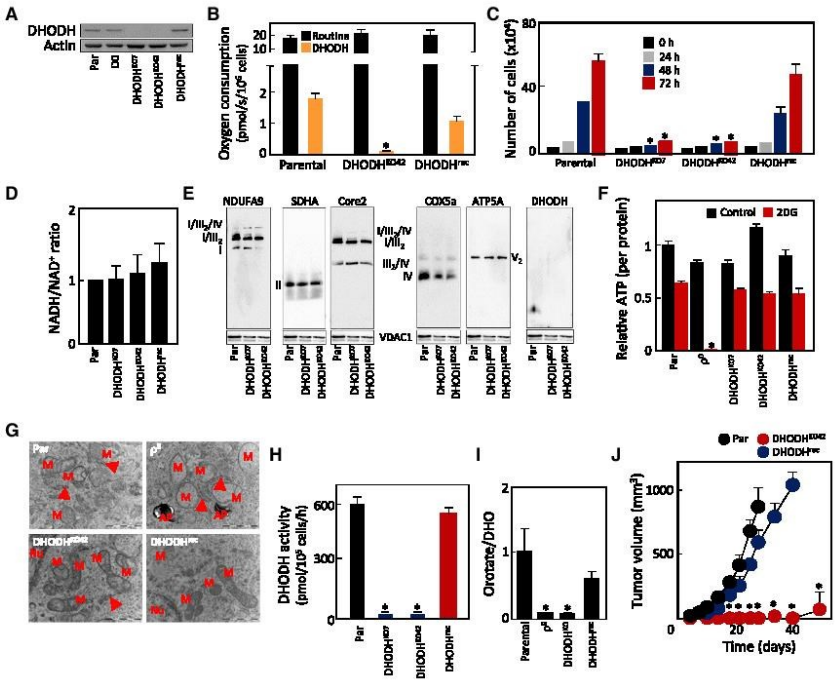

Figure 4. DHODH Is Essential for Tumor Growth

(A–I) WB shows the absence of DHODH in two clones of DHODH^{KO} 4T1 cells and its presence in DHODH^{rec} cells (A). Parental, DHODH^{KO}, and DHODH^{rec} cells were tested for routine and DHODH-dependent respiration (B), auxotrophy for uridine (C), NADH/NAD$^+$ ratio (D), assembly of RCs and SCs (E), ATP generation in the absence or presence of 50 mM 2DG (4.5 g/L glucose) (F), mitochondrial morphology using TEM (G), DHODH activity (H), and orotate-to-DHO ratio (I).

(J) Parental, DHODH^{KO}, and DHODH^{rec} cells were grafted s.c. in BALB/c mice at 10^6 per animal, and tumor formation was assessed by USI.

Data in (C), (D), (F), and (I) are mean values ± SD ($n \geq 3$); data in (B), (H), and (J) are mean values ± SEM ($n \geq 3$ for B and H, $n = 6$ for J). The symbol "*" indicates statistically significant differences from parental cells, with p.

(Figure 4H; *cf.* Figure 4B). Consistent with these results, DHODH^{KO} cells showed low orotate/DHO ratio, which increased to parental values in DHODH^{rec} cells (Figure 4I), verifying this parameter as a proxy for *in situ* DHODH activity. Finally, we found that DHODH^{KO} cells failed to produce tumors, while similar tumor-forming capacity was found for parental and DHODH^{rec} cells (Figure 4J).

To verify whether the presence of DHODH is required for tumor growth in another model, we examined B16 DHODH^{KO} and B16 DHODH^{rec} cells. Compared with the parental line, these cells had comparable levels of subunits of mitochondrial complexes (Figure S5A) and OXPHOS assembly (Figure S5B). The cell lines also had similar relative levels of ATP generated by OXPHOS and glycolysis (Figure S5C). We next found that B16 DHODH^{KO} cells failed to form tumors, while B16 DHODH^{rec} cells formed tumors with similar rate to parental cells (Figure S5E). As expected, while DHODH^{rec} cells grew in the absence of uridine, B16 DHODH^{KO} cells were auxotrophic (Figure S5F). Consistent with this, B16 DHODH^{KO} cells featured normal routine respiration but lacked DHODH-dependent respiration (Figure S5G). Finally, we tested B16 lines for DHODH activity and found that it was absent in DHODH^{KO} cells (Figure S6H).

To summarize, DHODH is essential for tumor growth in 4T1 breast cancer and B16 melanoma models.

DHODH Links Respiration to *De Novo* Pyrimidine Synthesis and to Cell-Cycle Progression

De novo pyrimidine synthesis involves reactions that convert glutamine to uridine 5-monophosphate (UMP), with DHODH catalyzing the "mitochondrial" step (Figure 5A). To understand whether this pathway is operational in 4T1 lines, we measured the conversion of $^{13}C_5{}^{15}N_2$-Gln into UMP. In agreement with low DHODH respiration, formation of the m+5 isotopomer of UMP was low in D0–D10 cells, while it increased in D15 cells (Figure 5B). We also evaluated the level of unlabeled pyrimidines and purines in parental and D0–D25 cells. Compared with parental cells, pyrimidine nucleotides were low in non-/low-respiring cells and increased in D15 cells, while the levels of purine nucleotides were only marginally affected (Figure S4H). We next assessed conversion of labeled glutamine to UMP in parental, DHODH^{KO},

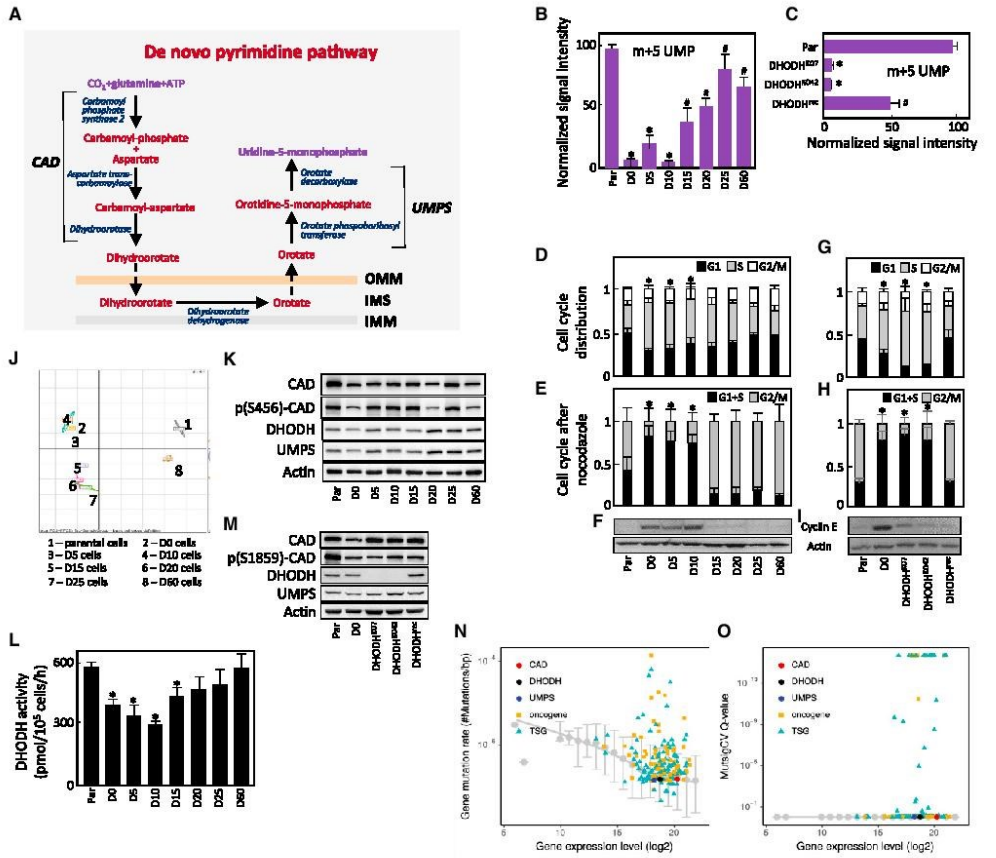

Figure 5. DHODH Links Respiration to *De Novo* Pyrimidine Synthesis and Cell-Cycle Progression

(A–L) *De novo* pyrimidine synthesis is catalyzed by the trifunctional CAD protein that includes the enzymatic activities of carbamoyl phosphate synthase 2, aspartate transcarbamoylase and dihydroorotase, the DHODH protein, the bifunctional UMPS protein with enzymatic activities of orotate phosphoribosyl transferase, and orotate decarboxylase (A). OMM, outer mitochondrial membrane; IMS, intermembrane space; IMM, inner mitochondrial membrane. 4T1 lines (B) and 4T1 cells with different DHODH status (C) were analyzed by liquid chromatography-mass spectrometry with $^{13}C_5{}^{15}N_2$-glutamine as the substrate for generation of the m+5 isotopomer of UMP, the product of the *de novo* pyrimidine pathway shown in (A). 4T1 lines were assessed for cell-cycle distribution (D), arrest in G2 following nocodazole treatment (10 μM, 1 hr) (E), and the level of cyclin E (F). 4T1 cells with different DHODH status were assessed for cell-cycle distribution (G), arrest in G2 following nocodazole treatment (H), and the level of cyclin E (I). Parental, D0, D5, D10, D15, D20, D25, and D60 cells were used for transcriptome analysis using the mouse Affymetrix chip, and the data were assessed by PCA (J). Parental and D0–D60 cells were assessed for members of the *de novo* pyrimidine pathway by WB (K) and for the DHODH enzymatic activity using an *in vitro* assay (L).

(M) Parental, D0, DHODH^{KO}, and DHODH^{rec} cells were assessed for components of the *de novo* pyrimidine pathway by WB.

(N) Raw mutation rates as a function of the average expression level. Mutations of oncogenes (in orange) and tumor suppressor genes (in blue) are compared with genes involved in the *de novo* pyrimidine biosynthesis. The baseline from median mutation rate of non-cancer genes is also shown as gray for comparison.

(O) Statistical significance of mutation rates over expected values (MutsigCV Q-value) as a function of the average expression level for cancer genes and genes involved in *de novo* pyrimidine biosynthesis, as compared with the baseline from non-cancer genes.

Data in (B)–(E), (G), and (H) are mean values ± SD; data in (L) are mean values ± SEM ($n \geq 3$). The symbol "*" indicates statistically significant differences from parental cells, and the symbol "#" indicates statistically significant difference from D0 cells, with $p < 0.05$. (F), (I), (K), and (M) show representative images of three biological replicates. Data in (N) and (O) represent analysis of more than 11,000 patients diagnosed with 33 different types of cancer listed in the Cosmic database.

and DHODH^{rec} cells. DHODH^{KO} cells contained lower UMP synthesis capacity compared with parental cells, and this was restored in DHODH^{rec} cells (Figure 5C).

Cancer cells are typified by rapid proliferation, which involves unhindered progression through the cell cycle. During the S phase, genomic DNA is replicated in a process that includes insertion of nucleotides produced by the *de novo* pyrimidine pathway into nascent DNA strands (Sigoillot et al., 2003). To test if respiration is linked to cell-cycle progression, we evaluated D0–D60 lines for cell-cycle distribution. This revealed that more D0–D10 cells were in the S phase compared with parental and D20–D60 cells (Figure 5D). We also found that upon nocodazole synchronization, a higher proportion of parental and D15–D60 cells were arrested in G2 compared with D0–D10 cells (Figure 5E). Finally, D0–D10, but not parental and D15–D60 cells, accumulated cyclin E, a marker of early S phase (Figure 5F).

We next investigated a link between S-phase arrest and DHODH activity. Cell-cycle evaluation revealed increased number of DHODH^{KO} cells in S phase compared with parental cells, with the proportion of DHODH^{rec} cells in S phase being comparable to parental cells (Figure 5G). A similar pattern was observed for G2 arrest after nocodazole treatment (Figure 5H) and for the cellular content of cyclin E (Figure 5I), consistent with a previous report (Mohamad Fairus et al., 2017). Finally, we found that B16 DHODH^{KO} cells were also arrested in S phase, while B16 DHODH^{rec} cells showed cell-cycle distribution similar to parental cells (Figure S5I). Hence, absence of DHODH activity suppresses pyrimidines and interferes with cell-cycle progression.

De Novo Pyrimidine Pathway Is Primed in OXPHOS-Deficient Cells

To understand the status of the pyrimidine pathway in D0–D60 lines and in parental 4T1 cells, we performed transcriptome analysis. Principal component analysis (PCA) in Figure 5J shows clustering of D0–D10 and D15–D25 cells. A similar pattern was observed for mitochondrial protein transcripts sourced from MitoCarta 2.0 (Calvo et al., 2015) (Figure S6A). Given the link between respiration, DHODH, pyrimidine synthesis, and tumor progression observed above, we analyzed microchip data for transcripts relevant for the *de novo* pyrimidine pathway (*cf.* Figure 5A) to test if the clustering pattern was maintained. This revealed no trend in the expression of *CAD*, *DHODH*, and *UMPS* transcripts in parental, D0–D25, and D60 cells (Figure S6B), consistent with the DHODH mRNA and protein levels shown in Figure 3B.

We next examined expression of proteins of the *de novo* pyrimidine pathway. Similar to DHODH, there were few differences in CAD, phosphorylated CAD, and UMPS among the lines tested (Figure 5K). Next, DHODH activity was 30%–50% lower in D0–D10 than in parental cells (Figure 5L), yet considerably higher than the very low DHODH-dependent respiration and low orotate/DHO ratio in these lines (*cf.* Figures 3D and 3E). Also, cells with manipulated DHODH content did not show significant changes in the expression of CAD and UMPS (Figure 5M).

The above results suggest that the *de novo* pyrimidine pathway is primed and preserved in OXPHOS-deficient cells. To interrogate this notion with patient data, we compared mutation rates of known cancer genes to genes of *de novo* pyrimidine synthesis (*CAD*, *DHODH*, and *UMPS*) as a function of average expression levels in >11,000 patients diagnosed with 33 different types of cancer listed in The Cancer Genome Atlas database. Both raw mutation rate (number of mutations per base pair in a gene) (Figure 5N) and statistical significance of mutations of a gene over expected mutations (Figure 5O) are shown for comparison. The median mutation rates (or significance) for other genes (not annotated as cancer genes) were utilized as a baseline. Raw mutation rates of *CAD*, *DHODH*, and *UMPS* were close to the baseline, and were statistically indistinguishable from the expected mutations according to MutsigCV (Q is nearly 1). By comparison, many known oncogenes and tumor suppressor genes had significantly higher mutation rates (20%, $Q < 0.1$). These results suggest that genes of the *de novo* pyrimidine pathway are rarely mutated in cancer.

To assess whether DHODH-dependent respiration and DHODH activity are conserved in different types of cancer, we examined breast, cervical, and pancreatic cancer cell lines as well as osteosarcoma cells. Routine and DHODH-dependent respiration varied between 30–80 and 2–4 pmol orotate/hr/10^5 cells, respectively (Figure S6C), while DHODH activity ranged from 200 to 450 pmol O_2/hr/10^6 cells (Figure S6D), indicating that DHODH/pyrimidine synthesis pathway function is preserved in cancer cells.

ATP5B^{KO} Cells Maintain Functional DHODH

Despite the absence of OXPHOS-derived ATP, ATP5B^{KO} cells form tumors in mice (Figures 2M and S5D) and should therefore maintain functional DHODH. We found that ATP5B^{KO} cells grew in the absence of uridine (Figure 6A), contained normal amounts of the DHODH protein (Figure 6A, insert), and featured DHODH-dependent respiration while routine respiration was decreased (Figure 6B). The relative NADH/NAD^+ ratio increased by 50%–60% in ATP5B^{KO} cells compared with parental cells (Figure 6C). ATP5B^{KO} cells had mitochondria without cristae (Figure 6F), in agreement with the literature (Daum et al., 2013). The finding of normal DHODH protein and DHODH-dependent respiration in ATP5B^{KO} cells was corroborated by normal DHODH activity (Figure 6H) and conserved proteins of the *de novo* pyrimidine pathway (Figure 6I). We also tested ATP5B^{KO} B16 cells and found a similar pattern for the corresponding lines (Figures S5F–S5H). Consistent with this, we observed fewer cells in S phase in both 4T1 ATP5B^{KO} and B16 ATP5B^{KO} cells than in their non-respiring counterparts (Figures 6K and S5I).

Complexes III and IV Propel DHODH-dependent Respiration to Promote Tumor Formation

The above data indicate that DHODH presents a link between respiration and tumor formation, controlling *de novo* pyrimidine synthesis independently of mitochondrial ATP generation. As DHODH connects to the mitochondrial pool of coenzyme Q (CoQ) that is redox-cycled by CIII/CIV, DHODH might be stalled when respiration is deficient due to lack of its electron acceptor before it is reconstituted in D15–D20 cells. We therefore expressed alternative oxidase (AOX) in 4T1ρ^0 and B16ρ^0 cells. This protein is present in lower eukaryotes where it replaces CIII + CIV, facilitating direct electron transfer from CoQ to oxygen (Hakkaart et al., 2006; Perales-Clemente et al., 2008).

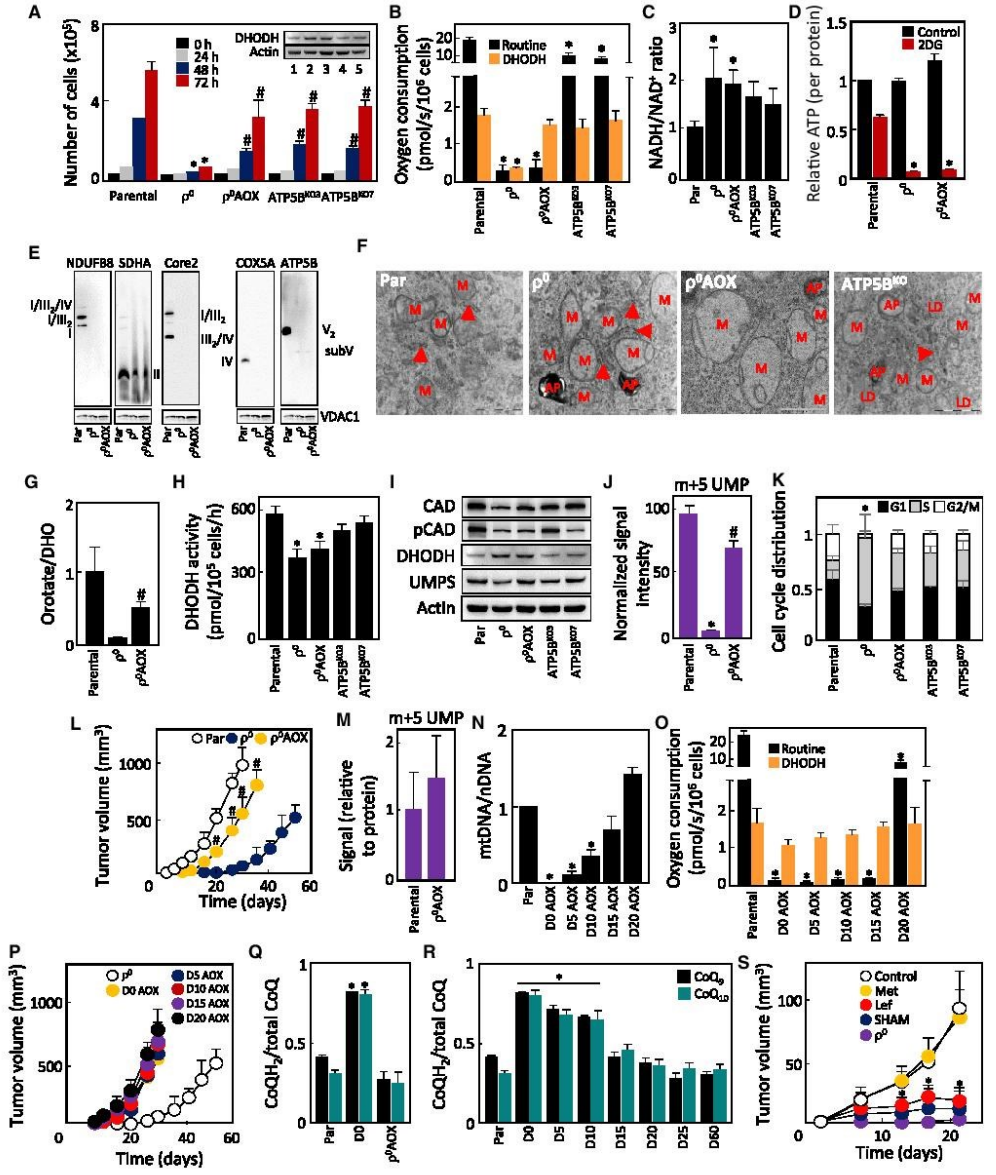

Figure 6. ATP5B Cells Maintain Functional DHODH, Propelled by CIII and CIV

(A–D) Parental, ρ^0, ρ^0 AOX, and ATP5B^{KO} cells were evaluated for growth in the absence of uridine (A), the level of the DHODH proteins by WB (A, insert), routine and DHODH-dependent respiration (B), NADH/NAD$^+$ ratio (C), and ATP generation in the absence or presence of 50 mM 2DG (4.5 g/L glucose) (D).

(E–K) Parental, ρ^0, and ρ^0 AOX cells were evaluated by NBGE for the assembly of RCs and SCs using antibodies against subunits of individual RCs (E). Cells as shown were evaluated for mitochondrial morphology using TEM (F); the ratio of orotate-to-DHO (G); DHODH activity (H); level of the CAD, p(S1859)-CAD, DHODH, and UMPS proteins (I); formation of m+5 UMP from $^{13}C_5$,$^{15}N_2$-Gln (J); and cell-cycle distribution (K).

(legend continued on next page)

4T1ρ^0 AOX cells proliferated in the absence of uridine (Figure 6A), suggesting that AOX reactivates DHODH in ρ^0 cells. Consistent with this, 4T1ρ^0 AOX cells contained normal DHODH protein (Figure 6A, insert) and DHODH-dependent respiration, while routine respiration was low and comparable to 4T1ρ^0 cells (Figure 6B). The virtual absence of routine respiration was reflected by increased NADH/NAD^+ ratio in ρ^0 AOX cells, which was similar to 4T1ρ^0 cells (Figure 6C). As with 4T1ρ^0 cells, 4T1ρ^0 AOX cells used glycolysis to maintain normal levels of ATP (Figure 6D), lacking assembled mitochondrial complexes (except for CII) (Figure 6E) and mitochondrial cristae (Figure 6F); 4T1ρ^0 AOX cells converted DHO to orotate (Figure 6G), exerted normal DHODH activity (Figure 6H), maintained proteins of the *de novo* pyrimidine pathway (Figure 6I), and efficiently converted glutamine to UMP (Figure 6J). As a result, 4T1ρ^0 AOX cells were unlocked from the S phase arrest (Figure 6K) and efficiently formed tumors in BALB/c mice (Figure 6L). To verify the AOX-driven reactivation of the *de novo* pyrimidine pathway in tumors *in vivo*, we performed a live labeling study, in which. $^{13}C_5{}^{15}N_2$-Gln was infused via the jugular vein into BALB/c mice carrying tumors derived from 4T1 (17 days after grafting) and 4T1ρ^0 AOX cells (14 days after grafting), and the abundance of the m+5 isotopomer of UMP was evaluated in isolated tumor tissue. Conversion of Gln to UMP was comparable in 4T1 and 4T1ρ^0 AOX cell-derived tumors (Figure 6M), consistent with normal flux through the *de novo* pyrimidine pathway in AOX-expressing tumors. B16 lines showed behavior similar to the corresponding 4T1ρ^0 lines (Figures S5J–S5P), and B16ρ^0 AOX cells formed tumors almost as efficiently as their parental counterparts (Figure S5Q).

To confirm that AOX acts *in vivo* by reactivating CoQ redox-cycling rather than by enhancing mitochondrial transfer into ρ^0 cells, we grafted 4T1ρ^0 AOX cells into BALB/c mice and derived lines on days 5, 10, 15, and 20. The temporal increase in mtDNA in 4T1ρ^0 AOX cells was similar to 4T1ρ^0 lines (Figure 6N; *cf.* Figures 1E and S1B). However, D0–D15 AOX cells had very low routine respiration that increased in D20 AOX cells to ≈40% of parental cells, while DHODH-dependent respiration remained close to parental cell levels (Figure 6O). To examine their tumor-forming propensity, we grafted D0–D20 AOX cells into BALB/c mice, and observed that D5 AOX–D20 AOX cells formed tumors similarly to D0 (ρ^0) AOX cells (Figure 6P; *cf.* Figure 6L).

The link between CIII + CIV and electrons generated upstream in the OXPHOS systems is mediated by redox-cycling of CoQ (i.e., oxidation of $CoQH_2$ to CoQ). To assess whether $CoQH_2$ is re-oxidized in 4T1ρ^0 AOX cells, where the AOX protein substitutes CIII + CIV in redox-cycling CoQ, we determined the CoQ redox state in parental, 4T1ρ^0 and 4T1ρ^0 AOX cells. In rodents, CoQ_9 is the major form of CoQ with the remainder made up by CoQ_{10}. We therefore assessed the $CoQH_2$/total CoQ (i.e., $CoQH_2$+CoQ) for both forms of CoQ. In parental cells, >50% of CoQ was in the oxidized state, while in 4T1ρ^0 cells most CoQ was in the reduced form (Figure 6Q). Expression of AOX in non-respiring cells shifted the redox state of CoQ to its more oxidized form (Figure 6Q), consistent with published data (Guarás et al., 2016). We next assessed the $CoQH_2$/total CoQ ratio in D0–D60 cells and found it higher in D0–D10 and lower in D15–D60 cells, suggesting that restoration of respiration resulted in efficient oxidation of the CoQ pool (Figure 6R).

To confirm that restoration of DHODH function by reactivation of CoQ redox-cycling is a major consequence of AOX expression in ρ^0 cells that supports tumor formation, we tested the effect of the AOX inhibitor salicylhydroxamic acid (SHAM) (Martínez-Reyes et al., 2016), the DHODH inhibitor leflunomide (Loffler et al., 2005), and the CI inhibitor metformin (Wheaton et al., 2014) on tumor formation in BALB/c mice with grafted 4T1ρ^0 AOX cells. Figure 6 shows the inhibitory effect of both SHAM and leflunomide but not that of metformin, pointing to the involvement of the AOX-DHODH axis in this process and excluding potential effects of AOX on the NADH/NAD^+ cycling via nascent CI.

Pyruvate May Not Be Limiting for Tumor Growth

Since low-respiring cells are auxotrophic for pyruvate and uridine, we tested whether the capacity of ρ^0 AOX cells to form tumors could be promoted by the presence of pyruvate in the microenvironment. By providing external oxidizing power, extracellular pyruvate could conceivably release the potential block in proliferation and tumor growth linked to defective aspartate biosynthesis due to the lack of NAD^+ recycling (Sullivan et al., 2015, 2018; Birsoy et al., 2015; Garcia-Bermudez et al., 2018). Pyruvate was suggested to be increased in malignant compared with normal tissues (Goveia et al., 2016). We thus analyzed pyruvate in tissue excised from the site of grafted 4T1ρ^0 cells at time points used to establish the lines, in parental and D5–D25 cells (*cf.* Figure 1B). At all time points, pyruvate concentrations in the tumor lesions/tissue were ≈20%–40% higher than in the liver (Figure S7A), being 2–3 nmol/mg of tumor tissue. Assuming a tissue density close to 1 g/mL, this corresponds to concentration of ≈2 mM (i.e., higher than the 1 mM pyruvate that

(L) Parental, ρ^0, and ρ^0 AOX cells were grafted s.c. in BALB/c mice at 10^6 per animal, and tumor formation was assessed by USI.
(M–O) BALB/c mice with 4T1 and 4T1ρ^0 AOX cell-derived tumors (≈250 mm^3) were cannulated via the jugular vein and infused with $^{13}C_5$, $^{15}N_2$-Gln, and the tumors were analyzed for the M+5 UMP isotopomer as detailed in STAR Methods (M). ρ^0 AOX (D0 AOX) cells were grafted into BALB/c mice s.c. at 10^6 per animal. On days 5, 10, 15, and 20 post-grafting, the (pre-)tumor plaques were excised from the animals and D5 AOX, D10 AOX, D15 AOX, and D20 AOX lines were established. Parental and D0 AOX-D20 AOX cells were assessed for mtDNA using qPCR (N) and for routine and DHODH-dependent respiration using the Oxygraph (O).
(P) Parental, D0, and D0 AOX to D20 AOX cells were grafted in BALB/c mice (10^6 cells/per animal), and tumor volume was assessed by USI.
(Q) Parental, ρ^0, and ρ^0 AOX cells were assessed for the ratio of $CoQH_2$ and total CoQ including the CoQ_9 and CoQ_{10} analogs.
(R) Parental and ρ^0 (D0) cells as well as D5–D60 lines were assessed for the ratio of $CoQH_2$ and total CoQ.
(S) BALB/c mice were grafted with ρ^0 AOX cells at 10^6 per animal; tumors were treated with metformin (Met), leflunomide (Lef), and salicylhydroxamic acid (SHAM) as detailed in STAR Methods; and tumor volume wasquantified.
Data in (A), (C), (D), (G), (J), (K), (M), (N), (Q), and (R) are mean values ± SD (n = 3); those in (B), (H), and (O) n ≥ 3; (L), (S) (n = 5), and P (n = 3) are mean values ±SEM. The symbol "*" indicates statistically significant differences from parental cells, with $p < 0.05$; the symbol "#" indicates statistically significant differences from ρ^0 cells, with $p < 0.05$. (A, insert), (E), (F), and (I) show representative images of three biological replicates.

supported proliferation of respiration-deficient cells in our *in vitro* experiments) (*cf.* Figure 3A) (King and Attardi, 1988, 1989).

To see whether pyruvate detected in tumors was extracellular (i.e., able to provide the oxidizing power for aspartate production), we analyzed serum (containing no intracellular pyruvate) from C57BL/6 and BALB/c mice with and without tumors as well as serum from cancer patients and healthy human subjects for pyruvate. The measured concentration was about 75–150 μM in mice and about 200 μM in human samples (Figure S7B), the latter being similar to published values (Landon et al., 1962).

To determine the effect of extracellular pyruvate on intracellular aspartate and on the proliferative potential of ρ^0 cells, we evaluated 4T1ρ^0 and B16ρ^0 cells maintained with uridine and increasing amounts of added pyruvate for intracellular aspartate. Figures S7C and S5R document ≈1.5-fold increase of intracellular aspartate with escalating extracellular concentrations of pyruvate over the range of 0–1 mM. Aspartate increased at extracellular pyruvate concentrations equivalent to those measured in mouse and human serum. Similarly, the same level of pyruvate as found in serum resulted in stimulation of cell proliferation (Figures S7D and S5S).

We next evaluated intracellular aspartate in the absence of extracellular pyruvate and uridine. While aspartate was reduced by ≈30% in non-respiring D0–D10 cells, it recovered in D15 cells (Figure S7E). Intracellular aspartate was unchanged in ATP5B^{KO} (Figure S7F) or DHODH-manipulated cells (Figure S7G). Further, AOX expression in 4T1ρ^0 cells did not increase aspartate, which remained similar as in the ρ^0 cells (Figure S7H). This demonstrates that AOX overexpression does not increase intracellular aspartate in our system and should not support growth of ρ^0 cells in the absence of pyruvate. Accordingly, ρ^0 AOX cells, similarly as ρ^0 cells, were auxotrophic for pyruvate (Figure S7I).

Finally, we tested the effect of uridine on proliferation of 4T1ρ^0 and B16ρ^0 cells cultured in the presence of serum prepared from BALB/c and C57BL/6 mice instead of FCS. We observed uridine to significantly enhance cell growth under these conditions (Figures S7J and S5T). To further document the importance of uridine limitation in tumor growth, we tested the effect of uridine supplementation of mice with grafted 4T1ρ^0 cells on tumor formation. Figure S7K shows that tumors appeared earlier in uridine-supplemented mice, and at a time that precedes mitochondrial transfer and the associated respiration recovery. Collectively, this further supports the notion that non-functional DHODH presents a severe limitation for tumor growth.

DISCUSSION

The importance of mitochondria for the initiation and progression of tumorigenesis is now emerging. It is evident that, despite the well-known Warburg effect, tumors have active mitochondrial bioenergetic metabolism (Marin-Valencia et al., 2012; Hensley et al., 2016). Disruption of the ETC shows promise in cancer therapy (Rohlena et al., 2011; Zhang et al., 2014; Rohlenova et al., 2017). Cells with deleterious mtDNA mutations fail to form tumors (Park et al., 2009), and genetic ablation of OXPHOS restrains tumorigenesis (Weinberg et al., 2010). mtDNA-depleted (ρ^0) tumor cells present a particularly instructive case. Having no functional OXPHOS, these cells cannot form tumors in mice unless they acquire host mtDNA (Tan et al., 2015) via horizontal transfer of whole mitochondria from the stroma (Dong et al., 2017). In this way, ρ^0 cells give rise to palpable tumors only after a long initial lag period (Tan et al., 2015; Dong et al., 2017). While these studies suggest that functional OXPHOS is necessary for tumorigenesis, previously published data did not pinpoint exactly which aspect of OXPHOS function is essential. The key finding of the current study is that DHODH-driven pyrimidine biosynthesis, rather than OXPHOS-mediated ATP production, is essential for tumorigenesis.

To further explore this issue, we developed a unique model that allowed us to characterize the link between OXPHOS function and tumor formation in unprecedented temporal detail. We followed the events associated with tumorigenesis of mtDNA-depleted ρ^0 cells in mice during the initial lag period and throughout the various stages of tumor progression and demonstrate that the appearance of tumors coincides with OXPHOS reconstitution at days 15–25 post-grafting, after the end of a "dormant" period when mtDNA is replenished and OXPHOS machinery re-assembled. This detailed investigation was possible because cancer cells isolated at various time points in the 4T1ρ^0 tumor model are remarkably stable in culture, and their properties, such as the level of mtDNA, respiration, or ETC assembly, did not change with time. This unexpected stability, observed by others in a different model (Picard et al., 2014), can be explained by the absence of selection pressure in the rich culture media containing uridine/pyruvate (see below).

Surprisingly, we found that the best known OXPHOS function, production of ATP by ATP synthase, is not essential for tumorigenesis. While increased mitochondrial contribution to total ATP production was concurrent with OXPHOS reconstitution, ATP synthase assembly and appearance of tumors, the total ATP content in the cells and energy charge were not, in general, significantly decreased, but maintained by glycolysis with its much faster kinetics compared with OXPHOS (Koppenol et al., 2011). Most strikingly, cells deficient in ATP synthase were found to readily produce tumors. This suggests that mitochondrial ATP production is not limiting for tumor growth, at least at its earlier stages. Instead, we found that the important OXPHOS-related feature that promotes tumorigenesis is *de novo* pyrimidine synthesis, directly driven by respiration via DHODH, which converts DHO to orotate. This was clearly demonstrated by the failure of DHODH-deficient cells to form tumors, despite the fact that these cells show otherwise fully functional OXPHOS and normal ATP levels. Furthermore, the DHO/orotate ratio was increased in DHODH^{KO} cells and non-respiring D0–D10 cells, and formation of UMP from glutamine was compromised. This indicates that the enzyme is inactive but is reactivated before tumors appear. The central role for DHODH in tumorigenesis is consistent with a recent report demonstrating upregulation of DHODH during the course of UV-induced skin tumorigenesis and its functional role therein (Hosseini et al., 2018).

The link between OXPHOS and DHODH is maintained by CoQ redox-cycling (Gregoire et al., 1984; Ayer et al., 2015). Electrons, removed from DHO by DHODH, are transferred to CoQ yielding $CoQH_2$, which is then re-oxidized at CIII. The CoQ redox cycle is broken in the absence of CIII/CIV activity when OXPHOS is non-functional due to mtDNA deficiency. This removes the only practical means of CoQ recovery in

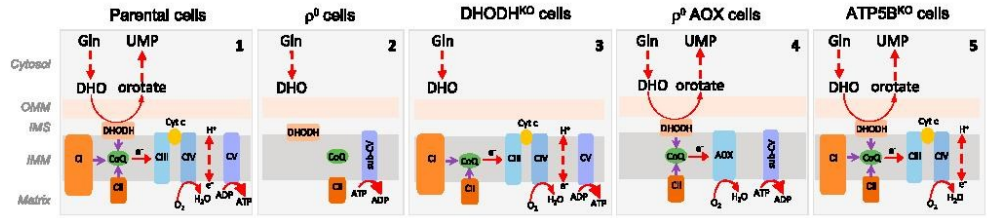

Figure 7. Scheme Depicting the Role of Respiration in Propelling *De Novo* Pyrimidine Synthesis

Individual schemes illustrating the role of respiration in *de novo* pyrimidine synthesis with central role of CoQ and DHODH, as documented using our cell models, including parental (1), ρ^0 (2), DHODH^{KO} (3), ρ^0 AOX (4), and ATP5B^{KO} cells (5).

mammalian cells, while maintaining upstream sources of electrons for CoQ reduction such as CII or DHODH itself. These sources of electrons reduce CoQ to the maximal attainable level before they stall due to the lack of the electron acceptor. Indeed, in non-respiring D0–D10 cells CoQ was present predominantly in the reduced form, whereas the $CoQH_2$/CoQ redox state decreased and approached parental cell values before the onset of tumor formation, coinciding with CIII/CIV reconstitution. AOX expression in ρ^0 cells was sufficient to reactivate DHODH-driven respiration, normalize the $CoQH_2$/CoQ and DHO/orotate ratios, reinitiate UMP synthesis both *in vitro* and *in vivo*, and restore tumorigenicity in the absence of mtDNA. Importantly, live labeling with $^{13}C_5$,$^{15}N_2$-Gln confirmed the *in vitro* results in a mouse model derived from 4T1 ρ^0 AOX cells 14 days after grafting the cells, i.e., at the stage when respiration is not recovered and tumor formation is largely dependent on AOX-propelled DHODH (Figures 6M–6P). It thus seems that lack of redox-cycling of CoQ, not OXPHOS deficiency per se, restricts tumorigenesis.

We therefore propose a scenario based on our experimental models and depicted schematically in Figure 7. In fully respiring cells, CI, CII, and DHODH transfer electrons to CoQ, which are then forwarded to CIII. This latter complex transfers electrons to CIV, which then produces water at the expense of molecular oxygen. CI, CIII, and CIV increase the proton-motive force in the form of $\Delta\Psi_{m,i}$ that, among other functions, drives formation of ATP catalyzed by CV. In ρ^0 cells, mtDNA is missing, resulting in the collapse of CI, CIII, and CIV, and in the assembly of CII and sub-CV. Under this scenario, DHODH cannot convert DHO to orotate, since CoQ cannot transfer electrons to CIII. ATP is generated by glycolysis and $\Delta\Psi_{m,i}$ maintained by ATP cleavage by the ATPase activity of sub-CV; ρ^0 cells form tumors only after acquisition of mtDNA from the host and restoration of respiration (Tan et al., 2015; Dong et al., 2017). DHODH^{KO} cells lack tumor-forming capacity and cannot be "repaired" by mtDNA acquisition, because the absence DHODH precludes conversion of DHO to orotate. On the other hand, ρ^0 AOX cells have normal DHODH-dependent respiration, since electrons generated by conversion of DHO to orotate are captured by CoQ and transferred to AOX, which substitutes for the combined activity of CIII and CIV. These cells efficiently form tumors. Finally, ATP5B^{KO} cells that are highly glycolytic have normal DHODH-dependent respiration and form tumors faster than ρ^0 cells. Together, our findings demonstrate an important role of DHODH and CoQ redox-cycling in tumor formation in cells with damaged mtDNA, resulting in mtDNA acquisition and restoration of respiration independent of OXPHOS-derived ATP.

A typical consequence of OXPHOS dysfunction is the auxotrophy for pyruvate and uridine. Pyruvate as an exogenous electron acceptor is required to produce aspartate, a precursor of *de novo* pyrimidine biosynthesis, and uridine to complement defective DHODH-linked pyrimidine synthesis via salvage pathways (Loffler, 1980; King and Attardi, 1988, 1989; Birsoy et al., 2015; Sullivan et al., 2015). We observed auxotrophy in D0–D15 cells, which was relieved by OXPHOS reconstitution following mtDNA transfer and prior to tumorigenesis, or in the case of uridine, by AOX expression. Given the efficacy of AOX-mediated restoration of tumorigenicity, this suggests that the DHODH dysfunction-induced defect in *de novo* pyrimidine synthesis could be a major obstacle for *in vivo* growth of respiration-compromised tumor cells, and that pyruvate might not be the limiting factor. Indeed, we consistently measured substantial pyruvate at the site of tumor growth throughout the course of the experiment, and levels of pyruvate in serum of mice and cancer patients were sufficient to support proliferation of ρ^0 cells *in vitro*, although suboptimal. In addition, it has been reported that cancer cells deficient in the CII subunit SDHB are addicted to pyruvate (Cardaci et al., 2015; Lussey-Lepoutre et al., 2015), yet they readily form tumors in mice (Guzy et al., 2008; Bezawork-Geleta et al., 2018). Importantly, SDHB-deficient neoplasias are relatively common in humans and have unfavorable prognosis (King et al., 2011). These data suggest that pyruvate may not be limiting *in vivo* under all circumstances.

To begin to place our results into context, we suggest that *de novo* pyrimidine biosynthesis, driven by functional OXPHOS, is crucial for tumor growth. This notion is supported by the failure of DHODH^{KO} cells to form tumors, and by the recovery of tumorigenicity when AOX is expressed in ρ^0 cells. Our results also suggest that DHODH represents a bottleneck for pyrimidine synthesis in non-respiring cells, although they do not rule out other limitations that might constrain *in vivo* growth in the absence of functional OXPHOS. While a deficiency in DHODH disrupts the pyrimidine biosynthesis pathway in a defined manner, expression of AOX restores DHODH activity as well as reactivating CoQ redox-cycling. AOX might also impact on additional metabolic pathways converging on the CoQ pool. It seems unlikely, however, that AOX indirectly supports the synthesis of aspartate via nascent CI. AOX expression did not affect the NADH/NAD^+

ratio or content of aspartate in ρ^0 cells, just as ρ^0 AOX cells are auxotrophic for pyruvate. Previous studies have reported that aspartate can be limiting for tumor growth *in vivo* due to its inefficient import into cells and proposed that CI inhibition constrains tumor growth by limiting aspartate biosynthesis (Garcia-Bermudez et al., 2018; Sullivan et al., 2018). However, while growth retardation by CI inhibition was complete *in vitro* in the absence of pyruvate, it was incomplete when CI was targeted *in vivo* (Sullivan et al., 2018). The remaining proliferation in that case could perhaps be supported by extracellular pyruvate. To summarize, while this and other reports clearly show that pyrimidine biosynthesis is essential for tumor growth in multiple cancer models, the identity of the rate-limiting steps in various conditions deserves further investigation, as it will likely be affected by the environment and by the experimental model employed.

What does this mean for cancer therapy? We found that components of the *de novo* pyrimidine synthesis pathway rarely mutate in cancer, clearly showing its importance. In our experimental models, the pathway, including DHODH itself, was primed to respond when the block in CoQ redox-cycling was removed. Inhibitors of DHODH are used in the clinic as anti-rheumatics (Olsen and Stein, 2004) and show efficacy in cancer settings either alone or in combination with anti-cancer agents (Brown et al., 2017; Mathur et al., 2017; Sykes et al., 2016; Shukla et al., 2017; Kim et al., 2017; Koundinya et al., 2018). A more effective therapeutic approach could involve intervention at the level of respiratory CIII. This would not only block DHODH activity and pyrimidine biosynthesis, but would also increase the generation of reactive oxygen species from the respiratory chain (Adam-Vizi and Chinopoulos, 2006; Murphy, 2009; Quinlan et al., 2012), striking the cancer cell on two fronts at once by way of combining the cell death inducing activity of excessive oxidative stress (Rohlena et al., 2011) with the cytostatic activity of DHODH inhibition. While anti-cancer agents directed at CIII exist (Le et al., 2007), their potential side effects on the hematopoietic and immune systems would need to be carefully evaluated (Anso et al., 2017).

In conclusion, we show here that cancer cells with dysfunctional OXPHOS due to mtDNA deficiency import mitochondria from the host to restore respiration and facilitate the DHODH-catalyzed conversion of DHO to orotate. Intriguingly, reactivation of CoQ redox-cycling is sufficient to drive DHODH and to allow cancer cells to form tumors. We propose that DHODH-mediated CoQ redox-cycling is an important link between de novo pyrimidine synthesis and respiration, and that it may be a promising target for broad-spectrum cancer therapy. This notion is corroborated by the emergence of tumor metabolism as a target for anti-cancer therapeutic strategies (Sullivan et al., 2016; Martinez-Outschoorn et al., 2017). Our reasoning is based on the concept that despite their high metabolic plasticity, that includes the ability to "import" mitochondria, cancer cells seem unable to "bypass" pyrimidine synthesis defects, presenting a novel aspects of cancer biology with potential therapeutic implications.

Limitations of Study

While we propose that targeting DHODH may present a novel, broad-spectrum anti-cancer strategy, we note that there are mitochondrial inhibitors that are under clinical trial, such as inhibitors of complex I (Molina et al., 2018; Rohlenova et al., 2017) or α-ketoglutarate dehydrogenase (Alistar et al., 2017), which effectively suppress tumor growth without DHODH inhibition. In addition, it can be expected that DHODH inhibition will not be effective in all types of tumors, and that combined targeting involving DHODH and complex I may provide a broader and more effective anti-cancer strategy by simultaneously interfering with two crucial steps of pyrimidine biosynthesis. In addition, while we do not see a direct effect of AOX overexpression on aspartate biosynthesis *in vitro* in the absence of complex I activity, it is possible that AOX expression, by altering cellular redox balance, could stimulate tumor growth *in vivo* in a complex I-independent manner or that as yet uncharacterized factors in the tumor microenvironment could synergize with AOX to stimulate tumor growth.

STAR★METHODS

Detailed methods are provided in the online version of this paper and include the following:

- KEY RESOURCES TABLE
- CONTACT FOR REAGENT AND RESOURCE SHARING
- EXPERIMENTAL MODEL AND SUBJECT DETAILS
- METHOD DETAILS
  - Cell Culture
  - Evaluation of Uridine and Pyruvate Auxotrophy
  - Preparation of Cells with Knocked Out or Reconstituted Genes
  - Mitochondrial Membrane Potential and Mitochondrial Superoxide Evaluation
  - Evaluation of ATP Level, Glucose Uptake and Lactate Formation
  - Evaluation of NADH/NAD^+ Ratio
  - Analysis of Coenzyme Q
  - Evaluation of Respiration and Glycolysis
  - DHODH Activity Assay
  - Cell-Cycle Analysis
  - Western Blotting
  - Native Blue Gel Electrophoresis (NBGE)
  - DNA Sequencing
  - mtDNA Level Assay
  - Quantitative Real-Time (Reverse Transcription) PCR
  - Single Cell qPCR
  - mTRIP Analysis
  - Mitochondrial Chromatin Immunoprecipitation (mitoChIP) Assay
  - Microarray Analysis
  - Stimulated Emission Depletion (STED) Microscopy
  - Mitochondrial NADH Assessment
  - Transmission Electron Microscopy (TEM)
  - Measurement of Dihydroorotate and Orotate
  - Flux Analysis of Conversion of Glutamine to UMP
  - Analysis of Aspartate and Nucleotides
  - *In Vivo* Metabolic Studies
  - Mutation Rates of Genes in the *De Novo* Pyrimidine Biosynthesis Pathway
  - Evaluation of Cell Proliferation in Tumor Tissue

- Evaluation of Pyruvate
- Formation of Syngeneic Tumors
- Statistical Analysis
- DATA AND SOFTWARE AVAILABILITY

SUPPLEMENTAL INFORMATION

Supplemental Information includes seven figures and two tables and can be found with this article online at https://doi.org/10.1016/j.cmet.2018.10.014.

ACKNOWLEDGMENTS

This work was supported in part by an Australian Research Council Discovery grant, Czech Science Foundation grants (15-02203S, 16-12719S, 17-07635S, and 17-0192J) and Czech Health Research Council grants (16-31604A and 17-30138A) to J.N., Czech Science Foundation grants (17-20904S and 16-22823S) to J.R., a Czech Science Foundation grant (16-12816S) to J.T., Czech Science Foundation grant (18-11275S) to K.D.-H., Czech Science Foundation grant (18-02550S) to S.H., by the institutional support from Czech Academy of Sciences (RVO: 86652036), by the Ministry of Education, Youth and Sports of the Czech Republic within the LQ1604 National Sustainability Program II (Project BIOCEV-FAR), and by the by the ERDF projects BIOCEV (CZ.1.05/1.100) and Mitenal (CZ.2.16/3.1.00/21531). Y.Z. was supported in part by the National Health and Medical Research Council (1059775 and 1083450). P.J.O. was funded in part by FEDER funds through the Operational Program Competitiveness Factors - COMPETE and national funds by FCT - Foundation for Science and Technology under projects PTDC/DTP-FTO/2433/2014, POCI-01-0145-FEDER-016659, POCI-01-0145-FEDER-007440, and POCI-01-0145-FEDER-016390:CANCEL STEM. R.S. acknowledges support from the National Health & Medical Research Council Senior Principal Research Fellowship 1111632, M.V.B. was supported by the Health Research Council of New Zealand, the Cancer Society of New Zealand and the Malaghan Institute, K.P. was supported by the Intramural Research Program of the NIH, NICHD, and M.S. and P.H. were supported by the Technology Agency of the Czech Republic (TE01020118). This work was also supported by the framework of international cooperation program (NRF-2016K2A9A1A06921853) and from a National Research Foundation of Korea (NRF) grant funded by the Korea government (MSIT) (NRF-2018R1A3B1052328). L.C. and M.R. were supported by DARRI (PasteurInnov 14/152). A.R.C. was supported by the FCT PhD scholarship SFRH/BD/103399/2014. M.B., Z.E., S.M.N., and E.D. were supported by the Grant Agency of Charles University (GA UK 362015, GA UK 1100217, GA UK 1552218, and GA UK 1560218, respectively). We acknowledge the Imaging Methods Core Facility at the BIOCEV supported by the Czech-BioImaging large RI projects (LM2015062 and CZ.02.1.01/0.0/0.0/16_013/0001775 Czech-BioImaging), funded by MEYS CR. We acknowledge as well the Electron Microscopy Core Facility at the IMG supported by the MEYS CR (LM2015062 Czech-BioImaging). We thank N.S. Chandel for providing the pWPI-AOX-IRES-GFP vector, C. Suarna for technical assistance with CoQ analysis, and C. Deus, T. Martins, and R. Couto for technical assistance with Seahorse analyses, and to T. Mracek for fruitful discussions.

AUTHOR CONTRIBUTIONS

J.N., J.R., L.D., J.K., and M.V.B. designed the research; J.K., M.B., A.R.C., S.B., K.R., K.V., Z.E., A.N., L.K., Z.N., B.E., K.J., A.B.-G., K.K., K.D.-H., S.M.N., and R.Z. performed most *in vitro* and *in vivo* experiments; D.S. and M.K. performed and analyzed single-cell qPCR studies; S.H. and E.D. performed cell-cycle experiments; S.O., Y.J.A., and S.P. designed, performed, and interpreted metabolomics and fluxomics studies; T.C.-O., T.L.S., V.A.S., and P.J.O. performed and interpreted mitochondrial respiration, membrane potential, and superoxide anion experiments; L.C. and M.R. performed and analyzed mTRIP experiments; G.J.M. and R.S. performed and analyzed CoQ assays; M.S. and P.H. performed and interpreted TEM; M.O. performed and interpreted STED microscopy; H.S. performed and interpreted microchip analyses; T.Z. and Y.Z. provided and interpreted bioinformatics data. W.J.H.K. provided methodology; J.T. and C.S.-A. designed and performed mitoChIP analyses, J.T. also performed and analyzed results of sequencing and revised the manuscript; T.H., K.P., and R.G. provided serum samples of healthy and neoplastic subjects; F.K. helped with *in vivo* labeling experiments; J.N., J.R., R.S., L.D., J.K., S.P., and M.V.B. wrote and revised the manuscript.

DECLARATION OF INTERESTS

The authors declare that they have no competing interests.

Received: November 15, 2017
Revised: August 4, 2018
Accepted: October 24, 2018
Published: November 15, 2018

REFERENCES

Acin-Perez, R., Fernandez-Silva, R., Peleato, M.L., Perez-Martos, A., and Enriquez, J.A. (2008). Respiratory active mitochondrial supercomplexes. Mol. Cell *32*, 529–539.

Adam-Vizi, V., and Chinopoulos, C. (2006). Bioenergetics and the formation of mitochondrial reactive oxygen species. Trends Pharmacol. Sci. *27*, 639–645.

Alistar, A., Morris, B.B., Desnoyer, R., Klepin, H.D., Hosseinzadeh, K., Clark, C., Cameron, A., Leyendecker, J., Topaloglu, U., Boteju, L.W., et al. (2017). Safety and tolerability of the first-in-class agent CPI-613 in combination with modified FOLFIRINOX in patients with metastatic pancreatic cancer: a single-centre, open-label, dose-escalation, phase 1 trial. Lancet Oncol. *18*, 770–778.

Althoff, T., Mills, D.J., Popot, J.L., and Kühlbrandt, W. (2011). Arrangement of electron transport chain components in bovine mitochondrial supercomplex I1III2IV1. EMBO J. *30*, 4652–4664.

Anso, E., Weinberg, S.E., Diebold, L.P., Thompson, B.J., Malinge, S., Schumacker, P.T., Liu, X., Zhang, Y., Shao, Z., Steadman, M., et al. (2017). The mitochondrial respiratory chain is essential for haematopoietic stem cell function. Nat. Cell Biol. *19*, 614–625.

Aslakson, C.J., and Miller, F.R. (1992). Selective events in the metastatic process defined by analysis of the sequential dissemination of subpopulations of a mouse mammary tumor. Cancer Res. *52*, 1399–1405.

Ayer, A., Macdonald, P., and Stocker, R. (2015). CoQ10 function and role in heart failure and ischemic heart disease. Annu. Rev. Nutr. *35*, 175–213.

Bayona-Bafaluy, M.P., Acín-Pérez, R., Mullikin, J.C., Park, J.S., Moreno-Loshuertos, R., Hu, P., Pérez-Martos, A., Fernández-Silva, P., Bai, Y., and Enríquez, J.A. (2003). Revisiting the mouse mitochondrial DNA sequence. Nucl. Acids Res. *31*, 5349–5355.

Bezawork-Geleta, A., Wen, H., Dong, L.F., Yan, B., Vider, J., Boukalova, S., Krobova, L., Vanova, K., Zobalova, R., Sobol, M., et al. (2018). Alternative assembly of respiratory complex II connects energy stress to metabolic checkpoints. Nat. Commun. *9*, 2221.

Birsoy, K., Wang, T., Chen, W.W., Freinkman, E., Abu-Remaileh, M., and Sabatini, D.M. (2015). An essential role of the mitochondrial electron transport chain in cell proliferation is to enable aspartate synthesis. Cell *162*, 540–551.

Blecha, J., Magalhães Novais, S., Rohlenova, K., Novotna, E., Lettlova, S., Schmitt, S., Zizchka, H., Neuzil, J., and Rohlena, J. (2017). Antioxidant defense in quiescent cells determines selectivity of electron transport chain inhibition-induced cell death. Free Radic. Biol. Med. *112*, 253–266.

Boukalova, S., Stursa, J., Werner, L., Ezrova, Z., Cerny, J., Bezawork-Geleta, A., Pecinova, A., Dong, L.F., Drahota, Z., and Neuzil, J. (2016). Mitochondrial targeting of metformin enhances its activity against pancreatic cancer. Mol. Cancer Ther. *15*, 2875–2886.

Brandon, M., Baldi, P., and Wallace, D.C. (2006). Mitochondrial mutations in cancer. Oncogene *25*, 4647–4662.

Brown, K.K., Spinelli, J.B., Asara, J.M., and Toker, A. (2017). Adaptive reprogramming of de novo pyrimidine synthesis is a metabolic vulnerability in triple-negative breast cancer. Cancer Discov. *7*, 391–399.

Bustin, S.A., Benes, V., Garson, J.A., Hellemans, J., Huggett, J., Kubista, M., Mueller, R., Nolan, T., Pfaffl, M.W., Shipley, G.L., et al. (2009). The MIQE guidelines: minimum information for publication of quantitative real-time PCR experiments. Clin. Chem. *55*, 611–622.

Calvo, S.E., Klauser, C.R., and Mootha, V.K. (2015). MitoCarta 2.0: an updated inventory of mammalian mitochondrial proteins. Nucleic Acids Res. *44*, D1251–D1257.

Cardaci, S., Zheng, L., MacKay, G., van den Broek, N.J., MacKenzie, E.D., Nixon, C., Stevenson, D., Tumanov, S., Bulusu, V., Kamphorst, J.J., et al. (2015). Pyruvate carboxylation enables growth of SDH-deficient cells by supporting aspartate biosynthesis. Nat. Cell Biol. *17*, 1317–1326.

Chatre, L., and Ricchetti, M. (2013). Prevalent coordination of mitochondrial DNA transcription and initiation of replication with the cell cycle. Nucl. Acids Res. *41*, 3068–3078.

Cogliati, S., Frezza, C., Soriano, M.E., Varanita, T., Quintana-Cabrera, R., Corrado, M., Cipolat, S., Costa, V., Casarin, A., Gomes, L.C., et al. (2013). Mitochondrial cristae shape determines respiratory chain supercomplexes assembly and respiratory efficiency. Cell *155*, 160–171.

Daum, B., Walter, A., Horst, A., Osiewacz, H.D., and Kühlbrandt, W. (2013). Age-dependent dissociation of ATP synthase dimers and loss of inner-membrane cristae in mitochondria. Proc. Natl. Acad. Sci. U S A *110*, 15301–15306.

Deus, C.M., Serafim, T.L., Magalhães-Novais, S., Vilaça, A., Moreira, A.C., Sardão, V.A., Cardoso, S.M., and Oliveira, P.J. (2017). Sirtuin 1-dependent resveratrol cytotoxicity and pro-differentiation activity on breast cancer cells. Arch. Toxicol. *91*, 1261–1278.

Dong, L.F., Kovarova, J., Bajzikova, M., Bezawork-Geleta, A., Svec, D., Endaya, B., Sachaphibulkij, K., Coelho, A.R., Sebkova, N., Ruzickova, A., et al. (2017). Horizontal transfer of whole mitochondria restores tumorigenic potential in mitochondrial DNA-deficient cancer cells. Elife *6*, e22187.

Frei, B., Kim, M.C., and Ames, B.N. (1990). Ubiquinol-10 is an effective lipid-soluble antioxidant at physiological concentrations. Proc. Natl. Acad. Sci. U S A *87*, 4879–4883.

Garcia-Bermudez, J., Baudrier, L., La, K., Zhu, X.G., Fidelin, J., Sviderskiy, V.O., Papagiannakopoulos, T., Molina, H., Snuderl, M., Lewis, C.A., et al. (2018). Aspartate is a limiting metabolite for cancer cell proliferation under hypoxia and in tumours. Nat. Cell Biol. *20*, 775–781.

Goveia, J., Pircher, A., Conradi, L.C., Kalucka, J., Lagani, V., Dewerchin, M., Eelen, G., DeBerardinis, R.J., Wilson, I.D., and Carmeliet, P. (2016). Meta-analysis of clinical metabolic profiling studies in cancer: challenges and opportunities. EMBO Mol. Med. *8*, 1134–1142.

Greene, S., Watanabe, K., Braatz-Trulson, J., and Lou, L. (1995). Inhibition of dihydroorotate dehydrogenase by the immunosuppressive agent leflunomide. Biochem. Pharmacol. *50*, 861–867.

Gregoire, M., Morais, R., Quilliam, M.A., and Gravel, D. (1984). On auxotrophy for pyrimidines of respiration-deficient chick embryo cells. Eur. J. Biochem. *142*, 49–55.

Gu, J., Wu, M., Guo, R., Yan, K., Lei, J., Gao, N., and Yang, M. (2016). The architecture of the mammalian respirasome. Nature *537*, 639–643.

Guarás, A., Perales-Clemente, E., Calvo, E., Acín-Pérez, R., Loureiro-Lopez, M., Pujol, C., Martínez-Carrascoso, I., Nuñez, E., García-Marqués, F., Rodríguez-Hernández, M.A., et al. (2016). The CoQH2/CoQ ratio serves as a sensor of respiratory chain efficiency. Cell Rep. *15*, 197–209.

Guzy, R.D., Sharma, B., Bell, E., Chandel, N.S., and Schumacker, P.T. (2008). Loss of the SdhB, but not the SdhA, subunit of complex II triggers reactive oxygen species-dependent hypoxia-inducible factor activation and tumorigenesis. Mol. Cell. Biol. *28*, 718–731.

Hakkaart, G.A., Dassa, E.P., Jacobs, H.T., and Rustin, P. (2006). Allotopic expression of a mitochondrial alternative oxidase confers cyanide resistance to human cell respiration. EMBO Rep. *7*, 341–345.

He, T., Haapa-Paananen, S., Kaminskyy, V.O., Kohonen, P., Fey, V., Zhivotovsky, B., Kallioniemi, O., and Perälä, M. (2014). Inhibition of the mitochondrial pyrimidine biosynthesis enzyme dihydroorotate dehydrogenase by doxorubicin and brequinar sensitizes cancer cells to TRAIL-induced apoptosis. Oncogene *33*, 3538–3549.

Hensley, C.T., Faubert, B., Yuan, Q., Lev-Cohain, N., Jin, E., Kim, J., Jiang, L., Ko, B., Skelton, R., Loudat, L., et al. (2016). Metabolic heterogeneity in human lung tumors. Cell *164*, 681–694.

Hosseini, M., Dousset, L., Mahfouf, W., Serrano-Sanchez, M., Redonnet-Vernhet, I., Mesli, S., Kasraian, Z., Obre, E., Bonneu, M., Claverol, S., et al. (2018). Energy metabolism rewiring precedes UVB-induced primary skin tumor formation. Cell Rep. *23*, 3621–3634.

Karnkowska, A., Vacek, V., Zubáčová, Z., Treitli, S.C., Petrželková, R., Eme, L., Novák, L., Žárský, V., Barlow, L.D., Herman, E.K., et al. (2016). A eukaryote without a mitochondrial organelle. Curr. Biol. *26*, 1274–1284.

Kim, J., Hu, Z., Cai, L., Li, K., Choi, E., Faubert, B., Bezwada, D., Rodriguez-Canales, J., Villalobos, P., Lin, Y.F., et al. (2017). CPS1 maintains pyrimidine pools and DNA synthesis in KRAS/LKB1-mutant cancer cells. Nature *546*, 168–172.

King, K.S., Prodanov, T., Kantorovich, V., Fojo, T., Hewitt, J.K., Zacharin, M., Wesley, R., Lodish, M., Raygada, M., Gimenez-Roqueplo, A.P., et al. (2011). Metastatic pheochromocytoma/paraganglioma related to primary tumor development in childhood or adolescence: significant link to SDHB mutations. J. Clin. Oncol. *29*, 4137–4142.

King, M.P., and Attardi, G. (1988). Injection of mitochondria into human cells leads to a rapid replacement of the endogenous mitochondrial DNA. Cell *52*, 811–819.

King, M.P., and Attardi, G. (1989). Human cells lacking mtDNA: repopulation with exogenous mitochondria by complementation. Science *246*, 500–503.

Koppenol, W.H., Bounds, P.L., and Dang, C.V. (2011). Otto Warburg's contributions to current concepts of cancer metabolism. Nat. Rev. Cancer *11*, 325–337.

Koundinya, M., Sudhalter, J., Courjaud, A., Lionne, B., Touyer, G., Bonnet, L., Menguy, I., Schreiber, I., Perrault, C., Vougier, S., et al. (2018). Dependence on the pyrimidine biosynthetic enzyme DHODH is a synthetic lethal vulnerability in mutant KRAS-driven cancers. Cell Chem. Biol. *225*, 705–717.

Kukat, C., Davies, K.M., Wurm, C.A., Spåhr, H., Bonekamp, N.A., Kühl, I., Joos, F., Polosa, P.L., Park, C.B., Posse, V., et al. (2015). Cross-strand binding of TFAM to a single mtDNA molecule forms the mitochondrial nucleoid. Proc. Natl. Acad. Sci. U S A *112*, 11288–11293.

Landon, J., Fawcett, J.K., and Wynn, V. (1962). Blood pyruvate concentration measured by a specific method in control subjects. J. Clin. Pathol. *15*, 579–584.

Le, S.B., Hailer, M.K., Buhrow, S., Wang, Q., Flatten, K., Pediaditakis, P., Bible, K.C., Lewis, L.D., Sausville, E.A., Pang, Y.P., et al. (2007). Inhibition of mitochondrial respiration as a source of adaphostin-induced reactive oxygen species and cytotoxicity. J. Biol. Chem. *282*, 8860–8872.

LeBleu, V.S., O'Connell, J.T., Gonzalez Herrera, K.N., Wikman, H., Pantel, K., Haigis, M.C., de Carvalho, F.M., Damascena, A., Domingos Chinen, L.T., Rocha, R.M., et al. (2014). PGC-1α mediates mitochondrial biogenesis and oxidative phosphorylation in cancer cells to promote metastasis. Nat. Cell Biol. *16*, 992–1003.

Lei, L., and Spradling, A.C. (2016). Mouse oocytes differentiate through organelle enrichment from sister cyst germ cells. Science *352*, 95–99.

Letts, J.A., Fiedorczuk, K., and Sazanov, L.A. (2016). The architecture of respiratory supercomplexes. Nature *537*, 644–648.

Loffler, M. (1980). On the role of dihydroorotate dehydrogenase in growth cessation of Ehrlich ascites tumor cells cultured under oxygen deficiency. Eur. J. Biochem. *107*, 207–215.

Loffler, M., Fairbanks, L.D., Zameitat, E., Marinaki, A.M., and Simmonds, H.A. (2005). Pyrimidine pathways in health and disease. Trends Mol. Med. *11*, 430–437.

Lussey-Lepoutre, C., Hollinshead, K.E., Ludwig, C., Menara, M., Morin, A., Castro-Vega, L.J., Parker, S.J., Janin, M., Martinelli, C., Ottolenghi, C., et al. (2015). Loss of succinate dehydrogenase activity results in dependency on pyruvate carboxylation for cellular anabolism. Nat. Commun. *6*, 8784.

Marin-Valencia, I., Yang, C., Mashimo, T., Cho, S., Baek, H., Yang, X.L., Rajagopalan, K.N., Maddie, M., Vemireddy, V., Zhao, Z., et al. (2012). Analysis of tumor metabolism reveals mitochondrial glucose oxidation in

genetically diverse human glioblastomas in the mouse brain in vivo. Cell Metab. *15*, 827–837.

Mashimo, T., Pichumani, K., Vemireddy, V., Hatanpaa, K.J., Singh, D.K., Sirasanagandla, S., Nannepaga, S., Piccirillo, S.G., Kovacs, Z., Foong, C., et al. (2014). Acetate is a bioenergetic substrate for human glioblastoma and brain metastases. Cell *159*, 1603–1614.

Martinez-Outschoorn, U.E., Peiris-Pagés, M., Pestell, R.G., Sotgia, F., and Lisanti, M.P. (2017). Cancer metabolism: a therapeutic perspective. Nat. Rev. Clin. Oncol. *14*, 11–31.

Martínez-Reyes, I., Diebold, L.P., Kong, H., Schieber, M., Huang, H., Hensley, C.T., Mehta, M.M., Wang, T., Santos, J.H., Woychik, R., et al. (2016). TCA cycle and mitochondrial membrane potential are necessary for diverse biological functions. Mol. Cell *61*, 199–209.

Mathur, D., Stratikopoulos, E., Ozturk, S., Steinbach, N., Pegno, S., Schoenfeld, S., Yong, R., Murty, V.V., Asara, J.M., Cantley, L.C., and Parsons, R. (2017). PTEN regulates glutamine flux to pyrimidine synthesis and sensitivity to dihydroorotate dehydrogenase inhibition. Cancer Discov. *7*, 380–390.

Molina, J.R., Sun, Y., Protopopova, M., Gera, S., Bandi, M., Bristow, C., McAfoos, T., Morlacchi, P., Ackroyd, T., Agip, A.A., et al. (2018). An inhibitor of oxidative phosphorylation exploits cancer vulnerability. Nat. Med. *24*, 1036–1046.

Mohamad Fairus, A.K., Choudhary, B., Hosahalli, S., Kavitha, N., and Shatrah, O. (2017). Dihydroorotate dehydrogenase (DHODH) inhibitors affect ATP depletion, endogenous ROS and mediate S-phase arrest in breast cancer cells. Biochimie *135*, 154–163.

Moreno-Lastres, D., Fontanesi, F., García-Consuegra, I., Martín, M.A., Arenas, J., Barrientos, A., and Ugalde, C. (2012). Mitochondrial complex I plays an essential role in human respirasome assembly. Cell Metab. *15*, 324–335.

Moschoi, R., Imbert, V., Nebout, M., Chiche, J., Mary, D., Prebet, T., Saland, E., Castellano, R., Pouyet, L., Collette, Y., et al. (2016). Protective mitochondrial transfer from bone marrow stromal cells to acute myeloid leukaemia cells during chemotherapy. Blood *128*, 253–264.

Murphy, M.P. (2009). How mitochondria produce reactive oxygen species. Biochem. J. *417*, 1–13.

Olsen, N.J., and Stein, C.M. (2004). New drugs for rheumatoid arthritis. N. Engl. J. Med. *350*, 2167–2179.

Osswald, M., Jung, E., Sahm, F., Solecki, G., Venkataramani, V., Blaes, J., Weil, S., Horstmann, H., Wiestler, B., Syed, M., et al. (2015). Brain tumour cells interconnect to a functional and resistant network. Nature *528*, 93–98.

Park, J.S., Sharma, L.K., Li, H., Xiang, R., Holstein, D., Wu, J., Lechleiter, J., Naylor, S.L., Deng, J.J., Lu, J., and Bai, Y. (2009). A heteroplasmic, not homoplasmic mitochondrial DNA mutation promotes tumorigenesis via alteration in reactive oxygen species generation and apoptosis. Hum. Mol. Genet. *18*, 1578–1589.

Perales-Clemente, E., Bayona-Bafaluy, M.P., Pérez-Martos, A., Barrientos, A., Fernández-Silva, P., and Enriquez, J.A. (2008). Restoration of electron transport without proton pumping in mammalian mitochondria. Proc. Natl. Acad. Sci. U S A *105*, 18735–18739.

Peters, G.J., van Dijk, J., Laurensse, E., van Groeningen, C.J., Lankelma, J., Leyva, A., Nadal, J.C., and Pinedo, H.M. (1988). *In vitro* biochemical and *in vivo* biological studies of the uridine 'rescue' of 5.fluorouracil. Br. J. Cancer *57*, 259–265.

Picard, M., Zhang, J., Hancock, S., Derbeneva, O., Golhar, R., Golik, P., O'Hearn, S., Levy, S., Potluri, P., Lvova, M., et al. (2014). Progressive increase in mtDNA 3243A>G heteroplasmy causes abrupt transcriptional reprogramming. Proc. Natl. Acad. Sci. U S A *111*, E4033.

Podda, M., Weber, C., Traber, M.G., Milbradt, R., and Packer, L. (1999). Sensitive high-performance liquid chromatography techniques for simultaneous determination of tocopherols, tocotrienols, ubiquinols, and ubiquinones in biological samples. Methods Enzymol. *299*, 330–341.

Quinlan, C.L., Orr, A.L., Perevoshchikova, I.V., Treberg, J.R., Ackrell, B.A., and Brand, M.D. (2012). Mitochondrial complex II can generate reactive oxygen species at high rates in both the forward and reverse reactions. J. Biol. Chem. *287*, 27255–27264.

Rohlena, J., Dong, L.F., Ralph, S.J., and Neuzil, J. (2011). Anticancer drugs targeting the mitochondrial electron transport chain. Antioxid. Redox Signal. *15*, 2951–2974.

Rohlenova, K., Sachaphibulkij, K., Stursa, J., Bezawork-Geleta, A., Blecha, J., Endaya, B., Werner, L., Cerny, J., Zobalova, R., Goodwin, J., et al. (2017). Selective disruption of respiratory supercomplexes as a new strategy to suppress Her2^{high} breast cancer. Antiox. Redox Signal. *26*, 84–103.

Schmitt, S., Saathoff, F., Meissner, L., Schropp, E.M., Lichtmannegger, J., Schulz, S., Eberhagen, C., Borchard, S., Aichler, M., Adamski, J., Plesnila, N., et al. (2013). A semi-automated method for isolating functionally intact mitochondria from cultured cells and tissue biopsies. Anal. Biochem. *443*, 66–74.

Shukla, S.K., Purohit, V., Mehla, K., Gunda, V., Chaika, N.V., Vernucci, E., King, R.J., Abrego, J., Goode, G.D., Dasgupta, A., et al. (2017). MUC1 and HIF-1a signaling crosstalk induces anabolic glucose metabolism to impart gemcitabine resistance to pancreatic cancer. Cancer Cell *32*, 71–87.

Sigoillot, F.D., Berkowski, J.A., Sigoillot, S.M., Kotsis, D.H., and Guy, H.I. (2003). Cell cycle-dependent regulation of pyrimidine biosynthesis. J. Biol. Chem. *278*, 3403–3409.

Shalem, O., Sanjana, N.E., Hartenian, E., Shi, X., Scott, D.A., Mikkelsen, T.S., Heckl, D., Ebert, B.L., Root, D.E., Doench, J.G., and Zhang, F. (2014). Genome-scale CRISPR-Cas9 knockout screening in human cells. Science *343*, 84–87.

Strakova, A., Ní Leathlobhair, M., Wang, G.D., Yin, T.T., Airikkala-Otter, I., Allen, J.L., Allum, K.M., Bansse-Issa, L., Bisson, J.L., Castillo Domracheva, A., et al. (2016). Mitochondrial genetic diversity, selection and recombination in a canine transmissible cancer. Elife *5*, e14552.

Sullivan, L.B., Gui, D.Y., Hosios, A.M., Bush, L.N., Freinkman, E., and Vander Heiden, M.G. (2015). Supporting aspartate biosynthesis is an essential function of respiration in proliferating cells. Cell *162*, 552–563.

Sullivan, L.B., Gui, D.Y., and Vander Heiden, M.G. (2016). Altered metabolite levels in cancer: implications for tumour biology and cancer therapy. Nat. Rev. Cancer *16*, 680–693.

Sullivan, L.B., Luengo, A., Danai, L.V., Bush, L.N., Diehl, F.F., Hosios, A.M., Lau, A.N., Elmiligy, S., Malstrom, S., Lewis, C.A., et al. (2018). Aspartate is an endogenous metabolic limitation for tumour growth. Nat. Cell Biol. *20*, 782–788.

Sykes, D.B., Kfoury, Y.S., Mercier, F.E., Wawer, M.J., Law, J.M., Haynes, M.K., Lewis, T.A., Schajnovitz, A., Jain, E., Lee, D., et al. (2016). Inhibition of dihydroorotate dehydrogenase overcomes differentiation blockade in acute myeloid leukemia. Cell *167*, 171–186.

Tan, A.S., Baty, J.W., Dong, L.F., Bezawork-Geleta, A., Endaya, B., Goodwin, J., Bajzikova, M., Kovarova, J., Peterka, M., Yan, B., et al. (2015). Mitochondrial genome acquisition restores respiratory function and tumorigenic potential in cancer cells without mitochondrial DNA. Cell Metab. *21*, 81–94.

Titov, D.V., Cracan, V., Goodman, R.P., Peng, J., Grabarek, Z., and Mootha, V.K. (2016). Complementation of mitochondrial electron transport chain by manipulation of the NAD$^+$/NADH ratio. Science *352*, 231–235.

Vander Heiden, M.G., and DeBerardinis, R.J. (2017). Understanding the intersections between metabolism and cancer biology. Cell *168*, 657–669.

Vander Heiden, M.G., Cantley, L.C., and Thompson, C.B. (2009). Understanding the Warburg effect: the metabolic requirements of cell proliferation. Science *324*, 1029–1033.

Viale, A., Pettazzoni, P., Lyssiotis, C.A., Ying, H., Sánchez, N., Marchesini, M., Carugo, A., Green, T., Seth, S., Giuliani, V., et al. (2014). Oncogene ablation-resistant pancreatic cancer cells depend on mitochondrial function. Nature *514*, 628–632.

Wallace, D.C. (2012). Mitochondria and cancer. Nat. Rev. Cancer *12*, 685–698.

Weinberg, F., Hamanaka, R., Wheaton, W.W., Weinberg, S., Joseph, J., Lopez, M., Kalyanaraman, B., Mutlu, G.M., Budinger, G.R., and Chandel,

N.S. (2010). Mitochondrial metabolism and ROS generation are essential for Kras-mediated tumorigenicity. Proc. Natl. Acad. Sci. U S A *107*, 8788–8793.

Wheaton, W.W., Weinberg, S.E., Hamanaka, R.B., Soberanes, S., Sullivan, L.B., Anso, E., Glasauer, A., Dufour, E., Mutlu, G.M., Budigner, G.S., and Chandel, N.S. (2014). Metformin inhibits mitochondrial complex I of cancer cells to reduce tumorigenesis. Elife *3*, e02242.

Wittig, I., Braun, H.P., and Schägger, H. (2006). Blue native PAGE. Nat. Protoc. *1*, 418–428.

Wu, M., Gu, J., Guo, R., Huang, Y., and Yang, M. (2016). Structure of mammalian respiratory supercomplex $I_1III_2IV_1$. Cell *167*, 1598–1609.

Yin, S., Kabashima, T., Zhu, Q., Shibata, T., and Kai, M. (2017). Fluorescence assay of dihydroorotate dehydrogenase that may become a cancer biomarker. Sci. Rep. *7*, 40670.

Zhang, X., Fryknäs, M., Hernlund, E., Fayad, W., De Milito, A., Olofsson, M.H., Gogvadze, V., Dang, L., Påhlman, S., Schughart, L.A., et al. (2014). Induction of mitochondrial dysfunction as a strategy for targeting tumour cells in metabolically compromised microenvironments. Nat. Commun. *5*, 3295.

STAR★METHODS

KEY RESOURCES TABLE

REAGENT or RESOURCE	SOURCE	IDENTIFIER
Antibodies		
anti-BrdU-FITC IgG	BD Biosciences	340649; RRID: AB_400443
anti-TFAM IgG	Sigma-Aldrich	HPA040648; RRID: AB_10795635
anti-SSB IgG	Sigma-Aldrich	HPA002866; RRID: AB_1080092
anti-ATP5B IgG	Sigma-Aldrich	HPA001520; RRID: AB_1078243
anti-POLG IgG	Thermo Fisher Scientific	PA5-35163; RRID: AB_2552473
anti-cyclin E IgG	Thermo Fisher Scientific	MA5-14336; RRID: AB_10984356
anti-mtCO4 IgG	Thermo Fisher Scientific	PA5-29992; RRID: AB_2547466
anti-UMPS IgG	Santa Cruz Biotechnology	sc-398086; RRID: AB_2750932
anti-DHODH IgG	Santa Cruz Biotechnology	sc-166348; RRID: AB_2091729
anti-TOM20 IgG	Santa Cruz Biotechnology	sc-136211; RRID: AB_2207538
anti-CAD IgG	Cell Signaling	93925; RRID: AB_2750933
anti-p(S1859)-CAD IgG	Cell Signaling	12662; RRID: AB_2750934
anti-HSP60 IgG	Cell Signaling	12165S; RRID: AB_2636980
anti-Ki67 IgG	Cell Signaling	9129; RRID: AB_2687446
anti-NDUFS3 IgG	Abcam	ab110246; RRID: AB_10861972
anti-NDUFA9 IgG	Abcam	ab14713; RRID: AB_301431
anti-NDUFB8 IgG	Abcam	ab110242; RRID: AB_10859122
anti-mtCO1 IgG	Abcam	ab14705; RRID: AB_2084810
anti-COXVa IgG	Abcam	ab110262; RRID: AB_10861723
anti-SDHA IgG	Abcam	ab14715; RRID: AB_301433
anti-SDHB IgG	Abcam	ab14714; RRID: AB_301432
anti-Core2 IgG	Abcam	ab14745; RRID: AB_2213640
anti-ATP5A IgG	Abcam	ab14748; RRID: AB_301447
anti-VDAC IgG	Abcam	ab15895; RRID: AB_2214787
anti-TFAM IgG	Abcam	ab47517; RRID: AB_945799
anti-DHODH IgG	Proteintech	14877-1-AP; RRID: AB_2091723
anti-DNA IgG	PROGEN	61014; RRID: AB_2750935
Critical Commercial Assays/Kits		
NADH/NAD Glo Assay	Promega	G9071
ATP CellTiter Glo Assay	Promega	G9241
Seahorse XF Cell Mito Stress Test Kit	Agilent	103015-100
Seahorse XF Glycolysis Stress TestKit	Agilent	103020-100
Colorimetric pyruvate assay	Abcam	ab65342
Pierce BCA Protein Assay Kit	Thermo Fisher Scientific	#23225
Atto488 NT Labeling Kit	Jena Bioscience	PP-305S-488
Atto550 NT Labeling Kit	Jena Bioscience	PP-305S-550
Chemicals, Peptides and Recombinant Proteins		
ATP	Sigma-Aldrich	A1852
2-nitrobenzodeoxyglucose	Thermo Fisher Scientific	N13195
Dihydroorotic acid	Sigma-Aldrich	D7128
Orotic acid	TCI	50887-69-9
6-thioguanine	Sigma-Aldrich	A4882
Metformin	Metformin	04635
Leflunomide	Sigma-Aldrich	L5025

(*Continued on next page*)

Continued

REAGENT or RESOURCE	SOURCE	IDENTIFIER
Salicylhydroxamic acid	Sigma-Aldrich	S607
$^{13}C_5$,$^{15}N_2$-glutamine	Sigma-Aldrich	607983
$^{13}C_5$,$^{15}N_2$-glutamine	Cambridge Isotope Laboratories	CNLM-1275-H-0.1
Coenzyme Q_9	Santa Cruz Biotechnology	sc-207451
Coenzyme Q_{10}	Fluka	27595
Tetramethylrhodamine ethyl ester	Sigma-Aldrich	87917
Carbonyl cyanide-4-(trifluoromethoxy) phenylhydrozone	Sigma-Aldrich	C2920
Carbonyl cyanide-3-chlorophenylhydrozone	Sigma-Aldrich	C2759
Oligomycin	Sigma-Aldrich	O4876
Antimycin A	Sigma-Aldrich	A8474
2-deoxyglucose	Sigma-Aldrich	D8375
4-(trifluoromethoxy) benzamidoxime	Sigma-Aldrich	422231
ADP	Sigma-Aldrich	A5285
Cytochrome c	Sigma-Aldrich	C7752
Rotenone	Sigma-Aldrich	R8875
Digitonin	Fluka	37008
K-lactobionate	Sigma-Aldrich	153516
Nocodazol	Sigma-Aldrich	M1404
Fluoroshield with DAPI	Sigma-Aldrich	F6057
MitoSOX	Thermo Fisher Scientific	M36008
Decylubiquinone	Sigma-Aldrich	D7911
Deposited Data		
Microarray Analysis Data	EBI ArrayExpress Database	ArrayExpress: MTAB-6150
Experimental Models: Cell Lines		
4T1	ATCC	CRL-2539
B16	ATCC	CRL-6323
MCF-7	ATCC	HTB-22
MDA-MB-231	ATCC	HTB-26
HeLa	ATCC	CCL-2
143B	ATCC	CRL-8303
P815	ATCC	TIB-64
PaTu8902	DSMZ	ACC-179
PANC-1	ATCC	CRL-1469
Experimental Models: Organisms/Strains		
C57BL/6 mice	Jackson Laboratories	C57BL/6
Balb-c mice	Jackson Laboratories	Balb-c
C57BL/6$^{su9\text{-}DsRed2}$ mice	Our laboratory	Dong et al., 2017
Oligonucleotides		
Forward mouse DHODH cloning primer	Sigma-Aldrich	AAA GAA TTC CAC CAT GGC GTG GAG ACA GCT G
Reverse mouse DHODH cloning primer	Sigma-Aldrich	ATA AAG GAT CCT CAC CTG CGG TGA TCT ACT C
Forward guide mouse DHODH	Sigma-Aldrich	CAC CGT CAG GTA CTC GGC GTA GAA A
Reverse guide mouse DHODH	Sigma-Aldrich	AAA CTT TCT ACG CCG AGT ACC TGA C
Forward guide mouse ATP5B	Sigma-Aldrich	CAC CGC ACT GCC ACC GGG CGA ATC G
Reverse guide mouse ATP5B	Sigma-Aldrich	AAA CCG ATT CGC CCG GTG GCA GTG C
Primer for 4T1_12S forward primer	This paper	*ctt ggt gat agc tgg tta*
Primer for 4T1_12S forward primer	This paper	*ggc cta caa tgg tta aaa g*
Probe for 4T1_12S_mut_HEX	This paper	*aat aGt gAa CaA ttA aCa Aaa ca*

(*Continued on next page*)

Continued

REAGENT or RESOURCE	SOURCE	IDENTIFIER
Probe for 4T1_12S_mut_HEX	This paper	*aat aGt gAa TaA ttA aCa Aaa ca*
Primer for POLG binding site, forward	This paper	TGA TCA ATT CTA GTA GTT CCC AAA A
Primer for POLG binding site, reverse	This paper	ACC TCT AAT TAA TTA TAA GGC CAG G
Primers for q(RT-)PCR	This paper	Table S2
Forward mREP	Eurogentec	ATA TGA CTA TCC CCT TCC CC
Reverse mREP	Eurogentec	AGT TTA ATG GGC CCG GAG CG
Forward mTRANS (MT1, MT6, MT11 mix)_ MT1	Eurogentec	GTT AAT GTA GCT TAA TAA
Reverse mTRANS (MT1, MT6, MT11 mix)_MT1	Eurogentec	TTC CAA GCA CAC TTT CCA
Forward mTRANS (MT1, MT6, MT11 mix_MT6	Eurogentec	CCC ATT CCA ACT TGG TCT
Reverse mTRANS (MT1, MT6, MT11 mix_MT6	Eurogentec	AAT GAT GGC TAC AAC GAT
Forward mTRANS (MT1, MT6, MT11 mix)_MT11	Eurogentec	GTC ATC TCA TAT AAT ATT
Reverse mTRANS(MT1, MT6, MT11 mix)_MT11	Eurogentec	TCG ACA AAT GTG TGT TAC
Recombinant DNA		
Salmon sperm DNA	Sigma-Aldrich	438545-06-3
pXPR_001	Addgene	49535
pCDH-CMV-MCS-EF1-Puro	SBI System Biosciences	CD510B-1
pWPI-AOX-IRES-GFP	Gift from N. Chandel	Martínez-Reyes et al., 2016
Software and Algorithms		
Image J	Fiji	http://Fiji.sc/
Photoshop	Adobe	http://www.adobe.com/uk/products/photoshop.html
Prism	GraphPad	http://graphpad.com/scientific-software/prism/
SeqManPro	DNASTAR Lasergene 11	https://www.dnastar.com/software/
CFX Manager 3.1	BioRad	http://www.bio-rad.com/en-cz/product/cfx-manager-software?ID=aed9803d-cb4d-4ecb-9263-3efc9e650edb
Genes (MultiD)	MIQE guidelines	Bustin et al., 2009
Huygens Professional version software 17.04	Scientific Volume Imaging	https://svi.nl/HuygensSoftware
Classic Maximum Likelihood Estimation algorithm		https://svi.nl/ClassicMaximumLikelihoodEstimation
R	Open source	https://www.r-project.org/
Tidyverse R packages	Rstudio	https://www/tidyverse.org/
Analyst 1.6 Software	SCIEX	https://sciex.com/products/software/analyst-software
MassHunter Software	Agilent	https://www.agilent.com/en/products/software-informatics/masshunter-suite/masshunter/masshunter-software
IMARIS 8.0	BitPlane	http://www.bitplane.com/releasenotes/imaris800.aspx
Other		
DMEM	Lonza	BE12-708F
RPMI medium	Lonza	12-115Q
Fetal calf serum	Sigma-Aldrich	F7524
Penicillin/streptomycin	Sigma-Aldrich	P3032/S9137
Uridine	Sigma	U3750
Pyruvate	Sigma	P5280
Protease Inhibitor Cocktail	Roche	39102.01
Phsophatase Inhibitor Cocktail	Sigma-Aldrich	P5726-5ML
RNAzol reagent	MRC	RB190/100

(*Continued on next page*)

Continued

REAGENT or RESOURCE	SOURCE	IDENTIFIER
HOT FIREPol Blend Master Mix	Solis BioDyne	08-36-00020
DNA clean-and-concentration kit	Zymo Research	D5205
AquaPure Genomic DNA Isolation Kit	BioRad	732-6340
2xRT^{2}SYBR Green qPCR Mastermix	Qiagen	330500
RNAeasy Mini Kit	Qiagen	74104
Revertaid First-Strand Synthesis System	Fermentas	K1621
EvaGreen	Solis BioDyne	08-24-00001
Grandmaster for probes	TATAA Biocenter	TA02-625
RNAse A	Sigma-Aldrich	R6513
Proteinase K	Sigma-Aldrich	P4032
Proteinase K	Eurobio	GEXPRK01-B05
PCR clean-up columns	Machery Nagel	740609
Affymetrix MouseGene 2.0 ST Array	Thermo Fisher	902119
Triton X-100	Sigma-Aldrich	X100
TWEEN-20	Sigma-Aldrich	P1379
Abberior Mount Liquid Antifade	Abberior Instruments	4-0100-004-3
Lipofectamine 3000	ThermoFisher	L3000008
FastDigest Esp3I	ThermoFisher	FD0454
FastDigest EcoRI	ThermoFisher	FD0274
FastDigest BamHI	ThermoFisher	FD0055
Puromycin	Invivogen	ant-pr-1
Q5 High-Fidelity DNA Polymerase	New England Biolabs	M0491S
XBridge Amide Column	Waters	Part#186004868
SeQuant ZIC-pHILIC Column	Merck	Cat#1504600001

CONTACT FOR REAGENT AND RESOURCE SHARING

Further information and requests for reagents may be directed and will be fulfilled by the Lead Contact, Jiri Neuzil (j.neuzil@griffith.edu.au).

EXPERIMENTAL MODEL AND SUBJECT DETAILS

We have used female Balb/c mice, and male and female C57BL mice. Human cell lines were authenticated.

METHOD DETAILS

Cell Culture

4T1 mouse metastatic breast cancer cells were purchased from the ATCC and maintained in the RPMI medium with 10% FCS and antibiotics. B16 mouse metastatic melanoma cells were purchased from the ATCC cells and maintained in DMEM with 10% FCS and antibiotics. Unless stated otherwise, the cells were cultivated in the presence of 1 mM pyruvate and 50 μg/mL uridine. 4T1ρ^0 and B16ρ^0 cells were prepared as described (Tan et al., 2015). D5, D10, D15, D20, D25, D30, D40, D50 and D60 sublines were prepared following injection of D0 (ρ^0) cells subcutaneously (s.c.) into Balb/c mice at 10^6 per animal into groups of 5-6 mice. On days 5, 10, 15, 20, 25, 30, 40, 50 and 60, mice were sacrificed, the pre-tumor lesions or tumors excised, and cells isolated from the tissue in the presence of 6TG as described (Tan et al., 2015). The isolated cells were used to establish sublines for further study. D5–D20 AOX cells were prepared identically, following grafting of 4T1ρ^0 AOX (D0 AOX) cells into Balb/c mice. The same procedure was applied to obtain cells derived from ATP5B^{KO} tumors. These cells were maintained in tissue culture media supplemented with uridine (50 μg/mL) and pyruvate (1 mM). Cells were moved into the same media without uridine/pyruvate, as indicated. B16 DP cells were derived from tumours grown in transgenic C57BL$^{su9\text{-}DsRed2}$ mice injected with B16ρ^0 cells with blue fluorescent protein nucleus as reported (Dong et al., 2017). The human breast cancer MCF7 and MDA-MB-231 cells, human cervical cancer HeLa cells, human osteosarcoma 143B cells, mouse mastocytoma P815 cells and human pancreatic cancer PANC-1 cells (all from the ATCC), as well as human pancreatic cancer PaTu8902 cells (DMSZ) were maintained in the same media as B16 cells without uridine and pyruvate.

Evaluation of Uridine and Pyruvate Auxotrophy

Cells were seeded in 6-well plates at a density of $2.5x10^5$ cells per well. Cells were then incubated in control RPMI medium or medium supplemented with 1 mM pyruvate (4T1 medium) or with 1 mM pyruvate and 50 μg/mL uridine (ρ^0 medium) for 24, 48 or 72 h at 37°C in 5% CO_2. At various time points, duplicates of cells were washed with PBS, harvested by trypsinization, and the number of cells counted using a Casy Cell Counter (Roche).

Preparation of Cells with Knocked Out or Reconstituted Genes

To prepare $DHODH^{KO}$ and $ATP5B^{KO}$ cells, we used CRISPR/Cas9 system (Shalem et al., 2014). Guide RNAs sequences from the GeCKO library (v2 09Mar2015) were synthesized and cloned into BsmBI-cleaved pXPR_001 vector containing the mammalian codon-optimized Cas9 nuclease expression cassette. Parental 4T1 or B16 cells were transiently transfected using Lipofectamine 3000 (Thermo Scientific), grown for 24 h and selected by puromycin for 48-72 h, or until all non-transfected control cells were eliminated. Surviving cells were sorted into 96 well plates, expanded, and clones unable to grow in media lacking uridine and pyruvate (for $DHODH^{KO}$ cells) or glucose ($ATP5B^{KO}$ cells) were selected. The absence of the targeted proteins was verified by WB. The guide RNA sequences used were as follows: DHODH, 5′-TCA GGT ACT CGG CGT AGA AA-3′; ATP5B, 5′-CAC TGC CAC CGG GCG AAT CG-3′.

To reconstitute DHODH protein expression, the DHODH coding sequence was PCR-amplified from cDNA obtained from mouse B16 cells. Primers used were 5′-ATA AAG AAT TCC ACC ATG GCG TGG AGA CAG CTG-3′ (forward) and 5′-ATA AAG GAT CCT CAC CTG CGG TGA TCT ACT C-3′ (reverse). Gel-purified PCR product was cleaved by fast-digest EcoRI and BamHI enzymes (Thermo Scientific) and ligated into the pCDH-CMV-MCS-EF1-Puro lentiviral vector (System Biosciences) digested in the same way. Lentiviral particles were produced as described (Blecha et al., 2017) and used to transduce 4T1 or B16 $DHODH^{KO}$ cells, followed by puromycin selection. DHODH expression was verified by WB. To express AOX in 4T1 ρ^0 cells, we used pWPI-AOX-IRES-GFP vector (a kind gift of N.S. Chandel; Martínez-Reyes et al., 2016). Lentiviral particles were produced as above and transduced cells were selected by sorting for GFP. To express AOX in B16 ρ^0 cells, we used lipofectamine transfection as described above, as lentiviral transduction was ineffective in these cells. Transfected cells were grown for 10 days, and selected by two rounds of sorting for GFP.

Mitochondrial Membrane Potential and Mitochondrial Superoxide Evaluation

To assess $\Delta\Psi_{m,i}$, cells were seeded at 80,000 per mL in 96-well plates and allowed to recover for 24 h. Tetramethylrhodamine ethyl ester (TMRE) at 50 nM was added to all wells and incubated for 30 min prior to analysis by flow cytometry (FACScalibur, Becton Diskinson). Prior to analysis, control cells were also pre-treated with 1 μM of carbonyl cyanide-4-(trifluoromethoxy) phenylhydrazone (FCCP) for 10 min.

Mitochondrial superoxide was assessed in cells seeded at 80,000 per well in a 96-well plate and incubated with 5 μM MitoSOX for 90 min at 37°C. Fluorescence was assessed at the excitation of 510 nm and emission of 580 nm in a Biotek Cytation 3 microplate reader (Biotek Instruments). Mitochondrial superoxide production was further stimulated by incubation with 1 μM antimycin A for 90 min, and MitoSOX fluorescence was measured under the same conditions.

Evaluation of ATP Level, Glucose Uptake and Lactate Formation

ATP was determined in cells seeded at 10^4 per well in 96-well plates in media containing either 4.5 g/L glucose and 50 mM or no 2DG using a luciferase-based assay (CellTiter-Glo Luminescent Assay, Promega). Results were normalised to the total protein level in cell lysates assessed by the bicinchoninic acid (BCA) method.

For glucose uptake, cells were pre-incubated in low-glucose (1 g/L) RPMI medium for 24 h at 37°C and 5% CO_2, followed by 15 min incubation in normal DMEM (4.5 g/L glucose) in the presence of 50 μM 2-nitrobenzodeoxyglucose (Life Technologies); glucose uptake was then analysed by flow cytometry.

For lactate evaluation, cells were seeded at 10^5 per well in 96-well plates. Aliquots of the medium were used for the analysis of lactate using a colorimetric kit (Trinity Biotech) following 24 h incubation. Results were normalised to the total protein level in cell lysates.

Evaluation of NADH/NAD^+ Ratio

Oxidized and reduced nicotinamide adenine dinucleotides (NAD^+ and NADH, respectively) were assessed in cells seeded at 1.5×10^4 per well in white-walled 96-well plates using the bioluminescent NADH/NAD^+ Glo Assay (Promega). Luminescence intensity was acquired with a Tecan Infinite M200 Microplate Reader.

Analysis of Coenzyme Q

Cells were grown in 60 mm culture dishes, washed with PBS and scraped. Pellets were collected in conical-bottom cryotubes filled with argon and stored in liquid nitrogen. During the procedure, all solutions used were bubbled with argon and all sample preparation steps were carried out under an atmosphere of argon. Vials containing the cells were centrifuged briefly (1 min) at 800 rpm and 4°C, before 100 μL the HES buffer containing protease inhibitors (10 mM Hepes pH 7.4, 250 mM sucrose, 1 mM EDTA, 100 μM DTPA and 1:50 protease inhibitors) were added. Cell lysate (90 μL) was then added to 2 mL methanol containing 0.02% acetic acid, followed by 10 mL Milli Q water-washed hexane, mixed vigorously for 30 sec and the mixture centrifuged for 5 min at 900 x *g* and 4°C. The resulting hexane layer was removed, evaporated under vacuum using a rotary evaporator, the vacuum released under argon, and the residue re-dissolved in 140 μL argon-flushed solvent mixture (73.375% ethanol, 22.5% methanol, 3.75% isopropyl alcohol,

0.375% MilliQ water and 5 mM $LiClO_4.3H_2O$). The re-dissolved lipids (100 μL) were subjected to isocratic HPLC performed using a C18 column (Supelcosil 250 x 4.6 mm, 5 μm; Supelco, Sigma-Aldrich) with guard column eluted with 65% ethanol, 30% methanol, 3% isopropyl alcohol and 2% ammonium acetate (1 M, pH 4.4) at 1 mL/min, with mobile phase being bubbled gently with a stream of argon gas. CoQ_9/CoQ_{10} and $CoQ_9H_2/CoQ_{10}H_2$ were determined by HPLC with coulometric multi-electrode electrochemical detection (CoulArray, Thermo Fisher Scientific), with the oxidation and reduction potentials set at +700 and -700 mV, respectively, and the gain range set at 100 nC. The concentrations of all analytes were determined from calibration curves generated using authentic standards of CoQ_9 and CoQ_{10} (Sigma-Aldrich). Standards of CoQ_9H_2 and $CoQ_{10}H_2$ were prepared from CoQ_9 and CoQ_{10}, respectively, by reduction with sodium borohydrate (Frei et al., 1990). Concentrations of CoQ_9, CoQ_{10}, CoQ_9H_2 and $CoQ_{10}H_2$ were determined by UV-VIS spectrophotometry (Agilent Technologies Cary 100 UV-VIS) using $\varepsilon_{275\,nm}$ for CoQ_9 and CoQ_{10} of 14,700 and 14,240 $M^{-1}cm^{-1}$, respectively, and $\varepsilon_{290\,nm}$ for CoQ_9H_2 and $CoQ_{10}H_2$ of 4,120 and 4,010 $M^{-1}cm^{-1}$, respectively (Podda et al., 1999).

Evaluation of Respiration and Glycolysis

As relevant, the high-resolution Oxygraph-2k respirometer (Oroboros) and the Seahorse XF96 Extracellular Flux Analyzer (Agilent Technologies) were used. Routine, CI- and CII-dependent respiration was assessed as published (Boukalova et al., 2016; Rohlenova et al., 2017). DHODH-dependent respiration was carried out as follows. In brief, cells were trypsinized, washed with PBS, re-suspended at $2x10^6$ cells per mL of the Mir05 medium (0.5 mM EGTA, 3 mM $MgCl_2$, 60 mM K-lactobionate, 20 mM taurine, 10 mM KH_2PO_4, 110 mM sucrose, 1 g/L essentially fatty acid-free bovine serum albumin, 20 mM Hepes, pH 7.1 at 30°C) and transferred to the chamber of the Oxygraph-2k instrument (Oroboros). Respiration measurements were performed at 37°C. Cells were permeabilized with 5 μg digitonin per 10^6 cells and a CI inhibitor (0.3 μM rotenone) was added prior to the addition of the substrate. DHODH-mediated respiration was assessed by subtracting the residual respiration rate remaining after addition of 30 μM leflunomide from the respiration rate in the presence of 1 mM dihydroorotate (DHO), 3 mM ADP, and 10 μM cytochrome c.

For evaluation of CI-, CII- and DHODH-dependent respiration in tumors, freshly excised tissue was weighed, homogenised in a PBI-Shredder (Oroboros), re-suspended in Mir05 medium and transferred to the chamber of the Oxygraph-2k instrument. The total oxygen consumption was monitored in the absence and presence of specific inhibitors and substrates of CI (rotenone or glutamate/malate/pyruvate, respectively), CII (malonate or succinate, respectively) and DHODH (leflunomide and DHO, respectively). Carbonyl cyanide 3-chlorophenylhydrazone (CCCP) was titrated to obtain maximal uncoupled respiration rate. Residual oxygen consumption after antimycin A addition was subtracted from all results to obtain mitochondria-specific rates.

The Seahorse XF96 Extracellular Flux Analyzer was used for assessment of both cellular oxygen consumption rate (OCR) and extracellular acidification rate (ECAR) as described (Deus et al., 2017). Cells were seeded in XF96 cell culture microplates at $8x10^4$ per well in standard culture media. After 24 h, the medium was replaced by serum-free RPMI containing 5 mM glucose, 1 mM pyruvate, and 50 μg/mL uridine of the Mitostress kit and without supplementation for the Glycostress kit, with pH adjusted to 7.4. Cells were incubated at 37°C for 30 min to allow the temperature and pH of the medium to reach equilibrium before measurement. The assay protocol for mitochondrial respiration consisted of consecutive injection steps in which 1 μM oligomycin, 1 μM FCCP, and the combination of 0.5 μM rotenone and 0.5 μM antimycin A were added. For glycolytic measurements, 10 mM glucose, 1 μM oligomycin, and 50 mM 2-deoxy-D-glucose (2DG) were consecutively added. OCR and ECAR measurements were made using the 3 min mix and 5 min measure cycle. Results were analyzed by the XF Stress Test Report Generators (Agilent Technologies). The results were normalized to cellular protein.

DHODH Activity Assay

DHODH activity measurements were performed using a modified protocol according to Yin et al. (2017). In brief, cells were collected, washed with PBS, re-suspended in potassium phosphate buffer (0.1 M, pH 7.0) and lysed using three freeze-thaw cycles; the lysates were incubated in the solution of 160 mM K_2CO_3-HCl (pH 8.0), 400 μM DHO, 80 μM decylubiquinone at 37°C for 60 min. The reference sample was kept on ice. The reaction mixture was supplemented with 20 mM K_2CO_3, 2 mM $K_3[Fe(CN)_6]$ and 1 mM 4-(trifluoromethoxy)benzamidoxime (4-TFMBAO), and heated at 80°C for 4 min. The reaction was stopped by cooling on ice and fluorescence intensity was measured using the Infinite M200 plate reader (Tecan); the excitation and emission wavelengths were 320 nm and 420 nm, respectively. The calibration curve was plotted using lysate-free samples containing 0.5, 0.75 and 1 μM orotic acid.

Cell-Cycle Analysis

For cell-cycle analysis, cells grown in medium without uridine for 48 h were pre-treated with 10 μM BrdU for 30 min 37°C, harvested and fixed with 500 μL of cold 80% EtOH added drop-wise during shaking, and incubated at -20°C. EtOH was then removed and 2M HCl was added for 30 min (room temperature) to denaturate DNA. HCl was removed and the pellet neutralised with 0.1M disodium tetraborate (pH 8.5) for 1 min. Cells were then incubated for 1 h with anti-BrdU-FITC IgG (BD Biosciences; 0.5 μg/mL of PBS) in the dark. Finally, cells were re-suspended in 150 μL of PSB containing 2.5 μg/mL propidium iodide and analysed by flow cytometry.

To assess G2 arrest, cells were grown in medium without uridine for 48 h and then treated with nocodazol (1 μg/mL) for 16 h. Cells ($5x10^4$) re-suspended in 60 μL PBS were as above. After fixation, EtOH was removed and cells were re-suspended in 150 μL of PSB containing 2.5 μg/mL of propidium iodide and analysed by flow cytometry.

Western Blotting

Cells were lysed in the RIPA buffer supplemented with the Complete Protease Inhibitor Cocktail (Roche) and the Phosphatase Inhibitor Cocktail (Sigma-Aldrich). The lysate was cleared by centrifugation and total protein determined. 50 μg of total protein were resolved by SDS-PAGE and transferred to nitrocellulose membranes, which were then probed with the following antibodies: anti-TFAM IgG HPA040648, anti-mtSSB IgG HPA002866, anti-ATP5B IgG HPA001520 (all Sigma), anti-POLG IgG PA5-35163, anti-cyclin E IgG MA5-14336, anti-mtCO4 IgG PA5-29992 (all Thermo Fisher Scientific), anti-UMPS IgG sc-398086 (Santa Cruz Biotechnology), anti-CAD IgG 93925, anti-p(S1859)-CAD IgG 12662 (both Cell Signaling), anti-NDUFS3 IgG ab110246, anti-NDUFA9 IgG ab14713, anti-mtCO1 IgG Ab14705, anti-SDHB IgG ab14714 (all Abcam); anti-DHODH IgG was either from Santa Cruz Biotechnology (sc-166348) or from Proteintech (14877-1-AP).

Native Blue Gel Electrophoresis (NBGE)

NBGE was accomplished basically as published (Wittig et al., 2006). In brief, mitochondria were isolated using a Balch-style homogenizer as detailed elsewhere (Schmitt et al., 2013; Blecha et al., 2017). Digitonin-solubilised mitochondria were separated on NativePAGE Novex Bis-Tris 3%-12% gradient gels. After electrophoresis, the gels were incubated in transfer buffer containing 0.1% SDS for 10 min and proteins were transferred to PVDF membranes probed with specific antibodies against complex I (NDUFA9, ab14713, Abcam; or NDUFB8, ab110242, Abcam), CII (SDHA, 14715, Abcam), CIII (Core2, ab14745, Abcam), CIV (COXVa, ab110262, Abcam) and CV (ATP5A, ab14748, Abcam; or ATP5B, HPA001520, Sigma Aldrich), and VDAC1 (ab15895, Abcam) or HSP60 (12165S, Cell Signaling) as the loading control.

DNA Sequencing

Total DNA containing mtDNA was isolated via the DNAzol reagent (MRC) according to manufacturer's instructions. Full-length mtDNA was sequenced by amplifying ten 1.8 kb dsDNA PCR products using the 5x HOT FIREPol Blend Master Mix with 10 mM MgCl2. PCR products were separated on agarose gels to confirm the specificity of the reaction and were purified using the DNA clean-and-concentrator kit (Zymoresearch). Purified products (200 to 400 ng) were combined with water and 0.5 μL of 100 μM primer stocks to yield 10 μL sequencing reaction mixture. Classical Sanger sequencing was performed via GACT Biotech sequencing service, and the resulting sequences aligned using the SeqManPro suite from the DNASTAR Lasergene 11 software.

mtDNA Level Assay

Total DNA was extracted using the AquaPure Genomic DNA Isolation Kit (BioRad). 50 ng of DNA was diluted with water to 4.5 μL, and 0.5 μL of the combined 10 μM forward and reverse primers added (for mtDNA, mMito1 primers; for nDNA mB2M1 primers; see Table S2 for sequences of primers) and 5 μL of 2xRT^2 SYBR Green qPCR Mastermix (Qiagen) added. The reaction was run on the Eco qPCR System (Illumina) with the following setting: one cycle of 50°C for 2 min; one cycle of 95°C for 10 min; 40 cycles of 95°C for 15 s and 60°C for 1 min.

Quantitative Real-Time (Reverse Transcription) PCR

RNA was obtained in triplicate from 4T1- and 4T1ρ^0- derived sublines using the RNeasy Mini Kit (Qiagen). The Revertaid First-Strand Synthesis System plus random hexamer primers (Fermentas) were used to reverse-transcribe total RNA into cDNA. Primers specific for all mitochondrial and nuclear encoded genes (see Table S2 for sequences of primers) were then assessed with 2x EvaGreen (Solis BioDyne) using the Eco qPCR System. Target genes were normalized to the housekeeping gene GAPDH, and change in gene expression was determined using the ΔΔCt method.

Single Cell qPCR

Single cell samples were obtained by automated FACS sorting (Influx, BD Biosciences). The cell suspension was filtered and nuclei stained with DAPI to identify viable cells. Individual cells were placed in 96 well plate at 1 cell per well containing 5 μl of nuclease-free water supplemented with 1 μg/μl BSA (ThermoFisher). The plate was sealed and placed on dry ice until use. Positive samples contained 100 sorted cells. Negative controls were medium only. For mtDNA analysis 80% of cell lysate was used (4 μl) in 10 μl of qPCR reagent following the manufacturer's recommendations using Grandmastermix for probes (TATAA Biocenter) supplemented with 400 nM primers, 200 nM probes (Sigma Aldrich) (for sequences see Table below). We used the CFX 96 (BioRad) thermocycler as follows: 95°C for 30 s, 40 cycles of 95°C for 5 s, 57°C for 30 s with signal acquisition. Cq values were obtained using the subtracted baseline curve fit and the common threshold method with manual setting in the CFX manager 3.1. Data were analysed with Genex (MultiD) according to the MIQE guidelines (Bustin et al., 2009).

Table. Primer and probe sequences used in sc/qPCR. Capital letters indicate LNA bases; polymorphism is shown in gray.

m_4T1_12S_Fw	*cttggtgatagctggtta*
m_4T1_12S_Rv	*ggcctacaatggttaaaag*
m_4T1_12S_mut_HEX (parental 4T1)	*aataGtgAaCaAttAaCaAaaca*
m_4T1_12S_WT_FAM (host mouse)	*aataGtgAaTaAttAaCaAaaca*

The annealing temperature for the 12S qPCR assay was optimized using a gradient run, validation of the FACS direct lysis for mtDNA was performed using 2-fold "serial dilution" sorting of 1, 2, 4, 8 up to 1024 cells per well and showed good linearity up to 128-256 cells (data not shown). Positive controls of 100 host cells, including all single cell samples showed no or negligible quantification of parental mtDNA. No template controls (NTC) as well as 4T1ρ^0 cells were negative.

mTRIP Analysis

The fluorescence *in situ* hybridization analysis mTRIP (mitochondrial Transcription and Replication Imaging Protocol) was performed and analysed as previously described (Chatre and Ricchetti, 2013). Experiments were performed in the presence of proteinase K that reveals mitochondrial nucleic acids unmasked from proteins. Briefly, the mtDNA probes were labeled by nick translation of PCR products, incorporating either Atto488-dUTP or Atto550-dUTP (Jena Bioscience), using the commercial kit Atto488/Atto550 Nick Translation Labeling kit (Jena Bioscience. Mitochondrial coordinates of mREP correspond to the non-coding region 446-544, which is labelled when initiation of mtDNA replication is activated, and mTRANS to the coordinates of three distinct probes (1905-2866, which covers part of *16S rDNA*; 7400-8518, which extends from *COI* end to *ATP8;* and 13416-14836 from *ND5* end until the beginning of *CYTB*). Cells were cultured on slides, fixed, permeabilized, and denaturated with formamide. Cells were treated with 5μg/mL of proteinase K for 5 min at 37°C, then hybridized with the mREP and mTRANS probes for 16 h at 37°C. DNA was counterstained with 10 μg/mL Hoechst 33342. Confocal acquisition was performed using a spinning-disk Perkin-Elmer Ultraview RS Nipkow Disk, an inverted laser-scanning confocal microscope Zeiss Axiovert 200M with an Apochromat 63x/1.4 oil objective and a Hamamatsu ORCA II ER camera (Imagopole, CiTech, Institut Pasteur). Images were acquired using non-saturating settings, and the same imaging parameters were used for all samples. Optical slices were taken every 200-nm interval along the z-axis covering the whole depth of the cell, at resolution of 1024/1024 pixels. All acquisitions were post-treated using the same Intensity Range (Min/Max), Maximum Intensity Projection, and background correction using the Imaris software (Bitplane), which automatically performs pixel averaging. Three-dimensional (3D)-reconstruction was achieved using the IMARIS software. Original 2D images generated from 3D volume rendering were used for fluorescence quantification using a single-imaging frame collection and ImageJ software (post-acquisition analysis). Graphic settings were applied to 2D images for the purpose of visualization (panels in figures). For each condition, one hundred 3D-reconstructed cells were analysed from three independent experiments.

Mitochondrial Chromatin Immunoprecipitation (mitoChIP) Assay

Cells were crosslinked with 1% formaldehyde, harvested, and cell pellets frozen. Pellets were then resuspended in the ChIP lysis buffer, sonicated for 12 min at cycles consisting of 15 s sonication at amplitude 5 (Qsonica Q700) and 30 s cooling in ice-water bath. An aliquot of the sheared chromatin was treated with RNAse A and proteinase K, and subjected to agarose electrophoresis to confirm correct shearing. Dynabeads were pre-absorbed with salmon sperm DNA (0.2 mg/mL) and BSA (0.5%) overnight, and 20 μL of bead slurry was combined with 5 μg of sheared chromatin and 1 μL of either anti-POLG1 IgG (Abcam, ab128899), anti-TFAM IgG (Abcam ab131607) or non-specific rabbit IgG, and incubated overnight on a rotating platform. After extensive washing, chromatin was eluted and treated with RNAseA and proteinase K to reverse the crosslinking, followed by purification using PCR clean-up columns (MachereyNagel). qRT-PCR was then run using the Eva Green system (Solis Biodyne) at 95°C for 12 min, 40 cycles of 95°C for 15 s, 60°C for 20 s, 72°C for 35 s, followed by melt curve analysis using primers for mouse mtDNA encompassing D-loop; the binding site of POLG: mPOLG ChIP F, TGA TCA ATT CTA GTA GTT CCC AAA A; mPOLG ChIP R, ACC TCT AAT TAA TTA TAA GGC CAGG. Data were quantified against a non-specific IgG via the ΔΔCt method.

Microarray Analysis

Transcriptomic analysis of parental, D0, D5, D10, D15, D20, D25 and D60 4T1 cells was performed using a standard protocol and the MouseGene 2.0 ST array (Affymetrix). The data are deposited under the accession number ArrayExpress: MTAB-6150 in the EBI ArrayExpress database.

Stimulated Emission Depletion (STED) Microscopy

Cells were grown on high precision coverslips overnight, fixed with 4% paraformaldehyde for 10 min at 37°C, permeabilized with 0.05% Triton X-100, 0.05% TWEEN-20 and 0.1 M glycin in PBS, blocked with 5% normal goat serum, and incubated with primary antibodies against DNA (PROGEN), TFAM (Abcam) or TOM20 (Santa Cruz Biotechnology). This was followed by appropriate secondary antibodies conjugated with Abberior STAR RED or Abberior STAR 580 (Abberior Instruments). Nuclei were labelled with Hoechst 33342 (Sigma-Aldrich). The coverslips were mounted on glass slides using Abberior Mount Liquid Antifade (Abberior Instruments). STED images were acquired on commercial Abberior STED 775 QUAD Scanning microscope (Abberior Instruments) equipped with Nikon CFI Plan Apo Lambda objective (60 x Oil, NA 1.40). Abberior STAR 580 and STAR RED labelled proteins were illuminated by pulsed 561 nm and 640 nm lasers and depleted by pulsed 775 nm STED depletion laser of 2D donut. Confocal images were acquired by illuminating the sample by cw 405 nm laser, all channels were obtained in line-interleaved acquisition mode. Fluorescence signal was filtered (emission bandpasses: 500-550 nm, 580-630 nm and 650-720 nm; pinhole 35 μm) and detected on single photon counting modules (Excelitas Technologies). Z-stacks of three planes in distance of 250 nm were acquired for each channel, images were scanned with pixel size of 25 x 25 nm and pixel dwell time 6 μs. All images were stabilized for drift, deconvolved with Huygens Professional version software 17.04 (Scientific Volume Imaging) using Classic Maximum Likelihood Estimation algorithm and processed by FiJi ImageJ software. The maximal intensity projection of 500 nm z-stack is shown.

Mitochondrial NADH Assessment

Mitochondrial NADH was assessed by two-photon microscopy using Zeiss LSM880 NLO inverted microscope equipped with Chameleon Ultra II and Compact OPO MP lasers (Coherent, Santa Clara, CA, USA) as described (Blecha et al., 2017); 3 independent experiments were performed, with more than 150 cells per condition imaged in each experiment.

Transmission Electron Microscopy (TEM)

Cells were grown on cover-slips, fixed with 2.5% glutaraldehyde (Agar Scientific) and post-fixed with 1% OsO_4 made up in Sorensen's phosphate buffer (0.1 M, pH 7.2-7.4), dehydrated, and embedded in Epon-Durkupan (Sigma-Aldrich). Ultrathin sections (~70-90 nm) were cut, contrasted with uranyl acetate (Agar Scientific), and examined in the Morgagni 268 transmission electron microscope (FEI) at 80 kV and in the TECNAI G2 20 LaB6 electron microscope (FEI) at 200 kV. Images were captured with Mega View III CCD camera (Olympus Soft Imaging Solutions) and Gatan Model 894 UltraScan 1000 camera (Gatan Incorporated).

Measurement of Dihydroorotate and Orotate

For measurement of DHO and orotate, $5x10^6$ cells were seeded in a 100 mm cell culture dish and incubated with growth medium at 37°C in 5% CO2. After 24 h, the cells were lysed for the metabolite extraction. All the cells were washed with DPBS two times and lysed with 2:1 methanol/chloroform mixture (total of 600 μL). The cell lysates were vortexed for 30 s, and incubated on liquid nitrogen for 60 s. It was then thawed at room temperature and 1:1 chloroform/water mixture (total of 400 μL) was added. After that, the lysates were centrifuged at 15,000 x *g* at 4°C for 30 min. The upper water phase was collected separately and evaporated using a centrifugal evaporator. The complete dried pellet samples were stored at -80°C until mass spectrometry analysis. Liquid chromatography-mass spectrometry (LC-MS) was done as described in Flux analysis of conversion of glutamine to UMP (see below).

Flux Analysis of Conversion of Glutamine to UMP

To evaluate UMP labeled with $^{13}C_3$,$^{15}N_2$ (M+5), $3x10^6$ cells were seeded in 100 mm cell culture dish with growth medium and incubated at 37°C in 5% CO_2. After 24 h incubation, media were changed to 1 mM L-glutamine ($^{13}C_5$, 99%; $^{15}N_2$, 99%; Cambridge Isotope Laboratories) containing medium, and the cells were labeled overnight. After that, the cells were lysed for the metabolite extraction. The dried pellet samples were dissolved with 1:1 acetonitrile/water mixture for mass spectrometry analysis. The Agilent 1100 Series HPLC System and XBridge Amide Column (3.5 μm, 4.6 mm x 100 mm; Waters) were used for the chromatography, with 20 mM ammonium acetate (pH was adjusted to 9 with ammonium hydroxide) and acetonitrile as mobile phases. API 2000 Mass Spectrometer with Analyst 1.6 Software (AB/SCIEX, Framingham) was used for the mass spectrometry analysis to measure DHOA, orotate and labeled UMP.

Analysis of Aspartate and Nucleotides

To measure aspartate and other nucleotides, $5x10^5$ cells were seeded in a 6-well cell culture dish and incubated with growth medium at 37°C in 5% CO2. The cells were lysed with 5:3:2 methanol/acetonitrile/water mixture (total of 200 μL). The lysates were centrifuged at 28,000 x *g* at 4°C for 30 min. The supernatant was collected separately and evaporated using a centrifugal evaporator. The Agilent 1290 Infinity LC System and SeQuant ZIC-pHILIC Column (5 μm, 150 mm x 2.1 mm; Merck KGaA, 64271 Darmstadt, Germany) were used for the chromatography, with 20 mM ammonium acetate (pH was adjusted to 9 with ammonium hydroxide) and acetonitrile as mobile phases. Agilent Technologies 6460 Triple Quad LC/MS with MassHunter Software (Agilent, United States) was used for the mass spectrometry analysis.

In Vivo Metabolic Studies

Balb/c mice with 4T1 and 4T1ρ^0 AOX cell-derived tumors (volume of about 150 mm^3) were infused with $^{13}C_5$,$^{15}N_2$-Gln (Sigma-Aldrich) according to a published protocol (Mashimo et al., 2014). Briefly, mice were anaesthetised with isoflurane and their jugular vein cannulated. The animals were then infused with labelled Gln at 0.28 mg/g body weight (in 0.3 mL saline) over 1 min and with Gln at 0.005 mg/g body weight (in 600 μL saline) at 200 μL/h for 180 min. After infusion, the mice were sacrificed and tumors excised. Tumor tissue was homogenised and assessed for labelled UMP as described above.

Mutation Rates of Genes in the *De Novo* Pyrimidine Biosynthesis Pathway

We obtained all somatic mutations from The Cancer Genome Atlas (TCGA), which contains 11,330 patients of 33 cancer types. Mutation maf files were downloaded from Firehose (http://gdac.broadinstitute.org/). The average gene expression levels (microarray RMA, log2ratio) for all genes in cancer cells were derived from 91 CCLE (Cancer Cell Line Encyclopedia) cell lines. Cancer genes were retrieved from CGC (cancer gene census, http://cancer.sanger.ac.uk/census COSMIC v81). To facilitate calculation of mutation rates, we excluded those cancer genes that are affected by translocation, amplifications or large deletions. This led to 262 cancer genes in which 67 are annotated as oncogenes, 100 as tumor suppressors. We calculated the raw mutation rate of a gene according to the number of mutations per base pair in the coding sequence (CDS) and normalised by sample size. For comparison, we used the mutation rates of 15,067 non-cancer genes as a background after excluding 1,090 genes lacking expression information and 2,440 putative cancer genes from CGC, uniprot oncogenes Proto-oncogenes/Tumor suppressor genes, NCG (Network of Cancer Genes) and DISEASE. They were firstly divided into 20 bins according to gene expression levels. An error bar was then calculated for each bin, marking 75 quantile, 25 quantile and median mutation rates, respectively. We then fitted a baseline for mutation rates of

non-cancer genes using the generalised additive model (GAM). Because different genes have different background (random) mutation rates, we utilised MutsigCV, which employs a sophisticated model for estimating gene-specific and patient-specific background mutation rate and calculating significantly mutated genes (Q-score, the smaller Q-score, the higher significance). For MutsigCV calculation, the combined pan-cancer mutation maf file was used as input and all other input files and default options were kept. Data analysis and visualisation were conducted in R using packages dplyr and ggplot2.

Evaluation of Cell Proliferation in Tumor Tissue

Immunohistochemistry was performed using paraffin-embedded tissue section (7 μm). Sections were dehydrated, heated in citrate buffer (70 mM, pH 6.0) for antigen retrieval, and blocked with PBS containing 10% normal goat serum (Jackson Immuno Research Labs) and 0.1% Tween 20 (Sigma). Anti-Ki67 IgG was purchased from Cell Signaling, the secondary antibody coupled to AlexaFluor 594 from Jackson Immuno Research Labs. To detect cell nuclei, sections were mounted on histology mounting medium Fluoroshield with DAPI (Sigma).The sections were imaging with fluorescence microscope Nikon Eclipse E400.

Evaluation of Pyruvate

The levels of pyruvate in tumor and liver tissue were measured using a colorimetric assay (Abcam) according to the manufacturer's instructions. In brief, serum from mice with and without tumors, and from cancer patients and healthy subjects, as well as mouse tumor and liver tissue (10 mg) was collected, washed with cold PBS, and lysed in the pyruvate assay buffer; the supernatant was collected by centrifugation at 20,000 x *g* for 5 min at 4°C. The reaction assay mixture (50 μL), prepared according to the manufacturer's instructions, was then added to each well containing 50 μL of the sample. The colorimetric signal was evaluated at 570 nm using the Tecan Infinite M200 plate reader. The following cancer patient serum was used in the analysis: colorectal cancer (7 patients), pancreatic cancer (9 patients), gastric cancer (1 patient), B-cell lymphoma (1 patient).

Formation of Syngeneic Tumors

4T1, 4T1ρ^0 (D0), D5, D10, D15 and D20 cells, D0 AOX, D5 AOX, D10 AOX, D15 AOX and D20 AOX cells, DHODH^{KO42} and DHODH^{rec} cells, and ρ^0 AOX and ATP5B^{KO7} cells were injected subcutaneously (s.c.) into the right flank of female Balb/c mice at 10^6 cells per animal. To examine the effect of uridine on tumor formation, 10 Balb/c mice were grafted with 10^6 4T1ρ^0 cells. Two days later, uridine (1 g/kg) was administered by intra-peritoneal injection to 5 mice 3 times per week (Peters et al., 1988), with the remaining 5 mice kept as control animals. To examine the effect of Met, Lef and SHAM on growth of tumors derived from 4T1ρ^0 AOX cells, the respective agent was administered by intra-peritoneal injection twice a week for 28 days as soon as USI-detectable tumors appeared in the mice. The following dosing was used: SHAM, 200 mg/kg in 5% DMSO in corn oil; lefluomide, 20 mg/kg in corn oil containing 4% ethanol; metformin, 125 mg/kg in PBS. Tumors were visualized and their volume precisely calculated using the USI device Vevo770 or Vevo3100 (Fuji Film). The experiments were terminated when tumor volume reached about 1,000 mm^3. Animal studies were performed according to the guidelines of the Australian and New Zealand Council for the Care and Use of Animals in Research and Teaching, as well as the Czech Animal Ethics Committee, and were approved by the respective local Animal Ethics Committee.

Statistical Analysis

Unless stated otherwise, data are mean values ± S.D. of at least three independent experiments. In mouse experiments, groups of 6 animals were used, unless stated otherwise. The two-tailed unpaired Student's t test was used to assess statistical significance with $p<0.05$ being regarded as significant, using GraphPad Prism software. Anova was used for multiple comparisons where applicable. Images are representative of at least three independent experiments.

DATA AND SOFTWARE AVAILABILITY

The accession number for the microarray data reported in this paper is ArrayExpress: MTAB-6150.

nature COMMUNICATIONS

ARTICLE

DOI: 10.1038/s41467-018-04603-z OPEN

Alternative assembly of respiratory complex II connects energy stress to metabolic checkpoints

Ayenachew Bezawork-Geleta[1,2], He Wen[3,4], LanFeng Dong[1], Bing Yan[1], Jelena Vider[1], Stepana Boukalova[5], Linda Krobova[5], Katerina Vanova[5], Renata Zobalova[5], Margarita Sobol[6], Pavel Hozak[6], Silvia Magalhaes Novais[5], Veronika Caisova[7,8], Pavel Abaffy[5], Ravindra Naraine[5], Ying Pang[7], Thiri Zaw[9], Ping Zhang[1], Radek Sindelka[5], Mikael Kubista[5,10], Steven Zuryn[2], Mark P. Molloy[9], Michael V. Berridge[11], Karel Pacak[7], Jakub Rohlena[5], Sunghyouk Park[4] & Jiri Neuzil[1,5]

Cell growth and survival depend on a delicate balance between energy production and synthesis of metabolites. Here, we provide evidence that an alternative mitochondrial complex II (CII) assembly, designated as CII_{low}, serves as a checkpoint for metabolite biosynthesis under bioenergetic stress, with cells suppressing their energy utilization by modulating DNA synthesis and cell cycle progression. Depletion of CII_{low} leads to an imbalance in energy utilization and metabolite synthesis, as evidenced by recovery of the de novo pyrimidine pathway and unlocking cell cycle arrest from the S-phase. In vitro experiments are further corroborated by analysis of paraganglioma tissues from patients with sporadic, SDHA and SDHB mutations. These findings suggest that CII_{low} is a core complex inside mitochondria that provides homeostatic control of cellular metabolism depending on the availability of energy.

[1] School of Medical Sciences, Griffith University, Southport 4222 Qld, Australia. [2] Clem Jones Centre for Ageing Dementia Research, Queensland Brain Institute, University of Queensland, Brisbane 4072 Qld, Australia. [3] Department of Biochemistry and Molecular Biology, Shenzhen University School of Medicine, Shenzhen 518060, China. [4] College of Pharmacy, Natural Product Research Institute, Seoul National University, Seoul 08826, Korea. [5] Institute of Biotechnology, Czech Academy of Sciences, Prague-West 25250, Czech Republic. [6] Institute of Molecular Genetics, Czech Academy of Sciences, Prague 14220, Czech Republic. [7] Eunice Kennedy Shriver National Institute of Child Health and Human Development, National Institutes of Health, Bethesda 20892 MD, USA. [8] Faculty of Science, University of South Bohemia, Ceske Budejovice 37005, Czech Republic. [9] Australian Proteome Analysis Facility, Macquarie University, North Ryde 2109 NSW, Australia. [10] TATAA Biocenter, Gothenburg 41103, Sweden. [11] Malaghan Institute of Medical Research, Wellington 6242, New Zealand. These authors contributed equally: Ayenachew Bezawork-Geleta, He Wen. Correspondence and requests for materials should be addressed to A.B.-G. (email: a.bezawork-geleta@griffith.edu.au) or to J.R. (email: jakub.rohlena@ibt.cas.cz) or to S.P. (email: psh@snu.ac.kr) or to J.N. (email: j.neuzil@griffith.edu.au)

Mitochondria are semi-autonomous organelles found in the majority of eukaryotic cells. They have their own genome (mitochondrial DNA, mtDNA), which encodes subunits of respiratory complexes and RNA components for mitochondrial protein synthesis. Major roles of mitochondria include generation of energy and synthesis of metabolites. Molecules that are a source of energy are oxidized in a series of biochemical reactions within the tricarboxylic acid (TCA) cycle. Intermediate products of the TCA cycle are used as signaling molecules and as building blocks for various macromolecules, while NADH and $FADH_2$ are metabolized via oxidative phosphorylation (OXPHOS) to yield ATP. OXPHOS comprises five complexes, CI–CV. CII (succinate dehydrogenase, SDH) contains nuclear-encoded SDHA, SDHB, SDHC, and SDHD subunits, which are recognized as tumor suppressors[1–3]. Besides its role in OXPHOS, CII converts succinate to fumarate in the TCA cycle, and is thus at the crossroad of the TCA cycle and OXPHOS[4].

Clinical data document the presence of somatic mutations in mtDNA in cancer in both the regulatory D-LOOP and the coding regions[5–8]. Previous research has mainly concerned the effects of mtDNA mutations on CI, CIII, CIV, and CV, with CII having been a relatively minor focus. This is explained by the fact that unlike all other OXPHOS complexes, CII does not contain mtDNA-encoded subunits, and therefore no direct effect of mtDNA defects on CII assembly and function has been expected. Further, individual respiratory complexes form supercomplexes (SCs)[9–11], while CII acts as a stand-alone complex, with only one report indicating that it can be an SC component[12].

This study investigates whether CII subunits and mtDNA could have any form of interaction in energy production, and if so, whether there is a functional relation that provides an advantage to cells with mtDNA mutations. We show that depletion of mtDNA has an unexpected effect on CII assembly, causing a shift from its tetrameric, fully processed, and assembled form to a slower migrating complex of ~100 kDa, referred to here as complex II_{low} (CII_{low}). Our data suggest that CII_{low} links bioenergetic stress to negative regulation of de novo pyrimidine synthesis and cell cycle progression, which is supported by clinical data from paraganglioma patients with mutations in SDH subunits, indicating that CII_{low} plays an important role in homeostatic control of metabolite synthesis under bioenergetic stress.

Results

mtDNA-linked bioenergetics defects affect the assembly of CII. Unlike other respiratory complexes, CII is encoded by nuclear DNA and is genetically independent of mtDNA. To understand if mtDNA dysfunction affects CII indirectly, we tested the effect of mtDNA perturbation[8,13–15] on CII assembly. Native blue gel electrophoresis (NBGE) of mitochondria isolated from murine 4T1 and human MCF7 cells without mtDNA (ρ^0 cells) revealed that CII exists in two hetero-oligomeric forms of ~100 kDa and 124 kDa (migrating on NBGE at ~140 kDa). In $4T1\rho^0$ and $MCF7\rho^0$ cells, SDHA was mainly present as CII_{low}, with no known biological function reported to date, and to a lesser degree within fully assembled CII (Fig. 1a). The finding of predominant CII_{low} in $4T1\rho^0$ and $MCF7\rho^0$ cells suggests that this form of CII may have a role in (patho)physiological situations where mtDNA is damaged. The size of the processed SDHA protein is ~69 kDa, while CII_{low} migrates on native gels at ~100 kDa. Hence, additional protein components beyond SDHA must be present in CII_{low}.

We next examined CII assembly in human MDA-MB-231 (MDA231) cells. Inhibition of mitochondrial protein synthesis with chloramphenicol (CAB), a blocker of mitochondrial translation[16–18], resulted in depletion of CIII and SCs (Fig. 1b, right panels). Similarly, as with $4T1\rho^0$ and $MCF\rho^0$ cells, CAB-treated MDA231 cells accumulated CII_{low} containing SDHA (Fig. 1b, left panels), suggesting that this form of CII may have (patho)physiological relevance when expression of mtDNA-encoded proteins is compromised.

SDHA is a stable constituent of CII_{low}. To better characterize the subunit composition of CII_{low}, SDHA, SDHB, and SDHC subunits were knocked down one at a time in 4T1 cells using two different siRNAs (siRNA1 and siRNA2), and CII assembly state was followed by NBGE. Depletion of any of the three subunits reduced the level of CII. Interestingly, only the knockdown of SDHA, but not of the other CII subunits, resulted in marked reduction of CII_{low} (Fig. 1c and d), corroborating the presence of SDHA, but not SDHB or SDHC, in CII_{low}.

The identification of SDHA in CII_{low} suggests that it may be more stable than the other CII subunits. We therefore examined the steady state of each subunit in our knockdown cell lines. Depletion of SDHB led to a decrease in the steady state of SDHC, and knockdown of SDHC led to a decrease in the steady state of SDHB. Interestingly, in SDHA knockdown cells, both SDHB and SDHC levels decreased by ~70%. Knocking down either SDHB or SDHC had no effect on the steady state of SDHA (Fig. 1e). It is likely that depletion of SDHA leads to low levels of SDHB and SDHC, probably due to low stability of unassembled subunits as indicated previously[19–21].

Characterization of the CII_{low} form of SDH. Based on crystal structure of CII[22] (Supplementary Fig. 1a) and our data in Fig. 1e, we hypothesized that depletion of SDHB will result in cells containing only CII_{low}. We thus generated SDHB knockout (KO) MDA231 cells targeting exon 1 (Fig. 2a and b). As with 4T1 cells (Fig. 1c and e), the steady-state level of SDHA was unchanged in $SDHB^{KO}$ MDA231 cells (Fig. 2c). In order to deplete CII_{low}, $SDHB^{KO}$ MDA231 cells were transfected with two different *SDHA* shRNAs ($SDHB^{KO}SDHA^{low}$-1 and $SDHB^{KO}SDHA^{low}$-2) and an empty vector ($SDHB^{KO}$EV) as a control (Fig. 2c; Supplementary Fig. 1b). NBGE analysis showed high levels of CII_{low} in $SDHB^{KO}$ MDA231 cells and little CII_{low} in $SDHB^{KO}SDHA^{low}$ cells (Fig. 2d). We thus prepared models of cells with three variants of CII assembly: fully assembled CII and low levels of CII_{low} (parental cells), cells with only CII_{low} ($SDHB^{KO}$ $SDHB^{KO}$EV cells), and cells lacking both CII and CII_{low} ($SDHB^{KO}SDHA^{low}$ cells). These models showed low proliferation for both $SDHB^{KO}$ and $SDHB^{KO}SDHA^{low}$ cells (Fig. 2e).

To specify its molecular composition, we transfected $SDHB^{KO}$ cells with SDHA-FLAG and immunoprecipitated the cell-free extract using anti-FLAG IgG. The immunoprecipitate was subjected to tryptic digest followed by MS analysis (Supplementary Fig. 2a), with results of the screen in Supplementary Fig. 2a and Supplementary Data 1. The analysis revealed the presence of the CII assembly factors SDHAF2 (16.7 kDa) and SDHAF4 (9.9 kDa). While SDHAF2 was readily detectable on NBGE membranes in CII_{low} (Supplementary Fig. 2b), the available antibodies did not allow reproducible detection of SDHAF4 after NBGE, and its presence was verified by other means (see below).

We next re-expressed SDHB-FLAG in $SDHB^{KO}$ cells to see whether this would rescue the parental phenotype and whether CII_{low} is reversible. SDHB-reconstituted ($SDHB^{rec}$) cells were assessed by Western blotting (WB) following SDS-PAGE for the presence of SDHA, SDHB, SDHAF2, and SDHAF4. Supplementary Fig. 2c documents similar levels of SDHA in all three sublines and high levels of SDHB in parental and $SDHB^{rec}$ cells. In contrast, both SDHAF2 and SDHAF4 were low in parental and

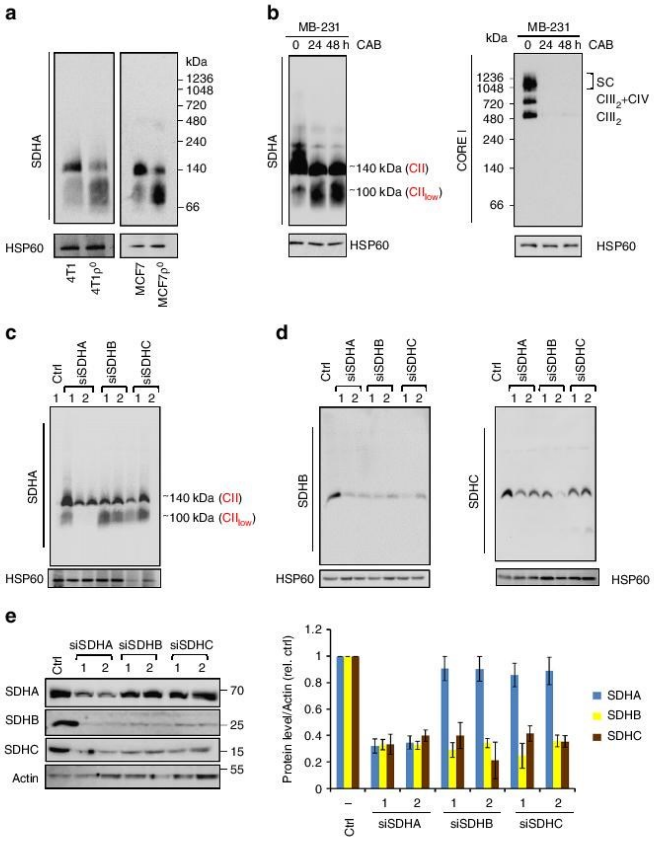

Fig. 1 mtDNA dysfunction affects CII assembly. **a** NBGE analyses of CII assembly from digitonin-solubilized mitochondria isolated from 4T1 and MCF7 cells and their ρ^0 counterparts. **b** NBGE showing formation of CII_{low} and depletion of CIII assembly upon suppression of expression of mtDNA-encoded genes with CAB at indicated time points. **c**, **d** NBGE of CII using mitochondria isolated from 4T1 cells transfected with siRNA against SDHA, SDHB, or SDHC. **e** WB after SDS-PAGE of steady-state levels of CII subunits in 4T1 cells treated with siRNAs as shown (left panel). Right panel shows quantification of WB in the left panel related to actin. The numbers '1' and '2' in **c**–**e** refer to two different siRNAs. Data shown are mean values ± SD; images are representative of three independent experiments

$SHDB^{rec}$ cells, but accumulated in $SDHB^{KO}$ cells. We then tested the three sublines by NBGE followed by WB using anti-SDHA IgG and anti-SDHAF2 IgG. Supplementary Fig. 2d reveals that mature CII is re-assembled and the amount of CII_{low} reverts to parental levels in $SDHB^{rec}$ cells, indicating SDHB-dependent reversibility of alternatively assembled CII. Furthermore, SDHAF2 and SDHAF4 were detectable only in $SDHB^{KO}$ cells that lack mature CII but feature CII_{low}, supporting the presence of these assembly factors in CII_{low} cells.

To verify the reversibility of CII_{low} in response to stress, we treated parental cells with CAB for 48 h, followed by 24 h recovery. The amount of CII_{low} was evaluated by NBGE using antibodies against SDHA and SDHAF2, two CII_{low} components readily detectable in this assay (Supplementary Fig. 2e). Treatment with CAB increased the level of CII_{low}, which reverted to baseline within 24 h of treatment cessation. Together with the $SDHB^{rec}$ data, this indicates reversibility of CII_{low} assembly, providing flexibility in response to mitochondrial bioenergetic stress.

CII_{low} does not modulate mitochondrial bioenergetics. We asked whether altered assembly of SDHA affects mitochondrial bioenergetics as well as expression and assembly of other mitochondrial complexes. We found that basal respiration, maximum respiratory capacity, and ATP production were decreased both in $SDHB^{KO}$EV and $SDHB^{KO}SDHA^{low}$ cells (Fig. 3a–e). Unlike parental cells, absence of spare respiratory capacity and low ATP production were found in $SDHB^{KO}$EV and $SDHB^{KO}SDHA^{low}$ cells (Fig. 3d, e), further indicating a state of bioenergetic stress. We next assessed oxygen consumption in permeabilized MDA231 cells by high-resolution respirometry. This showed that alteration of the CII assembly status resulted not only in complete suppression of CII-dependent respiration, but also considerably altered CI-dependent respiration (Fig. 3f). Consistent with the above results, we found that assembly of SCs was reduced in $SDHB^{KO}$ and $SDHB^{KO}SDHA^{low}$ cells (Fig. 3g). This is further supported by lower steady-state levels of CI subunits but not CIII, CIV, and CV subunits (Fig. 3h). However, there was no significant difference between $SDHB^{KO}$ and $SDHB^{KO}SDHA^{low}$ cells

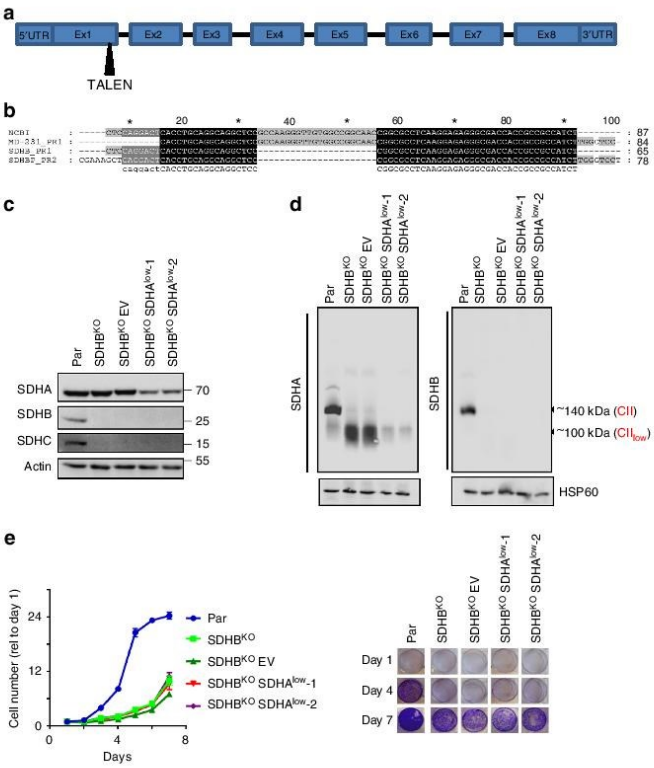

Fig. 2 SDHB depletion stabilizes CII_{low}. **a** A scheme showing the structure of the *SDHB* gene and exon1 as the TALEN target. **b** DNA sequence alignment of the *SDHB* exon 1 from the GenBank nucleotide sequence database, and parental and $SDHB^{KO}$ MDA231 cells. Sanger sequencing was done from the PCR product amplified using two pairs of primers (PR1 and PR2) using genomic DNA as a template. **c** WB after SDS-PAGE of CII subunits in individual sublines, as shown. $SDHB^{KO}$EV cells are $SDHB^{KO}$ cells transfected with empty vector and were used as a control for stable shRNA transfections. **d** NBGE of mitochondria isolated from parental, $SDHB^{KO}$, $SDHB^{KO}$EV, and $SDHB^{KO}SDHA^{low}$ cells showing three variants of SDHA, using anti-SDHA IgG and anti-SDHB IgG. **e** Proliferation of MDA231 subline was analyzed at the indicated time points using the crystal violet method. Panel on the right shows crystal violet staining at 1, 4, and 7 days. Data are normalized to day 1. Data shown are mean values ± SD ($n = 3$); images are representative of three independent experiments

for any of the assessed parameters. In contrast, re-expression of SDHB-FLAG ($SDHB^{rec}$ cells) substantially recovered the parental phenotype with respect to routine and CII-dependent respiration (Supplementary Fig. S2f).

Cells with severe defects in OXPHOS rely on glycolysis for ATP production and do not grow in the presence of galactose[23]. We tested proliferation of MDA231 sublines in galactose- and glucose-containing media, and found that both $SDHB^{KO}$EV and $SDHB^{KO}SDHA^{low}$ cells failed to proliferate in galactose-containing medium whereas parental cells proliferated efficiently (Fig. 3i). This is in agreement with previous reports on cells with defects in CI and CII assembly[23–26]. Again, re-expressed SDHB rescued proliferation in galactose-containing media (Supplementary Fig. 2g).

Similarly, analysis of mitochondrial morphology using transmission electron microscopy (TEM) revealed that both $SDHB^{KO}$EV and $SDHB^{KO}SDHA^{low}$ cells featured mitochondria with altered structure (Supplementary Fig. 3a), consistent with a previous report[27]. These changes did not affect the steady-state level of several key proteins associated with mitochondrial maintenance and biogenesis (Supplementary Fig. 3b). Thus, while CII assembly status affected whole-cell bioenergetics and proliferation, CII_{low} had little additional effect on mitochondrial bioenergetics and biogenesis.

Pyrimidine synthesis is attenuated in the presence of CII_{low}. Having found no direct effect on bioenergetics, we reasoned that CII_{low} could modulate adaptation to altered bioenergetic conditions. Thus, we first performed quantitative proteomic analysis in MDA231 sublines using SWATH-MS[28] that resulted in identification and quantification of 1699 individual proteins (Supplementary Data 2). The most downregulated pathway in $SDHB^{KO}$EV cells compared to parental cells was de novo pyrimidine synthesis (Fig. 4a). Quantification of the SWATH-MS data revealed that this downregulation is reversed in $SDHB^{KO}SDHA^{low}$ cells (Supplementary Fig. 4), indicating that $SDHB^{KO}$ cells may suppress anabolic processes to reduce the energy demand, and this is then relieved in $SDHB^{KO}SDHA^{low}$ cells. To further investigate this issue, we subjected parental, $SDHB^{KO}$, and $SDHB^{KO}SDHA^{low}$ cells to RNAseq analysis (Supplementary Fig. 5a and b), which revealed significant clusters

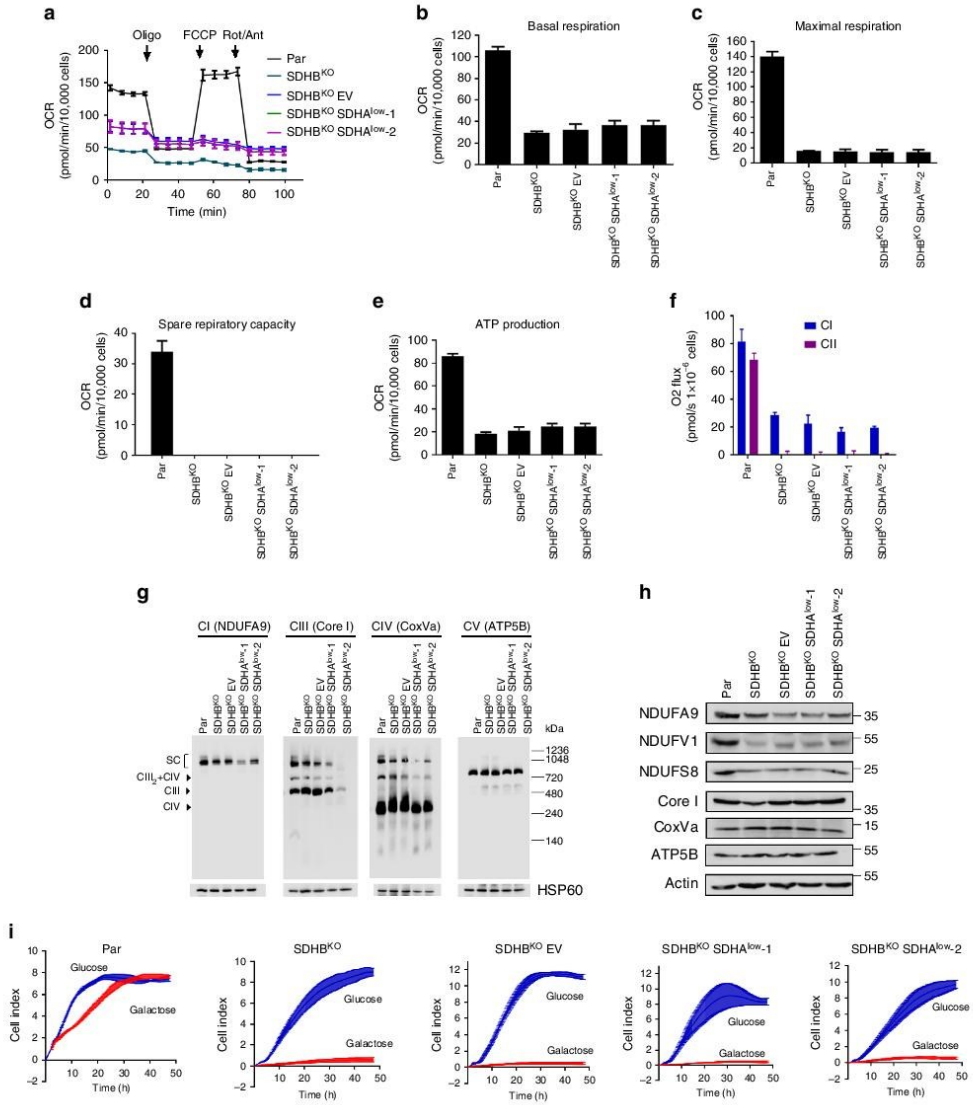

Fig. 3 CII_{low} does not regulate mitochondial bioenergetics. **a** Oxygen consumption rate (OCR) in MDA231 sublines was followed during sequential additions of oligomycin, FCCP, and combination with rotenone and antimycin. **b**–**e** Basal respiration, maximal respiration, spare respiratory capacity, and ATP production. **f** CI- and CII-dependent respiration was evaluated in permeabilized cells using the Oxygraph. **g** Mitochondria isolated from MDA231 sublines were subjected to NBGE followed by WB analysis using antibodies against NDUFA9, NDUFV1, NDUFS8 (CI), Core I (CIII), and COXVa (CIV) and ATP5B (CV). **h** MDA231 sublines were analyzed for subunits of OXOPHOS complexes using WB after SDS-PAGE. **i** MDA231 sublines grown in media containing either glucose or galactose were evaluated for proliferation using the xCELLingence instrument. Data shown are mean values ± SD ($n = 3$); images and graphs in **i** are representative of three independent experiments

of genes either upregulated or downregulated in $SDHB^{KO}$ cells with expression being reverted toward parental cell levels in $SDHB^{KO}SDHA^{low}$ cells (Groups 1 and 2 in Supplementary Fig. 5b–f). Gene set enrichment analysis revealed the presence of catabolism-related processes in these clusters, including heterocycle catabolic process (GO:0046700), aromatic compound catabolic process (GO:0019439), organic cyclic compound catabolic process (GO:1901361), and cellular macromolecule catabolic process (GO:0044265) that were all downregulated in $SDHB^{KO}SDHA^{low}$ cells compared to $SDHB^{KO}$ cells (Supplementary Fig. 5e and f). However, the de novo pyrimidine synthesis pathway did not show significant enrichment, pointing

to modest correlation of transcriptomic and proteomic data as previously reported[29–33]. Collectively, these data suggest that SDHB^{KO} cells may upregulate catabolic and salvage pathways to compensate for defects in pyrimidine biosynthesis.

We next focused our studies on pyrimidine biosynthesis. Initially, we evaluated representative proteins of this pathway using WB, and found that the trifunctional polypeptide CAD (carbamoyl-phosphate synthase 2, aspartate transcarbamylase,

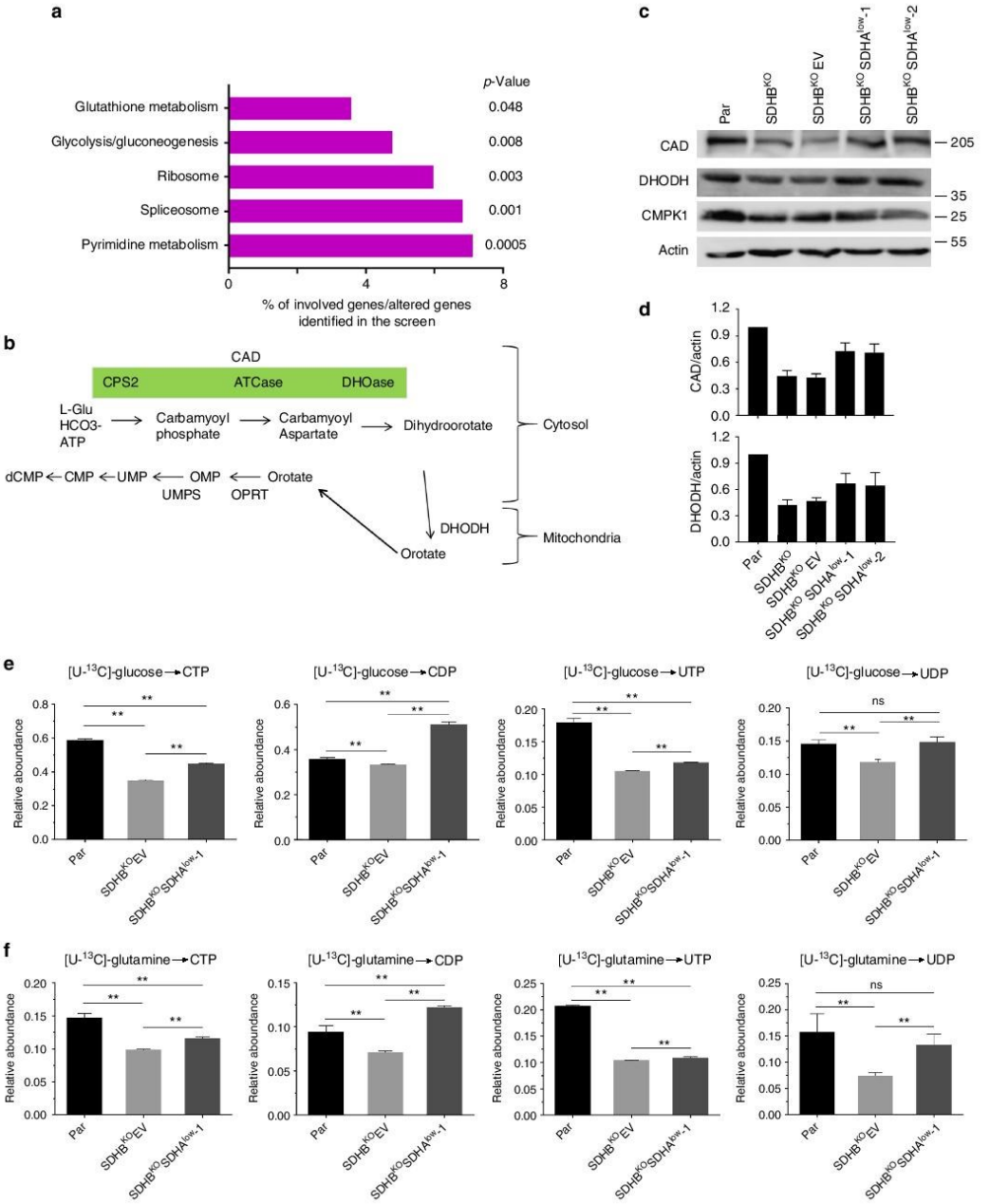

and dihydroorotase) and dihydroorotate dehydrogenase (DHODH) that catalyze the first four steps of de novo pyrimidine synthesis were attenuated in SDHB^{KO}EV but recovered in SDHB^{KO}SDHA^{low} cells (Fig. 4b–d). Re-expression of SDHB in SDHB^{KO} cells also restored CAD and DHODH (Supplementary Fig. 2h).

We then analyzed pyrimidine nucleotide synthesis directly using stable isotope labeling and LC-MS/MS. The data in Fig. 4e and f, and Supplementary Fig. 7, show that biosynthesis of CTP, CDP, UTP, and UDP from major nutrients glucose and glutamine was low in SDHB^{KO}EV cells but reversed variably in SDHB^{KO}SDHA^{low} cells. These results document that compared to the baseline situation (fully assembled CII), formation of CII$_{low}$ is linked to depressed de novo pyrimidine synthesis, which is reversed with its depletion. The data suggest that under low-energy conditions, CII$_{low}$ may activate cellular processes reducing ATP-consuming pathways such as DNA synthesis to maintain energy balance, which is deregulated in SDHB^{KO}SDHA^{low} cells.

CII$_{low}$ plays a role in cell cycle progression. De novo pyrimidine synthesis is essential for maintaining the nucleotide pool for replication of DNA, thereby controlling cell cycle progression[34–37]. We thus analyzed cell cycle distribution in MDA231 sublines, which showed that SDHB^{KO} and SDHB^{KO}EV cells were arrested in the S-phase. However, SDHB^{KO}SDHA^{low} cells partially recovered from S-phase arrest with cell cycle distribution similar to that of parental cells (Fig. 5a and b). Cell cycle is regulated by cyclins and cyclin-dependent kinases (CDKs). WB confirmed a marked decrease in the level of CDK6 as well as p16, phosphorylated histone H3 (HH3), and cMYC in SDHB^{KO} and SDHB^{KO}SDHA^{low} cells compared to parental cells (Fig. 5c). Interestingly, p18 was downregulated in SDHB^{KO} and SDHB^{KO}EV cells and recovered in SDHB^{KO}SDHA^{low} cells (Fig. 5c), similar to that seen for steady-state levels of CAD and DHODH and for nucleotide synthesis (Fig. 4). Further, we observed near parental levels of pHH3 in SDHB^{rec} cells (Supplementary Fig. 2h). This result suggests that alteration in SDHA assembly status affects de novo pyrimidine synthesis, and consequently cell cycle progression. Our data suggest that under low-energy conditions, the shift of CII to CII$_{low}$ is associated with a switch to bioenergetically less-demanding processes.

CII$_{low}$ supports growth of SDHB-deficient tumors. Figure 2e reveals no difference in proliferation between SDHB^{KO}EV and SDHB^{KO}SDHA^{low} cells, suggesting that CII$_{low}$ is not critical for proliferation under nutrient-rich conditions. However, imbalance of energy production and anabolic metabolism such as that linked to DNA synthesis could be critical for biomass production required for growth and survival under sub-optimal conditions[38]. To see whether CII$_{low}$ is important for the tumorigenic potential of MDA231 sublines, migration of parental, SDHB^{KO}EV, and SDHB^{KO}SDHA^{low} cells was tested. Contrary to the cell proliferation assay (Fig. 2e), SDHB^{KO}SDHA^{low} cells showed a lower rate of migration from serum-free media compared to both parental and SDHB^{KO} EV cells (Fig. 5d). To extend these results to a pathologically relevant situation, we tested the capacity of the sublines to form tumors. Parental, SDHB^{KO}EV, and SDHB^{KO}SDHA^{low} cells were grafted subcutaneously into Balb-c nu/nu mice, and tumor progression was analyzed by ultrasound imaging (USI). Compared to parental cells, SDHB^{KO}EV cells formed tumors with a delay of about 15 days and at lower rate, while SDHB^{KO}SDHA^{low} cells failed to form tumors 60 days post grafting (Fig. 5e and f). To understand whether the inability of SDHB^{KO}SDHA^{low} cells to form tumors is linked to their higher vulnerability under nutrient-poor conditions, we evaluated the level of cell death in individual sublines grown in galactose media. Supplementary Fig. 3c, d shows that all sublines are mostly viable in glucose-containing media, while SDHB^{KO}SDHA^{low} cells are more vulnerable to cell death than SDHB^{KO} cells in non-permissive, galactose-containing media. These data point to a link between CII$_{low}$ and energy balance regulation to maintain cellular fitness under nutrient-poor conditions.

CII$_{low}$ modulates the metabolome. In order to better understand metabolic consequences of alternative SDHA assembly, we examined the metabolic profiles of MDA231 sublines. Metabolomic data obtained by one-dimensional (1D) nuclear magnetic resonance (NMR) were combined with additional 16 metabolites, measured using targeted LC-MS/MS that are important in central energy metabolism but are not readily quantifiable by NMR (Supplementary Data 3). Results of this analysis, represented by the heat map in Fig. 6a, indicate an effect of CII$_{low}$ on the differential metabolite profile in MDA231 sublines. The data show that the metabolic profile of SDHB^{KO}EV cells has very little overlap with that of the parental cells, whereas SDHB^{KO}SDHA^{low} cells have significantly more overlap. This is consistent with partial least square discriminant analysis (PLS-DA) of the metabolomic data showing the metabolic differences between sublines and the closer position of the SDHB^{KO}SDHA^{low} cells to parental cells along the PLS1 axis (Fig. 6b). Taken together with the results in Fig. 1 which demonstrated CII$_{low}$ formation during OXPHOS dysfunction, these data suggest that CII$_{low}$ is linked to metabolic modulation when bioenergetics is compromised.

Depletion of CII$_{low}$ reverses accumulation of succinate. Given the role of SDHA in the TCA cycle, we expect that CII$_{low}$ could affect succinate metabolism and TCA cycle activity. We therefore subjected parental, SDHB^{KO}EV, and SDHB^{KO}SDHA^{low} cells to two-dimensional (2D) in-cell NMR analysis, which allows monitoring of metabolites in live cells in real time[39]. The approach detects metabolite levels as a function of time, as opposed to steady-state levels at a single time-point as reported above and in most metabolomics studies. This facilitates estimation of actual activities of metabolic pathways leading to particular metabolites in live cells. Thus, cells were incubated with [U-^{13}C]glucose, and production of ^{13}C isotope-containing pyruvate, lactate, alanine, and the TCA cycle intermediate succinate was monitored. As expected, parental cells differed in all assessed metabolites from the two sublines. SDHB^{KO}EV cells showed increased intracellular levels of lactate and alanine compared to SDHB^{KO}SDHA^{low} cells,

Fig. 4 Pyrimidine biosynthesis is suppressed in the presence of CII$_{low}$. **a** Label-free quantitative proteomic analysis of downregulated proteins in SDHB^{KO} MDAMB231 cells and the percentage of proteins identified per pathway relative to genes with significantly altered expression in SDHB^{KO} cells. **b** Scheme of the de novo pyrimidine nucleotide synthesis pathway. **c** SDS-PAGE following WB analysis of MDA231 sublines for proteins of the de novo pyrimidine pathway. **d** Densitometric evaluation of the level of the CAD and DHODH proteins by WB. Relative isotopomer amounts (M+1) of CTP, CDP, UTP, and UDP were assessed by LC-MS/MS using [U-^{13}C] glucose (**e**) and [U-^{13}C] glutamine (**f**) as tracers. Data shown are mean values ± SD ($n \geq 3$); images are representative of at least three independent experiments. The symbol ** indicates differences with $p < 0.05$ and 'ns' indicates non-significant differences, as assessed by the two-tailed unpaired Student's *t*-test

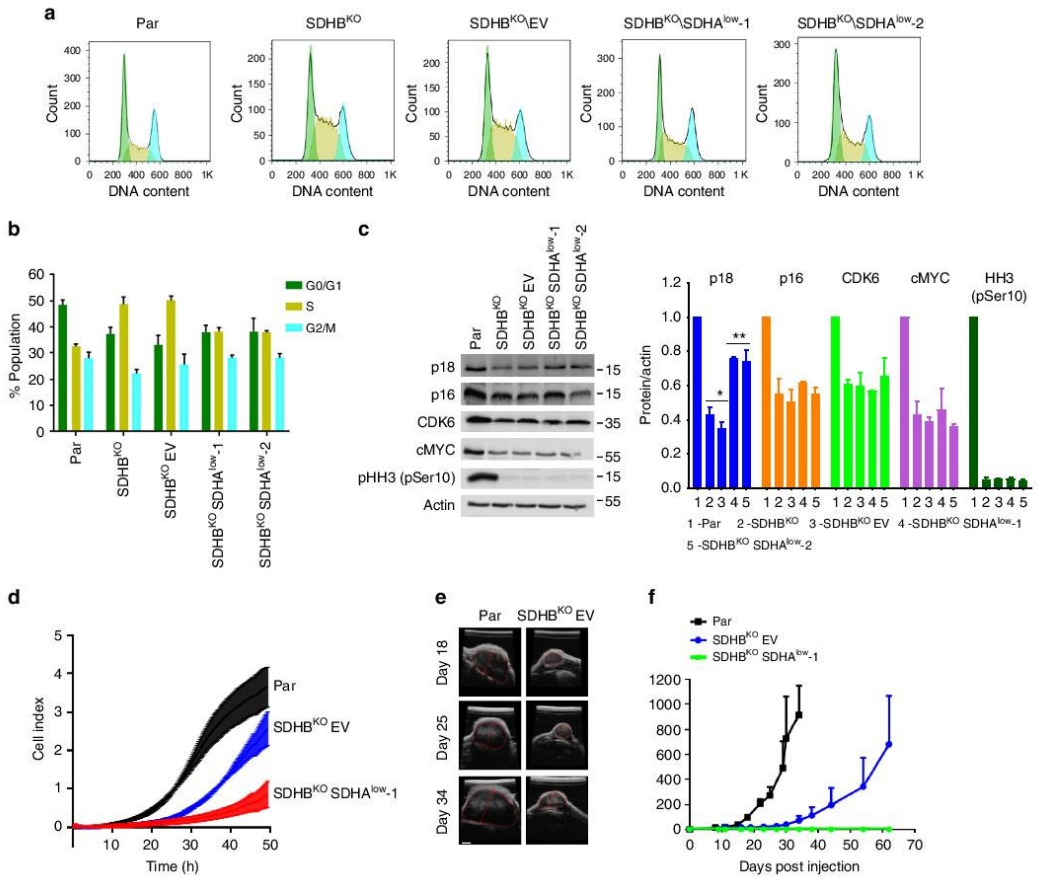

Fig. 5 CII_{low} supports growth of SDHB-deficient tumors. **a** MDA231 sublines were evaluated for cell cycle distribution using flow cytometry and staining with propidium iodide. Green color indicates cells in G0/G1 phase, yellow cells in S phase, and blue color cells in G2/M phase. **b** Histograms show evaluation of data in panel (**a**) representing 10^4 cells. **c** SDS-PAGE followed by WB analysis of proteins linked to the regulation of cell cycle progression and mitosis; images are representative of three independent experiments. **d** MDA231 sublines were assessed for migration capacity using the xCELLigence system. **e** MDA231 sublines were grafted in Balb-c nu/nu mice at 10^6 cells per animal, and tumor progression was visualized and quantified by ultrasound imaging. The bar represents the size of 2 mm. **f** Representative images of tumors derived from parental and $SDHB^{KO}$ EV cells. Data shown are mean values ± SD ($n = 5$ for **b** and **c**). The symbol * indicates significant differences compared to parental cells with $p < 0.05$ and ** significant differences compared to $SDHB^{KO}$ cells with $p < 0.05$, as assessed by the two-tailed unpaired Student's *t*-test

while fatty acid synthesis was not altered (Fig. 6c). Therefore, reduction of CII_{low} in $SDHB^{KO}SDHA^{low}$ cells seems to induce shuttling of pyruvate to pathways other than glycolysis without affecting fatty acid metabolism. Importantly, $SDHB^{KO}$EV cells had a higher level of succinate than parental cells, in agreement with previous reports for other $SDHB^{KO}$ models[40–44]. However, $SDHB^{KO}SDHA^{low}$ cells showed reduced succinate levels compared to $SDHB^{KO}$EV cells (Fig. 6c), suggesting a CII_{low}-dependent change in succinate metabolism, which may be due to activation of an alternative metabolic route of succinate utilization.

CII_{low} negatively regulates anabolic activity of TCA cycle. To obtain further insight into succinate metabolism as well as metabolism of other TCA cycle intermediates, we monitored the fate of [U-^{13}C] glucose and [U-^{13}C] glutamine in MDA231 sublines using LC-MS. The first cycle of TCA metabolism of [U-^{13}C] glucose via acetyl-CoA will generate four-carbon metabolites with two ^{13}C nuclei (m+2 isotopomer) through oxidative decarboxylation (Fig. 7a–f). Alternatively, an m+3 isotopomer can be formed if glucose enters the TCA cycle via the pyruvate carboxylase (PC) pathway (Fig. 7a). In agreement with the above NMR data (Fig. 6c), we observed increased m+2 isotopomers of succinate in $SDHB^{KO}$EV cells, and this was reduced in $SDHB^{KO}SDHA^{low}$ cells (Fig. 7d). Concurrently, the levels of m+2 isotopomers of aspartate, malate, and fumarate increased in $SDHB^{KO}SDHA^{low}$ cells compared to $SDHB^{KO}$EV cells (cf. Fig. 7e–g), suggesting more efficient consumption of succinate in cells with lower levels of CII_{low}. The increase in m+3

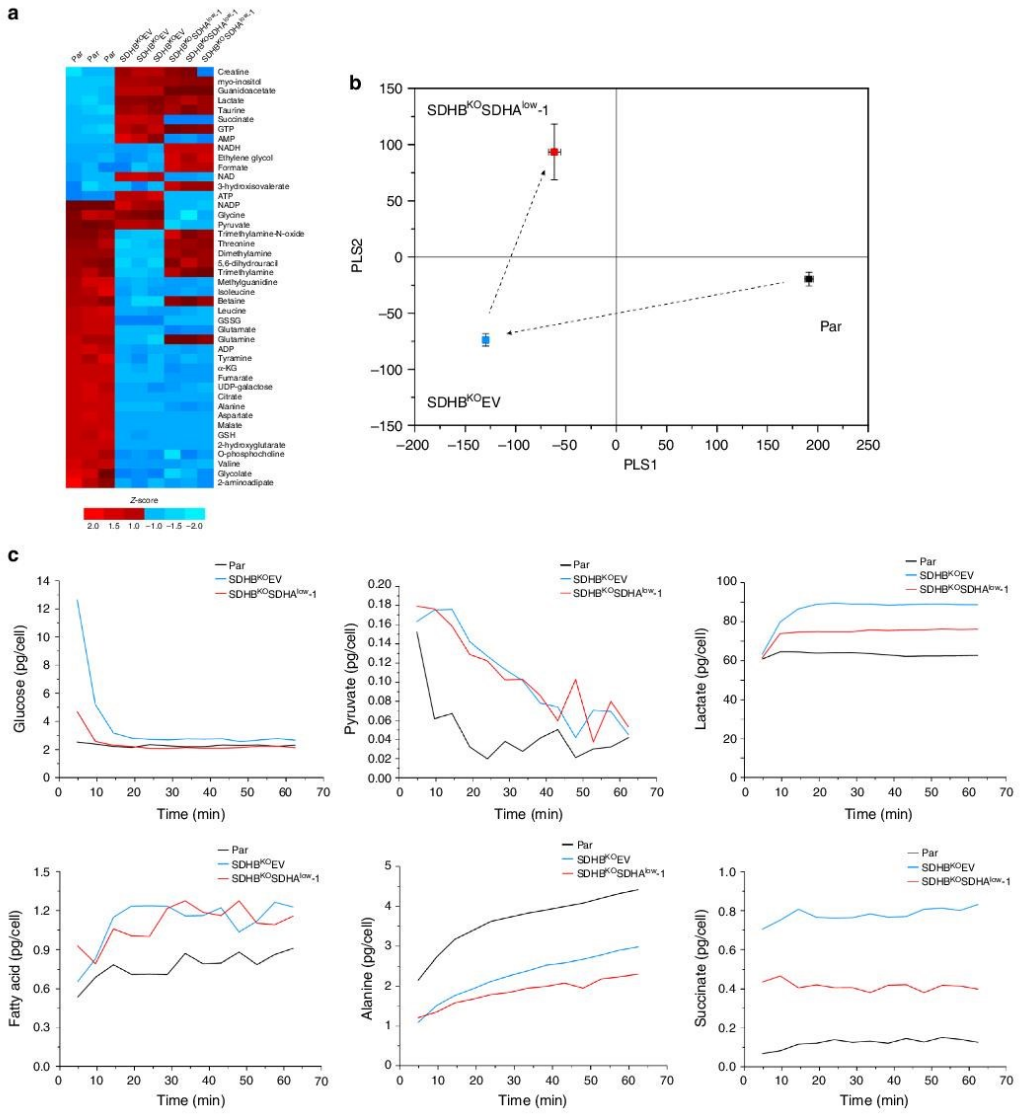

Fig. 6 CII_{low} modulates metabolome of MDA231 sublines. **a** The heat map was constructed with the *Z*-score of peak intensities of each metabolite identified by both 1D NMR and LC-MS/MS from parental, SDHB^{KO}EV, and SDHB^{KO}SDHA^{low} cells. The *Z*-score was obtained by dividing the difference between actual peak intensities and mean value by the standard deviation. **b** Score plot from partial least squares discriminant analysis (PLS-DA) on MDA231 sublines with the entire 1D NMR spectral data. PLS1 axis accounts for the major metabolic discrimination (63.5%), and the PLS2 16.8%. The symbols represent the mean score values from the multivariate analysis and the whiskers represent one standard deviation. Transitions are shown by arrows. **c** Real-time flux comparison in live parental, SDHB^{KO}EV, and SDHB^{KO}SDHA^{low} cells. Time-dependent metabolic changes were obtained using 2D in-cell NMR metabolomics approach. The absolute quantification is based on the level of ^{13}C carbon on a particular atom of metabolites detectable by NMR and was performed as described previously[39]. Although it is not possible to differentiate pre-existing natural abundance metabolites with those derived from ^{13}C-glucose with real-time NMR, the natural abundance of ^{13}C is 1% and pre-existing metabolites should not make significant contributions to the quantitation. Fatty acid represents the aggregate level of the ^{13}C-labeled CH_2 peak from free fatty acids at 1.36 and 32.0 ppm on the HSQC spectrum. Parental, black; SDHB^{KO}EV, blue; SDHB^{KO}SDHA^{low}, red

isotopomer of aspartate and malate in SDHB^{KO}SDHA^{low} cells, but not that of fumarate (Fig. 7e–g), suggests that the PC pathway may also contribute to the four-carbon metabolites in these cells.

[U-^{13}C] glutamine feeds carbons into the TCA cycle via α-ketoglutarate. A subsequent oxidative decarboxylation in the TCA cycle generates the m+4 isotopomer of succinate that can lead to m+4 aspartate (Fig. 7h, j–n). Succinate and aspartate m+2 isotopomers can also be formed through the TCA cycle if the m+4 succinate condenses with acetyl-CoA, followed by oxidative decarboxylation in subsequent TCA cycles (Fig. 7h, green). [U-^{13}C] glutamine can also contribute to formation of the m+3 isotopomer of aspartate via reductive carboxylation (Fig. 7h, red). In parental cell lines, we observed simultaneous oxidative decarboxylation and reductive carboxylation of glutamine as

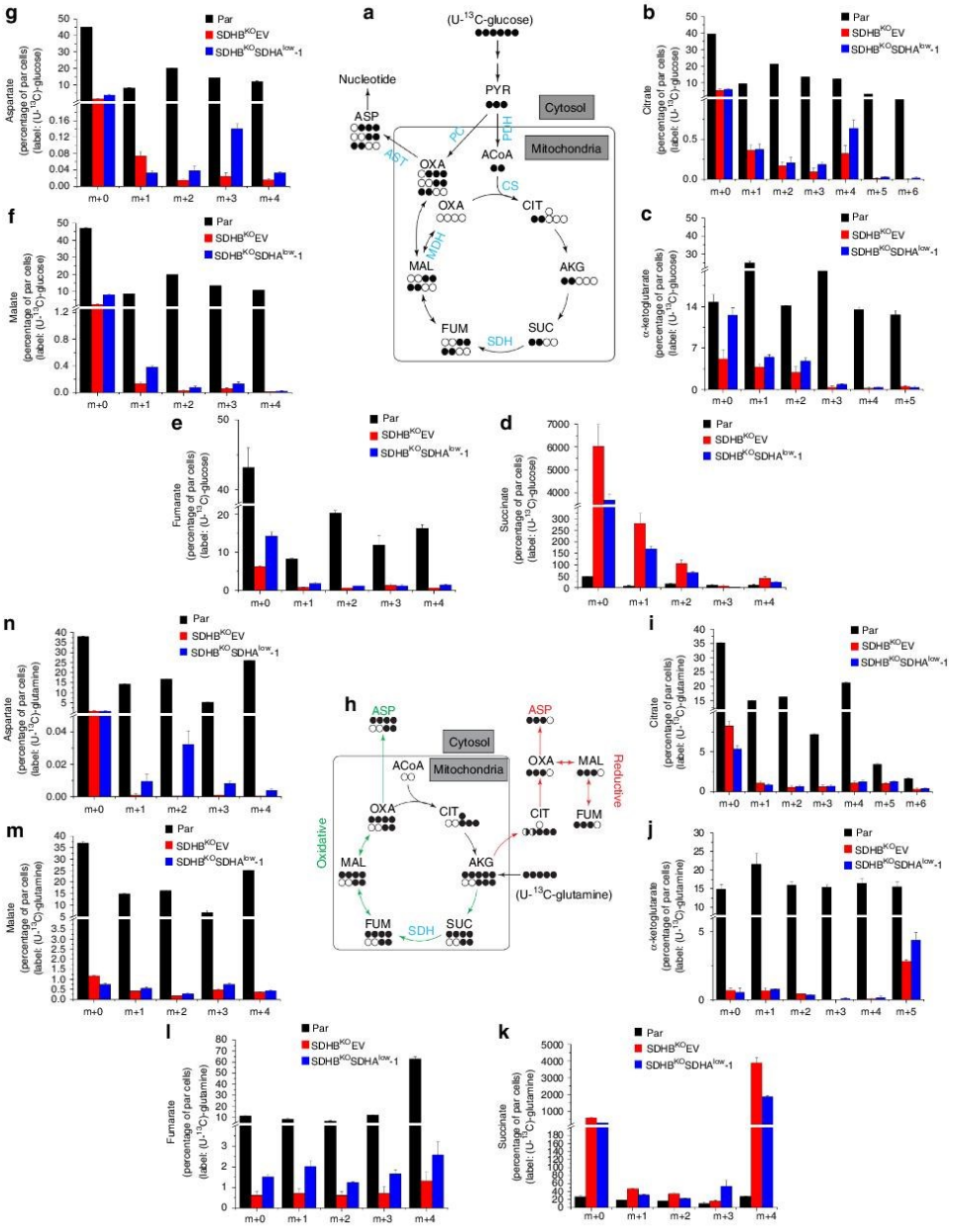

Fig. 7 CII_{low} restricts TCA-linked anabolism. **a** and **h**, Predicted labeling patterns of indicated metabolites from U-$^{13}C_6$-glucose (**a**) and from U-^{13}C-glutamine (**h**) (filled circles ^{13}C; open circles ^{12}C). The oxidative (green) and reductive (red) carboxylation pathways are indicated (**h**). Isotopologue distribution of intracellular citrate (**b**, **i**), a-ketoglutarate (**c**, **j**), succinate (**d**, **k**), fumarate (**e**, **l**), malate (**f**, **m**), and aspartate (**g**, **n**) after incubation for 24 h with 5 mM unlabeled glucose and 20 mM U-^{13}C-glucose or 4 mM U-^{13}C-glutamine, respectively. The data were obtained using LC-MS/MS analysis. The *Y* values are presented as the percent values of the sum of all the isotopologues per each metabolite in parental cells; 'm + ...' indicates the relevant isotopomer. Data are presented as mean ± SD, $n = 3$. PYR pyruvate, ACoA acetyl-CoA, CIT citrate, AKG α-ketoglutarate, SUC succinate, FUM fumarate, MAL malate, OXA oxaloacetate, ASP aspartate, PDH pyruvate dehydrogenase, PCX pyruvate carboxylase, CS citrate synthase, SDH succinate dehydrogenase, MDH malate dehydrogenase, AST aspartate transaminase

shown by high levels of incorporation of [U-^{13}C] glutamine into m+2, m+3, and m+4 aspartate isotopomers (Fig. 7n), consistent with reports on other cancer cells[45–48]. Significant formation of m+5 citrate isotopomer also suggests reductive carboxylation in parental cells (Fig. 7i). We observed very high absolute incorporation of [U-^{13}C] glutamine into m+4 succinate in $SDHB^{KO}$EV and a significant decrease to about half in $SDHB^{KO}SDHA^{low}$ cells (Fig. 7k). These were accompanied by higher incorporation of [U-^{13}C] glutamine into m+4 aspartate and fumarate in $SDHB^{KO}SDHA^{low}$ cells than $SDHB^{KO}$EV cells (Fig. 7l and n). Similar patterns were observed for the m+2 succinate isotopomer (Fig. 7k), although the absolute incorporation was much lower, probably due to a second round of the TCA cycle. These glutamine incorporation data clearly indicate that glutamine-derived succinate accumulates in $SDHB^{KO}$EV cells, whereas it is converted to fumarate and ultimately to aspartate more efficiently in $SDHB^{KO}SDHA^{low}$ cells.

Overall, both glucose and glutamine isotope incorporation experiments indicate a block in succinate metabolism in $SDHB^{KO}$EV cells that is at least partially lifted when the CII_{low} is depleted on the $SDHB^{KO}$ background (Supplementary Fig. 5a and c). This phenomenon is also consistent with the reverse trend of fumarate, whose level increased in $SDHB^{KO}SDHA^{low}$ cells (Supplementary Fig. 5b and d). This re-flow of succinate is suggested to induce redistribution of carbon atoms of glucose and glutamine to four-carbon metabolites leading to the recovery of synthesis of aspartate, a precursor for pyrimidine synthesis.

Previous studies showed that CII dysfunction caused by SDHB–SDHD mutations/deficiency results in accumulation of succinate[2,40,42–44,49,50]. Here we demonstrate that SDHA maintains high levels of succinate following CII dysfunction. Our data also implicate a switch of carbon metabolism in a CII_{low}-dependent manner, mainly from succinate accumulation to anabolic reactions, including synthesis of aspartate to produce pyrimidines. Further investigations are needed to elucidate the enzymatic activity of CII_{low}, especially in the context of succinate accumulation due to reductive carboxylation of glutamine (Fig. 7h).

CII_{low} is a feature of SDHB-deficient paraganglioma. To assess the clinical relevance of our findings, we inspected tumor tissue from paraganglioma patients with *SDHA* and *SDHB* mutations, as well as sporadic paraganglioma patients. We assessed tumors from six patients for the presence of SDHA and SDHB using immunohistochemistry. Fig. 8a shows that samples from patients with mutated *SDHB* exhibit high levels of SDHA, while tumor tissue derived from a patient with *SDHA* mutation showed very low levels of both SDHA and SDHB proteins. Next, tumors of these patients were evaluated for CII assembly and for the level of de novo pyrimidine synthesis. The rate-limiting trifunctional CAD protein as well as cell cycle regulatory proteins were assessed. NBGE showed high levels of CII_{low} and low levels of fully assembled CII in tumors with *SDHB* mutations, while tumors with *SDHA* mutations showed low levels of fully assembled CII and the absence of CII_{low} (Fig. 8b). Further, *SDHA*-mutated paragangliomas lacked FAD, a cofactor of CII associated with the catalytic subunit SDHA, while it was detected in sporadic paragangliomas or those with *SDHB* mutations. Paragangliomas with high levels of CII_{low} were found to contain low levels of CAD and p18 (Fig. 8c and d). These data are in agreement with results found for sublines of MDA231 cells with different CII assembly status (Fig. 2d; Fig. 4c; Fig. 5c). The data imply that CII_{low} may vary under different (patho)physiological conditions, giving our findings clinical relevance.

Discussion

In the present study, we show that alternative assembly of CII fine-tunes cellular metabolic homeostasis to compensate for chronic bioenergetic stress. SDHA is known to exist in a complex with other subunits of CII, with an overall molar mass of 124 kDa, migrating on native gels at ~140 kDa[22,51]. We found an assembly form of SDHA migrating at ~100 kDa (designated here as CII_{low}; Figs. 1 and 2), lacking SDHB and SDHC. This is consistent with previous studies using an experimental model of yeast, mammalian cell culture, and human pathological conditions showing that SDHA is stable in the absence of SDHB[40–44,52], although its biological function has never been investigated. In addition, CII_{low} is more prevalent when mtDNA is depleted or its expression is compromised (Fig. 1). This suggests biological relevance of CII_{low} with mtDNA mutations and under conditions that limit mitochondrial energy production. We propose that CII/CII_{low} has a role in mitochondria similar to that of pyruvate kinase 2 (PKM2), which changes its assembly from a highly active tetrameric to low-active dimeric form in response to different cellular signaling pathways. A switch from the tetrameric to dimeric form of PKM2 has profound consequences for cellular metabolism as well as proliferation in the context of diabetic nephropathy[53] and tumorigenic capacity of cancer cells[54–56].

The molecular weight of SDHA is about 70 kDa and thus there are likely to be other SDHA-interacting proteins in CII_{low} of approximately 100 kDa. To identify SDHA-interacting proteins, we used immunoprecipitation followed by MS analysis. This analysis, supported by WB, identified the assembly factors SDHAF2 and SDHAF4 as proteins that together with SDHA constitute CII_{low} accounting for its ~100 kDa mass (Supplementary Fig. 2). We have recently reported that SDHAF2 has redundant function in relation to CII activity in MDA231 cells[57]. While we do not know the function of SDHAF2 and SDHAF4 in CII_{low}, it is possible that these factors form a functional association with SDHA within CII_{low} and in the absence of the other three subunits (SDHB–D). The role of SDHAF2 and SDHAF4 in CII_{low} is the subject of current investigation.

To study the cellular function of CII_{low}, we established stable cellular models with three different assembly forms of SDHA (Fig. 2) and initially analyzed bioenergetics difference of these sublines. We found that $SDHB^{KO}$ cells with prominent presence of CII_{low} switched to low basal respiration with no spare respiratory capacity, indicating an energy stress situation. $SDHB^{KO}SDHA^{low}$ cells with depleted CII_{low} showed a bioenergetic pattern similar to that of $SDHB^{KO}$ cells (Fig. 3), indicating

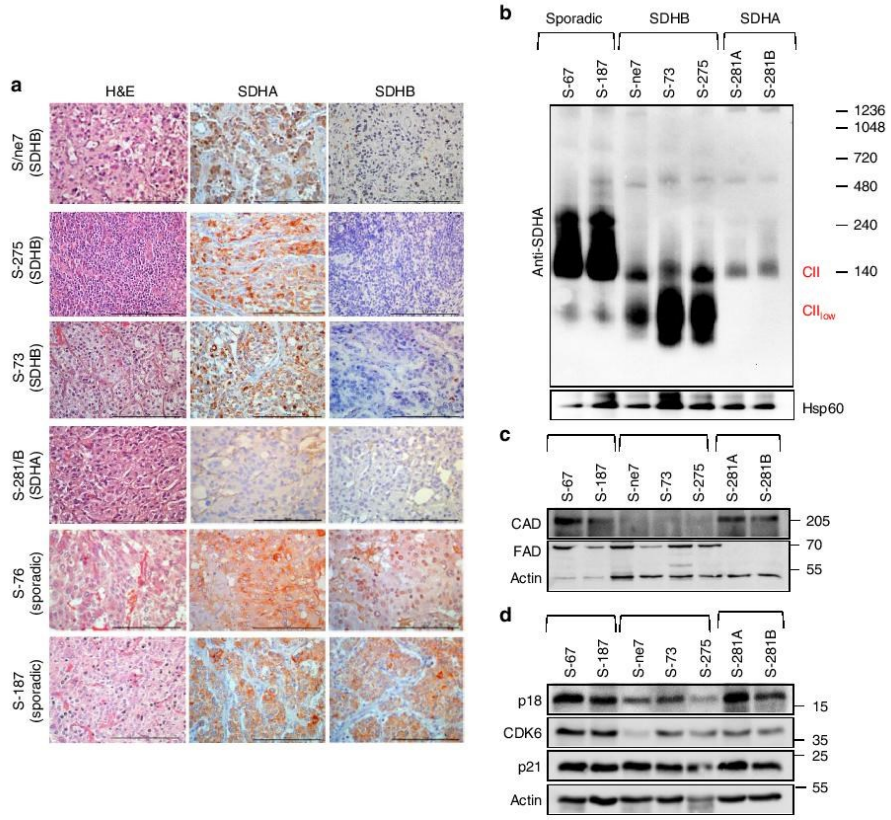

Fig. 8 CII assembly and de novo pyrimidine pathway in paragangliomas. **a** Histological examination of SDHA and SDHB expression from tumor tissue of paraganglioma patients with *SDHA* or *SDHB* mutations or with sporadic paragangliomas. Tissues were processed for H&E staining and immunohistochemistry using SDHA and SDHB IgGs. Representative images are collected using a 40× objective. Scale bars represent 100 µm. **b**–**d** Paraganglioma tissues, as shown, were assessed by WB following protein separation by NBGE for CII assembly using anti-SDHA IgG (**b**), and by SDS-PAGE for CAD and FAD (**c**) and for markers of cell cycle (**d**). Images are representative of three independent experiments

that CII_{low} plays only a minimal role in mitochondrial bioenergetics.

Label-free proteomic and pathway analysis allowed for identification of differences in the de novo pyrimidine pathway in MDA231 sublines. We found that CII_{low} abundance is inversely correlated with de novo pyrimidine pathway activity (Fig. 4), as exemplified by the steady-state level of CAD, a trifunctional and rate-limiting polypeptide in the pathway. The level of the CAD protein was reduced by approximately 60% in $SDHB^{KO}$ cells resulting in cell cycle arrest in the S-phase, and its re-expression in $SDHB^{KO}SDHA^{low}$ cells with depleted CII_{low} normalized cell cycle progression (Fig. 5). Recently, the de novo pyrimidine synthesis pathway has been shown to be essential in metabolic rewiring that modulates chemotherapy resistance of triple-negative breast cancer[58] and other neoplastic pathologies[59,60], supporting the notion that de novo pyrimidine synthesis improves plasticity of cancer cells at the expense of increased energy consumption. Further investigations will be needed to provide unequivocal evidence for a functional linkage between CII_{low} and pyrimidine biosynthesis. However, our data suggest that CII_{low} exerts its protective function not by modulating mitochondrial bioenergetics (i.e., OXPHOS), but through other mitochondria-related mechanisms, which are not yet fully defined but seem to involve energy conservation strategies such as a reduction of the de novo pyrimidine synthesis pathway. Therefore, we propose that restriction of this pathway and possibly of other energy-demanding processes by CII_{low} may provide a selective advantage under suboptimal nutrient conditions when bioenergetics is compromised, exemplified by increased cell death in galactose media and a the failure to form tumors in a mouse xenograft model (Fig. 5) when SDHB-deficient cells lose CII_{low}. In line with this, CII_{low} is less abundant in optimal physiological conditions and becomes the dominant SDHA form of CII during sub-optimal energy production (Fig. 1).

Our data suggest that deficiency of CII assembly and the shift of SDHA to CII_{low} modulates metabolism in response to compromised mitochondrial bioenergetics. It introduces checkpoints of cellular functions with high demands for energy, for example reducing formation of aspartate that is essential for pyrimidine nucleotide synthesis. This indicates that CII_{low} might be a sensor of bioenergetic stress, providing a feedback from OXPHOS to central carbon metabolism. Similarly, a number of proteins

capable of sensing mitochondrial energy production or metabolite levels that reflect energy status have been identified. AMP-activated protein kinase (AMPK) has been shown to sense the ratio of ATP to ADP and AMP level in order to initiate an energy compensating stress response[61,62]. Previous studies have also demonstrated that certain sirtuins are sensors of organelle energy production in relation to the NADH/NAD^+ ratio[63]. Recently the ubiqunol/ubiqunone ratio has been reported to sense mitochondrial energy production linked to the respiratory status[64]. Possible links between CII assembly forms and other sensors of mitochondrial bioenergetic dysfunction need to be further investigated. Merging these various individual components into a highly integrated regulatory system presents the next challenge.

Data shown here reveal that patients with *SDHB* and *SDHA* mutations have different CII assembly status. We found that CII_{low} is the remaining unit of CII present in patients with *SDHB* mutations, but is absent in patients with SDHA and sporadic mutations. In agreement with our cellular model of MDA231 sublines, patients that show high levels of CII_{low} also have reduced levels of the de novo pyrimidine synthesis regulatory enzyme CAD and the cell cycle modulator protein p18 (Fig. 8). Clinical data also indicate that SDHB mutation-associated paragangliomas are less proliferative but are associated with higher invasiveness and metastasis[42,65–67]. This may be one of the reasons why SDHA-deficient tumors are relatively rare, possibly due to an imbalance in energy and metabolic homeostasis. Thus, our data provide more detailed insights into established clinic-pathological features for incurable *SDHx*-related paragangliomas and may potentially serve as a diagnostic marker.

In summary, we found that following mtDNA depletion or SDHB deficiency, an alternative CII with different activity is formed. We suggest that the existence of CII_{low} in patients with *SDHB*-mutated paragangliomas may contribute to a cellular mechanism resulting in severe pathological outcomes, including enhanced migration and invasiveness. Hence, SDHA epitomizes a moonlighting protein, being an enzyme that is a baseline tumor suppressor but becomes a promoter of tumor growth in the context of bioenergetic deficiency.

Methods

Cells and transfection. MDA231 and MCF7 cells were obtained from the ATCC and cultured in DMEM (Life Technology) supplemented with 10% FCS and antibiotics plus antimycotics (Gibco). To generate $SDHB^{KO}$ cell lines, MDA231 cells were transfected with the TALEN construct obtained from Genecopoeia. Transfections were performed using Lipofectamine 2000 (Invitrogen) according to the manufacturer's instructions; transfectants were selected with hygromycin. Two shRNAs targeting the human *SDHA* gene and empty vector (EV) were purchased from OriGene. $SDHB^{KO}$ cells were transfected with the shRNA plasmids. After 36 h, cells were treated for 5 days with 0.8 µg/ml puromycin. Preparation of mtDNA-depleted cells ($4T1\rho^0$ and $MCF7\rho^0$) was accomplished by their long-term incubation with 50 µM EtBr[13,57]. Human SDHB was re-expressed in $SDHB^{KO}$ cells from the pLYS5-SDHB-Flag plasmid[68] (Addgene # 50055, a kind gift of Vamsi Mootha) using lentiviral transduction. Lentivirus particles were produced in Hek293T cells using second generation psPAX and pMD.2G plasmids and lipofection (Lipofectamine 3000, Invitrogen). Virus-containing media were collected after 48 h, centrifuged at 3000×*g* for 15 min and stored at −80 °C[69].

Proliferation, migration, and cell death assays. Parental, $SDHB^{KO}$EV, and $SDHB^{KO}SDHA^{low}$ cells were plated in a 24-well dish in DMEM. At indicated times, cell proliferation was assessed by crystal violet assay using a standard protocol. xCELLigence Real-Time Cellular Analysis system was used to evaluate cell proliferation in glucose- or galactose-containing medium and using dialyzed FBS (Gibco). For this, cells were seeded in 16-well E-plates (4 replications per cell type) as recommended by the manufacturer. For migration assays, cells were transferred to the CIM-16 plates and allowed to migrate toward FBS placed in the other compartment. Cell proliferation was monitored in real time using the xCELLigence instrument for 50 h, and the cell index was recorded every 5 min. Cell death was assessed using the standard annexin V/propidium iodide (PI) method.

siRNA transfections. Mouse Silencer-select pre-designed SDHA-, SDHB-, and SDHC-targeting siRNAs and non-silencing controls were obtained from Life Technologies. The sequences are as follows: SDHA target sequence-1 (s84146): GGA ACA CUC CAA AAA CAG Att; SDHA target sequence-2 (s211850): CCA GUU AUU UUG UGG AAU Att; SDHB target sequence-1 (s205969): GCU UUA AUC AAG AUC AAG Att; SDHB target sequence-2 (s205970): CCC UCU UCC ACA UAU GUA Utt; SDHC target sequence-1 (s82476): GAU CUA CUC GGC UAA GUU Utt; SDHC target sequence-2 (s205071): GAA CAC GAG UUC AAA CCG Utt. 4T1 cells were transiently transfected with 20 nM siRNA using Lipofectamine RNAiMAX transfection reagent (Invitrogen) according to the manufacturer's instructions and harvested for analysis 72 h after transfection.

Cell cycle analysis. Cells were harvested with trypsin, rinsed with PBS, fixed by drop-wise addition into 70% (v/v) ethanol and kept at −20 °C for at least 4 h. They were then centrifuged, rinsed in PBS, re-suspended in PBS containing 80 µg/ml RNase and 30 µg/ml of propidium iodide plus 100 µg/ml RNase A. After incubating for 30 min at room temperature, DNA content was assessed using the FACS Calibur flow cytometer (Becton Dickinson). Cell cycle distribution was estimated using the FlowJo software and the Watson distribution model.

Western blotting. Cells were lysed in 20 mM Tris (pH 8), 200 mM NaCl, 1 mM EDTA, 0.5% (v/v) NP-40, and 10% glycerol supplemented with protease inhibitors (Roche). After addition of the Laemmli solution to the samples, the proteins were separated by SDS-PAGE (8–15% gel) and then transferred to polyvinylidene difluoride (PVDF) membranes. After blocking with 5% non-fat milk, the blots were incubated with the primary antibodies overnight at 4 °C. The membranes were then treated with horseradish peroxidase-conjugated secondary antibodies for 2 h at room temperature, followed by visualization (SuperSignal West Pico Chemiluminescent Substrate, Pierce). The following antibodies were used in the study: SDHA (Abcam, ab14715; 1:2000); SDHB (Abcam, ab14714; 1:1000); SDHC (Abcam, ab155999; 1:1000); HSP60 (Abcam, ab137706; 1:2000; or Cell Signaling, 12165; 1:2000); CoxVa (Abcam, ab110262, 1:2000); NDUFA9 (Life Technologies/Thermo Fisher, 459100; 1:2000); Core I/UQCRC1 (Life Technologies/Thermo Fisher, 459140; 1:2000); NDUFV1 (Abcam, ab55535; 1:1000); NDUFS8 (Abcam, ab170936; 1:1000); SDHAF2 (Cell Signaling, 45849; 1:1000); SDHAF4 (Thermo Fisher, PA5-73014; 1:1000; or Sigma, HPA031824; 1:500); FAD (MyBioSource, MBS2015613; 1:500); HRP-conjugated tubulin (Thermo Scientific, MA5-16308-HRP; 1:2000); HRP-conjugated actin (Abcam, ab49900; 1:5000); actin (Abcam, ab14715 or 3700, or Cell Signaling, 4970 or 3700; all 1:3000); DHODH (Proteinech, 14877-1-AP; 1:500); CAD (Cell Signaling, 93925; 1:1000); phospho-Histone H3 (Ser10) (Cell Signaling, 3642; 1:1000); GAPDH (Cell Signaling, 8337; 1:3000). Uncropped western blots are in Supplementary Fig. 8.

Isolation of mitochondria and NBGE. Mitochondria were isolated using Dounce or Balch homogenizers, followed by standard differential centrifugation[13,50,70]. Experimental procedure and antibodies for NBGE were used as described previously[57,71]. In brief, digitonin-solubilised mitochondria were separated on NativePAGE Novex Bis-Tris 3–12% gradient gels. After electrophoresis, the gels were incubated in transfer buffer containing 0.1% SDS for 10 min and proteins were transferred to PVDF membranes probed with specific antibodies (all diluted 1:500, except for VDAC1 and HSP60 diluted 1:1000) against complex I (NDUFA9, ab14713, Abcam; or NDUFB8, ab110242, Abcam), CII (SDHA, 14715, Abcam), CIII (Core2, ab14745, Abcam), CIV (COXVa, ab110262, Abcam) and CV (ATP5A, ab14748, Abcam; or ATP5B, HPA001520, Sigma Aldrich), and VDAC1 (ab15895, Abcam) or HSP60 (12165S, Cell Signaling) as the loading control.

Evaluation of oxygen consumption rate. Cells were seeded into an XFp assay microplate (Agilent) 1 day prior to evaluation. On the day of the assay, the growth medium was replaced with the XF assay medium (Agilent) supplemented with glucose and glutamine. Oxygen consumption rate (OCR) measurements were made using the Seahorse Analyzer (Agilent) with sequential addition of oligomycin, FCCP, rotenone and antimycin A (using the Mitostress kit from Agilent) according to the manufacturer's protocol. OCR measurements were adjusted based on the cell number counted at the end of the experiment.

Respiration assays. Respiration was evaluated in digitonin-permeabilized MDA231 sublines and assessed as described previously.[72,73] In brief, the cells were trypsinized, washed with PBS, re-suspended at 1×10^6 cells per ml of the Mir05 medium (0.5 mM EGTA, 3 mM $MgCl_2$, 60 mM K-lactobionate, 20 mM taurine, 10 mM KH_2PO_4, 110 mM sucrose, 1 g/l essentially fatty acid-free bovine serum albumin, 20 mM Hepes, pH 7.1 at 30 °C) and transferred to the chamber of the Oxygraph-2k instrument (Oroboros). Respiration measurements were performed at 37 °C. Cells were permeabilized with 5 µg digitonin per 10^6 cells, followed by sequential additions of substrate and inhibitors. CI respiration was assessed in the presence of glutamate/malate and ADP, while CII respiration in the presence of succinate, ADP, and rotenone.

Xenograft experiments. All procedures with animals were performed according to the Institutional guidelines and ethical authorization by the Griffith University Animal Ethics Committee. MDA231 sublines were injected into the mammary fat pad of Balb-c nu/nu mice at 10^6 cells per animal. Tumor volume was quantified using the Vevo3100 USI system using a 30-µm resolution scan-head[70,74].

SWATH proteomic analysis. For proteomic analysis, cell pellets were lysed using 200 µl of sodium deoxycholate buffer (0.1% in 0.1 M triethyl ammonium bicarbonate). Following reduction with 5 mM dithiothretol and alkylation with 10 mM iodoacetamide, 100 µg of protein was digested with sequencing grade trypsin (Promega) at 37 °C for 16 h. The sample was acidified using formic acid and centrifuged for 10 min to remove the precipitated sodium deoxycholate salt. Tryptic peptides were recovered and fractionated using High pH Reversed-Phase Peptide Fractionation Kit (Pierce) according to manufacturer's instructions, with the exception that only six fractions were collected. To establish a reference spectral library for SWATH analysis, the fractionated sample was run by nanoLC-MS/MS using a 100 mm × 150 µm C18 column coupled to an Eksigent Ultra system over 90 min as described[75] using Information-Dependent Acquisition (IDA) on a 5600 + Triple TOF mass spectrometer (Sciex, Framingham, MA) using the Top 10 most intense multiply charged ions. MS/MS was conducted for 50 ms over the 100–1500 *m/z* range. Peptides were identified using ProteinPilot (v4.2) (Sciex) to search the UniProt Human protein database (20,198 entries, downloaded June 2015) and false-discovery controlled by searching a reversed-decoy Human database of identical size, selecting >99% confidence for protein identification. The Paragon group file was imported into PeakView software 2.1 using the SWATH MicroApp 2.0 to generate a sample specific spectral library.

For SWATH data acquisition of individual samples, we used the same MS setup but adjusted the method to use 60 variable *m/z* windows (400–1250 *m/z*) for precursor ion selection. The MS/MS spectra were accumulated for 60 ms in the *m/z* 350–1500 *m/z* range.

To extract SWATH peak areas with PeakView software 2.1, we carried out retention time calibration with endogenous peptides and data processing using following settings; 100 maximal peptides per protein, maximal 6 transitions per peptide, peptide confidence threshold of 99%, transition false discovery rate <1%, 10 min extraction window, and fragment extraction tolerance of 75 ppm, exclusion of shared peptides. The protein peak areas were normalized to the total peak area and log-transformed peak areas and subjected to Student's *t*-test to compare relative protein peak area between samples. Proteins were considered to be differentially expressed with $p < 0.05$ and protein fold change was ±1.5 fold. DAVID[76] was used for functional enrichment analysis. The Benjamini method (adjusted *p* value) was used to control the family-wide false discovery rate for enrichment analysis.

Identification of SDHA-interacting proteins. Mitochondria isolated from $SDHB^{KO}$ cell stably expressing SDHA-FLAG and empty vector were lysed using membrane solubilization buffer (1% *n*-dodecyl β-D-maltoside, 20 mM Tris-HCl, pH 7.4, 0.1 mM EDTA, 100 mM NaCl, 10% glycerol) supplemented with protease inhibitors (Roche). Protein concentrations were determined using the BCA protein assay kit. Equal amounts of protein were incubated with 20 µl anti-FLAG M2 agarose beads (Sigma) overnight at 4 °C. Beads were washed three times with the membrane solubilization buffer. The proteins bound to the beads were then eluted with 2× SDS lysis buffer and separated by 15% SDS-PAGE followed by silver staining (Mass spectrometry compatible, Life Technologies). Protein bands from control and treatment lanes were subjected to tryptic digest and analyzed by mass spectrometry.

Sample preparation for NMR spectroscopy and LC-MS. Metabolites were extracted from parental, $SDHB^{KO}$EV, and $SDHB^{KO}SDHA^{low}$ cells (3×10^6 cells) with 400 µl of mixture composed of methanol, acetonitrile, and distilled water (5:3:2). The samples were centrifuged at 15,000×*g* for 20 min at 4 °C. The supernatant was collected, divided into two portions at the ratio of 1:5 for LC-MS and NMR analysis, and dried with a vacuum centrifuge (Vision). The pellets for LC-MS were dissolved with 30 µl mixture of HPLC-grade acetonitrile and water (1:1), and those for NMR with 500 µl buffer composed of 2 mM Na_2HPO_4 and 5 mM NaH_2PO_4 in D_2O with 0.025% TSP (trimethylsilylpropionic acid sodium salt–D_4) as an internal standard. For the isotopologue distribution analysis, these cells were cultured in glucose and glutamine-free DMEM media (Gibco) supplemented with 10% dialyzed FBS (Welgene, Daegu, Korea), 10% D_2O, 5 mM unlabeled glucose, and 20 mM U-$^{13}C_6$-labeled glucose (Cambridge Isotope Laboratories) or 4 mM U-$^{13}C_5$-labeled glutamine (Cambridge Isotope Laboratories) for 24 h before metabolites extraction, respectively.

Measurement and analysis for NMR spectroscopy and LC-MS. Untargeted metabolomic profiling was performed using NMR, and targeted profiling by LC-MS multiple reaction monitoring for metabolites that are not readily discernible by NMR. Metabolites detected by both methods, such as succinate and glutamate, exhibited consistent results. 1D NMR spectra were obtained using a 500-MHz Bruker Avance spectrometer equipped with a cryogenic triple resonance probe (KBSI). For the pulse program, 'noesygppr1d' was used with 64 scans, and the final spectra were constructed to 16K points. The metabolites were identified with Chenomx spectral database (Edmonton, Alberta, Canada) and comparison with standard compounds[39]. LC-MS data were obtained with an LTQ XL high performance linear ion trap mass spectrometer (Thermo Fisher Scientific) equipped with an electrospray ionization source. The operating conditions of the mass spectrometer were as follows: 5 kV of ion spray voltage, heated capillary temperature of 275 °C, and sheath gas (nitrogen), auxiliary gas (nitrogen), and sweep gas (nitrogen) pressures of 35, 10, and 2 (arbitrary units), respectively. Full scanning analyses were performed in the range of *m/z* 85–1000, and a 35-V normalized collision energy was used for MS/MS. Mobile phases were 10 mM ammonium carbonate (pH 9.1) in distilled water (A) and acetonitrile (B), and the flowrate was 0.15 ml/min. The gradient scheme was as follows: 80% B at 0 min, 35% B at 10 min, 5% B at 12 min, 5% B at 25 min, 80% B at 25.1 min, and 80% B at 35 min. The ZicpHilic Polymeric Beads Peek Column (150 × 2.1 mm, 5 µm; Merck) was used at 35 °C, and the autosampler temperature was set at 4 °C. The peak areas of parental ion and its isotopologues were measured using Xcalibur (Thermo Fisher Scientific). The metabolites were identified by m/z values and MS/MS fragmentation patterns from Human Metabolome Database (HMDB) and METLIN databases and also by comparison with standard compounds[77]. For multivariate analysis, the NMR data were Fourier-transformed, phase-corrected, and baseline-corrected manually using MestReNova (Mestrelab Research, Santiago de Compostela, Spain). The signal intensities were normalized against the intensity of the 0.025% TSP signal at 0 ppm and total area values. The processed NMR data were saved into a text file and binned at a 0.004-ppm interval. The water region (4.66–5.0) was excluded from the spectra. The binning and normalization were performed using a Perl software written in-house[78]. The region corresponding to water (4.66–5.0 ppm) was removed from the spectra, and the data were imported into SIMCA-P software (Umetrics) for PLS-DA. The heat map was constructed with a relative *Z*-score of peak area of each metabolite identified by NMR and LC-MS.

RNA sequence analysis. RNA was isolated using RNAzol (Molecular Research Center) according to the manufacturer's instructions. RNA was dissolved in the TE buffer (Thermofisher), and remaining DNA contamination was removed using DNAse I (Sigma-Aldrich) for 30 min. To clean RNA, the same volume of 8 M LiCl (Sigma-Aldrich) was added and incubated overnight at −20 °C. Samples were centrifuged for 30 min at 16,100×*g*/2 °C; the supernatant was removed and the pellet washed twice in 80% ethanol, followed by centrifugation as above. The remaining ethanol was evaporated at 65 °C for 10 min, and RNA was dissolved in 20 µl of TE buffer. Total RNA concentration was measured by Nanodrop 2000, and its quality was assessed by the Fragment Analyzer (Advanced Analytical) using Standard Sensitivity RNA Analysis Kit (Advanced Analytical). The libraries were prepared from 2 µg of total RNA using QuantSeq 3'mRNA-Seq Library Prep Kit FWD for Illumina (Lexogen), pooled and sequenced on MiSeq v3 kit in the 150 bp SE mode.

About 2 million reads per sample were obtained, and low-quality reads were filtered out using TrimmomaticSE (v. 0.36[79]) with parameters "trimmomatic/TRIM_MDA_K4_1_sequence.fastq CROP:165 HEADCROP:12 ILLUMINACLIP:~/Lexogen_quantseq.fa:2:30:10 LEADING:3 TRAILING:3 SLIDINGWINDOW:4:15 MINLEN:36". Ribosomal and mitochondrial RNA reads were removed using Sortmerna (v 2.1b[80]) using default parameters. The remaining reads were aligned to the Human Genome Version GRCh38.87 and count tables were generated using STAR (v 2.5.2b[81,82]). Differentially expressed genes (DEGs) were analyzed by means of DESeq2 (v 1.18.0,[82]) using the default function "DESeq" without altered parameters. Result tables were generated as contrast between the $SDHB^{KO}$ and parental, $SDHB^{KO}SDHA^{low}$ and parental, and $SDHB^{KO}$ and $SDHB^{KO}SDHA^{low}$ cells. Genes with padj <0.1 for at least one pair of comparisons were chosen as DEGs. The function "plotPCA" from DESeq2 package with default parameters was used for PCA analysis. The heat-map was created from rlog transformed count data after subtraction of their mean values for every DEG. Altogether, we identified 523 significantly changed genes out of the total number of 7587 detected genes (DESeq2 BaseMean >5). The data have been deposited in NCBI's Gene Expression Omnibus and are accessible through GEO Series accession number GSE108938.

For gene set enrichment analysis, DEGs were filtered and used for clustering and ontology analysis. The normalized counts of these genes for all biological replicates and cell lines (parental–MDA231, $SDHB^{KO}$–SHB, and $SDHB^{KO}SDHA^{low}$–SH1) were used to analyze for patterns of expression across the three cell lines. The data were first normalized across cell lines by dividing the mean of the replicates by the sum of the mean of the replicates. The R package optCluster (R ver. 3.4.3) was then used to determine the best clustering algorithm among agnes, clara, diana, hierarchical, kmeans, pam, and sota clustering methods using the validation methods connectivity, Dunn index and silhouette width, and the number of clusters set to ten[83]. Clusters that showed similar expression profiles were then merged.

Gene ontology was performed on the genes from each unique cluster, using the R package gprofiler, to identify significantly (p-value < 0.05) enriched GO terms[84]. The genes were analyzed with no specified ranking while the gSCS (Set Counts and Sizes) algorithm was used to determine the significance threshold. All identified genes from the RNASeq were used as background. GO annotations inferred by in silico methods were included in the analysis.

After the genes were linked to their appropriate GO terms, REVIGO was used to cluster similar GO terms together while using the *p*-value output from gprofiler to create a ranked list[85]. A similarity of 0.7 using the SimRel semantic similarity method was used to group similar GO terms and the UniProt database (15 March 2017) was used to find the relevant GO term sizes. Output from REVIGO was visualized as treemaps.

2D in-cell NMR analysis. Six plates of 70% confluent cultured cells were harvested with centrifugation. After re-suspending the cells with 5 ml DPBS, the cells were counted and 3×10^7 cells were transferred into a fresh tube. After centrifugation, the harvested cells were re-suspended in 500 µl glucose-free DMEM media (Gibco) supplemented with 10% dialyzed FBS, 25 mM U-$^{13}C_6$-labeled glucose, and 10% D_2O. The cells were spun in an NMR (30 g, 100 s) to allow sedimentation, enough to cover the active region of the NMR detection coil. ^1H-^{13}C Heteronuclear Single Quantum Coherence (HSQC) NMR spectra were measured using the 800-MHz Bruker Avance spectrometer equipped with a cryogenic triple resonance probe (Seoul National University). The dataset comprises 1024 × 128 points for direct and indirect dimensions, respectively. The time course spectral measurement was obtained at 310 K for 24 time points, with each experiment lasting for 288 s (13 points). Each metabolite was identified by spiking the standard compound.

Transmission electron microscopy. TEM was accomplished as follows. Cells were grown on cover-slips, fixed with 2% glutaraldehyde (Agar Scientific) and post-fixed with 1% OsO_4 made up in Sorensen's phosphate buffer (0.1 M, pH 7.2–7.4), dehydrated, and embedded in Epon-Durkupan (Sigma-Aldrich). Ultrathin sections (~70–90 nm) were cut, contrasted with uranyl acetate (Agar Scientific), and examined in the Morgagni 268 transmission electron microscope (FEI) at 80 kV and in the TECNAI G2 20 LaB6 electron microscope (FEI) at 200 kV. Images were captured with Mega View III CCD camera (Olympus Soft Imaging Solutions).

Paraganglioma patients. Tumor tissue from 6 patients (3 with *SDHB* mutations, 1 with *SDHA* mutation, 2 sporadic) was used in this study. Tumor tissue was obtained during surgery at the National Institutes of Health (NIH). Genetic testing was performed by NIH in collaboration with the Mayo Clinic (Rochester, MN, USA) or the results were sent from external facilities to the NIH. Expression of SDHB and SDHA proteins was also evaluated by immunohistochemistry as previously described[86]. Signed written consent was obtained from all patients prior to any experimental work. The use of patient samples was allowed by the Eunice Kennedy Shriver NICHD IRB (Ethics Approval #00-CH-0093). The tumor samples examined were as follows (Sample code, affected subunit, DNA base pair change, protein amino acid change): S/ne7, SDHB, c.183T>G, p.Tyr61X; S-275, SDHB, c.526G>T, p.Glu17X; S-73, SDHB, c.268C>T, p.Arg90X; S-281 A/B, SDHA, c.91C>T, p.Arg31X; S-187, Sporadic, no CII subunit affected; S-76, Sporadic, no CII subunit affected.

Statistical evaluation. Unless stated otherwise, data are mean values ± SD of at least three independent experiments. In mouse experiments, groups of 6 animals were used, unless stated otherwise. The two-tailed unpaired Student's *t*-test was used to assess statistical significance with $p < 0.05$ being regarded as significant. Images are representative of three independent experiments.

Data availability. RNA sequence data are filed in NCBI's Gene Expression Omnibus and are accessible through GEO Series accession number GSE108938. The mass spectrometry proteomics data have been deposited to the ProteomeXchange Consortium via the PRIDE partner repository with the dataset identifier PXD009656. All other data that support findings of this study are available from the corresponding authors upon request.

Received: 3 September 2017 Accepted: 7 May 2018
Published online: 07 June 2018

References

1. Jones, R. G. & Thompson, C. B. Tumor suppressors and cell metabolism: a recipe for cancer growth. *Genes Dev.* **23**, 537–548 (2009).
2. King, A., Selak, M. A. & Gottlieb, E. Succinate dehydrogenase and fumarate hydratase: linking mitochondrial dysfunction and cancer. *Oncogene* **25**, 4675–4682 (2006).
3. Selak, M. A. et al. Succinate links TCA cycle dysfunction to oncogenesis by inhibiting HIF-alpha prolyl hydroxylase. *Cancer Cell.* **7**, 77–85 (2005).
4. Bezawork-Geleta, A., Rohlena, J., Dong, L., Pacak, K. & Neuzil, J. Mitochondrial Complex II: at the Crossroads. *Trends Biochem. Sci.* **42**, 312–325 (2017).
5. Fendt, L. et al. Accumulation of mutations over the entire mitochondrial genome of breast cancer cells obtained by tissue microdissection. *Breast Cancer Res. Treat.* **128**, 327–336 (2011).
6. Parrella, P. et al. Detection of mitochondrial DNA mutations in primary breast cancer and fine-needle aspirates. *Cancer Res.* **61**, 7623–7626 (2001).
7. Tseng, L. M. et al. Mitochondrial DNA mutations and mitochondrial DNA depletion in breast cancer. *Genes Chromosomes Cancer* **45**, 629–638 (2006).
8. Wallace, D. C. Mitochondria and cancer. *Nat. Rev. Cancer* **12**, 685–698 (2012).
9. McKenzie, M., Lazarou, M., Thorburn, D. R. & Ryan, M. T. Mitochondrial respiratory chain supercomplexes are destabilized in Barth Syndrome patients. *J. Mol. Biol.* **361**, 462–469 (2006).
10. Lapuente-Brun, E. et al. Supercomplex assembly determines electron flux in the mitochondrial electron transport chain. *Science* **340**, 1567–1570 (2013).
11. Acin-Perez, R., Fernandez-Silva, P., Peleato, M. L., Perez-Martos, A. & Enriquez, J. A. Respiratory active mitochondrial supercomplexes. *Mol. Cell* **32**, 529–539 (2008).
12. Kovarova, N. et al. High molecular weight forms of mammalian respiratory chain complex II. *PLoS ONE* **8**, e71869 (2013).
13. Tan, A. S. et al. Mitochondrial genome acquisition restores respiratory function and tumorigenic potential of cancer cells without mitochondrial DNA. *Cell Metab.* **21**, 81–94 (2015).
14. Plass, C. et al. Mutations in regulators of the epigenome and their connections to global chromatin patterns in cancer. *Nat. Rev. Genet.* **14**, 765–780 (2013).
15. Maiuri, M. C. & Kroemer, G. Essential role for oxidative phosphorylation in cancer progression. *Cell Metab.* **21**, 11–12 (2015).
16. Leach, K. L. et al. The site of action of oxazolidinone antibiotics in living bacteria and in human mitochondria. *Mol. Cell* **26**, 393–402 (2007).
17. Prezant, T. R. et al. Mitochondrial ribosomal RNA mutation associated with both antibiotic-induced and non-syndromic deafness. *Nat. Genet.* **4**, 289–294 (1993).
18. Ramachandran, A. et al. Inhibition of mitochondrial protein synthesis results in increased endothelial cell susceptibility to nitric oxide-induced apoptosis. *Proc. Natl Acad. Sci. USA* **99**, 6643–6648 (2002).
19. Maio, N. et al. Disease-causing SDHAF1 mutations impair transfer of Fe-S clusters to SDHB. *Cell Metab.* **23**, 292–302 (2016).
20. van Nederveen, F. H. et al. An immunohistochemical procedure to detect patients with paraganglioma and phaeochromocytoma with germline SDHB, SDHC, or SDHD gene mutations: a retrospective and prospective analysis. *Lancet Oncol.* **10**, 764–771 (2009).
21. Bezawork-Geleta, A., Saiyed, T., Dougan, D. A. & Truscott, K. N. Mitochondrial matrix proteostasis is linked to hereditary paraganglioma: LON-mediated turnover of the human flavinylation factor SDH5 is regulated by its interaction with SDHA. *FASEB J.* **28**, 1794–1804 (2014).
22. Sun, F. et al. Crystal structure of mitochondrial respiratory membrane protein complex II. *Cell* **121**, 1043–1057 (2005).
23. Robinson, B. H., Petrova-Benedict, R., Buncic, J. R. & Wallace, D. C. Nonviability of cells with oxidative defects in galactose medium: a screening test for affected patient fibroblasts. *Biochem. Med. Metab. Biol.* **48**, 122–126 (1992).
24. Benard, G. & Rossignol, R. Ultrastructure of the mitochondrion and its bearing on function and bioenergetics. *Antioxid. Redox Signal.* **10**, 1313–1342 (2008).
25. Stroud, D. A., Formosa, L. E., Wijeyeratne, X. W., Nguyen, T. N. & Ryan, M. T. Gene knockout using transcription activator-like effector nucleases (TALENs) reveals that human NDUFA9 protein is essential for stabilizing the junction between membrane and matrix arms of complex I. *J. Biol. Chem.* **288**, 1685–1690 (2013).
26. Oostveen, F. G., Au, H. C., Meijer, P. J. & Scheffler, I. E. A Chinese hamster mutant cell line with a defect in the integral membrane protein CII-3 of complex II of the mitochondrial electron transport chain. *J. Biol. Chem.* **270**, 26104–26108 (1995).
27. Housley, S. L. et al. Renal carcinoma with giant mitochondria associated with germ-line mutation and somatic loss of the succinate dehydrogenase B gene. *Histopathology* **56**, 405–408 (2010).
28. Rost, H. L. et al. OpenSWATH enables automated, targeted analysis of data-independent acquisition MS data. *Nat. Biotechnol.* **32**, 219–223 (2014).
29. Ghazalpour, A. et al. Comparative analysis of proteome and transcriptome variation in mouse. *PLoS Genet.* **7**, e1001393 (2011).
30. Huang, S. et al. Complementary iTRAQ proteomics and RNA-seq transcriptomics reveal multiple levels of regulation in response to nitrogen starvation in Synechocystis sp. PCC 6803. *Mol. Biosyst.* **9**, 2565–2574 (2013).
31. Cenik, C. et al. Integrative analysis of RNA, translation, and protein levels reveals distinct regulatory variation across humans. *Genome Res.* **25**, 1610–1621 (2015).
32. Liu, Y., Beyer, A. & Aebersold, R. On the dependency of cellular protein levels on mRNA abundance. *Cell* **165**, 535–550 (2016).
33. Bauernfeind, A. L. & Babbitt, C. C. The predictive nature of transcript expression levels on protein expression in adult human brain. *BMC Genomics* **18**, 322 (2017).
34. Mitchell, A. D. & Hoogenraad, N. J. De novo pyrimidine nucleotide biosynthesis in synchronized rat hepatoma (HTC) cells and mouse embryo fibroblast (3T3) cells. *Exp. Cell Res.* **93**, 105–110 (1975).

35. Sigoillot, F. D., Berkowski, J. A., Sigoillot, S. M., Kotsis, D. H. & Guy, H. I. Cell cycle-dependent regulation of pyrimidine biosynthesis. *J. Biol. Chem.* **278**, 3403–3409 (2003).
36. Lane, A. N. & Fan, T. W. Regulation of mammalian nucleotide metabolism and biosynthesis. *Nucleic Acids Res.* **43**, 2466–2485 (2015).
37. Vander Heiden, M. G., Cantley, L. C. & Thompson, C. B. Understanding the Warburg effect: the metabolic requirements of cell proliferation. *Science* **324**, 1029–1033 (2009).
38. Ackerman, D. & Simon, M. C. Hypoxia, lipids, and cancer: surviving the harsh tumor microenvironment. *Trends Cell Biol.* **24**, 472–478 (2014).
39. Wen, H., An, Y. J., Xu, W. J., Kang, K. W. & Park, S. Real-time monitoring of cancer cell metabolism and effects of an anticancer agent using 2D in-cell NMR spectroscopy. *Angew. Chem. Int. Ed. Engl.* **54**, 5374–5377 (2015).
40. Killian, J. K. et al. Succinate dehydrogenase mutation underlies global epigenomic divergence in gastrointestinal stromal tumor. *Cancer Discov.* **3**, 648–657 (2013).
41. Kitazawa, S. et al. Succinate dehydrogenase B-deficient cancer cells are highly sensitive to bromodomain and extra-terminal inhibitors. *Oncotarget* **8**, 28922–28938 (2017).
42. Letouze, E. et al. SDH mutations establish a hypermethylator phenotype in paraganglioma. *Cancer Cell* **23**, 739–752 (2013).
43. Lussey-Lepoutre, C. et al. Loss of succinate dehydrogenase activity results in dependency on pyruvate carboxylation for cellular anabolism. *Nat. Commun.* **6**, 8784 (2015).
44. Cardaci, S. et al. Pyruvate carboxylation enables growth of SDH-deficient cells by supporting aspartate biosynthesis. *Nat. Cell Biol.* **17**, 1317–1326 (2015).
45. DeBerardinis, R. J. & Chandel, N. S. Fundamentals of cancer metabolism. *Sci. Adv.* **2**, e1600200 (2016).
46. Boroughs, L. K. & DeBerardinis, R. J. Metabolic pathways promoting cancer cell survival and growth. *Nat. Cell Biol.* **17**, 351–359 (2015).
47. Yang, C. et al. Glutamine oxidation maintains the TCA cycle and cell survival during impaired mitochondrial pyruvate transport. *Mol. Cell* **56**, 414–424 (2014).
48. Mullen, A. R. et al. Reductive carboxylation supports growth in tumour cells with defective mitochondria. *Nature* **481**, 385–388 (2011).
49. Lendvai, N. et al. Succinate-to-fumarate ratio as a new metabolic marker to detect the presence of SDHB/D-related paraganglioma: initial experimental and ex vivo findings. *Endocrinology* **155**, 27–32 (2014).
50. Kluckova, K. et al. Ubiquinone-binding site mutagenesis reveals the role of mitochondrial complex II in cell death initiation. *Cell Death Dis.* **6**, e1749 (2015).
51. Cecchini, G. Function and structure of complex II of the respiratory chain. *Annu. Rev. Biochem.* **72**, 77–109 (2003).
52. Hao, H. X. et al. SDH5, a gene required for flavination of succinate dehydrogenase, is mutated in paraganglioma. *Science* **325**, 1139–1142 (2009).
53. Qi, W. et al. Pyruvate kinase M2 activation may protect against the progression of diabetic glomerular pathology and mitochondrial dysfunction. *Nat. Med.* **23**, 753–762 (2017).
54. Ye, J. et al. Pyruvate kinase M2 promotes de novo serine synthesis to sustain mTORC1 activity and cell proliferation. *Proc. Natl Acad. Sci. USA* **109**, 6904–6909 (2012).
55. Schulze, A. & Harris, A. L. How cancer metabolism is tuned for proliferation and vulnerable to disruption. *Nature* **491**, 364–373 (2012).
56. Christofk, H. R., Vander Heiden, M. G., Wu, N., Asara, J. M. & Cantley, L. C. Pyruvate kinase M2 is a phosphotyrosine-binding protein. *Nature* **452**, 181–186 (2008).
57. Bezawork-Geleta, A., Dong, L., Rohlena, J. & Neuzil, J. The assembly factor SDHAF2 is dispensable for flavination of the catalytic subunit of mitochondrial complex II in breast cancer cells. *J. Biol. Chem.* **291**, 21414–21420 (2016).
58. Brown, K. K., Spinelli, J. B., Asara, J. M. & Toker, A. Adaptive reprogramming of De Novo pyrimidine synthesis is a metabolic vulnerability in triple-negative breast cancer. *Cancer Discov.* **7**, 391–399 (2017).
59. Mathur, D. et al. PTEN regulates glutamine flux to pyrimidine synthesis and sensitivity to dihydroorotate dehydrogenase inhibition. *Cancer Discov.* **7**, 380–390 (2017).
60. Rabinovich, S. et al. Diversion of aspartate in ASS1-deficient tumours fosters de novo pyrimidine synthesis. *Nature* **527**, 379–383 (2015).
61. Zong, H. et al. AMP kinase is required for mitochondrial biogenesis in skeletal muscle in response to chronic energy deprivation. *Proc. Natl Acad. Sci. USA* **99**, 15983–15987 (2002).
62. Hardie, D. G., Ross, F. A. & Hawley, S. A. AMPK: a nutrient and energy sensor that maintains energy homeostasis. *Nat. Rev. Mol. Cell Biol.* **13**, 251–262 (2012).
63. Canto, C. et al. AMPK regulates energy expenditure by modulating NAD +metabolism and SIRT1 activity. *Nature* **458**, 1056–1060 (2009).
64. Guaras, A. et al. The CoQH2/CoQ ratio serves as a sensor of respiratory chain efficiency. *Cell Rep.* **15**, 197–209 (2016).
65. Benn, D. E. et al. Clinical presentation and penetrance of pheochromocytoma/paraganglioma syndromes. *J. Clin. Endocrinol. Metab.* **91**, 827–836 (2006).
66. Fishbein, L. et al. Comprehensive molecular characterization of pheochromocytoma and paraganglioma. *Cancer Cell* **31**, 181–193 (2017).
67. Jochmanova, I. & Pacak, K. Pheochromocytoma: the first metabolic endocrine cancer. *Clin. Cancer Res.* **22**, 5001–5011 (2016).
68. Sancak, Y. et al. EMRE is an essential component of the mitochondrial calcium uniporter complex. *Science* **342**, 1379–1382 (2013).
69. Blecha, J. et al. Antioxidant defense in quiescent cells determines selectivity of electron transport chain inhibition-induced cell death. *Free Radic. Biol. Med.* **112**, 253–266 (2017).
70. Rohlenova, K. et al. Selective disruption of respiratory supercomplexes as a new strategy to suppress Her2high breast cancer. *Antioxid. Redox Signal.* **26**, 84–103 (2017).
71. Vondrusova, M., Bezawork-Geleta, A., Sachaphibulkij, K., Truksa, J. & Neuzil, J. The effect of mitochondrially targeted anticancer agents on mitochondrial (super)complexes. *Methods Mol. Biol.* **1265**, 195–208 (2015).
72. Pasdar, E. A. et al. Characterisation of mesothelioma-initiating cells and their susceptibility to anti-cancer agents. *PLoS ONE* **10**, e0119549 (2015).
73. Yan, B. et al. Mitochondrially targeted vitamin E succinate efficiently kills breast tumour-initiating cells in a complex II-dependent manner. *BMC Cancer* **15**, 401 (2015).
74. Dong, L. F. et al. Horizontal transfer of whole mitochondria restores tumorigenic potential in mitochondrial DNA-deficient cancer cells. *Elife* **6**, 1–22 (2017).
75. Wu, J. X. et al. SWATH mass spectrometry performance using extended peptide MS/MS assay libraries. *Mol. Cell. Proteom.* **15**, 2501–2514 (2016).
76. Huang da, W., Sherman, B. T. & Lempicki, R. A. Bioinformatics enrichment tools: paths toward the comprehensive functional analysis of large gene lists. *Nucleic Acids Res.* **37**, 1–13 (2009).
77. Wen, H. et al. Enhanced phase II detoxification contributes to beneficial effects of dietary restriction as revealed by multi-platform metabolomics studies. *Mol. Cell. Proteomics* **12**, 575–586 (2013).
78. Wen, H. et al. A new NMR-based metabolomics approach for the diagnosis of biliary tract cancer. *J. Hepatol.* **52**, 228–233 (2010).
79. Bolger, A. M., Lohse, M. & Usadel, B. Trimmomatic: a flexible trimmer for Illumina sequence data. *Bioinformatics* **30**, 2114–2120 (2014).
80. Kopylova, E., Noe, L. & Touzet, H. SortMeRNA: fast and accurate filtering of ribosomal RNAs in metatranscriptomic data. *Bioinformatics* **28**, 3211–3217 (2012).
81. Dobin, A. et al. STAR: ultrafast universal RNA-seq aligner. *Bioinformatics* 29, (15–21 (2013).
82. Love, M. I., Huber, W. & Anders, S. Moderated estimation of fold change and dispersion for RNA-seq data with DESeq2. *Genome Biol.* **15**, 550 (2014).
83. Sekula, M., Datta, S. & Datta, S. optCluster: an R Package for Determining the Optimal Clustering Algorithm. *Bioinformation* **13**, 101–103 (2017).
84. Reimand, J. et al. g:Profiler-a web server for functional interpretation of gene lists (2016 update). *Nucleic Acids Res.* **44**, W83–W89 (2016).
85. Supek, F., Bosnjak, M., Skunca, N. & Smuc, T. REVIGO summarizes and visualizes long lists of gene ontology terms. *PLoS ONE* **6**, e21800 (2011).
86. Papathomas, T. G. et al. SDHB/SDHA immunohistochemistry in pheochromocytomas and paragangliomas: a multicenter interobserver variation analysis using virtual microscopy: a Multinational Study of the European Network for the Study of Adrenal Tumors (ENS@T). *Mod. Pathol.* **28**, 807–821 (2015).

Acknowledgements

The work was supported in part by the ARC Discovery grant, Czech Science Foundation (15-02203S) and Czech Health Foundation grant (17-30138A) to J.N., bilateral funding by the Czech Science Foundation and National Science Foundation of Korea (17-01192J/NRF-2016K2A9A1A06921853) to J.N. and S.P., Czech Science Foundation grant (17-20904S and 16-22823S) to J.R., funding by Genesis Oncology Trust, the Cancer Society of New Zealand and the Health Research Council of New Zealand to M.V.B., the Basic Science Research Program (2009-83533), the Bio-Synergy Research Project (NRF-2015M3A9C4075818) through the National Research Foundation of Korea funded by the Ministry of Education Science and Technology and Ministry of Science, ICT and Future Planning to S.P., by the Technology Agency of the Czech Republic (TE01020118) IMG grant (RVO: 68378050) to M.S. and P.H., and the institutional support of the Institute of Biotechnology RVO: 86652036, by the BIOCEV European Regional Development Fund CZ.1.05/1.100, and by the Intramural Research Program of the NIH, NICHD. H.W. was supported by the National Key Research and Development Program of China (2017YFA0503900) and Science and Technology Foundation of Shenzhen City (JCYJ20170302144650949). Proteomic analysis was facilitated by access to the Australian Proteome Analysis Facility supported in part by the Australian Government's National Collaborative Research Infrastructure Strategy. The electron microscopy data were produced at the Microscopy Centre—Electron Microscopy Core Facility (Institute of Molecular Genetics, Czech Academy of Sciences, Prague, Czech Republic) supported by Ministry of Education, Youth and Sports of the Czech Republic (LM2015062 Czech-BioImaging).

Author contributions

A.B.-G. and J.N. conceived the project and designed the study. A.B.-G. performed the majority of the experiments. H.W. and S.P. designed and performed metabolomics study and analyzed the data. V.C., Y.P., and K.P. provided patient data and samples, and they performed H&E and ICH analysis. L.K., K.V., R.Z., S.M.N., and S.B. performed the respiration studies, WB, and SDHB re-expression. M.S. and P.H. performed TEM analysis. T.Z. and M.P.M. performed SWATH-MS and bioinformatics analysis. L.D., B.Y., J. V., J.R., S.Z., and M.V.B. contributed reagents, materials, analytical tools, technical support, and ideas. P.A., R.N., R.S., S.M.N., and M.K. performed RNA sequence analysis and interpreted the data. A.B.-G., J.R., and J.N. wrote the manuscript. All authors discussed the results and edited the manuscript.

Additional information

Supplementary Information accompanies this paper at https://doi.org/10.1038/s41467-018-04603-z.

Competing interests: The authors declare no competing interests.

Reprints and permission information is available online at http://npg.nature.com/reprintsandpermissions/

Publisher's note: Springer Nature remains neutral with regard to jurisdictional claims in published maps and institutional affiliations.

Open Access This article is licensed under a Creative Commons Attribution 4.0 International License, which permits use, sharing, adaptation, distribution and reproduction in any medium or format, as long as you give appropriate credit to the original author(s) and the source, provide a link to the Creative Commons license, and indicate if changes were made. The images or other third party material in this article are included in the article's Creative Commons license, unless indicated otherwise in a credit line to the material. If material is not included in the article's Creative Commons license and your intended use is not permitted by statutory regulation or exceeds the permitted use, you will need to obtain permission directly from the copyright holder. To view a copy of this license, visit http://creativecommons.org/licenses/by/4.0/.

© The Author(s) 2018

Free Radical Biology and Medicine 112 (2017) 253–266

Contents lists available at ScienceDirect

Free Radical Biology and Medicine

journal homepage: www.elsevier.com/locate/freeradbiomed

Original article

Antioxidant defense in quiescent cells determines selectivity of electron transport chain inhibition-induced cell death

Jan Blecha[a,b], Silvia Magalhaes Novais[a], Katerina Rohlenova[a], Eliska Novotna[a], Sandra Lettlova[a], Sabine Schmitt[c], Hans Zischka[c,d], Jiri Neuzil[a,e,*], Jakub Rohlena[a,**]

[a] Institute of Biotechnology, Czech Academy of Sciences, BIOCEV, Vestec, Prague-West, Czech Republic
[b] Faculty of Science, Charles University, Prague, Czech Republic
[c] Institute of Toxicology and Environmental Hygiene, Technical University Munich, Munich, Germany
[d] Institute of Molecular Toxicology and Pharmacology, Helmholtz Center Munich, German Research Center for Environmental Health, D-85764 Neuherberg, Germany
[e] School of Medical Science, Griffith University, Southport, Qld, Australia

ARTICLE INFO

Keywords:
Electron transport chain
Supercomplexes
Antioxidant defense
SOD2
Thioredoxin

ABSTRACT

Mitochondrial electron transport chain (ETC) targeting shows a great promise in cancer therapy. It is particularly effective in tumors with high ETC activity where ETC-derived reactive oxygen species (ROS) are efficiently induced. Why modern ETC-targeted compounds are tolerated on the organismal level remains unclear. As most somatic cells are in non-proliferative state, the features associated with the ETC in quiescence could account for some of the specificity observed. Here we report that quiescent cells, despite increased utilization of the ETC and enhanced supercomplex assembly, are less susceptible to cell death induced by ETC disruption when glucose is not limiting. Mechanistically, this is mediated by the increased detoxification of ETC-derived ROS by mitochondrial antioxidant defense, principally by the superoxide dismutase 2 – thioredoxin axis. In contrast, under conditions of glucose limitation, cell death is induced preferentially in quiescent cells and is correlated with intracellular ATP depletion but not with ROS. This is related to the inability of quiescent cells to compensate for the lost mitochondrial ATP production by the upregulation of glucose uptake. Hence, elevated ROS, not the loss of mitochondrially-generated ATP, are responsible for cell death induction by ETC disruption in ample nutrients condition, *e.g.* in well perfused healthy tissues, where antioxidant defense imparts specificity. However, in conditions of limited glucose, *e.g.* in poorly perfused tumors, ETC disruption causes rapid depletion of cellular ATP, optimizing impact towards tumor-associated dormant cells. In summary, we propose that antioxidant defense in quiescent cells is aided by local glucose limitations to ensure selectivity of ETC inhibition-induced cell death.

1. Introduction

Mitochondria play a key role in multiple cellular processes, including energy production, metabolism and cell death. Functional mitochondria are essential in tumorigenesis [1–3], and targeting of the mitochondrial electron transport chain (ETC) emerges as an effective strategy to suppress and eliminate cancer cells [4–8]. ETC consists of four macromolecular protein complexes (referred to as CI, CII, CIII and CIV) that associate further into supercomplexes (SCs) [9,10], and work together to maintain mitochondrial inner membrane potential, used by the mitochondrial ATP synthase (a.k.a complex V, CV) to produce ATP. Because of high electron traffic and presence of redox centers, the ETC is a significant source of reactive oxygen species (ROS) [11,12]. To counter ETC-derived ROS, mitochondria are equipped with several antioxidant mechanisms, such as manganese superoxide dismutase (SOD2), as well as the glutathione and thioredoxin systems [13–15]. Inhibition of the ETC interferes with mitochondrial ATP synthesis, but also substantially increases ETC-derived ROS production, leading to cell

Abbreviations: BNE, blue native electrophoresis; CAT, catalase; CCCP, carbonyl cyanide 3-chlorophenylhydrazone; DCF, 2',7'-dichlorofluorescin diacetate; DHE, dihydroethidium; DHR123, dihydrorhodamine 123; ETC, electron transport chain; FCCP, carbonyl cyanide p-(trifluoromethoxyl)-phenyl-hydrozone; GPX1, glutathione peroxidase-1; GSR, glutathione reductase; hrCNE, high-resolution clear native electrophoresis; NAC, N-acetyl cysteine; PEITC, phenethyl-isothiocyanate; PRX3, peroxiredoxin-3; ROS, reactive oxygen species; SCs, supercomplexes; SOD1, superoxide dismutase 1; SOD2, manganese superoxide dismutase; TRX2, thioredoxin-2; TXNRD2, thioredoxin reductase 2; WB, western blot

* Correspondence to: Mitochondria, Apoptosis and Cancer Research Group, School of Medical Science and Menzies Health Institute Queensland, Griffith University, Southport, Qld 4222, Australia.
** Correspondence to: Institute of Biotechnology, CAS, BIOCEV, Molecular Therapy, Prumyslova 595, 25250 Vestec, Czech Republic.
E-mail addresses: j.neuzil@griffith.edu.au (J. Neuzil), jakub.rohlena@ibt.cas.cz (J. Rohlena).

http://dx.doi.org/10.1016/j.freeradbiomed.2017.07.033
Received 30 May 2017; Received in revised form 24 July 2017; Accepted 30 July 2017
Available online 31 July 2017
0891-5849/ © 2017 Elsevier Inc. All rights reserved.

death [4]. The susceptibility to cell death upon ETC inhibition will therefore be governed by the degree of cell's reliance on mitochondrial ATP production, and by the balance between the propensity to form and detoxify ETC-derived ROS.

Recent findings indicate that ETC targeting is particularly effective in cancer cells and subtypes with increased dependence on mitochondrial respiration and higher SC assembly [5,16–18]. At the same time, pharmacologically relevant ETC inhibitors, such as metformin or the recently developed mitochondrial-targeted agents such as MitoTam and MitoVES, are well tolerated in animals, suggesting selectivity for cancer cells [5,19]. However, despite its obvious translational relevance, the molecular reasons for this selectivity are unclear.

While cancer cells are hard-wired for proliferation, the majority of normal somatic cells are in a non-proliferative, post-mitotic state. Features associated with quiescence and non-proliferative state could therefore partially account for the specificity we observed previously: quiescent cells were resistant to agents that induce ROS from the ETC [20,21], but molecular reasons remained uncharacterized. Hence, specific configuration of the ETC in quiescent cells, different handling of ROS, or changes in the dependence on mitochondrial ATP production could all significantly contribute to the therapeutic window associated with the ETC inhibition in cancer. Understanding the paradigms that govern sensitivity to cell death in quiescent cells under various circumstances is therefore of high importance for the development of efficient and non-toxic ETC-directed cancer therapy.

In the current study we attempted to resolve the selectivity issue by characterizing the ETC and the ability to form and detoxify ROS upon ETC inhibition in proliferating and quiescent, non-transformed cells. Using pharmacological and genetic manipulations, we show that the capacity to detoxify ROS is increased in quiescent cells, significantly contributing to the resistance of these cells to ETC inhibition, despite their increased reliance on the ETC. Furthermore, under conditions of nutrient limitations expected to occur in poorly vascularized areas of tumors, ETC inhibition brings an additional benefit by interfering with mitochondrial ATP production, further improving specificity.

2. Material and methods

2.1. Reagents

All reagents were purchased from Sigma Aldrich (St. Louis, MO, USA), unless stated otherwise.

2.2. Cell culture

The cells used in the study were obtained from ATCC and were authenticated. The Ea.hy926 cells were cultured in high glucose (4.5 g/l) (Lonza, Basel, Switzerland) or low glucose (1 g/l) (Lonza) DMEM media supplemented with 10% fetal bovine serum (ThermoFisher, Waltham, MA, USA), hypoxanthine aminopterin thymidine (HAT) supplement 2% (ThermoFisher) and 1% antibiotics (penicilin G 100 U/ml and streptomycin 100 µg/ml) and, for low glucose media only, L-glutamine 0,03% in a 5% CO_2, 37 °C incubator. MCF10A cells were cultured in DMEM:F12 (Lonza) media supplemented with 5% horse serum (Sigma-Aldrich), human insulin 0.1%, 20 ng/ml epidermal growth factor (ThermoFisher), hydrocortisone 0.5 mg/ml, cholera toxin 100 ng/ml. For the experiments the media was changed for low glucose or high glucose DMEM supplemented as DMEM:F12 above. All cultures were negative for mycoplasma as determined by the MycoAlert kit (Lonza). For experiments requiring pharmacological treatments, equal numbers of cells (5–7 × 10^5) were exposed to the studied compounds. For quiescent cultures, the cells were seeded into 24-well plates at 80% density, and cultured for 4 days post-confluence. For proliferating cultures, cells were seeded into 6-well plates at 2 × 10^5 cells per well two days before the experiment. 1 ml of medium per well were used for both proliferating and quiescent cultures.

2.3. Lentiviral production and RNA interference

pLKO1 plasmids containing shRNA sequences against the targeted transcripts were obtained from Sigma-Aldrich. The specific shRNA used were as follows: SOD2 – TRCN0000320739, GPX1TRCN0000046231, TXNRD2 – TRCN0000433391, GSR - TRCN0000046425. Lentiviral particles were produced in Hek293-FT cells using second generation psPAX and pMD.2G plasmids and calcium phosphate or Lipofectamine 3000 (ThermoFisher) transfections. Virus-containing medium was collected after 48 h, centrifuged at 3000 ×*g* for 15 min, and in some cases the viruses were concentrated by overnight incubation with PEG-it (SBI-System Biosciences, Palo Alto, CA, USA). The supernatants were aliquoted and stored at −80 °C. To induce silencing, the lentivirus-containing supernatants were added to cells grown in normal culture medium overnight. The transduced cells were selected by puromycin, and the level of silencing was assessed by western blotting (WB).

2.4. Respiration assessment

Cellular respiration was assessed by Seahorse XF24 analyzer (Seahorse Biosciences, Santa Clara, CA, USA). For quiescent cultures the cells were seeded at 80% density in the Seahorse XF 24-well microplates and cultured 4 days post-confluence. Proliferating cells were seeded at 20,000 per well two days before the experiment. Medium was switched before the experiment for the base medium of pH 7.4, containing 0.2% BSA and 10 mM glucose. Oxygen consumption rate (OCR) was measured in the basal state and after sequential addition of 10 µM oligomycin, 1 and 2 µM carbonyl cyanide p-(trifluoromethoxyl)-phenylhydrazone (FCCP) and combined 10 µM rotenone plus 25 µM antimycin. Data were normalized to DNA content measured by the Quant-iT™ PicoGreen® dsDNA reagent (ThermoFisher). To determine the efficacy of ETC inhibition by the tested compounds, the respiration of proliferating endothelial Ea.hy926 cells under both low glucose (1 g/l) and high glucose (4.5 g/l) conditions was monitored by the Oroboros Oxygraph 2-K instrument (Oroboros Instruments, Innsbruck, Austria) as described [22], using 2 × 10^6 of non-permeabilized cells per chamber. Basal routine respiration was established after adding succinate (10 mM) and ADP (3 mM), after that pharmacological agents were added.

2.5. SDS-PAGE and western blot analysis

SDS-PAGE and WB analysis were performed using standard methods as detailed elsewhere [1]. Antibodies used were: anti-peroxiredoxin III (SantaCruz, Dallas, TX, USA, sc-23973), anti-thioredoxin 2 (Abcam, Cambridge, United Kingdom, ab185544), anti-SOD1 (SantaCruz, sc-11407), anti-catalase (Abcam, ab1877), anti-GPX-1 (Abcam, ab108427), anti-SOD2 (Acris, Herford, Germany, AP03024-PU-N), anti-GSR (Proteintech, Manchester, United Kingdom, 18257-1-AP), anti-TXNRD2 (Abcam, ab180493). The anti-β-Actin HRP conjugate (Cell-Signaling, Danvers, MA, USA, #5125) was used for visualization.

2.6. Blue native electrophoresis (BNE) and high-resolution clear native electrophoresis (hrCNE)

Mitochondria were isolated using a Balch-style homogenizer as detailed elsewhere [4,23]. The published protocols were modified by using hand-driven 1 ml disposable syringes (Becton Dickinson, Franklin Lakes, NJ, USA). BNE followed by immunoblotting and hrCNE followed by in-gel activity assays was performed using digitonine-solubilised mitochondria as described [24]. Primary antibodies used were as follows. CI – anti-NDUFB8 (Abcam, ab110242), CII – anti-SDHA (Abcam, ab14715), CIII – anti-UQCRFS1 (Abcam, ab14746), CIV – anti-MTCO2 (Abcam, ab110258), CV – anti-ATP5A (Abcam, ab110273). Samples used for native gels were also run on SDS-PAGE/WB to verify equal mitochondrial loading using anti-mtHSP70 antibody (ThermoFisher,

MA3-028).

2.7. Mitochondrial NAD(P)H measurements

Mitochondrial NADH was measured by two-photon microscopy using Zeiss LSM880 NLO inverted microscope, equipped with Chameleon Ultra II and Compact OPO MP lasers (Coherent, Santa Clara, CA, USA) using non-descanned BiG-2 GaAsP detector, 63x/1.4 Plan-Apochromat oil immersion objective, 740 nm laser line at 8 mW power (6 mW in scanning mode during image acquisition which includes blanking), and emission range 390–480 nm. The cells were grown in glass-bottom microscopy plates in normal culture medium, pre-treated with 1 nM TMRM for 30 min and examined either untreated, exposed to 5 μM CCCP, or to 1.25 μM rotenone. Mitochondrial NAD(P)H was quantified *via* the Fiji software by segmenting cells using thresholding and averaging signal over mitochondrial ROIs. 3–4 independent experiments were performed, with more than 150 cells per condition imaged in each experiment.

2.8. Detection of cell death and ROS

For the detection of cell death, cells were seeded before the experiment as described above. If required, the cells were pre-incubated with N-acetylcysteine 1 mM (NAC) or auranofin 0.75 μM (Enzo Life Sciences, Farmingdale, NY, USA) for 1 or 2 h, respectively. Incubation time with the tested compounds was 22 h, after which cell death was assessed by flow cytometry using Annexin V/propidium iodide (PI) staining as described [4]. Cells positive for Annexin V, PI, or Annexin V/PI were considered dead. The tested agents were as follows: H_2O_2, phenethyl isothiocyanate (PEITC), rotenone, piericidin A (Enzo), myxothiazol, oligomycin A, and CCCP. MitoVES and MitoTam were synthetized in-house [5,6]. For ROS measurements, cells cultured as described were exposed to the tested compounds for one hour. For the last 20 min, the cells were co-incubated with 5 μM 2′,7′-dichlordihydrofluorescein diacetate (DCF), 5 μM dihydroethidium (DHE) or 10 μM dihydrorhodamine 123 (DHR123). The level of fluorescence was assessed by flow cytometry as described [4].

2.9. Assessment of glucose uptake, lactate production, and glucose content in culture media

Glucose uptake was evaluated after 15 min incubation with 50 μM 2-nitrobenzodeoxyglucose (2-NBDG; ThermoFisher) by flow cytometry as described [5]. In some experiments, cells were pre-treated for 6 h by 0.5 or 5 μM MitoVES or 7.5 μM myxothiazol. Lactate concentration in the culture medium was assessed after 19 h of cell cultivation using lactate detection kit (TrinityBiotech, Bray, Ireland), following manufacturer's instructions with all volumes scaled down 10 times. Glucose content in the cultured media was determined after 6, 16, 24 and 38 h of cultivation under normal experimental conditions (proliferating cells in 6-well format, quiescent cells in 24-well format, both in 1 ml of media) using low and high glucose media and Amplex™ Red Glucose/Glucose oxidase assay kit (ThermoFisher) following manufacturer's instructions. Data were normalized to glucose content in fresh media.

2.10. Evaluation of intracellular ATP

Intracellular ATP levels were assessed by the CellTiter-Glo kit (Promega, Madison, WI, USA) following manufacturer's instructions in 96-well format. Data were normalized to the cell number measured by crystal violet in a parallel 96-well plate, and are shown as relative to non-treated controls.

2.11. Measurements of surface GLUT1 exposure

Cells were exposed to the indicated agents and collected by trypsinization, incubated for 30 min in 100 ul PBS with 1:200 Anti-GLUT1 antibody (Abcam, ab15309), sedimented by centrifugation and resuspended in PBS with 1:100 secondary Cy3-stained antibody (Sigma-Aldrich). Both incubations were performed at 37 °C, 5% CO_2 incubator. Fluorescence intensity was determined by flow cytometry.

2.12. In-gel assessment of antioxidant protein activity

In-gel activity of antioxidant proteins was determined as described [25], with minor changes. Samples were prepared on the Misonix Sonicator 3000 instrument (QSonica, Newtown, CT, USA) at 30% power using microtip ~3 W, 3 × 15 s with 25 s pause performed on ice. The incubation time in the SOD2 activity assay was reduced to 7 min.

2.13. NADPH/NADP and GSH/GSSG measurements

Cells were seeded in a 96 well plate and ratios of GSH/GSSG and NADPH/$NADP^+$ were determined using luminescence assays (GSH/GSSG-Glo™, Promega and NADP/NADPH-Glo™, Promega) according to manufacturer's instructions.

2.14. Cell cycle evaluation and visualization of adherence junctions

For cell cycle assay, cells were harvested by trypsin, stained by Hoechst 33342 (10 μg/ml) for 35 min at 37 °C, 5% CO_2 in normal culture media. After that pyronin Y was added to the final concentration of 0.5 μg/ml for 15 min. 2×10^5 of stained cells were examined by flow cytometry at a flow rate of 400 cells/s. Hoechst-low/pyronin Y-low cells were assigned to G_0 phase of the cell cycle. For detection of adherence junctions, cells grown on coverslips were permeabilized and blocked with 5% fetal bovine serum, 0.075% Tween-20, 0.075% Triton-X100, 100 mM glycine (Serva, Heidelberg, Germany) in PBS for 1 h, incubated with anti-VE cadherin (Santa Cruz, sc-9989) or anti-E-cadherin (Santa Cruz, sc-21791) primary antibodies (1:100) for 1 h at room temperature, followed by 1 h incubation with anti-mouse Alexa Fluor 647-conjugated antibody (Thermo Fisher, 1:1000). Samples were embedded in DAPI-containing mowiol and imaged by the Leica TCS SP8 confocal microscope (Leica Microsystems, Wetzlar, Germany). Images were deconvolved in Huygens Professional software and processed in Fiji.

2.15. Statistical analysis

Data were analyzed using the GraphPad Prism 5.04 software, and are presented as mean values ± S.E.M. of at least three independent experiments, unless indicated otherwise. Statistical significance was determined using unpaired Student's *t*-test or ANOVA when suitable; $p < 0.05$ was considered statistically significant.

3. Results

3.1. Electron transport chain activity is increased in quiescent cells

Increased ETC assembly in cancer cells has been linked to the susceptibility to ETC-dependent cell death [5]. To understand if this relationship is maintained in non-transformed quiescent cells, we first examined the ETC utilization and assembly in proliferating and quiescent endothelial-derived Ea.hy926 and breast epithelia-derived MCF10A cells. To investigate the effect of nutrient availability (which can be scarce for example in poorly-perfused areas of tumors), the cells were grown in high (4.5 g/l) and low (1 g/l) glucose media that are expected to represent situations of ample and limited glucose supply. Both tested cell types undergo contact growth inhibition upon reaching confluence, as evidenced by the increase of the G_0 cell cycle subpopulation (Fig S1A, B) and assembly of adherence junctions (Fig. S1C, D), and represent therefore a plausible experimental model of

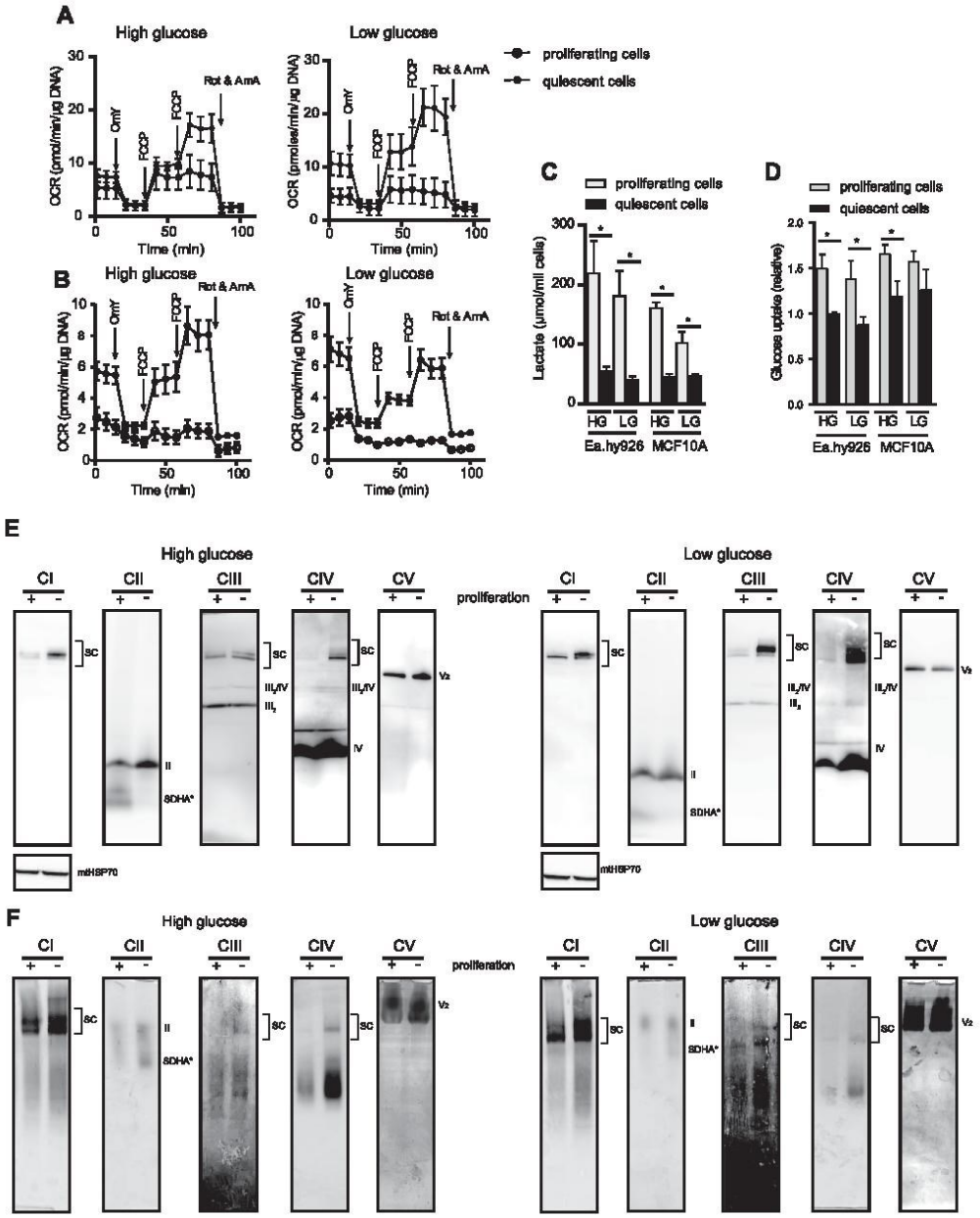

Fig. 1. Electron transport chain activity and assembly is enhanced in quiescent cells. (**A, B**) Oxygen consumption rate (OCR, pMoles/min) profiles in (**A**) Ea.hy926 (**B**) and MCF10A cells in both low glucose (1 g/l) and high glucose (4.5 g/l) was measured using Seahorse Bioscience XF24 extracellular flux analyzer. Data correlated to DNA content are present as means ± S.E.M. from at least three independent experiments. (**C**) Excreted lactate was measured in the culture medium after 19 h cultivation. Data represent means ± S.E.M. of 5 independent experiments, and are correlated to cell number. The symbol * indicates values significantly different between proliferating and quiescent cells. (**D**) Glucose consumption of Ea.hy926 and MCF10A cells was measured upon 24 h pre-incubation in low glucose media (1 g/l glucose) by flow cytometry using 2-NBDG. Data are correlated to quiescent Ea.hy926 cells in high glucose condition. Data represent means ± S.E.M., n ≥ 4. The symbol * indicates values significantly different between proliferating and quiescent cells. (**E**) Isolated mitochondrial fraction were probed for the presence of SCs by WB following BNE with the following antibodies: CI, NDUFB8; CII, SDHA; CIII, MTCO2; CIV, UQCRFS1; and CV, ATP5A; mtHSP70 was used as loading control. A representative experiment is shown. (**F**) In-gel assessment of enzymatic activity of respiratory SCs was performed in isolated mitochondrial fraction following hrCNE as follows: CI-NADH:NTB reductase, CII-succinate:NTB reductase, CIII-DAB oxidase, CIV- DAB: cytochrome c reductase, CVATP hydrolase. A representative experiment is shown.

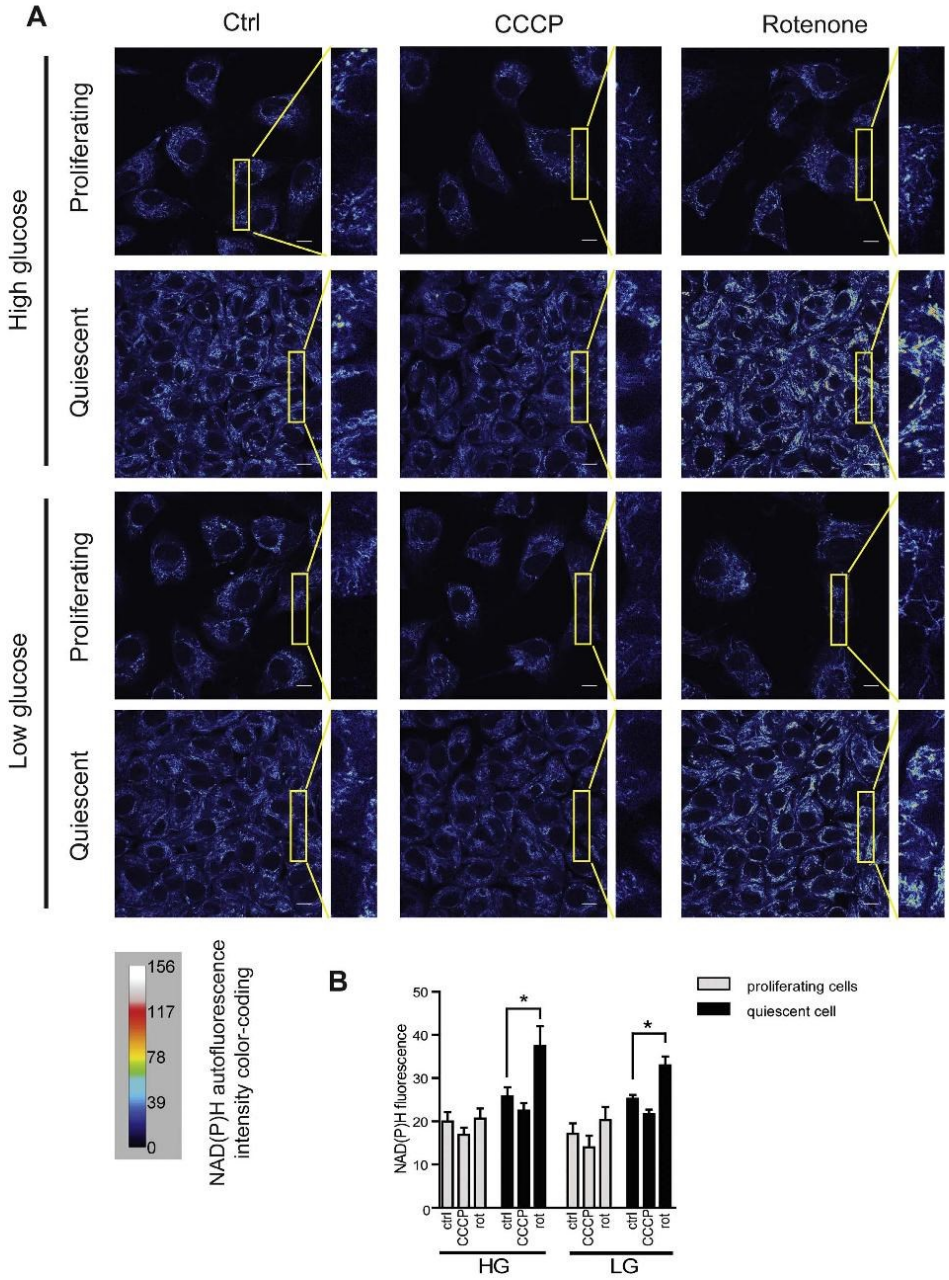

Fig. 2. In-situ measurements of mitochondrial NAD(P)H indicate increased NADH utilization by the ETC in quiescent cells. (A) Mitochondrial NAD(P)H signal was measured by two-photon microscopy in control, CCCP (5 μM) or rotenone (1.25 μM)-treated cells. Intensity is color-coded as shown; note the increased NAD(P)H signal in mitochondria of rotenone-treated quiescent cells. Regions marked by yellow rectangles are magnified for clarity. Scale bars indicate 10 μm. Representative images are shown. (**B**) Average values of NAD(P)H signal quantified in Fiji as described in Section 2. Data represent the means ± S.E.M. of 4 independent experiments. The symbol * indicates values significantly different between control and rotenone-treated cells.

quiescence induced by contact inhibition. Respiration measurements revealed that oxygen consumption was increased in quiescent cells in both cell types (Fig. 1A, B), suggesting that ETC activity is elevated when cells become quiescent. On the other hand, lactate production and glucose uptake were reduced in quiescent cells (Fig. 1C, D), indicating lower rate of glycolysis, in agreement with previously-reported data [26–28].

We then performed a more detailed analysis of the ETC in Ea.hy926 cells. Blue native electrophoresis (BNE) of mitochondria isolated from proliferating and quiescent cells revealed more SCs in quiescent cells (Fig. 1E), and in-gel activity measurements using high resolution clear native electrophoresis (hrCNE) demonstrated that these SCs were enzymatically active (Fig. 1F). This suggests that the ETC in quiescent cells is primed for increased performance, consistent with the proposed role of respiratory SCs [29,30]. Finally, *in situ* examination by two photon microscopy documented that mitochondrial NADH was significantly elevated upon addition of the CI inhibitor rotenone in quiescent but not proliferating cells (Fig. 2A, B). This points to increased mitochondrial NADH production in quiescent cells, which is at baseline avidly consumed by the ETC, but is substantially elevated when CI activity is suppressed by rotenone. In summary, these results demonstrate that ETC gains prominence in quiescence. Consequently, ETC blockade should have more profound consequences in quiescent cells than in proliferating (*i.e.* cancer) cells.

3.2. Quiescent cells are protected from cell death induced by the ETC blockade when glucose is not limiting

While in cancer the dependence on oxidative phosphorylation and higher ETC SC assembly correlate with sensitivity to ETC inhibition, in non-transformed cells this relationship has not been rigorously tested. Importantly, ETC blockade may result in both the suppression of mitochondrial ATP generation due to an impaired proton-motive force, but also in the stimulation of ROS production, due to accumulating electrons at the ETC complexes. However, the relative importance of elevated ROS or ATP depletion in cell death induction may vary depending on the cellular state (proliferating or quiescent), and on the nutritional status (availability of glucose). We therefore exposed proliferating and quiescent Ea.hy926 and MCF10A cells to three distinct classes of agents. The first group consisted of compounds that generate ROS without acute inhibition of the ETC, hydrogen peroxide and phenethyl-isothiocyanate (PEITC) [31], (Fig. S2A, B), expected to induce cell death solely in an ROS-dependent manner. The second group comprised agents that block the ETC (Fig. S2C–G), the CI inhibitors rotenone, pierecidin A and MitoTam [5], the CII inhibitor MitoVES [4,6], and the CIII inhibitor myxothiazol. These compounds may either induce ROS *via* the ETC, but may also suppress mitochondrial ATP synthesis. The third group contained agents that specifically block mitochondrial ATP generation, the ATP synthase inhibitor oligomycin, and mitochondrial uncoupler carbonyl cyanide 3-chlorophenylhydrazone (CCCP) (Fig. S2H, I).

When compared to quiescent cells, proliferating cells under high glucose conditions were more susceptible to ROS inducers (Fig. 3A, G), ETC inhibitors (Fig. 3B, H), as well as to oligomycin and CCCP (Fig. 3C, I). Under low glucose, this sensitivity pattern was maintained only for pure ROS inducers (Fig. 3D, J). Importantly, however, upon treatment with ETC inhibitors (Fig. 3E, K), oligomycin and CCCP (Fig. 3F, L), quiescent cells became highly susceptible to cell death induction. This suggests that the sensitivity of quiescent cells to ETC and ATP synthase inhibitors, but not to pure ROS inducers, is significantly altered based on the availability of glucose. Moreover, under conditions of ample glucose supply, quiescent cells are much less sensitive to cell death induction by ROS inducers and inhibitors of the ETC.

3.3. ETC inhibition in quiescent cells leads to ATP depletion when ambient glucose is below the physiological range

To properly interpret the above results, we first assessed glucose levels at various time points in the cell-conditioned media. This revealed that in low glucose media, the glucose concentration is less than 20% of the initial 5.5 mM concentration (corresponding to less than 1 mM) at the time of the treatment (16 h after the media change), while in high glucose media it was about half of the initial 25 mM concentration (10–15 mM) (Fig. 4A). Thus, in low glucose cultures the glucose concentration is significantly below physiological levels of well perfused tissues (about 5 mM) [32], but in high glucose media such conditions of glucose limitation are not reached. ATP production by glycolysis requires glucose, therefore generation of ATP by oxidative phosphorylation may gain prominence when glucose is limiting. For this reason, we assessed the consequences of ETC blockade on intracellular ATP levels. To this end we exposed proliferating and quiescent cells to ETC inhibitors and disruptors of mitochondrial ATP production described above, and assessed total cellular ATP by a luminescence-based assay. While this treatment did not affect ATP levels in proliferating or quiescent cells in high glucose media (Fig. 4B, C), it resulted in a severe depletion of ATP in quiescent cells cultured in low glucose media (Fig. 4D, E). This ATP depletion correlated with enhanced cell death (cf. Fig. 3E, F, K, L), suggesting that the shortage of intracellular ATP is the defining factor for cell death in quiescent cells when glucose is below the normal physiological range, but not when glucose is in ample supply. In support of this notion, when quiescent cells were exposed to ETC inhibitors in media containing the physiological glucose level (5.5 mM), depletion of intracellular ATP was not observed (Fig. 4F).

3.4. Quiescent cells cannot compensate for the loss of mitochondrial ATP synthesis when glucose is limiting

ATP depletion in quiescent cells after inhibition of the ETC at sub-physiological glucose levels suggests that quiescent cells may be unable to compensate for the defect in mitochondrial ATP production when glucose is a limiting factor. As the observed ATP depletion could result from the failure of quiescent cells to switch to glycolysis, we assessed changes in the rate of glucose uptake upon ETC inhibition in Ea.hy926 cells to characterize the possible compensatory regulation. Indeed, we found that upon ETC blockade the proliferating cells increased their glucose uptake much more efficiently than quiescent cells (Fig. 4G). Glucose uptake is mediated by glucose transporters [33], therefore we next assessed the level of GLUT1 using flow cytometry after immunostaining of non-permeabilized cells. This analysis revealed that whereas ETC suppression significantly increased the level of GLUT1 in proliferating cells, little or no increase was observed in quiescent cells (Fig. 4H). Hence, the reduced flexibility of glucose uptake in quiescent cells renders these cells vulnerable to ETC blockade in glucose concentrations significantly below the physiological range.

3.5. Generation of ROS upon ETC inhibition corresponds to cell death when glucose is not limiting

Having established that factors other than ATP depletion determine sensitivity to cell death in quiescent cells at physiological glucose concentrations, we next assessed the relevance of increased ROS as another major consequence of ETC blockade [4,11,12]. We used flow cytometry and 2',7'-dichlorofluorescin diacetate (DCF) to assess the amount of ROS produced upon the administration of tested compounds to proliferating and quiescent Ea.hy926 and MCF10A cells and compared these results to cell death levels presented in Fig. 3. For ROS inducers hydrogen peroxide and PEITC, the magnitude of ROS generation correlated with the cells' sensitivity to cell death both in high (Fig. 5A, G) and low (Fig. 5D, J) glucose conditions. In contrast, for ETC

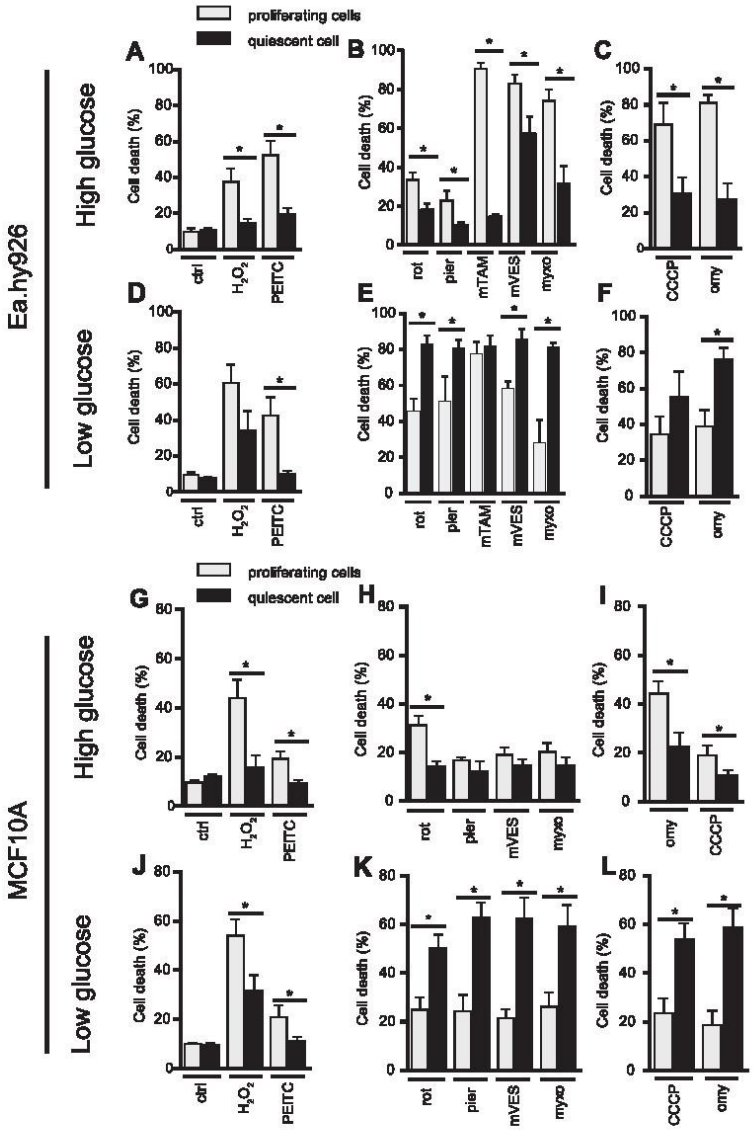

Fig. 3. Glucose availability affects sensitivity of quiescent cells to cell death induced by inhibitors of the ETC and ATP synthesis, and not by oxidant agents. (**A–F**) Ea.hy926 and (**G–L**) MCF10A cells cultivated in high glucose (4.5 g/l glucose, **A–C, G–I**) or low glucose (1 g/l glucose, D–F, J–L) media, respectively, were treated with H_2O_2 (800 mM), PEITC (10 μM), rotenone (Rot, 2 μM), piericidin (Pier, 80 μM high glucose, 0.05 μM low glucose), MitoTam (mTAM, 4 μM high glucose and 2 μM low glucose), MitoVES (mVES, 10 μM), myxothiazol (Myxo, 15 μM high glucose and 0,1 μM low glucose), CCCP (75 μM high glucose and 10 μM low glucose), oligomycin (Omy, 25 μM high glucose and 0.5 μM low glucose) for 22 h. The cells were stained with Annexin V-FITC/PI, and evaluated by flow cytometry as described in 'Materials and methods'. Data represent the means ± S.E.M., n ≥ 4. The symbol * indicates values significantly different between proliferating and quiescent cells.

inhibitors oligomycin and CCCP the correlation between ROS generation and cell death was found only under high glucose media (Fig. 5B, C, H, I), and this was confirmed by additional ROS probes dihydrorhodamine (DHR123) and dihydroethidium (DHE) (Fig. S3). However, no clear correlation between cell death and ROS was apparent under low glucose conditions (Fig. 5E, F, K, L). These results support the notion that the level of formed ROS determines the level of cell death induced by ETC inhibition when glucose is not limiting. In addition, lower ROS in quiescent cells, despite their more active ETC, suggests that these cells can neutralize ROS more efficiently.

3.6. Antioxidant defense is upregulated in quiescent cells

To further elaborate why quiescent cells produce less ROS upon ETC inhibition and why they are protected from cell death despite their more active ETC, we investigated the status of relevant antioxidant defense components. In mitochondria, this includes SOD2 that detoxifies superoxide, and glutathione and thioredoxin systems that inactivate hydrogen peroxide [14,15]. In Ea.hy926 cells, the expression of mitochondrial antioxidant defense proteins SOD2 and glutathione peroxidase-1 (GPX1) was elevated in quiescent cells, while peroxiredoxin-3 (PRX3), thioredoxin-2 (TRX2) were not significantly changed, irrespective of glucose concentration (Fig. 6A). Cytoplasmic catalase

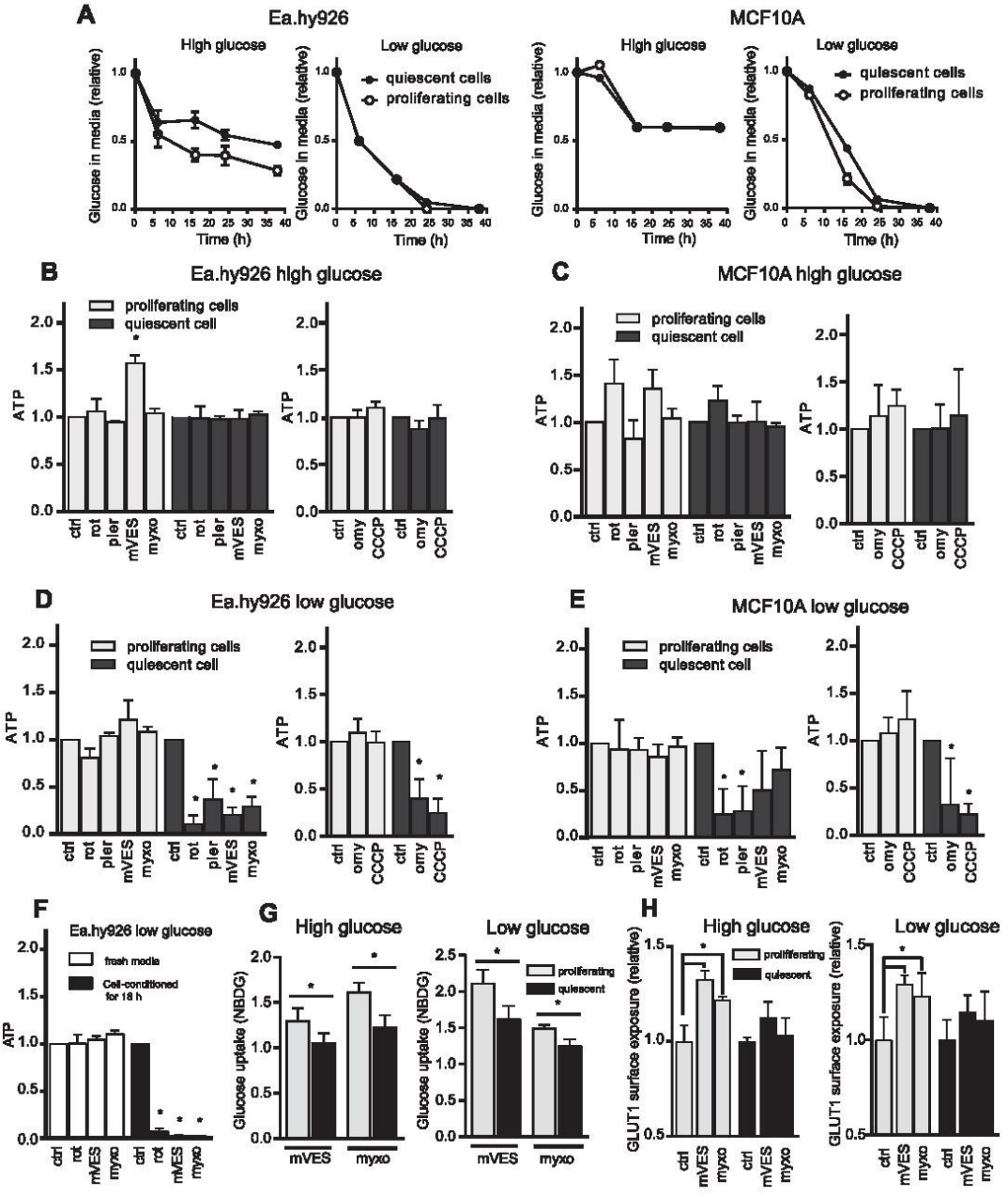

(caption on next page)

(CAT) and superoxide dismutase 1 (SOD1) were slightly increased in proliferating cells (Fig. 6A). This was corroborated by in-gel activity assays for superoxide dismutase, glutathione peroxidase and catalase (Fig. 6C, quantified in Fig. 6E), showing that the enzymatic activity of SOD2 and glutathione peroxidase was significantly increased in quiescent cells. In MCF10A cells, the protein expression of antioxidant defense components was similar in proliferating and quiescent cells both in high and low glucose (Fig. 6B), but the in-gel activity assays revealed

Fig. 4. Cellular ATP is depleted in quiescent cells upon ETC inhibition in sub-physiological glucose levels. (**A**) Glucose concentration in cell-conditioned media was determined after 6, 16, 24 and 38 h of cultivation using amplex red-based assay. Data are correlated to fresh media and presented as means ± S.E.M., n = 3. (**B, D**) Ea.hy926 and (**C, E**) MCF10A cells in (**B, C**) high and (**D, E**) low glucose media were treated for 0.5 h with rotenone (2 μM), piericidin (5 μM), mVES (10 μM), myxothiazol (15 μM), oligomycin (25 μM), CCCP (75 μM) and ATP level was assessed using luminescent assay. Results were corrected to cell number measured by crystal violet in a parallel plate. Data represent means ± S.E.M. of 3 independent experiments, the symbol * indicates significant differences to untreated control. (**F**) Quiescent Ea.hy926 cells in fresh low glucose (5.5 mM) media or low glucose media cell-conditioned for 18 h were exposed to the indicated agents as described above, and the ATP content was determined. Data represent means ± S.E.M., n = 3. The symbol * indicates significant differences to untreated control. (**G**) Glucose uptake was assessed using 2-NBDG staining and flow cytometry after 6 h treatment with MitoVES (0.5 μM low glucose or 5 μM high glucose) and myxothiazol (7.5 μM). Data shown represent means ± S.E.M. of at least 3 independent experiments, and are expressed relative to the untreated control. The symbol * indicates values significantly different between proliferating and quiescent cells. (**H**) Surface GLUT1 was determined by immunostaining of non-permeabilized cells using primary anti-GLUT1 IgG and secondary Cy3 labelled anti-Rabbit IgG and flow cytometry. Cells were pretreated for 2 h by MitoVES (5 μM) and myxothiazol (7.5 μM). Data shown represent means ± S.E.M. of 4–7 independent experiments, and are expressed relative to the untreated control. The symbol * indicates values significantly different from untreated control.

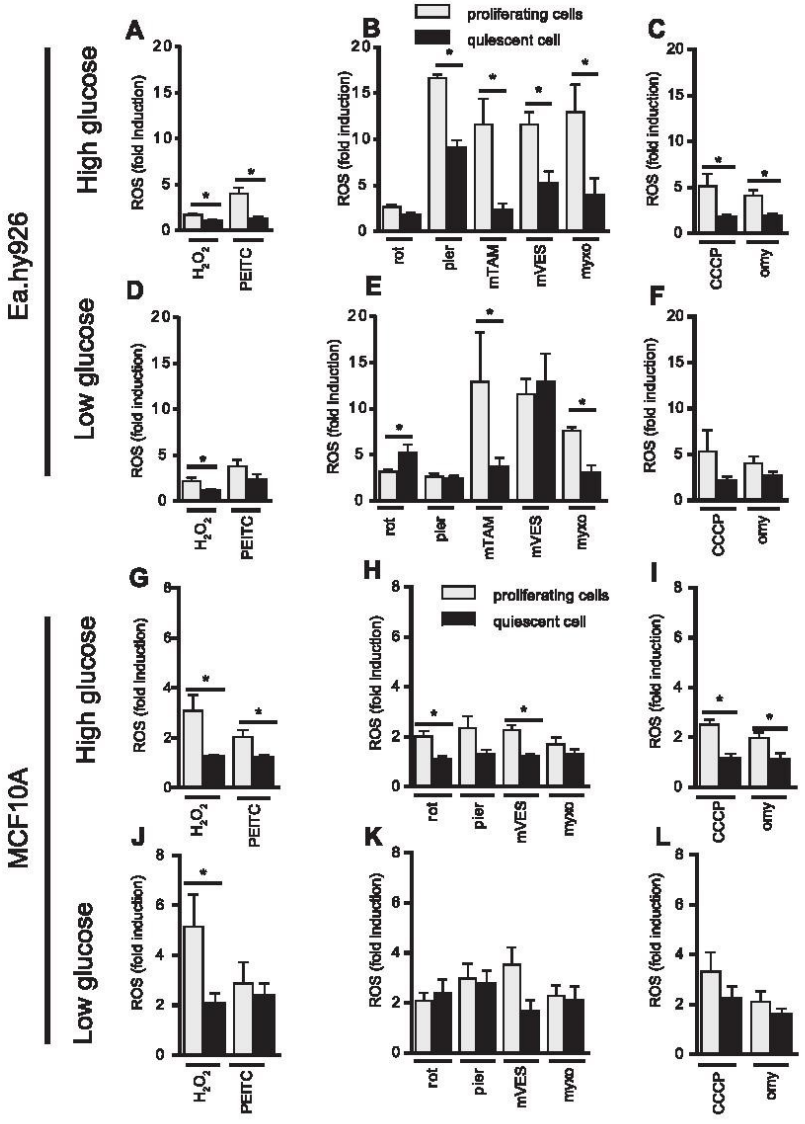

Fig. 5. ROS production upon treatment by oxidant agents and oxidative phosphorylation inhibitors is reduced in quiescent cells. (A–F) Ea.hy926 cells cultivated in high glucose (4.5 g/l glucose, **A–C**) or in low glucose (1 g/l glucose, D–F) media were treated with H_2O_2 (800 μM), PEITC (3 μM), rotenone (rot, 20 μM), piericidin (pier, 50 μM high glucose, 10 μM low glucose), MitoTAM (mTAM, 7.5 μM) MitoVES (mVES, 10 μM), myxothiazol (myxo, 15 μM), CCCP (75 μM), and oligomycin (omy, 2.5 μM) for 1 h, followed by staining with the DCF fluorescent probe. (**G–L**) MCF10A cells cultivated in high glucose (4.5 g/l glucose, **G–I**) or in low glucose (1 g/l glucose, **J–L**) media were treated with H_2O_2 (800 μM), PEITC (10 μM), rotenone (2 μM), piericidin (50 μM), mVES (10 μM), myxothiazol (25 μM), CCCP (75 μM), oligomycin (2.5 μM) for 1 h and then stained using the DCF fluorescent probe. Data are expressed relative to the non-treated controls and represent the mean ± S.E.M. of more than 4 independent experiments. The symbol * indicates values significantly different in proliferating and quiescent cells.

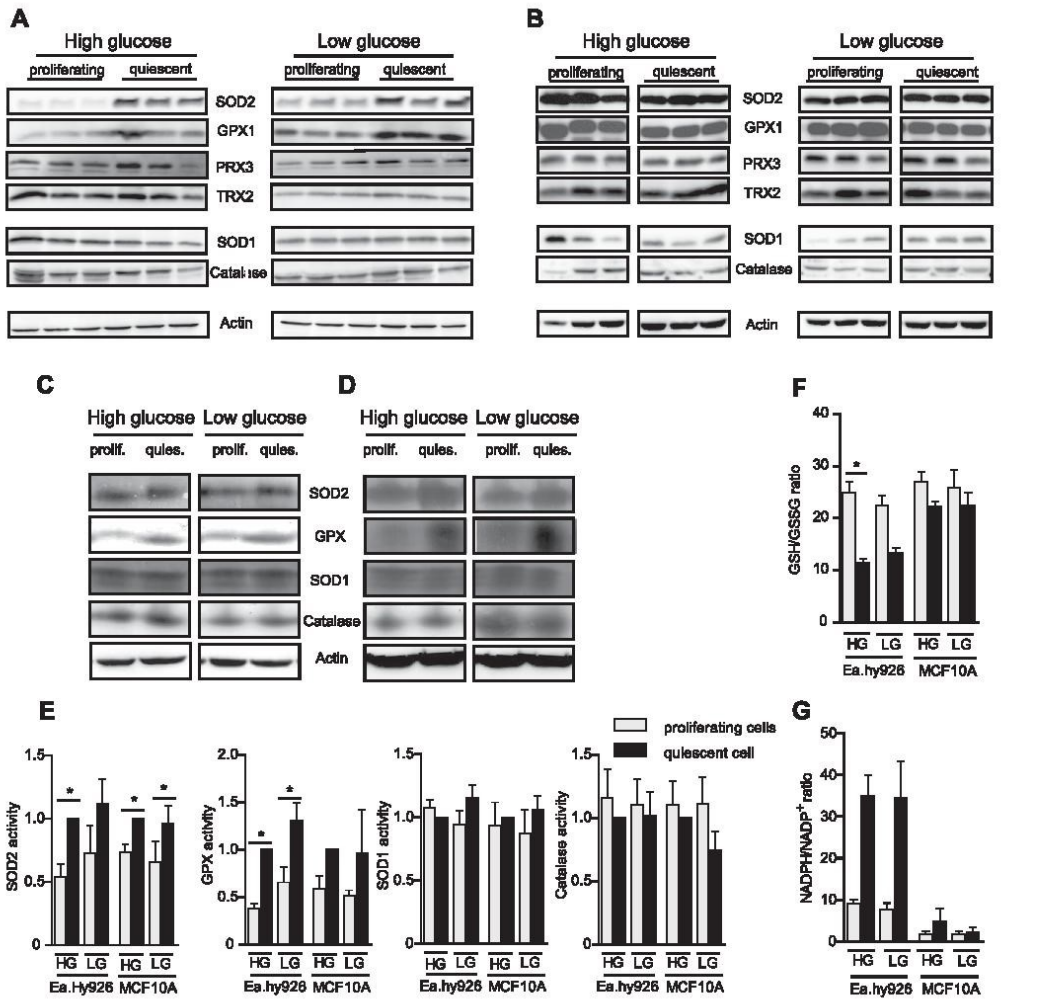

Fig. 6. Activity of antioxidant defense is increased in quiescent cells. Whole cell lysates from **(A)** Ea.hy926 and **(B)** MCF10A cultured in high and low glucose media were assessed by WB for expression of the indicated antioxidant proteins. Data represent 3 independent experiments. **(C–E)** In-gel activities of indicated antioxidant enzymes were assessed in **(C)** Ea.hy926 and **(D)** MCF10A cells in high and low glucose media. **(E)** Data were quantified by densitometry, and correlated to quiescent cells in high glucose media. Data shown are means ± S.E.M. of at least 4 independent experiments. **(F, G)** GSH/GSSG ratio **(F)** and NADPH/NADP+ ratio **(G)** was determined by luminescence assay in whole cell extracts. Data shown are means ± S.E.M., n = 4. The symbol * indicates significantly different values between proliferating and quiescent cells.

that the enzymatic activity of GPX and SOD2, but not that of SOD1 or catalase, is increased in quiescent cells (Fig. 6D, quantified in Fig. 6E). This was again independent of glucose concentration. Furthermore, the ratio of reduced to oxidized glutathione was reduced and NADPH/NADP ratios were increased in quiescent cells (Fig. 6F, G). Collectively, this suggests that the mitochondrial antioxidant defense is more active in quiescent cells and these cells are well equipped to deal with the oxidative insult induced by ETC inhibition.

3.7. Antioxidant defense is functionally relevant in protection of quiescent cells from ETC blockade-induced cell death

To evaluate the functional relevance of the elevated antioxidant defense for the protection of quiescent cells from ETC-induced cell death under the condition where glucose is not limiting, we used lentiviral delivery of shRNA to suppress its individual protein components. We performed these experiments in Ea.hy926 cells, as the down-regulation of antioxidant defense components was only poorly tolerated by MCF10A cells. SOD2 controls mitochondrial superoxide, which is the major ROS species produced when ETC is blocked [11]. Down-regulation of SOD2 by a specific shRNA resulted in a significantly increased cell death upon treatment of quiescent cells with ETC inhibitors, while little or no effect of SOD2 knockdown was observed in proliferating cells (Fig. 7A). This was accompanied by increased ROS production in quiescent cells, as assessed both by dihydroethidium (DHE), a fluorescent probe that preferentially detects superoxide, and

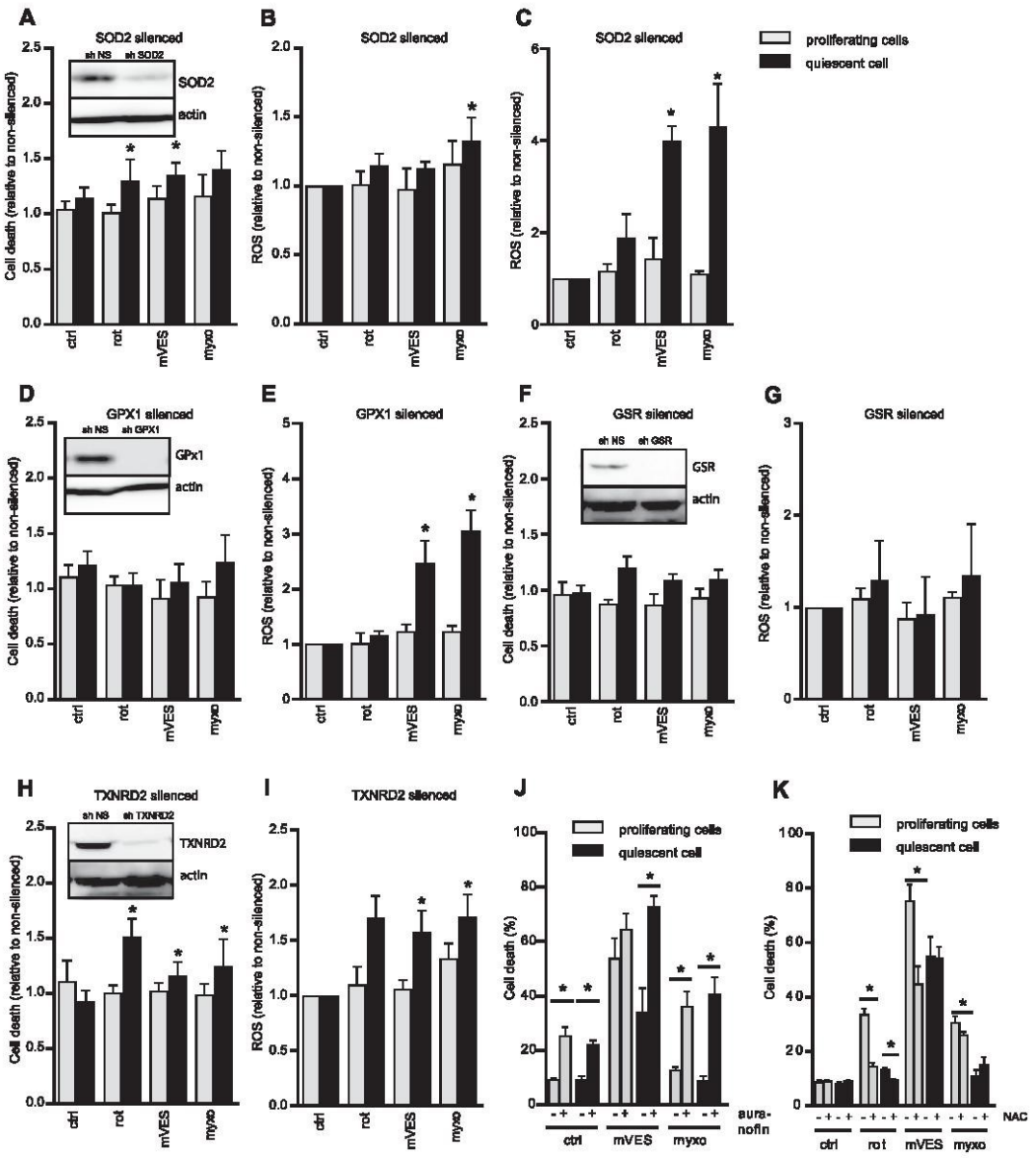

Fig. 7. Antioxidant defense protects quiescent cells from cell death when glucose is not limiting. (A–C) Ea.hy926 cells were silenced for SOD2 and assessed for (**A**) cell death by the Annexin V-FITC/ PI method, (**B**) ROS production by DHE and (**C**) DCF. (**D, E**) GPX1-silenced cells were assessed for (**D**) cell death and (**E**) ROS production by DCF. (**F, G**) GSR silenced cells were assessed (**F**) for cell death and (**G**) ROS production by DCF. (**H, I**) TXNRD2-silenced cells were assessed for (**H**) cell death and (**I**) ROS production by DCF. Data represent means ± S.E.M., n ≥ 4, are given relative to cells expressing non-silencing shRNA treated in the identical manner, and measured as described in the legends to Figs. 3 and 5. The symbol * indicates values significantly different between cells expressing specific shRNA and non-silencing shRNA. (**J**) Cell were pre-treated by auranofin (0.75 μM) for 2 h, followed by MitoVES (mVES, 10 μM) and myxothiazol (myxo, 15 μM) treatment. After 22 h, cell death was assessed using Annexin V-FITC/ PI staining. Data are shown as means ± S.E.M. of at least 5 independent experiments. (**K**) Cells were pre-treated with NAC (1 mM) for 1 h, followed by rotenone (5 μM), MitoVES (mVES, 10 μM) and myxothiazol (myxo, 15 μM) treatment. After 22 h, cell death was assessed using Annexin V-FITC/PI staining. Data shown are means ± S.E.M., n ≥ 5. The symbol * indicates values significantly different with or without (**J**) auranofin and (**K**) NAC pre-treatment.

by DCF, a more general oxidative stress indicator (Fig. 7B,C). We then knocked down GPX1, which inactivates hydrogen peroxide in mitochondria in a glutathione-dependent manner. GPX1 knock-down had much less effect on cell death upon application of ETC inhibitors in quiescent cells than SOD2 knockdown (Fig. 7D), but resulted in an increased ROS signal (Fig. 7E). This indicates that in GPX1 knock-down cells, ROS is uncoupled from cell death. Similar to GPX1, knock-down of glutathione reductase (GSR), a glutathione recycling enzyme, did not significantly increase cell death in quiescent cells (Fig. 7F), and the effect on ROS was moderate (Fig. 7G). Finally, interference with thioredoxin reductase 2 (TXNRD2), a mitochondrial thioredoxin recycling enzyme [34], significantly increased cell death (Fig. 7H), and also increased ROS generation (Fig. 7I). In line with the shRNA data, thioredoxin reductase inhibitor auranofin-dependent cell death was increased in quiescent cells treated with ETC inhibitors more than in proliferating cells (Fig. 7J).

To complement the above results, we also took an inverse approach and boosted the available antioxidant capacity by administration of the antioxidant N-acetyl cysteine (NAC). While little or no effect of this treatment was observed in quiescent cells, a significant reduction in cell death was detected in proliferating cells (Fig. 7K). Importantly, in low glucose media the knock downs of antioxidant enzymes described above did not affect cell death in quiescent cells (Fig. S4A–D), in line with the notion that ROS are not the causal agents of cell death in that situation. Collectively, these results demonstrate that antioxidant defense is functionally relevant in protecting quiescent cells from cell death, and determines to a large degree their sensitivity to ETC inhibition in a situation when cells are not affected by nutrient limitation.

4. Discussion

Targeting of the ETC holds promise for cancer therapy and has demonstrated its efficacy and low toxicity in multiple pre-clinical cancer models [5,6,8]. Considerable effort has been invested in uncovering the rules that govern susceptibility of cancer cells to ETC inhibition-induced cell death and a direct correlation has been found between oxygen consumption, assembly of ETC SCs and sensitivity to ETC disruption [5]. On the other hand, the question why these ETC disrupting agents are well tolerated on the organismal level and in non-cancerous cells has received much less attention, even though it is of high importance for efficient and save cancer therapy. For this reason, the key finding of the present study is that the elevated antioxidant defense in non-proliferating cells ensures resistance to ETC inhibition in a situation when glucose is not limiting.

Most somatic cells in an organisms are in a quiescent, post-mitotic state, and features associated with quiescence may play an important role in resistance to ETC inhibition, as suggested by our previous work [20,21]. In the current study we found that quiescent cells feature increased respiration, elevated SC assembly and mitochondria that produce more NADH, consistent with fully active TCA cycle [26]. Apparently, the ETC gains prominence in quiescence, and quiescent non-transformed cells should be susceptible to cell death induced by ETC inhibition, resulting either from increased ROS generation or mitochondrial ATP loss (discussed below). Elevated NADH is expected to stimulate ROS generation from the ETC [11]. Indeed, NADH accumulation is efficiently induced in mitochondria of quiescent cells upon ETC blockade.

Notwithstanding the above reasoning, inhibition of ETC under ample glucose supply leads to reduced ROS production and reduced cell death in quiescent cells when compared to proliferating cells, suggesting that ROS detoxification is increased in quiescent cells as proposed previously [35–37]. Data presented herein point to ROS, and not to ATP depletion, being the dominant factor in cell death induction upon ETC inhibition in quiescent cells when glucose is not limiting, and imply that ROS detoxification, not the ETC status or increased ETC-mediated ATP production, determine sensitivity to cell death in quiescent cells. This is in direct contrast to cancer cells, where correlation between ETC activity/assembly and the efficacy of ETC inhibitors to induce cell death has been established in multiple studies [4,5,17,18,38,39]. Furthermore, it is in line with reports showing that redox modulation may be an effective anti-cancer strategy [31,40].

Pharmacological and genetic manipulations of SOD2 and TXNRD2, the mitochondrial thioredoxin reductase [34], revealed that the SOD2 - thioredoxin axis plays a principal role in efficient protection of quiescent cells from ETC blockade-induced ROS and cell death. In contrast, interference with the glutathione system (GPX1 and GSR) led to some elevation of ROS upon ETC blockade in quiescent cells without increase in cell death, suggesting that this system plays a less important role in quiescent cells. This is consistent with the notion that superoxide is the primary species of ROS-induced damage, possibly leading to direct oxidation of various mitochondrial components [41–43]. The thioredoxin system may counter this oxidative damage, consistent with its role in the regulation of cell death [14,44–46]. In agreement, deletion of SOD2, TRX2 or TXNRD2 in mice is incompatible with life [47–49], while genetic inactivation of GSR or GPX1 is not associated with lethality [50,51].

The sensitivities of proliferating vs. quiescent cells to ETC inhibition change dramatically in the conditions of glucose limitation. Here, a substantial decrease of cellular ATP upon ETC blockade in quiescent cells was observed, which correlates with increased cell death. Downregulation of antioxidant defense components did not increase cell death any further, suggesting that cell death in this situation is largely ROS-independent, instead relating to acute bioenergetic stress. In contrast to quiescent cells, proliferating cells strongly upregulate glucose uptake upon ETC suppression by increasing the level of glucose transporters, which likely compensates for the loss of ATP production in mitochondria. This effect may be particularly important for scavenging glucose when its availability is low, and may explain why quiescent cells are more sensitive to ETC inhibition when glucose is below its normal physiological range. A similar mechanism has been reported in cancer cells, where the failure to upregulate glucose transporters and glucose uptake sensitized to ETC inhibition only when glucose availability was limiting [52].

To interpret the results of this study, it is important to realize that the high and low glucose media represent situations of ample and limited glucose supply. In low glucose media, the glucose concentrations found in our system within the time frame of the experiment are much lower than those that are regularly encountered *in vivo* in well perfused tissues [32,53]. In fact, when ETC inhibitors were applied in fresh low (1 g/l) glucose media corresponding to the physiological 5 mM glucose concentration, no ATP depletion was observed. This means that in normal healthy tissues where perfusion is intact, glucose does not present a limiting factor, and it is expected that effective inactivation of ETC blockade-induced ROS by antioxidant defense will play the primary role in governing sensitivity. On the other hand, in poorly perfused regions, such as hypoxic areas of tumors where the availability of nutrients is low, the application of ETC inhibitors may significantly accelerate cell death in a ROS-independent manner. This is consistent with reports of low glucose availability in tumors [53–55], and with previous findings showing that ETC inhibition was highly effective in non-perfused hypoxic regions [56]. We therefore propose that the mechanism for the observed selectivity of ETC inhibition in cancer is two-fold. First, elevated antioxidant defense limits ROS production upon ETC inhibition in somatic quiescent cells that do not suffer from glucose limitation, the large majority of cells in an organism. Second, in poorly perfused tumors where glucose is limiting, the application of ETC inhibitors will lead to a bioenergetic catastrophe, amplifying the ROS-related effects, and broadening effectivity to cancer cells that might have a ‘quiescent’-like phenotype [17].

The mechanism discussed above is not exhaustive, particularly because not all somatic cells in the body are quiescent. In addition, factors specific to each ETC inhibitor, such as its pharmacological properties,

blood-brain barrier penetrance, specific accumulation in tumor tissues and off-target effects will also be important, and so will be the rate of ROS production induced by the inhibitor for the given level of ETC suppression. Consistent with this, we propose that ETC inhibitors that induce maximal ROS will kill proliferating cancer cells most efficiently. Yet, this study introduces a general concept that is relevant to all ETC-targeted agents that produce ROS, and describes the molecular mechanisms with the potential to contribute to the specificity observed [5,19]. To conclude, ETC targeting represent a new, promising approach for treatment of multiple cancer types, including neoplasias that are difficult-to-treat, and resistant populations of cancer cells within tumors [5,16,18,38]. As such, this study is relevant for future development and optimization of very interesting, novel anti-cancer agents that target the ETC and present potential broad-spectrum therapeutics for a range of malignancies.

5. Conclusion

In summary, we propose that specificity of ETC inhibition in cancer is in part conferred by the increased antioxidant defense in non-proliferating non-transformed cells. ROS production from the ETC is the dominant factor that determines susceptibility to cell death induced by ETC disruption in a situation when glucose is not limiting. Hence, ETC inhibitors that induce maximal ROS will kill proliferating cancer cells most efficiently while maintaining specificity. On the other hand, in a situation of glucose limitation characteristic for tumors, ATP depletion upon ETC disruption gains prominence, and non-proliferating cells become highly susceptible to cell death because they are unable to upregulate glucose uptake. This will supplement the ROS-related effects and optimize impact towards cancer, including cancer cells with a dormant-like phenotype.

Funding sources

This work was supported by Czech Science Foundation [Grants nos. 16-22823S, 17-20904S, 16-12719S], Czech Health Research Council [Grant no. 16-31604A], Grant Agency of Charles University [Grant no. GAUK 98215], ERDF and MEYS CR [CZ.1.05/1.1.00/02.0109 BIOCEV, LQ1604 NPU II], institutional support from Czech Academy of Sciences [RVO: 86652036]. Imaging Methods Core Facility at BIOCEV is supported by large infrastructure Czech-BioImaging project provided by MEYS [LM2015062]. Funders had no involvement in study design, the collection, analysis or interpretation of data.

Author's disclosure statement

J.N. is an inventor of a patent 'Tamoxifen analogues for treatment of neoplastic diseases, especially with high Her2 protein level'. The authors declare no additional competing financial interests.

Acknowledgements

We would like to thank the Imaging Methods Core Facility at BIOCEV, Faculty of Science, Charles University MEYS [LM2015062], for their support with obtaining imaging and flow cytometry data presented in this paper.

Appendix A. Supplementary material

Supplementary data associated with this article can be found in the online version at http://dx.doi.org/10.1016/j.freeradbiomed.2017.07.033.

References

[1] A.S. Tan, J.W. Baty, L.F. Dong, A. Bezawork-Geleta, B. Endaya, J. Goodwin, M. Bajzikova, J. Kovarova, M. Peterka, B. Yan, E.A. Pesdar, M. Sobol, A. Filimonenko, S. Stuart, M. Vondrusova, K. Kluckova, K. Sachaphibulkij, J. Rohlena, P. Hozak, J. Truksa, D. Eccles, L.M. Haupt, L.R. Griffiths, J. Neuzil, M.V. Berridge, Mitochondrial genome acquisition restores respiratory function and tumorigenic potential of cancer cells without mitochondrial DNA, Cell Metab. 21 (1) (2015) 81–94.

[2] F. Weinberg, R. Hamanaka, W.W. Wheaton, S. Weinberg, J. Joseph, M. Lopez, B. Kalyanaraman, G.M. Mutlu, G.R. Budinger, N.S. Chandel, Mitochondrial metabolism and ROS generation are essential for Kras-mediated tumorigenicity, Proc. Natl. Acad. Sci. USA 107 (19) (2010) 8788–8793.

[3] L.F. Dong, J. Kovarova, M. Bajzikova, A. Bezawork-Geleta, D. Svec, B. Endaya, K. Sachaphibulkij, A.R. Coelho, N. Sebkova, A. Ruzickova, A.S. Tan, K. Kluckova, K. Judasova, K. Zamecnikova, Z. Rychtarcikova, V. Gopalan, L. Andera, M. Sobol, B. Yan, B. Pattnaik, N. Bhatraju, J. Truksa, P. Stopka, P. Hozak, A.K. Lam, R. Sedlacek, P.J. Oliveira, M. Kubista, A. Agrawal, K. Dvorakova-Hortova, J. Rohlena, M.V. Berridge, J. Neuzil, Horizontal transfer of whole mitochondria restores tumorigenic potential in mitochondrial DNA-deficient cancer cells, Elife 6 (2017).

[4] K. Kluckova, M. Sticha, J. Cerny, T. Mracek, L. Dong, Z. Drahota, E. Gottlieb, J. Neuzil, J. Rohlena, Ubiquinone-binding site mutagenesis reveals the role of mitochondrial complex II in cell death initiation, Cell Death Dis. 6 (2015) e1749.

[5] K. Rohlenova, K. Sachaphibulkij, J. Stursa, A. Bezawork-Geleta, J. Blecha, B. Endaya, L. Werner, J. Cerny, R. Zobalova, J. Goodwin, T. Spacek, E. Alizadeh Pesdar, B. Yan, M.N. Nguyen, M. Vondrusova, M. Sobol, P. Jezek, P. Hozak, J. Truksa, J. Rohlena, L.F. Dong, J. Neuzil, Selective disruption of respiratory supercomplexes as a new strategy to suppress Her2high breast cancer, Antioxid. Redox Signal. 26 (2) (2017) 84–103.

[6] L.F. Dong, V.J. Jameson, D. Tilly, J. Cerny, E. Mahdavian, A. Marin-Hernandez, L. Hernandez-Esquivel, S. Rodriguez-Enriquez, J. Stursa, P.K. Witting, B. Stantic, J. Rohlena, J. Truksa, K. Kluckova, J.C. Dyason, M. Ledvina, B.A. Salvatore, R. Moreno-Sanchez, M.J. Coster, S.J. Ralph, R.A. Smith, J. Neuzil, Mitochondrial targeting of vitamin E succinate enhances its pro-apoptotic and anti-cancer activity via mitochondrial complex II, J. Biol. Chem. 286 (5) (2011) 3717–3728.

[7] J. Rohlena, L.F. Dong, S.J. Ralph, J. Neuzil, Anticancer drugs targeting the mitochondrial electron transport chain, Antioxid. Redox Signal. 15 (12) (2011) 2951–2974.

[8] G. Cheng, J. Zielonka, O. Ouari, M. Lopez, D. McAllister, K. Boyle, C.S. Barrios, J.J. Weber, B.D. Johnson, M. Hardy, M.B. Dwinell, B. Kalyanaraman, Mitochondria-targeted analogues of metformin exhibit enhanced antiproliferative and radiosensitizing effects in pancreatic cancer cells, Cancer Res. 76 (13) (2016) 3904–3915.

[9] H. Schagger, K. Pfeiffer, Supercomplexes in the respiratory chains of yeast and mammalian mitochondria, EMBO J. 19 (8) (2000) 1777–1783.

[10] R. Acin-Perez, P. Fernandez-Silva, M.L. Peleato, A. Perez-Martos, J.A. Enriquez, Respiratory active mitochondrial supercomplexes, Mol. Cell 32 (4) (2008) 529–539.

[11] M.P. Murphy, How mitochondria produce reactive oxygen species, Biochem. J. 417 (1) (2009) 1–13.

[12] M.D. Brand, Mitochondrial generation of superoxide and hydrogen peroxide as the source of mitochondrial redox signaling, Free Radic. Biol. Med. 100 (2016) 14–31.

[13] T. Rabilloud, M. Heller, M.P. Rigobello, A. Bindoli, R. Aebersold, J. Lunardi, The mitochondrial antioxidant defence system and its response to oxidative stress, Proteomics 1 (9) (2001) 1105–1110.

[14] A.G. Cox, C.C. Winterbourn, M.B. Hampton, Mitochondrial peroxiredoxin involvement in antioxidant defence and redox signalling, Biochem. J. 425 (2) (2009) 313–325.

[15] M. Mari, A. Morales, A. Colell, C. Garcia-Ruiz, J.C. Fernandez-Checa, Mitochondrial glutathione, a key survival antioxidant, Antioxid. Redox Signal. 11 (11) (2009) 2685–2700.

[16] R. Haq, J. Shoag, P. Andreu-Perez, S. Yokoyama, H. Edelman, G.C. Rowe, D.T. Frederick, A.D. Hurley, A. Nellore, A.L. Kung, J.A. Wargo, J.S. Song, D.E. Fisher, Z. Arany, H.R. Widlund, Oncogenic BRAF regulates oxidative metabolism via PGC1alpha and MITF, Cancer Cell 23 (3) (2013) 302–315.

[17] A. Viale, P. Pettazzoni, C.A. Lyssiotis, H. Ying, N. Sanchez, M. Marchesini, A. Carugo, T. Green, S. Seth, V. Giuliani, M. Kost-Alimova, F. Muller, S. Colla, L. Nezi, G. Genovese, A.K. Deem, A. Kapoor, W. Yao, E. Brunetto, Y. Kang, M. Yuan, J.M. Asara, Y.A. Wang, T.P. Heffernan, A.C. Kimmelman, H. Wang, J.B. Fleming, L.C. Cantley, R.A. DePinho, G.F. Draetta, Oncogene ablation-resistant pancreatic cancer cells depend on mitochondrial function, Nature 514 (7524) (2014) 628–632.

[18] A. Roesch, A. Vultur, I. Bogeski, H. Wang, K.M. Zimmermann, D. Speicher, C. Korbel, M.W. Laschke, P.A. Gimotty, S.E. Philipp, E. Krause, S. Patzold, J. Villanueva, C. Krepler, M. Fukunaga-Kalabis, M. Hoth, B.C. Bastian, T. Vogt, M. Herlyn, Overcoming intrinsic multidrug resistance in melanoma by blocking the mitochondrial respiratory chain of slow-cycling JARID1B(high) cells, Cancer Cell 23 (6) (2013) 811–825.

[19] L.F. Dong, V.J. Jameson, D. Tilly, L. Prochazka, J. Rohlena, K. Valis, J. Truksa, R. Zobalova, E. Mahdavian, K. Kluckova, M. Stantic, J. Stursa, R. Freeman, P.K. Witting, E. Norberg, J. Goodwin, B.A. Salvatore, J. Novotna, J. Turanek, M. Ledvina, P. Hozak, B. Zhivotovsky, M.J. Coster, S.J. Ralph, R.A. Smith, J. Neuzil, Mitochondrial targeting of alpha-tocopheryl succinate enhances its pro-apoptotic efficacy: a new paradigm for effective cancer therapy, Free Radic. Biol. Med. 50 (11) (2011) 1546–1555.

[20] J. Rohlena, L.F. Dong, K. Kluckova, R. Zobalova, J. Goodwin, D. Tilly, J. Stursa, A. Pecinova, A. Philimonenko, P. Hozak, J. Banerjee, M. Ledvina, C.K. Sen, J. Houstek, M.J. Coster, J. Neuzil, Mitochondrially targeted alpha-tocopheryl succinate is antiangiogenic: potential benefit against tumor angiogenesis but caution against wound healing, Antioxid. Redox Signal. 15 (12) (2011) 2923–2935.

[21] L.F. Dong, E. Swettenham, J. Eliasson, X.F. Wang, M. Gold, Y. Medunic, M. Stantic, P. Low, L. Prochazka, P.K. Witting, J. Turanek, E.T. Akporiaye, S.J. Ralph, J. Neuzil, Vitamin E analogues inhibit angiogenesis by selective induction of apoptosis in proliferating endothelial cells: the role of oxidative stress, Cancer Res. 67 (24) (2007) 11906–11913.
[22] J. Truksa, L.F. Dong, J. Rohlena, J. Stursa, M. Vondrusova, J. Goodwin, M. Nguyen, K. Kluckova, Z. Rychtarcikova, S. Lettlova, J. Spacilova, M. Stapelberg, M. Zoratti, J. Neuzil, Mitochondrially targeted vitamin E succinate modulates expression of mitochondrial DNA transcripts and mitochondrial biogenesis, Antioxid. Redox Signal. 22 (11) (2015) 883–900.
[23] S. Schmitt, F. Saathoff, L. Meissner, E.M. Schropp, J. Lichtmannegger, S. Schulz, C. Eberhagen, S. Borchard, M. Aichler, J. Adamski, N. Plesnila, S. Rothenfusser, G. Kroemer, H. Zischka, A semi-automated method for isolating functionally intact mitochondria from cultured cells and tissue biopsies, Anal. Biochem. 443 (1) (2013) 66–74.
[24] M. Vondrusova, A. Bezawork-Geleta, K. Sachaphibulkij, J. Truksa, J. Neuzil, The effect of mitochondrially targeted anticancer agents on mitochondrial (super) complexes, Methods Mol. Biol. 1265 (2015) 195–208.
[25] C.J. Weydert, J.J. Cullen, Measurement of superoxide dismutase, catalase and glutathione peroxidase in cultured cells and tissue, Nat. Protoc. 5 (1) (2010) 51–66.
[26] J.M. Lemons, X.J. Feng, B.D. Bennett, A. Legesse-Miller, E.L. Johnson, I. Raitman, E.A. Pollina, H.A. Rabitz, J.D. Rabinowitz, H.A. Coller, Quiescent fibroblasts exhibit high metabolic activity, PLoS Biol. 8 (10) (2010) e1000514.
[27] S. Schoors, K. De Bock, A.R. Cantelmo, M. Georgiadou, B. Ghesquiere, S. Cauwenberghs, A. Kuchnio, B.W. Wong, A. Quaegebeur, J. Goveia, F. Bifari, X. Wang, R. Blanco, B. Tembuyser, I. Cornelissen, A. Bouche, S. Vinckier, S. Diaz-Moralli, H. Gerhardt, S. Telang, M. Cascante, J. Chesney, M. Dewerchin, P. Carmeliet, Partial and transient reduction of glycolysis by PFKFB3 blockade reduces pathological angiogenesis, Cell Metab. 19 (1) (2014) 37–48.
[28] I. Diamond, A. Legg, J.A. Schneider, E. Rozengurt, Glycolysis in quiescent cultures of 3T3 cells. Stimulation by serum, epidermal growth factor, and insulin in intact cells and persistence of the stimulation after cell homogenization, J. Biol. Chem. 253 (3) (1978) 866–871.
[29] E. Maranzana, G. Barbero, A.I. Falasca, G. Lenaz, M.L. Genova, Mitochondrial respiratory supercomplex association limits production of reactive oxygen species from complex I, Antioxid. Redox Signal. 19 (13) (2013) 1469–1480.
[30] J.A. Letts, K. Fiedorczuk, L.A. Sazanov, The architecture of respiratory supercomplexes, Nature 537 (7622) (2016) 644–648.
[31] D. Trachootham, Y. Zhou, H. Zhang, Y. Demizu, Z. Chen, H. Pelicano, P.J. Chiao, G. Achanta, R.B. Arlinghaus, J. Liu, P. Huang, Selective killing of oncogenically transformed cells through a ROS-mediated mechanism by beta-phenylethyl isothiocyanate, Cancer Cell 10 (3) (2006) 241–252.
[32] M.Z. Shrayyef, J.E. Gerich, Normal glucose homeostasis, in: L. Poretsky (Ed.), Principles of Diabetes Mellitus, Springer, US, Boston, MA, 2010, pp. 19–35.
[33] M. Mueckler, B. Thorens, The SLC2 (GLUT) family of membrane transporters, Mol. Asp. Med. 34 (2–3) (2013) 121–138.
[34] S.R. Lee, J.R. Kim, K.S. Kwon, H.W. Yoon, R.L. Levine, A. Ginsburg, S.G. Rhee, Molecular cloning and characterization of a mitochondrial selenocysteine-containing thioredoxin reductase from rat liver, J. Biol. Chem. 274 (8) (1999) 4722–4734.
[35] G.J. Kops, T.B. Dansen, P.E. Polderman, I. Saarloos, K.W. Wirtz, P.J. Coffer, T.T. Huang, J.L. Bos, R.H. Medema, B.M. Burgering, Forkhead transcription factor FOXO3a protects quiescent cells from oxidative stress, Nature 419 (6904) (2002) 316–321.
[36] E.H. Sarsour, S. Venkataraman, A.L. Kalen, L.W. Oberley, P.C. Goswami, Manganese superoxide dismutase activity regulates transitions between quiescent and proliferative growth, Aging Cell 7 (3) (2008) 405–417.
[37] J. Naderi, M. Hung, S. Pandey, Oxidative stress-induced apoptosis in dividing fibroblasts involves activation of p38 MAP kinase and over-expression of Bax: resistance of quiescent cells to oxidative stress, Apoptosis 8 (1) (2003) 91–100.
[38] B. Yan, M. Stantic, R. Zobalova, A. Bezawork-Geleta, M. Stapelberg, J. Stursa, K. Prokopova, L. Dong, J. Neuzil, Mitochondrially targeted vitamin E succinate efficiently kills breast tumour-initiating cells in a complex II-dependent manner, BMC Cancer 15 (2015) 401.
[39] S. Boukalova, J. Stursa, L. Werner, Z. Ezrova, J. Cerny, A. Bezawork-Geleta, A. Pecinova, L. Dong, Z. Drahota, J. Neuzil, Mitochondrial targeting of metformin enhances its activity against pancreatic cancer, Mol. Cancer Ther. 15 (12) (2016) 2875–2886.
[40] D. Trachootham, J. Alexandre, P. Huang, Targeting cancer cells by ROS-mediated mechanisms: a radical therapeutic approach? Nat. Rev. Drug Discov. 8 (7) (2009) 579–591.
[41] Z. Dong, S. Shanmughapriya, D. Tomar, N. Siddiqui, S. Lynch, N. Nemani, S.L. Breves, X. Zhang, A. Tripathi, P. Palaniappan, M.F. Riitano, A.M. Worth, A. Seelam, E. Carvalho, R. Subbiah, F. Jana, J. Soboloff, Y. Peng, J.Y. Cheung, S.K. Joseph, J. Caplan, S. Rajan, P.B. Stathopulos, M. Madesh, Mitochondrial Ca2+ uniporter is a mitochondrial luminal redox sensor that augments MCU channel activity, Mol. Cell 65 (6) (2017) (1014-1028e7).
[42] V.E. Kagan, V.A. Tyurin, J. Jiang, Y.Y. Tyurina, V.B. Ritov, A.A. Amoscato, A.N. Osipov, N.A. Belikova, A.A. Kapralov, V. Kini, Vlasova II, Q. Zhao, M. Zou, P. Di, D.A. Svistunenko, I.V. Kurnikov, G.G. Borisenko, Cytochrome c acts as a cardiolipin oxygenase required for release of proapoptotic factors, Nat. Chem. Biol. 1 (4) (2005) 223–232.
[43] M. Ott, J.D. Robertson, V. Gogvadze, B. Zhivotovsky, S. Orrenius, Cytochrome c release from mitochondria proceeds by a two-step process, Proc. Natl. Acad. Sci. USA 99 (3) (2002) 1259–1263.
[44] K.K. Brown, S.E. Eriksson, E.S. Arner, M.B. Hampton, Mitochondrial peroxiredoxin 3 is rapidly oxidized in cells treated with isothiocyanates, Free Radic. Biol. Med. 45 (4) (2008) 494–502.
[45] A.G. Cox, K.K. Brown, E.S. Arner, M.B. Hampton, The thioredoxin reductase inhibitor auranofin triggers apoptosis through a Bax/Bak-dependent process that involves peroxiredoxin 3 oxidation, Biochem. Pharmacol. 76 (9) (2008) 1097–1109.
[46] Y. Chen, J. Cai, D.P. Jones, Mitochondrial thioredoxin in regulation of oxidant-induced cell death, FEBS Lett. 580 (28–29) (2006) 6596–6602.
[47] M. Conrad, C. Jakupoglu, S.G. Moreno, S. Lippl, A. Banjac, M. Schneider, H. Beck, A.K. Hatzopoulos, U. Just, F. Sinowatz, W. Schmahl, K.R. Chien, W. Wurst, G.W. Bornkamm, M. Brielmeier, Essential role for mitochondrial thioredoxin reductase in hematopoiesis, heart development, and heart function, Mol. Cell. Biol. 24 (21) (2004) 9414–9423.
[48] L. Nonn, R.R. Williams, R.P. Erickson, G. Powis, The absence of mitochondrial thioredoxin 2 causes massive apoptosis, exencephaly, and early embryonic lethality in homozygous mice, Mol. Cell. Biol. 23 (3) (2003) 916–922.
[49] Y. Li, T.T. Huang, E.J. Carlson, S. Melov, P.C. Ursell, J.L. Olson, L.J. Noble, M.P. Yoshimura, C. Berger, P.H. Chan, D.C. Wallace, C.J. Epstein, Dilated cardiomyopathy and neonatal lethality in mutant mice lacking manganese superoxide dismutase, Nat. Genet. 11 (4) (1995) 376–381.
[50] L.K. Rogers, T. Tamura, B.J. Rogers, S.E. Welty, T.N. Hansen, C.V. Smith, Analyses of glutathione reductase hypomorphic mice indicate a genetic knockout, Toxicol. Sci. 82 (2) (2004) 367–373.
[51] Y.S. Ho, J.L. Magnenat, R.T. Bronson, J. Cao, M. Gargano, M. Sugawara, C.D. Funk, Mice deficient in cellular glutathione peroxidase develop normally and show no increased sensitivity to hyperoxia, J. Biol. Chem. 272 (26) (1997) 16644–16651.
[52] K. Birsoy, R. Possemato, F.K. Lorbeer, E.C. Bayraktar, P. Thiru, B. Yucel, T. Wang, W.W. Chen, C.B. Clish, D.M. Sabatini, Metabolic determinants of cancer cell sensitivity to glucose limitation and biguanides, Nature 508 (7494) (2014) 108–112.
[53] T.B. Rodrigues, E.M. Serrao, B.W. Kennedy, D.E. Hu, M.I. Kettunen, K.M. Brindle, Magnetic resonance imaging of tumor glycolysis using hyperpolarized 13C-labeled glucose, Nat. Med. 20 (1) (2014) 93–97.
[54] A. Hirayama, K. Kami, M. Sugimoto, M. Sugawara, N. Toki, H. Onozuka, T. Kinoshita, N. Saito, A. Ochiai, M. Tomita, H. Esumi, T. Soga, Quantitative metabolome profiling of colon and stomach cancer microenvironment by capillary electrophoresis time-of-flight mass spectrometry, Cancer Res. 69 (11) (2009) 4918–4925.
[55] J. Goveia, A. Pircher, L.C. Conradi, J. Kalucka, V. Lagani, M. Dewerchin, G. Eelen, R.J. DeBerardinis, I.D. Wilson, P. Carmeliet, Meta-analysis of clinical metabolic profiling studies in cancer: challenges and opportunities, EMBO Mol. Med. 8 (10) (2016) 1134–1142.
[56] X. Zhang, M. Fryknas, E. Hernlund, W. Fayad, A. De Milito, M.H. Olofsson, V. Gogvadze, L. Dang, S. Pahlman, L.A. Schughart, L. Rickardson, P. D'Arcy, J. Gulibo, P. Nygren, R. Larsson, S. Linder, Induction of mitochondrial dysfunction as a strategy for targeting tumour cells in metabolically compromised microenvironments, Nat. Commun. 5 (2014) 3295.

AUTOPHAGY
https://doi.org/10.1080/15548627.2022.2038898

Taylor & Francis
Taylor & Francis Group

RESEARCH PAPER

OPEN ACCESS Check for updates

Mitochondrial respiration supports autophagy to provide stress resistance during quiescence

Silvia Magalhaes-Novais[a,b], Jan Blecha[a], Ravindra Naraine[a], Jana Mikesova[a], Pavel Abaffy[a], Alena Pecinova[c], Mirko Milosevic[a,b], Romana Bohuslavova[a], Jan Prochazka[d], Shawez Khan[e,†], Eliska Novotna[a,b], Radek Sindelka[a], Radek Machan[b], Mieke Dewerchin[e], Erik Vlcak[d], Joanna Kalucka[f,g], Sona Stemberkova Hubackova[a,h], Ales Benda[b], Jermaine Goveia[e], Tomas Mracek[c], Cyril Barinka[a], Peter Carmeliet[e,f,i], Jiri Neuzil[a,j], Katerina Rohlenova[a,e], and Jakub Rohlena[a]

[a]Institute of Biotechnology, Czech Academy of Sciences, BIOCEV, Vestec, Czech Republic; [b]Faculty of Science, Charles University, Prague, Czech Republic; [c]Institute of Physiology, Czech Academy of Sciences, Prague, Czech Republic; [d]Institute of Molecular Genetics, Czech Academy of Sciences, Prague, Czech Republic; [e]VIB-KU Leuven Center for Cancer Biology, Department of Oncology, KU Leuven, Leuven, Belgium; [f]Department of Biomedicine, Aarhus University, Aarhus, Denmark; [g]Aarhus Institute of Advanced Studies (AIAS), Aarhus University, Aarhus C, Denmark; [h]Centre for Experimental Medicine, Institute for Clinical and Experimental Medicine, Prague, Czech Republic; [i]State Key Laboratory of Ophthalmology, Zhongshan Ophthalmic Center, Sun Yat-sen University, Guangzhou, P. R. China; [j]School of Medical Science, Griffith University, Southport, Qld, Australia

ABSTRACT

Mitochondrial oxidative phosphorylation (OXPHOS) generates ATP, but OXPHOS also supports biosynthesis during proliferation. In contrast, the role of OXPHOS during quiescence, beyond ATP production, is not well understood. Using mouse models of inducible OXPHOS deficiency in all cell types or specifically in the vascular endothelium that negligibly relies on OXPHOS-derived ATP, we show that selectively during quiescence OXPHOS provides oxidative stress resistance by supporting macroautophagy/autophagy. Mechanistically, OXPHOS constitutively generates low levels of endogenous ROS that induce autophagy via attenuation of ATG4B activity, which provides protection from ROS insult. Physiologically, the OXPHOS-autophagy system (i) protects healthy tissue from toxicity of ROS-based anticancer therapy, and (ii) provides ROS resistance in the endothelium, ameliorating systemic LPS-induced inflammation as well as inflammatory bowel disease. Hence, cells acquired mitochondria during evolution to profit from oxidative metabolism, but also built in an autophagy-based ROS-induced protective mechanism to guard against oxidative stress associated with OXPHOS function during quiescence.

Abbreviations: AMPK: AMP-activated protein kinase; AOX: alternative oxidase; Baf A: bafilomycin A_1; CI, respiratory complexes I; DCF-DA: 2′,7′-dichlordihydrofluorescein diacetate; DHE: dihydroethidium; DSS: dextran sodium sulfate; ΔΨmi: mitochondrial inner membrane potential; EdU: 5-ethynyl-2′-deoxyuridine; ETC: electron transport chain; FA: formaldehyde; HUVEC; human umbilical cord endothelial cells; IBD: inflammatory bowel disease; LC3B: microtubule associated protein 1 light chain 3 beta; LPS: lipopolysaccharide; MEFs: mouse embryonic fibroblasts; MTORC1: mechanistic target of rapamycin kinase complex 1; mtDNA: mitochondrial DNA; NAC: N-acetyl cysteine; OXPHOS: oxidative phosphorylation; PCs: proliferating cells; PE: phosphatidylethanolamine; PEITC: phenethyl isothiocyanate; QCs: quiescent cells; ROS: reactive oxygen species; PLA2: phospholipase A2, WB: western blot.

KEYWORDS
ATG4B; biosynthesis; cell death; electron transport chain; endothelial cells; mitochondria; oxidative phosphorylation; oxidative stress; reactive oxygen species

Introduction

Proliferation vs. quiescence is one of the biggest contrasts for a mammalian cell. Proliferating cells in developing organisms or in tumors engage in biosynthesis to build up biomass for rapid cell division and feature fast nucleic acid and protein turnover. In contrast, quiescent cells, which we define here as non-dividing metabolically active cells that represent most somatic cells in an adult organism, primarily need to maintain their long-lived components to support their extended life span [1]. For this reason, stress response pathways and quality control systems such as macroautophagy/autophagy and antioxidant defense are elevated during quiescence [2-6], and quiescent cells are better equipped to withstand oxidative insult [7-9]. Autophagy facilitates elimination of damaged organelles and proteins by segregation into specialized structures called autophagosomes for lysosomal delivery, cargo degradation and recycling [10]. Autophagy is induced by the AMP-activated protein kinase (AMPK) and inhibited by the MTOR (mechanistic target of rapamycin kinase) complex 1 (MTORC1) via ULK1 (unc-51 like autophagy activating kinase 1) [11,12], a central switch in the canonical autophagic signaling. Autophagy can also respond to altered NADH and

CONTACT Jakub Rohlena jakub.rohlena@ibt.cas.cz; Katerina Rohlenova katerina.rohlenova@ibt.cas.cz; Jiri Neuzil j.neuzil@griffith.edu.au Institute of Biotechnology, Czech Academy of Sciences, BIOCEV, Vestec, Czech Republic
[†]Present address: National Center for Cancer Immune Therapy, Department of Oncology, Copenhagen University Hospital, Herlev, Denmark
Supplemental data for this article can be accessed here.

© 2022 The Author(s). Published by Informa UK Limited, trading as Taylor & Francis Group.
This is an Open Access article distributed under the terms of the Creative Commons Attribution-NonCommercial-NoDerivatives License (http://creativecommons.org/licenses/by-nc-nd/4.0/), which permits non-commercial re-use, distribution, and reproduction in any medium, provided the original work is properly cited, and is not altered, transformed, or built upon in any way.

reactive oxygen species (ROS) levels [13-15]. However, these findings come predominantly from proliferating cells and the mechanisms that modulate stress resistance and autophagy during quiescence have not been fully resolved.

Mitochondrial oxidative phosphorylation (OXPHOS) is best known for its role in ATP generation. In this process, respiratory complexes I-IV of the electron transport chain (ETC) produce a proton gradient ($\Delta\Psi_{mi}$) across the inner mitochondrial membrane, which propels ATP synthase. ETC of OXPHOS also supports biosynthesis of essential metabolites, NADH/NAD^+ redox-cycling by complex I (CI), and generation of ROS that arise when electrons transported through the ETC "leak" and react prematurely with oxygen [16]. ROS are potentially damaging but may also have physiological functions [17]. In proliferating cells ETC is required for biosynthesis, primarily for de novo synthesis of pyrimidines that enables DNA/RNA replication/transcription [18-22]. In contrast, ATP generation is considered the dominant function of OXPHOS in quiescent cells, as the limited need of quiescent cells for DNA/RNA synthesis predicts reduced dependence on de novo pyrimidine synthesis. Additional functions of OXPHOS during quiescence, including their contribution to physiology and disease, have not been explored.

Quiescent cells need protection from oxidative damage induced by ROS in pathological settings, such as during cancer therapy or inflammation. Indeed, resistance to oxidative stress maintains anti-inflammatory properties of quiescent vascular endothelium [6]. However, systematic examination of OXPHOS, a prominent intracellular source of damaging ROS, has never been performed in these settings. We hypothesized that OXPHOS could initiate mechanisms that regulate stress resistance of quiescent cells and tissues to counter oxidative damage inherent to its function. Using multiple in vitro and in vivo models of OXPHOS deficiency, we aimed to systematically explore possible mechanistic links between OXPHOS, quiescence, oxidative stress resistance and autophagy, as well as the role of OXPHOS-induced ROS-resistance in pathology.

Results

OXPHOS deficiency sensitizes to oxidative stress in vivo

To explore specific roles of OXPHOS in quiescent cells, we made use of the fact that several essential subunits of OXPHOS complexes (except for complex II) are encoded by mitochondrial (mt)DNA. Removal of mtDNA or a block in its transcription thus results in OXPHOS deficiency (Figure 1A), yielding mitochondria that lack the ETC and maintain $\Delta\Psi_{mi}$ via ATP hydrolysis catalyzed by a subcomplex of ATP synthase (Figure 1A) [23,24]. We applied this approach in adult mice, as adult tissues contain mostly quiescent cells. We therefore generated a mouse model of conditional OXPHOS deficiency by systemic tamoxifen-induced deletion of TFAM (transcription factor A, mitochondrial) (Figure 1A and B), essential for mtDNA maintenance and transcription (*tfam* KO mice, see Materials and Methods, Figure 1B) [25]. Preliminary screening upon induction revealed that TFAM was most consistently deleted in the liver, kidney and pancreas. In these organs the TFAM protein and mtDNA-encoded subunits of OXPHOS complexes were markedly (albeit not fully) reduced in *tfam* KO animals on day 11 post induction (Fig. S1A and B), and in situ measurements of cytochrome c oxidase activity revealed that ETC was suppressed in most cells (Fig. S1C).

We reasoned that if OXPHOS provides stress resistance during quiescence, then OXPHOS-deficient quiescent cells will be sensitized to cell death induced by exogenous administration of pro-oxidant agents. Hence, we challenged control and *tfam* KO mice with phenethylisocyanate (PEITC), a compound which induces ROS independent of the ETC by interfering with the glutathione system [26]. Strikingly, 16 h after a single dose of PEITC *tfam* KO mice displayed a large increase in the number of apoptotic (TUNEL-positive) cells in all tested organs (Figure 1C and D), and we detected increased apoptotic markers, such as CASP3 (caspase 3) activation and PARP1 (poly(ADP-ribose) polymerase 1) cleavage (Figure 1E-G). In contrast, little cell death was observed in untreated or PEITC-treated control mice.

OXPHOS-mediated ROS protection is specific to quiescent cells

To investigate whether OXPHOS deficiency selectively sensitizes quiescent cells to ROS-induced cell death (Figure 2A), we co-stained liver sections (that contain a minor fraction of proliferating cells) for TUNEL and 5-ethynyl-2'-deoxyuridine (EdU), a marker of proliferation. The increased TUNEL signal in PEITC-treated *tfam* KO animals was detected predominantly in EdU-negative cells (Figure 2B and C), suggesting that quiescent cells are indeed selectively sensitized to ROS by OXPHOS ablation in vivo.

To confirm that OXPHOS provides oxidative stress protection selectively in quiescent cells, we used in vitro models where proliferation can be controlled by contact inhibition to directly compare proliferating (PCs) and contact-inhibited quiescent cells (QCs) under defined conditions. We reasoned that ideally the cellular model should not/minimally depend on OXPHOS for energy production. Endothelial cells generate most ATP via glycolysis [27,28], and are therefore expected to cope with the lack of OXPHOS-produced ATP. Indeed, OXPHOS-deficient immortalized EA.hy926 endothelial QCs (ρ^0 cells, see Materials and methods, Fig. S1D) featured normal ATP levels (Fig. S1E), energy charge (Fig. S1F) and mitochondrial content (not shown). Furthermore, OXPHOS deficiency did not compromise contact inhibition or entry into quiescence, as evidenced by correct adherence junction assembly (Fig. S1G), enrichment of cells in the G_0 phase of the cell cycle (Fig. S1H), and arrest of proliferation (Fig. S1I) in the absence of senescence (Fig. S1J). Strikingly, however, OXPHOS-deficient EA.hy926 as well as primary human umbilical cord endothelial cells QCs (HUVEC, sh*TFAM*, Fig. S2A) were markedly sensitized to cell death when exposed to pro-oxidants PEITC or hydrogen peroxide (H_2O_2) (Figure 2D and E, Fig. S2B), while no such effect was observed in corresponding PCs. Similarly, PEITC or H_2O_2 treatment induced more ROS in OXPHOS-deficient QCs (but not in PCs) than

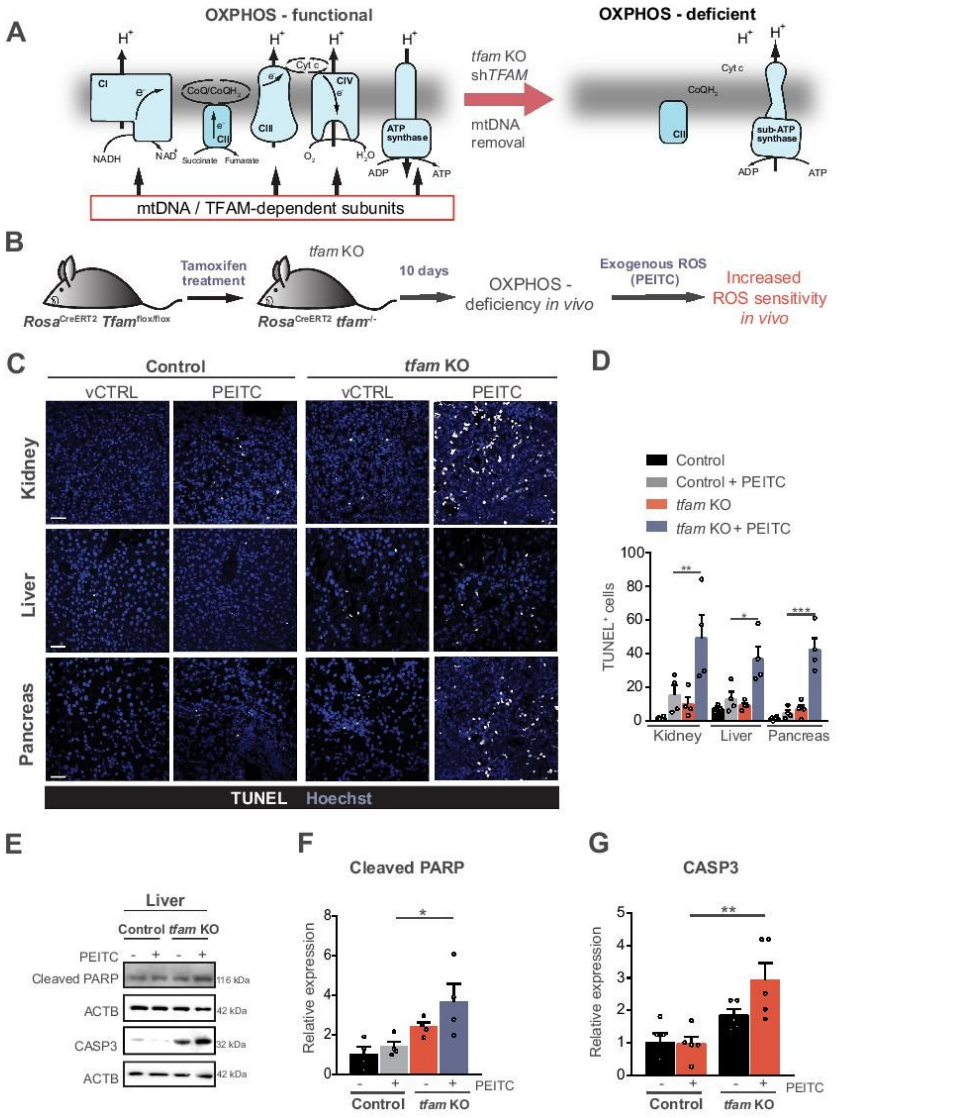

Figure 1. OXPHOS deficiency sensitizes to oxidative stress in vivo. (A) mtDNA removal, *TFAM* silencing or *tfam* deletion results in OXPHOS-deficient cells that lack ETC and contain a subcomplex of ATP synthase (sub-ATP synthase) that functions in reverse to hydrolyze ATP for $\Delta\Psi_{mi}$ maintenance. (B) *tfam* deletion strategy in $Rosa^{CreERT2}$ $Tfam^{flox/flox}$ mice (referred to as *tfam* KO). (C) Representative images of cell death analyzed by TUNEL assay in kidney, liver and pancreas from vehicle-treated (vCTRL) and PEITC-treated control and *tfam* KO mice. Scale bar: 300 µm. (D) Quantification of $TUNEL^+$ cells as shown in (C) (mean ± S.E.M., n = 4 mice per condition, *p < 0.05, **p < 0.01, ***p < 0.001, one-way ANOVA with Sidak's multiple comparisons test). (E) Representative WB images of the cleaved PARP and cleaved CASP3 in liver tissue of control and *tfam* KO mice treated or not with PEITC. (F and G) Densitometric quantification of WB in E and 3-4 additional independent experiments (normalized to ACTB, mean ± S.E.M., n ≥ 3 mice per condition, *p < 0.05, **p < 0.01, one-way ANOVA with Sidak's multiple comparisons test).

in parental cells (Fig. S2C-E). These results indicate that OXPHOS in endothelial QCs is required for oxidative stress resistance.

To evaluate whether OXPHOS provides ROS resistance also in QCs of non-endothelial origin, we eliminated OXPHOS by TFAM recombination/silencing in primary mouse embryonic fibroblasts (MEFs, isolated from $Rosa^{CreERT2}$ $Tfam^{flox/flox}$ embryos, see Materials and methods, Fig. S2F) and MCF10A (Fig. S2G) mammary epithelial immortalized cells, frequently used cellular models of quiescence [29]. Similarly to endothelial cells, we detected increased cell death (Fig. S2H and I) and exogenously induced

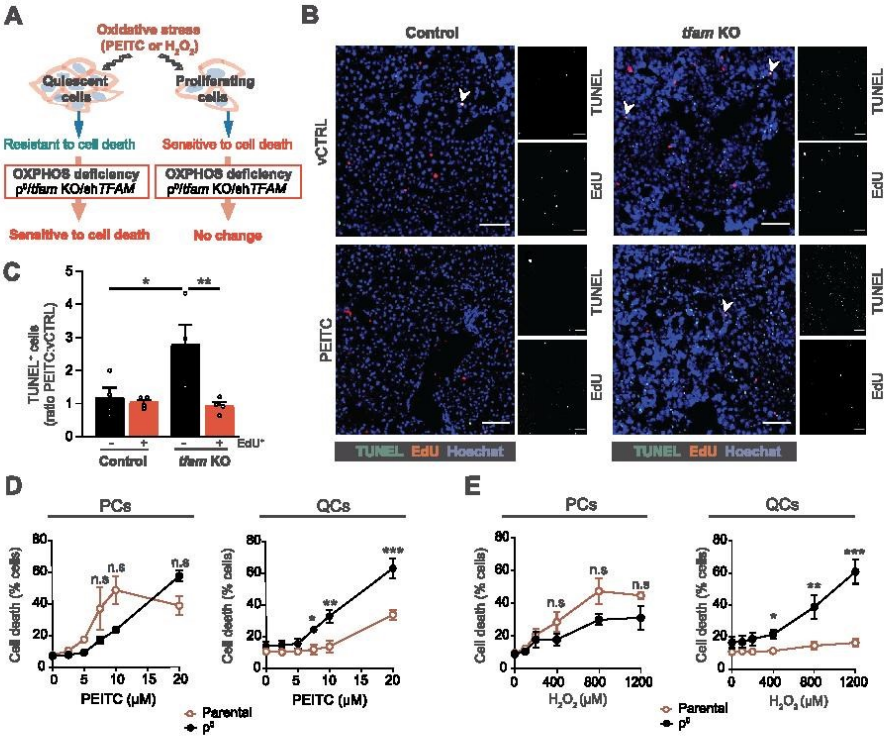

Figure 2. OXPHOS deficiency selectively sensitizes quiescent cells to oxidative stress. (A) OXPHOSdeficiency in quiescent cells leads to increased cell death upon oxidative damage. (B) Representative images of cell death and cell proliferation analyzed by TUNEL and EdU staining, respectively, in the liver of vCTRL and PEITC-treated mice. Scale bar: 500 μm. (C) Quantification of TUNEL positivity (ratio between PEITC and vCTRL) in EdU^+ (proliferating, PCs) and EdU^- (quiescent, QCs) cells (mean ± S.E.M., n = 4 mice per condition, *p < 0.05, **p < 0.01, one-way ANOVA with Sidak's multiple comparisons test). (D and E) Cell death in EA.hy926 PCs and QCs with (ρ^0) or without OXPHOS deficiency and treated with (D) PEITC and (E) H_2O_2 for 22 h evaluated by ANXA5-FITC and PI using flow cytometry (mean ± S.E.M., n ≥ 4, $^{n.s}$p > 0.05, *p < 0.05, **p < 0.01, ***p < 0.001 versus parental cells, two-way ANOVA with Tukey's multiple comparisons test).

ROS levels (Fig. S2J and K) upon PEITC treatment in QCs, whereas this was not observed in PCs.

Oxidative stress resistance during quiescence is provided by OXPHOS-stimulated autophagy

Next, we investigated if metabolic consequences of OXPHOS deficiency in QCs could underly the reduced oxidative stress resistance. While OXPHOS supports nucleotide synthesis in PCs [18,19,21,22,30,31], it was not required for this purpose in QCs (Figure 3A and B). In contrast, OXPHOS deficiency in QCs (but not in PCs) selectively reduced intracellular levels of free amino acids (Figure 3C and D).

Decreased ROS resistance combined with reduced amino acid levels suggested a possible defect of autophagy, which targets (ROS-damaged) proteins and organelles into autophagosomes for lysosomal delivery and recycling and provides stress resistance as well as free amino acids [10,32,33]. Autophagy was selectively suppressed in OXPHOS deficient QCs, shown by the reduced level of activated microtubule associated protein 1 light chain 3 beta (LC3B-II) in ρ^0 QCs (but not in PCs) (Figure 3E and F) and in tissues from *tfam* KO mice (Figure 3H and I). This was due to reduced autophagy flux, as revealed by negligible accumulation of LC3B-II in several types of OXPHOS-deficient QCs treated with bafilomycin A (Baf A), an inhibitor of lysosomal acidification (Figure 3E and F, Fig. S3A-C), and by elevated steady state levels of SQSTM1/p62, a canonical autophagy substrate (Figure 3E and G). A genetically encoded dual fluorescence reporter of autophagic flux pHluorin-mKate2-LC3 [34] (see Materials and methods for details), displayed a reduced red:green fluorescence ratio (Figure 3J, Fig. S3D) and a smaller fraction of red (lysosome-resident) LC3 puncta in OXPHOS-deficient QCs (Figure 3K and L), consistent with compromised delivery of LC3 into the lysosome.

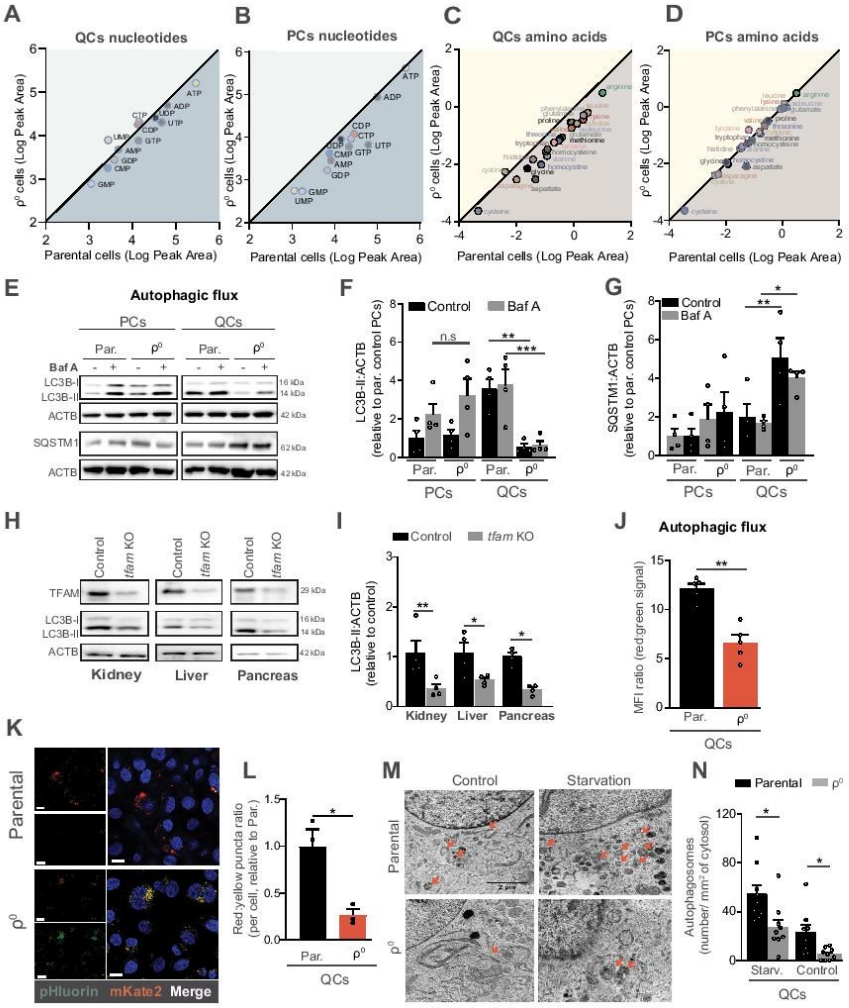

Figure 3. Autophagy is suppressed in OXPHOS-deficient quiescent cells and tissues. (A-D) Mass spectrometry quantification of intracellular levels of nucleotides and amino acids in parental and ρ^0 EA.hy926 cells. Nucleotides QCs (A), nucleotides PCs (B), amino acids QCs (C), amino acids PCs (D). The plots show the logarithms of peak area for individual nucleotides and amino acids (mean of n > 3 independent experiments). The values below the diagonal are reduced in ρ^0 compared to parental cells. (E) Representative WB images of activated LC3B (LC3B-II) and SQSTM1 in PCs and QCs in the presence or absence of 50 nM of Baf A for 4 h. (F and G) Densitometric quantification of LC3B-II (F) and SQSTM1 (G) (mean ± S.E.M., n = 4, $^{n.s}p > 0.05$, *p < 0.05, **p < 0.01, one-way ANOVA with Sidak's multiple comparisons test). (H) Representative WB images of TFAM protein expression and activated LC3B (LC3B-II) in kidney, liver and pancreas of control and *tfam* KO mice. (I) Densitometric quantification of activated LC3B (LC3B-II) as in H (mean ± S.E.M, n = 4 mice, *p < 0.05, **p < 0.01, unpaired two-tailed t test). (J) Fluorescent signal of the pHluorin-mKate2-LC3 autophagy flux reporter in parental and OXPHOS deficient EA.hy926 QCs assessed by flow cytometry (mean ± S.E.M., n = 5, **p < 0.01, unpaired two-tailed t test). Note: red:green fluorescence ratio is proportional to the native autophagic flux. (K and L) Representative images pHluorin-mKate2-LC3 flux reporter (K) and quantification of LC3 puncta (L) in parental and OXPHOS deficient EA.hy926 QCs assessed by confocal microscopy. Puncta counts were normalized to the number of cells (mean ± S.E.M., n = 3, **p < 0.01, unpaired two-tailed t test). Scale bar: 40 µm. (M) Representative transmission electron microscopy images and (N) autophagosome quantification of control and starved EA.hy926 parental and ρ^0 QCs cells. Autophagosomes are indicated by red arrows (n = 9 cells per condition, *p < 0.05, unpaired two-tailed t test). Scale bar: 2 µm.

Similarly, transmission electron microcopy showed a lower number of autophagosomes in ρ^0 QCs in both control conditions and upon starvation to induce autophagy (Figure 3M and N). These findings could not be explained by altered ATG7 (autophagy related 7) levels, which were similar in all tested conditions (Fig. S3E).

Next, we attenuated autophagy in parental QCs to ascertain its role in OXPHOS-mediated stress resistance

(Figure 4A). Inhibition of autophagy by pre-treatment with Baf A or silencing of ATG5 (autophagy related 5), an essential autophagy enzyme (Figure 4B-D; Fig. S3F- H), sensitized parental (but not OXPHOS-deficient) QCs to PEITC (Figure 4E and F, Fig. S3I-K), without affecting respiration (Fig. S3L). OXPHOS-maintained autophagy thus provides oxidative stress resistance in QCs.

Autophagy-mediated oxidative stress resistance during quiescence depends on ETC-derived ROS

We further investigated the mechanism of OXPHOS-maintained autophagy/stress resistance in QCs. We excluded a role for gene transcription/expression (Fig. S4A-D, Tables S3 and S4), canonical autophagy signaling via MTORC1, AMPK, or ULK1 [11,35] (Fig. S4E-K), and, in contrast to proliferating cells [14,15,36], the NADH:NAD ratio (Fig. S4L-S). However, the ETC is a major source of ROS and autophagy can respond to elevated intracellular ROS levels [13,37,38]. We hypothesized that continuous low-level endogenous ROS production from the ETC may be required to maintain basal autophagic flux (Figure 5A), paradoxically protecting the cell from exogenous ROS insult. Baseline ROS levels were reduced by OXPHOS deficiency both in mitochondria and in the cytoplasm (Figure 5B, Fig. S5A and B), showing that the ETC is crucial for endogenous ROS production in QCs. Furthermore, the elevation of antioxidant defense in QCs [2,6,7] was not compromised by OXPHOS deficiency (Fig. S5C-F), and likely further enhances depletion of ROS in OXPHOS-deficient QCs.

To functionally link ETC-produced ROS to autophagy, we manipulated basal ROS levels by (i) suppressing ROS in parental QCs and (ii) reconstituting ROS in OXPHOS-deficient QCs. First, we treated QCs with an antioxidant N-acetyl cysteine (NAC) or overexpressed catalase, an antioxidant enzyme (Figure 5C). Both manipulations reduced intracellular ROS levels and autophagic flux in parental QCs to the level found in ρ^0 QCs (where they had no further effect) (Figure 5D-G, Fig. S5G and H). Vice versa, autophagic flux was rescued in ρ^0 QCs by the administration of exogenous H_2O_2 (Figure 5H and I), and preconditioning with low concentrations of H_2O_2 restored ROS-resistance of ρ^0 QCs to the parental cell levels (Figure 5J). The rescue effect of H_2O_2 was abrogated by the autophagy inhibitor Baf A (Figure 5J), indicating that the reactivation of autophagy is essential for the recovery of oxidative stress resistance. Overall, we show that endogenous ROS generated by the ETC maintain basal autophagy in quiescent cells, which is protective against exogenous ROS challenge.

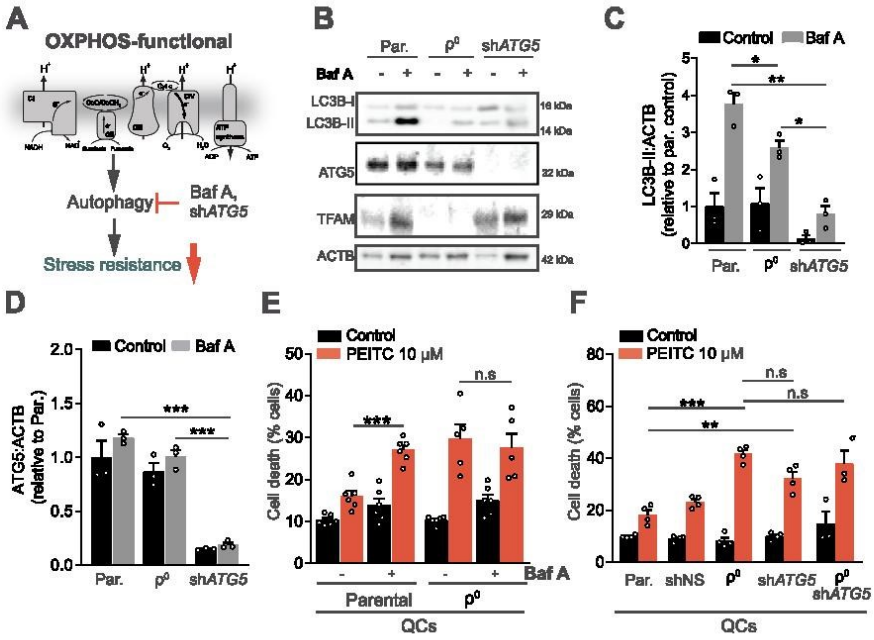

Figure 4. Suppression of autophagy in quiescent cells recapitulates the effects of OXPHOS deficiency on resistance to stress. (A) Pharmacological (Baf A) and genetic (sh*ATG5*) suppression of autophagy in parental QCs was used to explore its potential effects downstream of OXPHOS deficiency. (B, C, D) Representative WB images (B) and quantifications of LC3B-II (C) and ATG5 (D) in parental and ρ^0 EA.hy926 QCs (mean ± S.E.M., n = 3, $^{n.s}p > 0.05$, $^{*}p < 0.05$, $^{**}p < 0.01$, $^{***}p < 0.001$, one-way ANOVA with Sidak's multiple comparisons test). (E) Cell death in EA.hy926 QCs with or without OXPHOS deficiency, pre-incubated or not with 50 nM of Baf A for 2 h followed by 10 µM PEITC for 22 h, evaluated by ANXA5-FITC and PI (mean ± S.E.M., n ≥ 4, $^{n.s}p > 0.05$, $^{***}p < 0.001$, one-way ANOVA with Sidak's multiple comparisons test). (F) Cell death in indicated EA.hy926 QCs treated with 10 µM of PEITC for 22 h, evaluated by ANXA5-FITC and PI (mean ± S.E.M., n = 4, $^{n.s}p > 0.05$, $^{**}p < 0.01$, $^{***}p < 0.001$, one-way ANOVA with Sidak's multiple comparisons test).

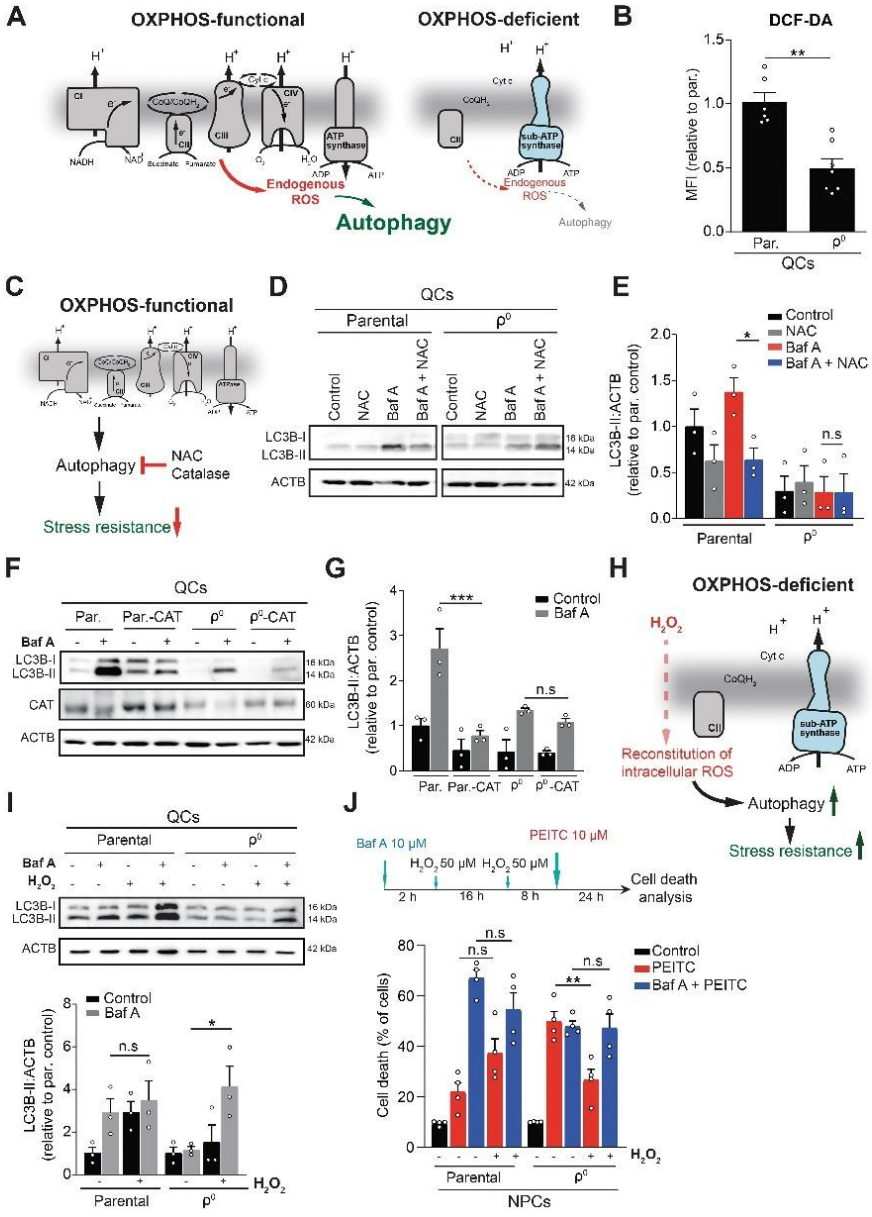

Figure 5. OXPHOS-derived ROS maintain autophagy and ROS resistance in quiescent cells. (A) OXPHOS-deficient QCs lack respiratory complexes and are therefore expected to produce less ROS from the ETC, possibly affecting autophagy. (B) Baseline ROS levels in EA.hy926 QCs assessed using DCF-DA fluorescent probe by flow cytometry (mean ± S.E.M., n ≥ 6, **p < 0.01, unpaired two-tailed t test). (C) Pharmacological (NAC) and genetic (catalase overexpression) reduction of endogenous ROS in parental QCs was used to recapitulated effects of OXPHOS deficiency on autophagy. (D and E) Representative WB image (D) and quantification (E) of activated LC3B (LC3B-II) in parental or ρ^0 EA.hy926 QCs treated or not with NAC (1 mM) for 6 h and/or with Baf A (50 nM) for 4 h (mean ± S.E.M., n = 3, $^{n.s}$p > 0.05, *p < 0.05, unpaired two-tailed t test). (F and G) Representative WB image (F) and quantification (G) of activated LC3B (LC3B-II) protein levels in parental and ρ^0 EA.hy926 QCs with or without overexpression of catalase in the presence or absence of Baf A (50 nM) (mean ± S.E.M., n = 3, $^{n.s}$p > 0.05, ***p < 0.001, unpaired two-tailed t test). (H) Treatment with low levels of exogenous ROS (H_2O_2) in OXPHOS deficient QCs was used to restore autophagy and cell death resistance. (I) Representative WB image (top) and quantification (bottom) of the activated LC3B (LC3B-II) protein expression in EA.hy926 parental and ρ^0 QCs treated or not with H_2O_2 (1 mM) for 4 h in the presence or absence of Baf A (50 nM) (mean ± S.E.M., n = 3, $^{n.s}$p > 0.05, *p < 0.05, unpaired two-tailed t test). (J) PEITC-induced cell death in parental and ρ^0 EA.hy926 QCs pre-treated or not with Baf A (10 μM), with or without pre-conditioning by H_2O_2 as shown in the scheme, measured by ANXA5 and PI (mean ± S.E.M, n = 4, $^{n.s}$p > 0.05, **p < 0.01, one-way ANOVA with Sidak's multiple comparisons test).

ETC-derived ROS attenuate ATG4B activity to support autophagy and stress resistance during quiescence.

ROS can regulate autophagic flux transcriptionally via the ROS-responsive TFEB (transcription factor EB) [39,40], or post-translationally via phosphorylation of BECN1 (beclin 1) [41] or via ATG4B (autophagy related 4B cysteine peptidase) [38,42]. OXPHOS deficiency during quiescence neither suppressed TFEB-regulated transcripts (Fig. S6A) nor altered BECN1 phosphorylation in QCs (Fig. S6B and C). We thus focused on ATG4B, a protease sensitive to ROS-inhibition due to cysteine residues in its active site. Normally ATG4B promotes autophagy by converting pre-LC3B into LC3B-I, which, upon conjugation to phosphatidylethanolamine (PE), yields the active LC3B-II (Figure 6A). However, when ATG4B activity is too high, such as in the absence of ROS, it can also remove PE from LC3B-II and inhibit autophagy [38] (Figure 6A and B). Accordingly, optimal level of endogenous ROS, present in parental but not in OXPHOS-deficient QCs, may be needed to attenuate ATG4B activity and maintain basal autophagic flux (Figure 6B).

To assess the activity of ATG4B in OXPHOS-deficient QCs and test if it regulates autophagy/stress resistance, we used an ATG4B-specific phospholipase A2-based reporter (Figure 6C) [43,44]. ATG4B activity was high in OXPHOS-deficient and

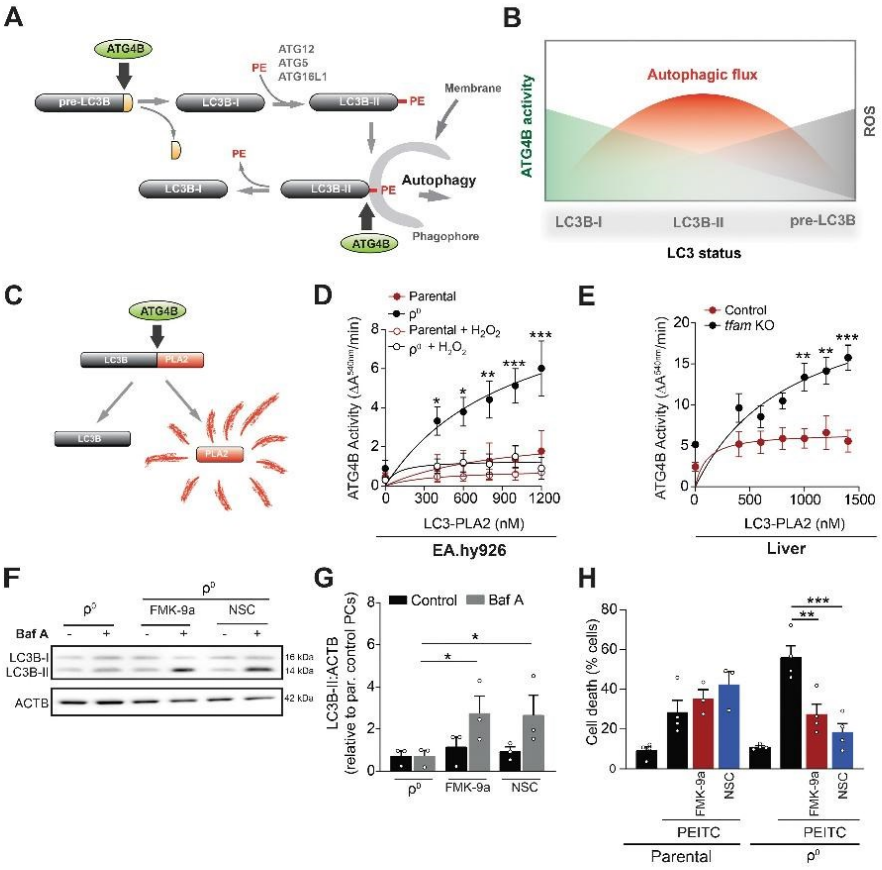

Figure 6. ETC-derived ROS regulate autophagy during quiescence via ATG4B. (A and B) ROS-sensitive ATG4B both activates (by cleaving pre-LC3) and inhibits (by removing PE) LC3B (A), leading to a complex relationship between ATG4B activity, ROS and autophagy (B). At optimal ROS levels ATG4B activity is partially attenuated, the activating pre-LC3 cleavage can proceed while the inhibitory removal of PE is suppressed, leading to the maximal autophagic flux. (C) The LC3B-PLA2 (phospholipase A2)-based reporter to assess ATG4B function. Active ATG4B liberates PLA2, producing signal in a fluorogenic assay. (D) ATG4B activity in cell lysates from EA.hy926 QCs treated or not with H_2O_2 (1 mM) for 4 h and incubated with increasing concentrations of LC3B-PLA2 fusion protein substrate (mean ± S.E.M., n ≥ 4, *p < 0.05, **p < 0.01, ***p < 0.001, versus parental cells, two-Way ANOVA with Tukey's multiple comparisons test). (E) ATG4B activity in cell lysates from liver of control or *tfam* KO mice incubated with increasing concentrations of LC3B-PLA2 fusion protein substrate (mean ± S.E.M., n = 4 mice, **p < 0.01, ***p < 0.001, versus control cells, two-way ANOVA with Tukey's multiple comparisons test). (F and G) Representative WB image (F) and quantification (G) of the activated LC3B (LC3B-II) protein in EA.hy926 ρ^0 QCs treated with FMK-9a (1 μM) and NSC185058 (0.1 μM) for 4h (mean ± S.E.M., n = 3, *p < 0.05, unpaired two-tailed t test). (H) PEITC-induced cell death in parental and ρ^0 EA.hy926 QCs pre-treated or not with FMK-9a (1 μM) and NSC185058 (0.1 μM) for 2 h, measured by ANXA5 and PI. (mean ± S.E.M, n = 4, $^{n.s.}$p > 0.05, **p < 0.01, one-way ANOVA with Sidak's multiple comparisons test).

low in parental QCs (Figure 6D; Fig. S6D). Exposure of OXPHOS-deficient QCs to H_2O_2 reduced ATG4B activity to the level of parental cells (Figure 6D; Fig. S6D), consistent with the capacity of exogenous H_2O_2 to stimulate autophagy and restore stress resistance in the absence of functional OXPHOS (c.f. Figure 5I and J). Addition of recombinant human ATG4B further increased the signal of the ATG4B reporter in the lysates from OXPHOS-deficient but not from parental QCs (Fig. S6E and F), demonstrating that OXPHOS deficiency provides an environment permitting ATG4B over-activation. Consistently, ATG4B activity was elevated in liver and kidney tissue from *tfam* KO mice (Figure 6E, Fig. S6G). Next, we employed two distinct ATG4B inhibitors as well as RNA interference to normalize ATG4B activity in OXPHOS-deficient QCs to the level of parental cells (Figure S6H and I). Interestingly, both inhibitors, NSC185058 [45] and FMK-9a [46], upregulated LC3B-II in ρ^0 QCs (Figure 6F and G) and restored resistance to PEITC (Figure 6H), while providing no additional protection for parental cells. Similarly, ATG4B silencing upregulated LC3B-II and recovered resistance to PEITC (Figure S6J and K). Accordingly, excessive ATG4B activity in OXPHOS-deficient QCs suppresses autophagy, leading to reduced oxidative stress resistance.

OXPHOS maintains specificity of ROS-based anticancer treatment by protecting normal tissue

Having shown that OXPHOS provides oxidative stress resistance in QCs, we next investigate if such protection has relevance in disease conditions. During cancer therapy, both tumor cells (mostly PCs) and normal somatic cells (mostly QCs) are exposed to ROS-inducing anticancer agents, yet cell death is selectively triggered in proliferating cancer cells [7,26]. We thus explored if OXPHOS-induced resistance to ROS in normal tissues underlies the therapeutic window, contributing to specificity. We grafted syngeneic B16 melanoma cells subcutaneously into *tfam* KO mice to generate respiration-competent tumors on an OXPHOS deficient background (Figure 7A). Tumor-bearing mice were treated with two ROS-inducing compounds: (i) PEITC, an experimental anticancer agent [26], or (ii) doxorubicin, a clinically used cancer therapeutic associated with ROS-linked toxicity in normal tissues (Fig. S7A) [47]. Subsequently, we assessed cell death in tissues and determined a specificity index (SI), defined as the ratio of cell death induction in the tumor versus non-malignant tissue (liver) (Figure 7A). In case the specificity of treatment is reduced, the SI should decrease. Indeed, the SI was reduced more than 2-fold in PEITC-treated *tfam* KO animals compared to PEITC-treated controls (Figure 7B, Fig. S7B), and a similar SI reduction was observed upon administration of doxorubicin (Figure 7B, Fig. S7B), mainly due to increased cell death in normal tissue (Fig. S7C). Inhibition of autophagy by chloroquine also lowered the specificity of PEITC treatment in tumor-bearing mice due to increased cell death in normal tissue (Figure 7C, Fig. S7D and E), similarly to OXPHOS deficiency. Hence, the selectivity of ROS-based anti-cancer therapy is, at least in part, determined by functional OXPHOS/autophagy that maintain oxidative stress resistance in non-malignant tissues.

OXPHOS controls ROS in quiescent endothelium in vivo and limits inflammation-linked pathology

To examine the role of OXPHOS-mediated oxidative stress resistance in pathologies other than cancer, we focused on inflammation, often accompanied by increased oxidative stress [48]. Reduced oxidative stress resistance of quiescent vascular endothelium exacerbates inflammation by decreasing endothelial barrier function, facilitating leukocyte extravasation, and increasing vessel permeability [6]. In addition, the endothelium does not rely on OXPHOS-derived ATP. We thus explored the role of OXPHOS in oxidative stress resistance specifically in the endothelium in the context of (i) systemic inflammation and (ii) inflammation of the colon linked to inflammatory bowel disease (IBD).

To selectively disable OXPHOS in the endothelium in vivo, we used an established endothelium-specific tamoxifen-inducible *Cdh5*^{CreERT2} driver to ablate TFAM in the endothelium of adult mice (*tfam* ECKO mice, see Materials and methods) (Figure 7D). *tfam* deletion was confirmed by immunohistochemistry, which showed no colocalization of the TFAM signal with an endothelial marker ENG/CD105 in *tfam* ECKO animals (Fig. S7F). To induce systemic inflammation, control and *tfam* ECKO mice were challenged with LPS, a (patho)-physiological inducer of ROS in endothelial cells [49]. Interestingly, LPS-treated *tfam* ECKO mice featured elevated ROS levels in the endothelium in vivo, as demonstrated by dihydroethidium (DHE) staining of intact aortas (Figure 7E and F), and presented increased leukocyte infiltration in the lungs compared to LPS-treated controls (Figure 7G and H). In contrast, there was no apparent effect of *tfam* deletion in non-treated animals.

To assess the relevance of OXPHOS-linked oxidative stress resistance in IBD, we used a model of dextran sodium sulfate (DSS)-induced colitis. We previously established that increased susceptibility of the endothelium to oxidative stress promotes the disease by disrupting the endothelial barrier in the inflamed colon [6]. Indeed, whereas no adverse effects of TFAM deficiency were observed in non-treated animals, DSS-treated *tfam* ECKO mice had more severe disease as shown by a higher disease activity index (scoring body weight loss, stool consistency, and blood in the stool and anal region) (Figure 7I), shortened colon (Figure 7J, Fig. S7G), and showed more pronounced signs of colitis, including loss of crypts, separation of the crypt base from the muscularis mucosa and colonic wall thickening (Figure 7K). Furthermore, the DSS-treated *tfam* ECKO colons suffered from elevated leukocyte infiltration (Figure 7L, Fig. S7H) and increased vessel leakiness, demonstrated as rhodamine-dextran extravasation (Figure 7M, Fig. S7I). Co-treatment with tempol, an antioxidant [50], normalized the phenotype of DSS-treated *tfam* ECKO mice to the level of DSS-treated controls (Fig. S7J and K), confirming that ROS are responsible for the increased severity of colitis in *tfam* ECKO animals. To summarize, the selective ablation of endothelial OXPHOS exacerbates systemic inflammation

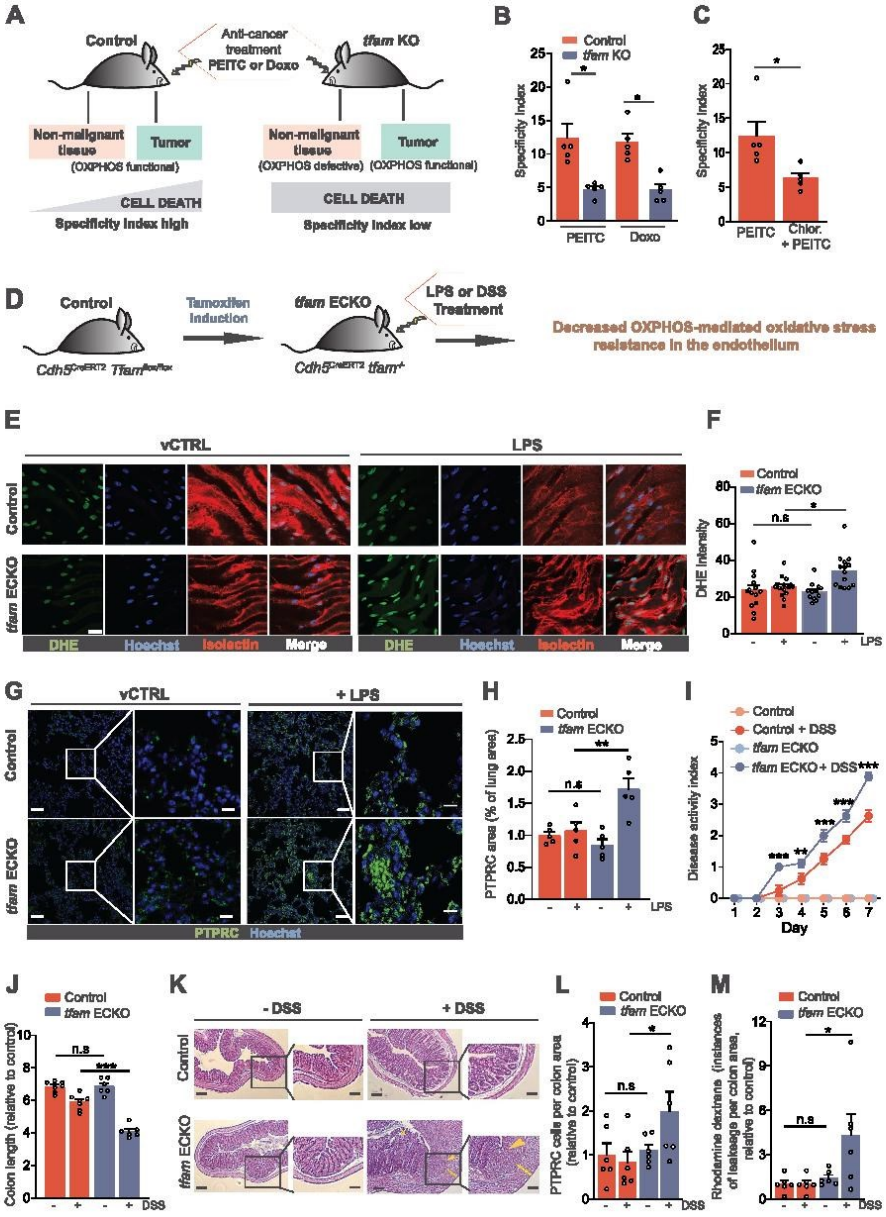

Figure 7. OXPHOS-mediated stress resistance during quiescence maintains therapeutic window in cancer and limits inflammation-linked pathology. (A) OXPHOS maintains therapeutic window by supporting resistance to ROS in non-malignant tissue during ROS-based cancer therapy. Treatment-induced cell death in non-malignant tissues (contain mostly QCs) is increased in tumor-bearing *tfam* KO mice, compromising specificity of treatment. (B) Specificity index (SI) assessed by quantification of the ratio of TUNEL$^+$ cells in tumor and liver tissue from control and *tfam* KO mice after treatment with PEITC and doxorubicin (Doxo). (C) Specificity index (SI) assessed by quantification of the ratio of TUNEL$^+$ cells in tumor and liver tissues from control mice treated with PEITC (1.25 mg/25 g mouse in corn oil) or PEITC + chloroquine (1 mg/20 g mouse in corn oil), (mean ± S.E.M., n = 5 mice per condition, *p < 0.05, **p < 0.01, one-way ANOVA with Sidak's multiple comparisons test). (D) Endothelium-specific *tfam* deletion strategy in $Cdh5^{CreERT2}$ $Tfam^{flox/flox}$ mice (referred to as *tfam* ECKO). (E and F) Representative images (E) and quantification (F) of aorta open book preparations from control and *tfam* ECKO mice treated with LPS for 4 h, stained for DHE (green), the EC marker isolectin B4 (red) and nuclei (Hoechst-blue). Scale bar: 20 µm. (n ≥ 12 mice per group, $^{n.s}$p > 0.05, *p < 0.05, one-way ANOVA with Sidak's multiple comparisons test). (G and H) Representative images (G) and quantification (H) of lungs from control and *tfam* ECKO mice 4 h after injection of LPS or vehicle solution stained with PTPRC/CD45 (green) and Hoechst (blue) (n = 5 mice per group, $^{n.s}$p > 0.05, **p < 0.01, one-way ANOVA with Sidak's multiple comparisons test). Right panels in G are magnifications of the boxed areas on the left. Scale bar: 40 µm (left panels) and 20 µm (right panels). (I) Disease activity index of colitis in control and *tfam* ECKO

as well as IBD, a frequent pathology in humans, demonstrating that oxidative stress resistance provided by OXPHOS in the endothelium is clinically relevant.

Discussion

Mitochondrial respiration sustained by the OXPHOS system is crucial for most living organisms. OXPHOS is a source of ATP and supports nucleotide biosynthesis in proliferating cells [18,19,21], yet whether OXPHOS has other essential roles specific to quiescent cells and tissues remained unclear. The key finding of our study therefore is that OXPHOS is necessary to combat oxidative stress in quiescent cells and tissues by supporting autophagy. Interestingly, a link between OXPHOS, autophagy and stress resistance was not found in proliferating cells, suggesting that regulation of autophagy by OXPHOS is proliferation-sensitive.

We provide evidence that OXPHOS/autophagy-mediated oxidative stress resistance during quiescence is relevant in several patho-physiological scenarios. First, we document that OXPHOS/autophagy ensure specificity of anti-cancer therapy by protecting normal non-proliferative tissues when tumors are treated with ROS-inducing anticancer agents, providing a therapeutic window. Hence, while many investigations focused on why tumors are sensitive to therapy, here we address an equally important, yet understudied question of why normal tissues are resistant. Our findings thus warrant caution when using autophagy inhibitors (chloroquine is in clinical trials in cancer) with ROS-inducing agents. Such a combination has the potential to compromise selectivity and thereby increase toxicity of cancer therapy.

Second, by selectively ablating OXPHOS in adult quiescent endothelium, which is relatively independent of ATP production via OXPHOS, we document increased susceptibility of mice to systemic as well as local inflammation, conditions associated with oxidative stress in endothelial cells. OXPHOS ablation exacerbated oxidative stress in endothelial cells during inflammation, leading to increased vessel permeability and leukocyte extravasation. A similar phenotype was observed when resistance of endothelial cells to oxidative stress was reduced by alternative manipulations [6]. This demonstrates that OXPHOS/autophagy protect endothelial cells during inflammatory conditions such as colitis associated with IBD, documenting a new role for OXPHOS as a guardian against oxidative stress in quiescent endothelium. Others have shown that OXPHOS-mediated biosynthesis is crucial for biomass buildup in proliferating endothelial cells during angiogenesis [51], demonstrating that distinct functions of OXPHOS during proliferation and quiescence (i.e., biomass buildup versus stress protection) are maintained in vivo.

Our findings point to stark differences in regulation of stress resistance/autophagy in proliferating and quiescent cells. While in quiescent cells OXPHOS deficiency abrogated autophagy and resistance to stress, it had no effect in proliferating cells. Furthermore, our results indicate that during quiescence ETC signals to autophagy via ROS, but not via NADH. In contrast, NADH has been found to regulate autophagy in proliferating cells [14,15], pointing to distinct autophagy regulation during proliferation and quiescence. Consequently, NADH may be the dominant regulator of autophagy in proliferating cells which require biosynthesis (NADH:NAD^+ ratio is crucial for biosynthesis), while ROS become important in quiescent cells that accentuate stress resistance (ROS are important stressors). This is consistent with the dual role of OXPHOS which provides biosynthesis during proliferation and stress resistance during quiescence, reflecting the distinct needs of these two states (Figure 8).

How does OXPHOS, the main producer of intracellular ROS, induce protection against oxidative stress in quiescent cells? We propose that this is an active process where continuous low-level generation of endogenous ROS from the ETC attenuates the activity of ATG4B, a redox-regulated member of the autophagy cascade [38]. Such ROS-mediated ATG4B modulation sustains the basal, protective autophagy. The absence of ETC-produced ROS in OXPHOS-deficient cells is amplified by the quiescence-induced elevation of antioxidant defense, leading to unrestrained ATG4B activity that suppresses autophagy. Supplementation of OXPHOS-deficient quiescent cells with ROS normalized ATG4B activity and rescued autophagy as well as ROS resistance, which was phenocopied by direct attenuation of ATG4B activity by specific inhibitors or by RNA silencing. These findings favor a model where OXPHOS supports autophagy during quiescence by maintaining the optimal intracellular redox balance. In this way, OXPHOS/autophagy, along with the antioxidant defense, represent a basal, constitutive layer of ROS resistance in quiescent cells.

OXPHOS-mediated resistance to oxidative stress is conserved over multiple tissues and cell types, suggesting its ancient origin. This may have interesting evolutionary connotations. Eukaryotic cells acquired mitochondria to benefit from oxygen through oxidative metabolism for efficient ATP production and biosynthesis, making complex life possible. At the same time, they apparently built in an autophagy-based mechanism to protect against oxygen levels that rose throughout the evolution of multicellular

mice during treatment with 2.5% DSS in the drinking water for 7 consecutive days (n = 6 mice, ***p < 0.001, two-way ANOVA Tukey's multiple comparisons test). (J) Colon length in control and *tfam* ECKO mice after 2.5% DSS treatment (n = 6; 3 males, 3 females per group), $^{n.s}$p > 0.05, **p < 0.01, ***p < 0.001, one-way ANOVA with Sidak's multiple comparisons test). (K) Representative images of hematoxylin and eosin-stained sections of colon from control and *tfam* ECKO mice treated as in I. Right panels are magnifications of the respective boxed areas. Asterisks denotes loss of crypts; arrowhead denotes more severe separation of the crypt base from the muscularis mucosa, infiltrated with inflammatory cells; yellow line visualizes the thickness of the colonic wall. Scale bar: 500 µm. (L) Quantification of colon PTPRC/CD45$^+$ cells per total area of tissue from control and *tfam* ECKO mice after 2.5% DSS treatment (n = 6 mice, $^{n.s}$p > 0.05, *p < 0.05, one-way ANOVA with Sidak's multiple comparisons test). (M) Quantification of vascular leakiness (dextran-rhodamine signal) in colon from control and *tfam* ECKO mice after 2.5% DSS treatment (n = 6 mice, $^{n.s}$p > 0.05, *p < 0.05, one-way ANOVA with Sidak's multiple comparisons test).

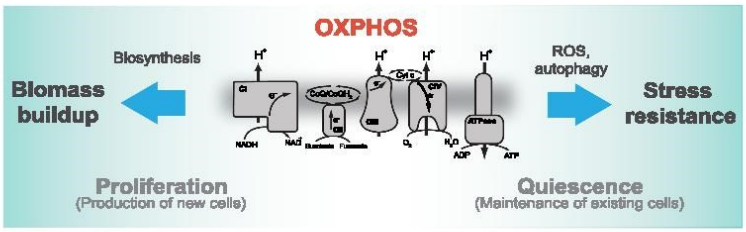

Figure 8. Distinct roles of OXPHOS during proliferation and quiescence. The proposed model depicts specific roles of OXPHOS in proliferating and quiescent cells. In proliferating cells OXPHOS supports biosynthesis, whereas in quiescent cells it provides stress resistance via ROS-stimulated autophagy.

life forms [52] and that predispose to oxidative stress. In addition, by coupling OXPHOS to autophagy evolution would devise a safety measure against ROS-induced damage inherent to energy generation by mitochondria. The OXPHOS system thus features unexpected plasticity and readily adapts to specific requirements of cellular proliferation and quiescence with prominent functional consequences for pathology.

Materials and methods

Mice

Whole-body model: C57BL/6J *Tfam*$^{flox/flox}$ mice (Jackson Laboratory, 026123)[53] were bred with C57BL/6J *Rosa*^{CreERT2} mice (Jackson Laboratory, 008463) to produce C57BL/6J *Rosa*^{CreERT2}*Tfam*$^{flox/flox}$ mice. The mice were kept homozygous for both *Rosa*^{CreERT2} and *Tfam*^{flox}. TFAM deficiency was induced in 7-8-week-old mice by 3 doses of tamoxifen (Sigma-Aldrich, T5648), 0.25 mg/g body weight in corn oil (Sigma-Aldrich, C8267, concentration 9 mg/ml) every 12 h, intraperitoneally (i.p.). Tamoxifen-treated *Tfam*$^{flox/flox}$ mice served as controls. Experiments were performed 11 days post induction. At day 12-13 post induction, the mice started to show slowness of movement and apathy. Endothelial model: *Cdh5*^{CreERT2} *Tfam*$^{flox/flox}$ mice were produced by crossing C57BL/6J *Cdh5*^{CreERT2} mice [54] (kindly provided by Dr. R. Boon) with *Tfam*$^{flox/flox}$ animals. The *Cdh5*^{CreERT2} *Tfam*$^{flox/flox}$ mice were kept heterozygous for Cre. Endothelial specific TFAM deficiency was induced in 8-week-old-mice by 5 doses of tamoxifen, 0.10 mg/g body weight in corn oil every 24 h (i.p.). Tamoxifen-treated *Tfam*$^{flox/flox}$ mice were used as controls. Experiments were started 16 days post induction. Induced *Cdh5*^{CreERT2} *Tfam*$^{flox/flox}$ animals behaved normally and showed no adverse signs for 2 months post induction (we did not follow them longer). Animals were maintained under SPF conditions in individually ventilated cages with controlled temperature (22 ± 2°C) and humidity under a 12 h light/12 h dark cycle and with food and drink ad libitum. Animals were closely followed-up by the animal caretakers and the experimenters, with regular inspection by a veterinarian, as per the standard health and animal welfare procedures of the local animal facility. No statistical method was used to predetermine sample size. All animal experiments were approved by the Animal Ethics Committee of the Czech Academy of Sciences and were performed according to Czech guidelines for the Care and Use of Animals in Research and Teaching. None of the animals showed signs of distress during the experiments.

Cell lines

Primary cells: Mouse embryonic fibroblasts (MEFs) were isolated from non-induced 12 - 13 days embryos of *Rosa*^{CreERT2} *Tfam*$^{flox/flox}$ mice using standard procedures and cultivated in high glucose (4.5 g/l) DMEM (Sigma-Aldrich, D6429) supplemented with 10% fetal bovine serum (FBS; Sigma-Aldrich, F7524), and 1% antibiotics (penicillin G, 100 U/ml; Sigma-Aldrich, P3032) and streptomycin (100 µg/ml; Sigma-Aldrich, S9137)). TFAM deficiency was induced by supplementation of 3 µM of 4-hydroxytamoxifen (Sigma-Aldrich, H6278) to the culture medium for 5 days. OXPHOS dysfunction was verified by respirometry and/or absence of TFAM. Human umbilical vein endothelial cells (HUVECs) were obtained from PromoCell (C-12208) and cultivated in endothelial cell basal medium (EGM2) (PromoCell, C22011) supplemented with endothelial cell growth medium supplement pack (PromoCell, C-30120) and were used before passage 5.

Cell lines: Human endothelial EA.hy926, epithelial MCF10A and B16 melanoma cell lines were obtained from the ATCC (CRL-2922, CRL-10317, CRL-6323, respectively). The Ea.hy926 cells were cultured in high glucose (4.5 g/l) DMEM media supplemented with 10% FBS, 2% hypoxanthine aminopterin thymidine (HAT) supplement (Thermo Fisher Scientific, 21060017) and 1% antibiotics (penicillin G 100 U/ml and streptomycin 100 µg/ml). MCF10A cells were cultured in DMEM:F12 (Lonza, 12-719F) supplemented with 5% horse serum (Sigma-Aldrich, H1138), 0.1% human insulin, 20 ng/ml (Sigma-Aldrich, I9278) epidermal growth factor (Thermo Fisher Scientific, PHG0311), 0.5 mg/ml hydrocortisone (Sigma-Aldrich, H0888), 100 ng/ml cholera toxin (Sigma-Aldrich, C8052) and 1% antibiotics (penicillin G, 100 U/ml and streptomycin, 100 µg/ml). B16 melanoma cells were maintained in DMEM supplemented with 10% FBS and 1% antibiotics (penicillin G 100 U/ml and streptomycin 100 µg/ml). For quiescent cultures, the cells were seeded into 24-well

plates at 80% density and cultured for 4 days post-confluence. For proliferating cultures, cells were seeded into 6-well plates at 2×10^5 cells per well 2 days before experiment. Ea.hy926 cells deficient in mtDNA (ρ^0 phenotype) were prepared by long-term culture with 0.2 μg/ml of ethidium bromide as described (Tan et al., 2015). OXPHOS-deficient MCF10A cells are described below. OXPHOS deficient cells were cultured in the media corresponding to the given cell type supplemented with 1 mM sodium pyruvate (Sigma-Aldrich, P5280) and 50 μg/ml uridine (Sigma-Aldrich, U3003) unless indicated otherwise. Under these culture conditions, all OXPHOS deficient cell showed normal viability. All cultures were maintained in a 5% CO_2, 37°C incubator.

Gene silencing and overexpression

HUVEC, EA.hy926 and MCF10A cells were silenced for *ATG5, NDUFV1* and *TFAM* genes by lentiviral transduction using the following predesigned shRNAs in pLKO1 vector: *ATG5*-TRCN0000150940; *NDUFV1*-TRCN0000025872; *TFAM*-TRCN0000329819; non-silencing control-SHC002 (Sigma-Aldrich). Silencing efficacy was more than 85% in all cases. Expression of CAT (catalase) from the pLenti6/V5-MCS plasmid, a gift of S. Lortz (Hannover Medical School, Hannover, Germany) [55] and pHluorin-mKate2-hLC3 reporter from the FUGW lentiviral plasmid (a gift of I. Tanida; Addgene, 61460) [34] was achieved by lentiviral transduction. Cells were used for experiments 2-4 weeks post transduction.

Western blotting (WB)

Cells were lysed in RIPA buffer (20 mM Tris-HCl, pH 7.5, 150 mM NaCl, 1 mM EDTA, 1 mM EGTA, 1% NP-40 [Fluka, 74385], 0.5% sodium deoxycholate [Sigma-Aldrich, D6750], 0.1% SDS) supplemented with 1% of protease (SERVA, 3910201) and 1% of phosphatase (Sigma-Aldrich, P5726) inhibitor cocktail. The lysate was cleared by centrifugation and total protein determined by BCA assay (Thermo Fisher Scientific, 23227). Murine tissues were homogenized 3 x 20s, 5000 rpm, with an interval of 2 min on ice, using a Precellys 24 tissue homogenizer (Bertin Technologies, Montigny-le-Bretonneux, France) in prefilled lysis tubes (Bertin, KT03961-1-203.05) in RIPA buffer containing 1% protease and 1% phosphatase inhibitors. 30 mg of total protein were resolved by SDS-PAGE and transferred to nitrocellulose membranes, and probed with the following primary antibodies: TFAM (Abcam, ab131607); ATG5 (Cell Signaling Technology, cs12994); LC3B (Cell Signaling Technology, cs2775); NDUFV1 (Abcam, ab55535); MTOR (Cell Signaling Technology, cs2972); phospho-MTOR (Cell Signaling Technology, cs2971); PRKAA/AMPKα (Cell Signaling Technology, cs2532); phospho-PRKAA/AMPKα (Cell Signaling Technology, cs2531); ULK1 (D8H5; Cell Signaling Technology, cs8054); phospho-ULK1 (Ser757; Cell Signaling Technology, cs6888); phospho-ULK1 (Ser555; Cell Signaling Technology, cs5869); RPS6KB/p70S6 kinase (Santa Cruz Biotechnology, sc-8418); phospho-RPS6KB /p70S6 kinase (Santa Cruz Biotechnology, sc-8416); cleaved CASP3 (Asp175, 5A1E; Cell Signaling Technology, 9664); cleaved CASP3 (ENZO, 31A1067); cleaved-PARP (Cell Signaling Technology, cs9541); MT-ND5 (Abcam, ab92624) MT-CO1 (Abcam, ab110258); SOD2 (Acris, AP03024-PU-N); GPX1 (Abcam, ab108427, BECN1 (Santa Cruz Biotechnology, sc-11427), phospho-BECN1 (Ser93; Cell Signaling Technology, 14717); SQSTM1/p62 (Santa Cruz Biotechnology, sc-2557); ATG7 (Cell Signaling Technology, d12b11); PTPRC/CD45 (Thermo Fisher Scientific, 14-0451-85); ENG/CD105 (Bio-Techne R&D Systems, AF1320) and anti-ACTB/β-Actin HRP conjugate (Cell Signaling Technology, cs5125).

Autophagic flux measurements

Cells were treated or not with 50 nM of bafilomycin A_1 (Santa Cruz Biotechnology, sc-201550) for 4 h and collected for WB analysis to detect non-activated LC3B-I and activated, phosphatidylethanolamine (PE)-conjugated, LC3B-II protein, and SQSTM1. Where indicated, cells were pre-incubated with the antioxidant N-acetylcysteine 1 mM (NAC; Sigma-Aldrich, A7250-10G) for 2 h or with MTOR inhibitor everolimus 20 μM (Invivogen, tlrl-eve) for 4 h.

Autophagy flux was also assessed using a genetically encoded fluorescent reporter, pHluorin-mKate2-LC3. This reporter contains pHluorin (green) and mKate2 (red) fluorescent proteins fused to LC3B for autophagosome targeting. The green fluorescence of pHluorin is pH-sensitive and is quenched when the autophagosome enters the low pH of the lysosome, while the red fluorescence of mKate2 is pH-independent and is retained. Therefore, red:green (or red: yellow) ratio is proportional to the native autophagic flux. Cells expressing pHluorin-mKate2-LC3 were washed with phosphate-buffered saline (PBS; 137 mM NaCl, 2.7 mM KCl, 10 mM Na_2HPO_4, 1.8 mM KH_2PO_4, pH 7.4) trypsinized, resuspended in PBS and analyzed by flow cytometry (LSRFortessaTM SORP, Becton Dickinson, New Jersey, USA). To detect pHluorin (green) and mKate2 (red) fluorescence, 488 nm and 561 nm lasers were used for excitation. Emission was measured at 530±15 nm for pHluorin and 610 ±10 nm for mKate2. For microscopy experiments cells expressing pHluorin-mKate2-LC3 were washed, fixed with 4% of formaldehyde (FA; VWR, 9713.1) and nuclei were counterstained with Hoechst 33342 (Sigma-Aldrich, B2261). Imaging was performed using the Carl Zeiss LSM880 NLO inverted point scanning microscope (Carl Zeiss, Jena, Germany) using a 63x objective. Puncta of mKate2 and pHluorin were quantified using "Particle analyzer" in ImageJ and the ratio of mKate2-positive (red) to mKate2+pHluorin-positive (yellow) puncta per cell was calculated.

Transmission electron microscopy

Cells were seeded on a glass coverslip and grown in culture medium (as described above) or kept in HBSS medium (Sigma-Aldrich, H6648) for 24 h to induce starvation. After the incubation, cells were quickly washed with Sörensen buffer (SB; 0.1 M sodium/potassium phosphate buffer, pH 7.3) at

37°C, fixed with 2.5% glutaraldehyde (Sigma-Aldrich, G5882) in SB for 2 h (1 h at room temperature and 1 h in 4°C), washed with SB, and post-fixed with 1% OsO_4 (Sigma-Aldrich, 75632) solution in SB for 2 h at room temperature. Cells were dehydrated in series of acetone (Penta, 10060-11000) with increasing concentration and embedded in Epon-Durcupan resin (Sigma-Aldrich, 45345, 44611-13) and left to polymerize for 72 h at 60°C. Polymerized blocks were cut into 80-nm ultrathin sections and collected on 200-mesh size copper grids (Agar Scientific, AGG2200C). The sections were examined at 80 kV in FEI Morgagni 268 transmission electron microscope (FEI, Netherlands) using Mega View III CCD camera (Olympus Soft Imaging Solutions, Germany), in JEOL JEM-1011 (Jeol, Japan) equipped with Veleta CCD camera (Olympus Soft Imaging Solution, Germany) and in Jeol JEM-1400 FLASH equipped with Matataki camera (Jeol, Japan). Multiple images at 25,000x and 30,000x were taken from each analyzed cell to cover the whole area of the cell profile in ultrathin section. Quantification was performed using Ellipse image analysis program (ViDiTo, Slovakia).

Cloning, expression, and purification of LC3B-PLA2

The LC3B-PLA2 fusion was generated using custom-made codon-optimized DNA template gene-string synthesis protocol (Thermo Fisher Scientific, see Table S1 for the corresponding DNA and protein sequences). The coding sequence was PCR amplified with a pair of gene-specific primers (Table S2) and cloned into the pMT/BiP/SF-TEV vector in frame with the BiP secretion signal and the N-terminal Twin-Strep purification tag [56]. The identity of the expression plasmid, designated pMT/SLIN-LC3B-PLA2, was verified by Sanger sequencing.

The expression and purification of the LC3B-PLA2 fusion protein was carried out using protocols described previously [56]. Briefly, the pMT/SLIN-LC3B-PLA2 plasmid, together with pCoBLAST which confers resistance to Blasticidin (InvivoGen, ant-bl-1), were transfected into Schneider's S2 cells using Effectene (Qiagen, 301425) according to the manufacturer's protocol. Transfectants were selected in the Insect-Xpress medium (Lonza, BELN12-730Q) supplemented with 10% v:v FBS and 40 µg/ml Blasticidin. Four weeks post transfection, the Blasticidin-resistant S2 cells were transferred into the SFX medium, expanded and expression of SF-LC3B-PLA2 induced by the addition of 0.7 mM $CuSO_4$ (Sigma-Aldrich, C8027) at a cell density of 1 x 10^6/ml. Seven days post induction, cells were harvested by centrifugation, the conditioned medium supplemented with recombinant Streptavidin (10 µg/ml, produced in-house) and loaded on a StrepTactin XT affinity column (IBA, 2-4010-025). Following extensive washing with 100 mM Tris-HCl, 300 mM NaCl, pH 8.0, StrepTactin-bound fusion protein was eluted with 5 mM D-Biotin (IBA, 2-1016-005) in 100 mM Tris-HCl, 300 mM NaCl, pH 8.0. Pooled elution fractions containing pure SF-LC3B-PLA2 were concentrated to 1 mg/ml, snap-frozen in liquid nitrogen and stored at -80°C until further use. The typical yield of SF-LC3B-PLA2 was approximately 15 mg per liter of S2 culture with purity > 95%.

ATG4 activity assay

The assay was performed as described [43]. Cells and murine tissues were harvested in lysis buffer (25 mM Tris-HCl, pH 8.0, 100 mM NaCl, 1 mM CaCl2, 5 mM $MgCl_2$, 5% glycerol, 0.1% NP-40). Cell lysates were sonicated on ice (2 x 2 s) and tissues were homogenized 3 x 20s, 5000 rpm, with an interval of 2 min on ice, in prefilled lysing kits using a Precellys 24 tissue homogenizer and clarified using centrifugation. Cellular ATG4B activity was assessed by incubation of equal amounts of lysate with various concentrations of LC3B-PLA2 fusion protein substrate (200-1400 nM) or ATG4B (200, 400 and 600 nM) in reaction buffer (20 mM Tris-HCl, pH 8.0, 2 mM $CaCl_2$) in the presence of 20 mM Red/Green BODIPY PC-A2 (Thermo Fisher Scientific, A10072). If required, cells were pretreated with 1 mM of H_2O_2 (Sigma-Aldrich, 516813) for 4 h, or with 1 µM FMK-9a (MedChemExpress, HY-100522) or 0.1 µM NSC185058 (Cayman Chemical, 23957) for 2 h prior to harvesting. Fluorescence intensity was measured for 1 h at 2-min intervals (60 measurements per data point) using a Tecan Infinite M200 Microplate Reader (TECAN, Mannedorf, Switzerland) at 30°C with excitation and emission wavelength of 485 nm and 530 nm, respectively. Signal was normalized to the protein content determined by the BCA assay. To assess catalytic efficiency, the Km of ATG4B on LC3B-PLA2 was determined using Michaelis Menten non-linear regression fitting of a series of progress curves.

Assessment of cell death and ROS production

Cells were seeded as above, harvested by trypsin, washed by PBS and cell death was quantified using ANXA5/Annexin V-FITC (Exbio, P030-F500) and propidium iodide (PI) (Sigma-Aldrich, P4170) by flow cytometry. If required, the cells were pre-incubated with H_2O_2 or PEITC (Sigma-Aldrich, 253731) for 22 h. In some cases, 10 - 50 nM bafilomycin A_1 for 2 h, or 1 µM FMK-9a or 0.1 µM NSC185058 for 2 h, were applied prior to ROS inducers. Cells positive for ANXA5, PI, or ANXA5 and PI were considered dead. For experiments including Ndi1 (rotenone-insensitive NADH-ubiquinone oxidoreductase) and AOX expressing cells, ANXA5-Dy647 (Exbio, EXB0023) and Hoechst33258 (Sigma-Aldrich, 861405) was used instead (these cells express also GFP and RFP).

For ROS measurements, cells in the basal state or exposed to H_2O_2 or PEITC for 1 h were incubated for 20 min with 5 µM 2′,7′-dichlordihydrofluorescein diacetate (DCF-DA) (Sigma-Aldrich, D6883) and the levels of ROS were evaluated by flow cytometry. Data are expressed as geometric mean normalized to the control.

Targeted metabolomic analysis

For measurement of intracellular amino acids, cells were rinsed twice with ice-cold 0.9% NaCl (Lach-Ner, 30093-APO), scraped, washed at 15,000 g, 10 min at 4°C and stored at -80°C. Metabolites were extracted with ice-cold 75% acetonitrile (Fluka, 34967-1L) containing internal standards (Chromsystems, 55000) sonicated (10 times for 0.5 s), spun

(12,000 g, 10 min at 4°C) and supernatant was filtered using Multiscreen filter plate (Merck, MSRLN0410). The levels of metabolites were estimated by hydrophilic interaction liquid chromatography coupled to Qtrap 5500 mass spectrometer (Sciex, MA, USA) as described [57]. The data were analyzed using Skyline software[58] and processed according to Dunn et al [57,59].

For measurement of intracellular nucleotides and energy charge, cells grown in a 6-well plate for 24 h without uridine and pyruvate supplementation were washed with ice cold 0.9% NaCl solution, scraped into cold extraction buffer (80% LC-MS grade methanol in water) and stored at -80°C. Next, proteins were pelleted by centrifugation at 20,000 g for 15 min at 4°C. Part of the supernatant was transferred to LC-MS vials. The cell pellet was lysed in 200 mM NaOH for 20 min at 95°C. After centrifugation at 1,000 g for 10 min, protein levels were measured by BCA for normalization purposes. Target measurements of nucleotides and energy balance ([ATP + ½ ADP]/[ATP+ADP+AMP]) were performed using a Dionex UltiMate 3000 LC System (Thermo Fisher Scientific, Massachusetts, USA) in-line connected to a Q-Exactive Orbitrap mass spectrometer (Thermo Fisher Scientific, Massachusetts, USA). Ten microliters of the sample extracts (collected in 80% LC-MS grade methanol in water as described above) were separated on an Acquity HSS T3 UPLC column (Waters Corp, 2.1 mm x 150 mm, 1.8 µm particle size) using an Ultimate 3000 HPLC (Dionex, Thermo Fisher Scientific, MA, USA). Column temperature was held at 40°C throughout the analysis. Elution of metabolites was performed using a quaternary solvent system consisting of solvent A (10 mM Tributylamine, 15 mM acetic acid 5% methanol in water) and solvent B (100% methanol). The flow rate is kept constant at 250 µl/min and the following linear gradient is applied: at 0 min 0% B, from 2 to 7 min an increase to 37% B is accomplished; from 7 min to 14 min an increase to 41% B is carried out, from 14 to 26 min the gradient increases to 100% B and is maintained until 30 min. At 31 min the gradient progressively decreases to 0% B and lasts until 40 min. The data was then collected in "centroid data acquisition" mode, with negative electron spray ionization over a mass range of 70 – 1050 m/z and an extra filter of 300-850m850 m/z starting from the 8th min, both at a mass resolution of 70,000 (at m/z 200). The detector was an Orbitrap Qexactive (Thermo Fisher Scientific, MA, USA). We used following source settings: sheath gas flow rate at 50, aux gas flow rate at 10, spray voltage at 4 kV, capillary temperature at 350°C and the S-lens RF level was set at 60. DATA PROCESSING: mass spectrometry files were converted to the mzXML format using msConvert available from the proteowizard toolkit [60]. Analysis was performed using the Quan software (Thermo Fisher Scientific, Xcalibur version 4.0) and manually verified.

Determination of cell death sensitivity in vivo - TUNEL assay

Tamoxifen-induced mice were treated with a single dose of PEITC (1.25 mg/25 g mouse in corn oil) or vehicle-control on day 10 postinduction. Where indicated, mice were grafted with B16 melanoma cells (1 x 10^6 in 100 ml PBS) 24 h after the last tamoxifen injection and treated with a single dose of PEITC (1.25 mg/25 g mouse in corn oil) or doxorubicin (0.2 mg/20 g mouse in 0.9% NaCl; Sigma-Aldrich, D1515) on day 10. Where indicated, mice were treated with chloroquine (Sigma-Aldrich, 50-63-5; 1 mg/20 g mouse in corn oil) (on 3 consecutive days, the last dose being co-administered with PEITC (as above). Mice were sacrificed 16 h post application and non-malignant as well as tumor tissues were dissected, fixed in 4% FA overnight, dehydrated, embedded in paraffin or in cryo embedding matrix (OCT) (Leica, 14020108926) and sectioned. Paraffin sections (8 µm) were deparaffinized using xylene and decreasing concentration of ethanol (100% - 70%), rehydrated in PBS followed by permeabilization using 20 µg/ml of proteinase K (Sigma-Aldrich, P5568) for 1 h. Fixed frozen sections (5 µm) were permeabilized with 0.1% Triton X-100 (Sigma-Aldrich, T8787) 5 min at room temperature. Cell death was detected using the In Situ Cell Death Detection Kit, Fluorescein (Roche, 11684795910) according to the manufacturer's instructions. The positive and negative control tissue slides were incubated with DNAase (Sigma-Aldrich, D4527-10KU) (for 12 min) and/or TUNEL-label solution (1 h), respectively. Where indicated, TUNEL assay was combined with EdU staining for detection of proliferation. Mice were injected with 50 µg of EdU (Cayman Chemical, 20518) in PBS 4 h prior to the end of the experiment. EdU was detected by a Click reaction using 100 mM copper sulfate (Thermo Fisher Scientific, C10337) 200 mg/ml sodium ascorbate (Sigma-Aldrich, A4034) and 10 µM Alexa Fluor™ 647 Azide, (Invitrogen, A10277) for 45 min at room temperature. Hoechst 33342 (10 µg/ml) was used to visualize cell nuclei. Imaging was performed using the Carl Zeiss LSM880 NLO inverted point scanning microscope. Cell death was quantified as number of TUNEL-positive cells per area of the tissue.

In situ detection of ROS in the endothelium

Tamoxifen induced control and *tfam* ECKO mice were treated for 4 h with LPS (10 mg/kg in PBS, i.p.) (Sigma-Aldrich, L2630) or vehicle control. Aortas were harvested, opened longitudinally and stained with 20 µM of dihydroethidium (DHE) (Sigma-Aldrich, 37291) in PBS for 30 min in the dark at 37°C, followed by staining with Hoechst 33342 for 15 min and Isolectin B4 (Thermo Fisher Scientific, 132450) at 10 µg/ml for 1 h as previously described [6]. Imaging was performed using a Leica TCS SP8 WLL SMD-FLIM microscope (Leica Microsystems, Wetzlar, Germany) and DHE fluorescence intensity was quantified using Fiji/ImageJ software. Seven images per aorta were analyzed. The images were segmented based on the Hoechst signal and the average intensity of the DHE signal in the nuclear region was calculated using Fiji/ImageJ for each image. Results for each animal were averaged.

Leukocyte infiltration into the lungs

Lungs from LPS-treated mice were dissected and fixed in 4% FA overnight, dehydrated, embedded in paraffin, and sectioned. Immune cells were stained using rat anti-mouse

PTPRC/CD45 antibody (Invitrogen, 14-0451-85) followed by an appropriate secondary antibody. Nuclei were counterstained with Hoechst 33342. Imaging was performed using a Carl Zeiss LSM880 NLO inverted point scanning microscope and the PTPRC/CD45-positive area was quantified using Fiji/ImageJ software. The infiltration of leukocytes is expressed as a percentage of PTPRC/CD45-positive region per lung section area. Results for each animal were averaged.

DSS-induced acute colitis model

Tamoxifen induced control and *tfam* ECKO mice were exposed to 2.5% dextran sulfate sodium (DSS), 36,000-50,000 M. Wt. (MP Biomedicals, ICNA0216011080) in the drinking water for 7 consecutive days. Where indicated mice were co-treated with 15 mg/kg/day of 4-Hydroxy-TEMPO (Sigma-Aldrich, 176141) in PBS or with solvent control administered every 12 h by subcutaneous injections. The disease activity index, which scores body weight loss, stool consistency, and blood in the stool and the anal region, indicates the severity of colitis under DSS treatment (score 0: no weight loss, normal stool consistency, no bleeding; score 1: 1-5% weight loss, normal stool consistency, occult blood; score 2: 5-10% weight loss, loose stool, occult blood; score 3: 10-15% weight loss, loose stool, occult blood; score 4: > 15% weight loss, diarrhea, gross bleeding). On day 7, mice were injected via the tail vein with 0.25 mg dextran-rhodamine, 70,000 kDA (Thermo Fisher Scientific, D1818) and 10 min after injection, mice were perfused and fixed using 1% FA. Colon was harvested and fixed in 4% FA overnight, dehydrated, embedded in paraffin, and sectioned. Colon sections were stained with Hematoxylin/Eosin for morphological analyses, with anti-ENG/CD105 antibody (RD Systems, AF1320) to identify blood vessels and with an anti-PTPRC/CD45 antibody to analyze immune cell infiltration, followed by incubation with an appropriate secondary antibody. Nuclei were counterstained with Hoechst 33342. Imaging was performed using a Carl Zeiss LSM880 NLO inverted point scanning microscope. Fiji/ImageJ software was used to quantify the number of PTPRC/CD45-positive cells per colon area as well as the instances of the extravascular dextran-rhodamine leakages per colon area. Results were averaged per mouse.

Quantification and statistical analysis

Data were analyzed in GraphPad Prism 5.04 software (GraphPad Software) using unpaired Student's t-test analysis, one-way ANOVA or two-way ANOVA for comparisons of more than two parameters. Data shown are mean values ± S.E.M. of at least 3 independent experiments. A statistical difference of $p < 0.05$ was considered significant.

Acknowledgment

We acknowledge Imaging Methods Core Facility of Faculty of Science, Charles University at BIOCEV and the Electron Microscopy Core Facility of Institute of Molecular Genetics, Czech Academy of Sciences, for assistance with light and electron imaging. We thank the Laboratory of Electron Microscopy, Faculty of Science, Charles University, for the possibility to use the transmission electron microscope JEOL JEM-1011. Nucleotide analysis was performed at the Metabolomics Expertise Center, VIB, Leuven, Belgium. Proteomics LC/MS analysis was done by K. Harant and P. Talacko from Laboratory of Mass Spectrometry, Biocev, Faculty of Science, Charles University. We thank B. Havlinova (Institute of Biotechnology, Czech Academy of Sciences) for help with LC3B-PLA2 fusion protein construction, T. Michalcikova and I. Bukova (Czech Center for Phenogenomics/Institute of Molecular Genetics, Czech Academy of Sciences) for help and advice on MEF isolation and to R. Boon (Goethe University, Frankfurt am Mein, Germany) for providing the *Cdh5*^{CreERT2} mice.

Disclosure statement

The authors declare no competing interests.

Funding

This work was supported by Czech Science Foundation (20-18513S, 17-24441S, 20-05942S, 18-02550S, 19-10354S, 21-04607X, 22-34507S, 18-24753Y), Czech Health Research Council (17-30138A, 17-32727A, NU21-03-00545, NU20J-02-00035), Charles University Grant Agency (1552218, 1506318, 1435320). J.K. is supported by AIAS-CO-FUND II: GA: MSCA: 754513, Lundbeckfonden: R307-2018-3667, Carlsberg Fonden: CF19-0687, Kræftens Bekæmpelse: R302-A17296, A.P. Møller Fonden: 20-L-0317, Riisfort Fonden and Steno Diabetes Center Aarhus (SDCA). P.C. is supported by long-term structural Methusalem funding by the Flemish Government, FWO-Vlaanderen, a Novo Nordisk Foundation Laureate grant, and an ERC Advanced Research Grant (EU-ERC743074). K.R is supported by Marie Skłodowska-Curie Individual Fellowship (101027977) and by EMBO Installation Grant (IG 5068-2022). Infrastructure support was from ERDF and MEYS CR (CZ.02.1.01/0.0/0.0/16_013/0001775, CZ.02.1.01/0.0/0.0/18_046/0016045), ESIF and MEYS CR (CZ.02.1.01/0.0/0.0/18_046/0015861), MEYS CR (LM2018129, LM2015040, LM2018126) and from Czech Academy of Sciences (RVO:86652036, RVO:68378050, RVO:67985823).

Data availability

All raw sequencing data are available in Gene Expression Omnibus under accession number GSE146025. Raw proteomics data are available in the Pride database under accession number PXD021376.

ORCID

Joanna Kalucka http://orcid.org/0000-0003-4887-7672
Sona Stemberkova Hubackova http://orcid.org/0000-0002-3454-6840
Tomas Mracek http://orcid.org/0000-0002-9492-0718
Cyril Barinka http://orcid.org/0000-0003-2751-3060
Jiri Neuzil http://orcid.org/0000-0002-2478-2460
Katerina Rohlenova http://orcid.org/0000-0003-3964-8472
Jakub Rohlena http://orcid.org/0000-0001-5427-6502

References

1. Arrojo EDR, Lev-Ram V, Tyagi S *et al.* Age Mosaicism across Multiple Scales in Adult Tissues. Cell Metab. 2019;30(2):343–351 e343. PubMed PMID: 31178361
2. Kops GJ, Dansen TB, Polderman PE *et al.* Forkhead transcription factor FOXO3a protects quiescent cells from oxidative stress. Nature. 2002;419(6904):316–321. PubMed PMID: 12239572
3. Naderi J, Hung M, Pandey S. Oxidative stress-induced apoptosis in dividing fibroblasts involves activation of p38 MAP kinase and over-expression of Bax: resistance of quiescent cells to oxidative stress. Apoptosis. 2003;8(1):91–100. PubMed PMID: 12510156

4. Legesse-Miller A, Raitman I, Haley EM *et al*. Quiescent fibroblasts are protected from proteasome inhibition-mediated toxicity. Mol Biol Cell. 2012;23(18):3566–3581. PubMed PMID: 22875985
5. Valentin M, Yang E. Autophagy is activated, but is not required for the G0 function of BCL-2 or BCL-xL. Cell Cycle. 2008;7 (17):2762–2768. PubMed PMID: 18758240
6. Kalucka J, Bierhansl L, Conchinha NV *et al*. Quiescent Endothelial Cells Upregulate Fatty Acid beta-Oxidation for Vasculoprotection via Redox Homeostasis. Cell Metab. 2018;28 (6):881–894 e813. PubMed PMID: 30146488
7. Blecha J, Novais SM, Rohlenova K *et al*. Antioxidant defense in quiescent cells determines selectivity of electron transport chain inhibition-induced cell death. Free Radic Biol Med. 2017;112:253–266. PubMed PMID: 28774815
8. Rohlena J, Dong LF, Kluckova K *et al*. Mitochondrially targeted alpha-tocopheryl succinate is antiangiogenic: potential benefit against tumor angiogenesis but caution against wound healing. Antioxid Redox Signal. 2011;15(12):2923–2935. PubMed PMID: 21902599
9. Dong LF, Swettenham E, Eliasson J *et al*. Vitamin E analogues inhibit angiogenesis by selective induction of apoptosis in proliferating endothelial cells: the role of oxidative stress. Cancer Res. 2007;67(24):11906–11913. PubMed PMID: 18089821
10. Dikic I, Elazar Z. Mechanism and medical implications of mammalian autophagy. Nat Rev Mol Cell Biol. 2018;19(6):349–364. PubMed PMID: 29618831
11. Egan DF, Chun MG, Vamos M *et al*. Small Molecule Inhibition of the Autophagy Kinase ULK1 and Identification of ULK1 Substrates. Mol Cell. 2015;59(2):285–297. PubMed PMID: 26118643
12. Kim J, Kundu M, and Viollet B *et al*. AMPK and mTOR regulate autophagy through direct phosphorylation of Ulk1. Nat Cell Biol. 2011;13:132. PubMed PMID: 21258367
13. Scherz-Shouval R, and Elazar Z. ROS, mitochondria and the regulation of autophagy. Trends Cell Biol. 2007;17(9):422–427. PubMed PMID: 17804237
14. Santidrian AF, Matsuno-Yagi A, Ritland M *et al*. Mitochondrial complex I activity and NAD+/NADH balance regulate breast cancer progression. J Clin Invest. 2013;123(3):1068–1081. PubMed PMID: 23426180
15. Thomas HE, Zhang Y, Stefely JA *et al*. Mitochondrial Complex I Activity Is Required for Maximal Autophagy. Cell Rep. 2018;24 (9):2404–2417 e2408. PubMed PMID: 30157433
16. Murphy MP. How mitochondria produce reactive oxygen species. Biochem J. 2009;417(1):1–13. PubMed PMID: 19061483
17. Mills EL, Kelly B, Logan A *et al*. Succinate Dehydrogenase Supports Metabolic Repurposing of Mitochondria to Drive Inflammatory Macrophages. Cell. 2016;167(2):457–470 e413. PubMed PMID: 27667687
18. Birsoy K, Wang T, Chen WW *et al*. An Essential Role of the Mitochondrial Electron Transport Chain in Cell Proliferation Is to Enable Aspartate Synthesis. Cell. 2015;162(3):540–551. PubMed PMID: 26232224
19. Sullivan LB, Gui DY, Hosios AM *et al*. Supporting Aspartate Biosynthesis Is an Essential Function of Respiration in Proliferating Cells. Cell. 2015;162(3):552–563. PubMed PMID: 26232225
20. Titov DV, Cracan V, Goodman RP *et al*. Complementation of mitochondrial electron transport chain by manipulation of the NAD+/NADH ratio. Science. 2016;352(6282):231–235. PubMed PMID: 27124460
21. Bajzikova M, Kovarova J, Coelho AR *et al*. Reactivation of Dihydroorotate Dehydrogenase-Driven Pyrimidine Biosynthesis Restores Tumor Growth of Respiration-Deficient Cancer Cells. Cell Metab. 2019;29(2):399–416 e310. PubMed PMID: 30449682
22. Martinez-Reyes I, Cardona LR, Kong H *et al*. Mitochondrial ubiquinol oxidation is necessary for tumour growth. Nature. 2020;585(7824):288–292. PubMed PMID: 32641834
23. Appleby RD, Porteous WK, Hughes G *et al*. Quantitation and origin of the mitochondrial membrane potential in human cells lacking mitochondrial DNA. Eur J Biochem. 1999;262(1):108–116. PubMed PMID: 10231371
24. Buchet K, Godinot C. Functional F1-ATPase essential in maintaining growth and membrane potential of human mitochondrial DNA-depleted rho degrees cells. J Biol Chem. 1998;273 (36):22983–22989. PubMed PMID: 9722521
25. Larsson NG, Wang J, Wilhelmsson H *et al*. Mitochondrial transcription factor A is necessary for mtDNA maintenance and embryogenesis in mice. Nat Genet. 1998;18(3):231–236. PubMed PMID: 9500544
26. Trachootham D, Zhou Y, Zhang H *et al*. Selective killing of oncogenically transformed cells through a ROS-mediated mechanism by beta-phenylethyl isothiocyanate. Cancer Cell. 2006;10(3):241–252. PubMed PMID: 16959615
27. De Bock K, Georgiadou M, Schoors S *et al*. Role of PFKFB3-driven glycolysis in vessel sprouting. Cell. 2013;154 (3):651–663. PubMed PMID: 23911327
28. Falkenberg KD, Rohlenova K, Luo Y *et al*. The metabolic engine of endothelial cells. Nat Metab. 2019;1(10):937–946. PubMed PMID: 32694836
29. Aragona M, Panciera T, Manfrin A *et al*. A mechanical checkpoint controls multicellular growth through YAP/TAZ regulation by actin-processing factors. Cell. 2013;154(5):1047–1059. PubMed PMID: 23954413
30. Tan AS, Baty JW, Dong LF *et al*. Mitochondrial genome acquisition restores respiratory function and tumorigenic potential of cancer cells without mitochondrial DNA. Cell Metab. 2015;21 (1):81–94. PubMed PMID: 25565207
31. King MP, Attardi G. Human cells lacking mtDNA: repopulation with exogenous mitochondria by complementation. Science. 1989;246(4929):500–503. PubMed PMID: 2814477
32. Kuma A, Hatano M, Matsui M *et al*. The role of autophagy during the early neonatal starvation period. Nature. 2004;432 (7020):1032–1036. PubMed PMID: 15525940
33. Carroll B, Korolchuk VI, Sarkar S. Amino acids and autophagy: cross-talk and co-operation to control cellular homeostasis. Amino Acids. 2015;47(10):2065–2088. PubMed PMID: 24965527
34. Tanida I, Ueno T, Uchiyama Y. A super-ecliptic, pHluorin-mKate2, tandem fluorescent protein-tagged human LC3 for the monitoring of mammalian autophagy. PLoS One. 2014;9(10):e110600. PubMed PMID: 25340751
35. Kim J, Kundu M, Viollet B *et al*. AMPK and mTOR regulate autophagy through direct phosphorylation of Ulk1. Nat Cell Biol. 2011;13(2):132–141. PubMed PMID: 21258367
36. Cardenas C, Lovy A, Silva-Pavez E *et al*. Cancer cells with defective oxidative phosphorylation require endoplasmic reticulum-to-mitochondria Ca(2+) transfer for survival. Sci Signal. 2020;13 (640):eaay1212. PubMed PMID: 32665411
37. Filomeni G, De Zio D, Cecconi F. Oxidative stress and autophagy: the clash between damage and metabolic needs. Cell Death Differ. 2015;22(3):377–388. PubMed PMID: 25257172
38. Scherz-Shouval R, Shvets E, Fass E *et al*. Reactive oxygen species are essential for autophagy and specifically regulate the activity of Atg4. EMBO J. 2007;26(7):1749–1760. PubMed PMID: 17347651
39. Zhang X, Cheng X, Yu L *et al*. MCOLN1 is a ROS sensor in lysosomes that regulates autophagy. Nat Commun. 2016;7:12109. PubMed PMID: 27357649
40. Settembre C, Di Malta C, Polito VA *et al*. TFEB links autophagy to lysosomal biogenesis. Science. 2011;332(6036):1429–1433. PubMed PMID: 21617040
41. Guo QQ, Wang SS, Zhang SS *et al*. ATM-CHK2-Beclin 1 axis promotes autophagy to maintain ROS homeostasis under oxidative stress. EMBO J. 2020;39(10):e103111. PubMed PMID: 32187724
42. Zheng X, Yang Z, Gu Q *et al*. The protease activity of human ATG4B is regulated by reversible oxidative modification. Autophagy. 2020;16(10):1838–1850. PubMed PMID: 31880198
43. Shu CW, Drag M, Bekes M *et al*. Synthetic substrates for measuring activity of autophagy proteases: autophagins (Atg4). Autophagy. 2010;6(7):936–947. PubMed PMID: 20818167

44. Qiao S, Dennis M, Song X *et al.* A REDD1/TXNIP pro-oxidant complex regulates ATG4B activity to control stress-induced autophagy and sustain exercise capacity. Nat Commun. 2015;6:7014. PubMed PMID: 25916556
45. Akin D, Wang SK, Habibzadegah-Tari P *et al.* A novel ATG4B antagonist inhibits autophagy and has a negative impact on osteosarcoma tumors. Autophagy. 2014;10(11):2021–2035. PubMed PMID: 25483883
46. Qiu Z, Kuhn B, Aebi J *et al.* Discovery of Fluoromethylketone-Based Peptidomimetics as Covalent ATG4B (Autophagin-1) Inhibitors. ACS Med Chem Lett. 2016;7(8):802–806. PubMed PMID: 27563406
47. Wang S, Konorev EA, Kotamraju S *et al.* Doxorubicin induces apoptosis in normal and tumor cells via distinctly different mechanisms. intermediacy of H(2)O(2)- and p53-dependent pathways. J Biol Chem. 2004;279(24):25535–25543. PubMed PMID: 15054096
48. Incalza MA, D'Oria R, Natalicchio A *et al.* Oxidative stress and reactive oxygen species in endothelial dysfunction associated with cardiovascular and metabolic diseases. Vascul Pharmacol. 2018;100:1–19. PubMed PMID: 28579545
49. Kratzer E, Tian Y, Sarich N *et al.* Oxidative stress contributes to lung injury and barrier dysfunction via microtubule destabilization. Am J Respir Cell Mol Biol. 2012;47(5):688–697. PubMed PMID: 22842495
50. Araki Y, Sugihara H, Hattori T. The free radical scavengers edaravone and tempol suppress experimental dextran sulfate sodium-induced colitis in mice. Int J Mol Med. 2006;17(2):331–334. PubMed PMID: 16391834
51. Diebold LP, Gil HJ, Gao P *et al.* Mitochondrial complex III is necessary for endothelial cell proliferation during angiogenesis. Nat Metab. 2019;1(1):158–171. PubMed PMID: 31106291
52. Planavsky NJ, Reinhard CT, Wang X *et al.* Earth history. Low mid-Proterozoic atmospheric oxygen levels and the delayed rise of animals. Science. 2014;346(6209):635–638. PubMed PMID: 25359975
53. Hamanaka RB, Glasauer A, Hoover P *et al.* Mitochondrial reactive oxygen species promote epidermal differentiation and hair follicle development. Sci Signal. 2013;6(261):ra8. PubMed PMID: 23386745
54. Pitulescu ME, Schmidt I, Benedito R *et al.* Inducible gene targeting in the neonatal vasculature and analysis of retinal angiogenesis in mice. Nat Protoc. 2010;5(9):1518–1534. PubMed PMID: 20725067
55. Lortz S, Gurgul-Convey E, Naujok O *et al.* Overexpression of the antioxidant enzyme catalase does not interfere with the glucose responsiveness of insulin-secreting INS-1E cells and rat islets. Diabetologia. 2013;56(4):774–782. PubMed PMID: 23306382
56. Barinka C, Ptacek J, Richter A *et al.* Selection and characterization of Anticalins targeting human prostate-specific membrane antigen (PSMA). Protein Eng Des Sel. 2016;29(3):105–115. PubMed PMID: 26802163
57. Yuan M, Breitkopf SB, Yang X *et al.* A positive/negative ion-switching, targeted mass spectrometry-based metabolomics platform for bodily fluids, cells, and fresh and fixed tissue. Nat Protoc. 2012;7(5):872–881. PubMed PMID: 22498707
58. MacLean B, Tomazela DM, Shulman N *et al.* Skyline: an open source document editor for creating and analyzing targeted proteomics experiments. Bioinformatics. 2010;26(7):966–968. PubMed PMID: 20147306
59. Dunn WB, Broadhurst D, Begley P *et al.* Procedures for large-scale metabolic profiling of serum and plasma using gas chromatography and liquid chromatography coupled to mass spectrometry. Nat Protoc. 2011;6(7):1060–1083. PubMed PMID: 21720319
60. Chambers MC, Maclean B, Burke R *et al.* A cross-platform toolkit for mass spectrometry and proteomics. Nat Biotechnol. 2012;30(10):918–920. PubMed PMID: 23051804

Supplementary Materials and Methods

Cloning of the roGFP2-ORP1 reporter, AOX and Ndi1 overexpression.

The untargeted pEIGW roGFP2-Orp1 lentiviral construct (Addgene, 64993) was a gift from T. Dick [1]. To express the mitochondria-targeted variant of the roGFP2-ORP1 construct lentivirally, the mito-roGFP2-Orp1 sequence was PCR-amplified from the retroviral plasmid pLPCX mito roGFP2-Orp1 (Addgene, 64992) [1], digested by XbaI/NotI fast digestion enzymes (Thermo Fisher Scientific, FD0684/FD0594) and ligated into the XbaI/NotI-digested pCDH-CMV-MSC-EF1-PURO lentiviral plasmid (System Biosciences, CD510B-1) using T4 ligase (Thermo Fisher Scientific, 15224-017). The final construct was verified by DNA sequencing. The cloning primers used were 5'- TAA GCA TCT AGA ATG GCC TCC ACT CGT GTC CTC -3' (forward) and 5'-TGC TTA GCG GCC GCC TAT TCC ACC TCT TTC AAA AGT TCT TCG-3' (reverse).

To express AOX and Ndi1, we used pWPI-AOX-IRES-GFP and pCDH-CMV-NDI1-EF1-RFP-WPRE lentiviral plasmids, a gift of N. Chandel (Northwestern University, Chicago, IL, USA) [2].

Lentiviral particles were produced in Hek293-FT cells as described previously [3]. shRNA transduced cells were selected by puromycin (Invivogen, ant-pr-1), CAT transduced cells by blasticidin (Invivogen, ant-bl-05). Cells transduced with the fluorescent reporter constructs or Ndi1+AOX were FACS-sorted to enrich for positive cells when the efficacy of transduction was too low. Cells were used for experiments within 1-month post-transduction.

ATG4B silencing.

Transfection with esiRNA targeting *ATG4B* (Sigma-Aldrich, EHU113921-20UG) were performed using Lipofectamine 3000 (Thermo Scientific, L3000008). Cells were transfected with increasing concentrations (0.05, 0.1, 0.2, 0.3 µg) of esiRNA 16 h before they reached confluence.

Cell cycle analysis and visualization of adherence junctions.

Cell cycle analysis and visualization of adherent junctions were performed as described previously [3]. Briefly, the cell cycle analysis was performed using pyronin-y/Hoechst 33342 (0.5 μg/ml / 10 μg/ml) by flow cytometry. Immunofluorescence detection of CDH5/VE-cadherin (Santa Cruz Biotechnology, sc-9989) staining was performed using Leica TCS SP8 WLL SMD-FLIM microscope.

EdU staining in vitro.

For EdU staining, cells were seeded as described above. EdU staining was performed using the Click-iT™ EdU Cell Proliferation kit (Molecular probes, C10337) following the manufacturer's instructions, except that the reaction buffer supplied was replaced by PBS.

Assessment of cellular senescence.

SA-GBA1/β-gal activity was detected as previously described with slight modifications [4]. Cells were washed with PBS, fixed with 0.5 % glutaraldehyde (Fluka, 100.12) in PBS; pH 7.2, and washed with PBS (pH 6.0) supplemented with 1 mM $MgCl_2$. Cells were stained with the X-gal solution (1 mg/ml X-gal [Roche, 10651745001], 0.12 mM $K_3Fe[CN]_6$, 0.12 mM $K_4Fe[CN]_6$, 1 mM $MgCl_2$ in PBS at pH 6.0) at 37°C for 2 h. As a positive control, cells were treated with 100 μM 5-bromo-2′-deoxyuridine (BrdU; Sigma-Aldrich, 307.1) for 9 days. The signal was detected using the Leica DMIL Led microscope (Leica Microsystems, Wetzlar, Germany).

In-gel enzymatic activity assays.

In-gel activity of antioxidant proteins was assessed as described before [5]. Briefly, samples were sonicated using the Misonix Sonicator 3000 instrument (QSonica, CT, USA) at 30 % power using microtip ~3 W, 3 × 15 s with 25 s pause on ice, cleared by centrifugation and 50 mg of protein

extract was loaded onto non-denaturing SDS-PAGE gels. The incubation time for the SOD2 activity stain was reduced to 7 min.

NADH/NAD$^+$ measurements.

Cells were seeded in a 96-well plate and ratio of NADH:NAD$^+$ was determined using luminescence assays NADP/NADPH-Glo™ (Promega, G9071) according to the manufacturer's instructions. The measurements were corrected to protein content.

Cloning, expression, and purification of recombinant ATG4B.

The codon-optimized DNA template (Genscript) for human ATG4B (UNIPROT NO: Q9Y4P1) was PCR amplified using the F_ATG4B_GWT/R_ATG4B_GTW primer pair (Table S2) and cloned into the pD221 plasmid (Invitrogen, 12536017) using the BP recombination reaction (Invitrogen, 11789-100), according to the manufacturer's protocol. The identity of the resulting entry clone was confirmed by Sanger sequencing. The expression plasmid was generated via LR recombination reaction between the entry clone and the pEC566 destination vector featuring an N-terminal TEV-cleavable His-MBP tag.

His-MBP-ATG4B fusion protein was expressed in BL21-DE3-RIPL cells (Agilent, 230280) upon induction with 0.5 mM isopropyl β-D-1-thiogalactopyranoside (IPTG; MP Biomedicals, 194029) for 17 h at 16°C. Cells from two liters of culture were harvested by centrifugation, lysed in 20 ml of lysis Buffer (50 mM NaH_2PO_4, 0.30 M NaCl, 10 % w:v glycerol, 20 mM imidazole, pH 8.0) supplemented with an EDTA-free protease inhibitor cocktail (Roche, 05056489001) using Emulsiflex (Avestin, Mannheim, Germany) The lysate was cleared by centrifugation at 7200 x g (20 min), then 40,000 x g (40 min).

The supernatant was loaded onto a Ni-NTA affinity column (IBA Lifesciences, 2-3206-025) equilibrated in the lysis buffer and the His-MBT-ATG4B fusion protein was eluted using a

stepwise gradient of the lysis buffer supplemented with 500 mM imidazole (Serva, 26081.02). Fractions containing the fusion construct were pooled, concentrated to 1 mg/ml and stored at -80°C. Purity of the final preparation was evaluated by SDS-PAGE.

Measurement of respiration and intracellular ATP.

Cellular respiration was assessed using the high-resolution Oxygraph-2k respirometer (O2k; Oroboros Instruments). Cells were trypsinized, washed with PBS and resuspended at 1.0 - 1.5 x 10^6 cells per ml of the Mir05 medium (0.5 mM EGTA, 3 mM $MgCl_2$, 60 mM K-lactobionate [Sigma-Aldrich, 153516], 20 mM taurine [Sigma-Aldrich, T0625], 10 mM KH_2PO_4, 110 mM sucrose, 1 g/l essential fatty acid-free bovine serum albumin [Sigma-Aldrich, A7030], 20 mM HEPES, pH 7.1 at 30°C). The total oxygen concentration and consumption were monitored in the presence of specific substrates (10 mM glutamate [56-86-0], 2 mM malate [63474-37-3], 10 mM succinate [59637], 3 mM ADP [A5285], all from Sigma-Aldrich), inhibitors (2.5 µM oligomycin [04876], 0.5 µM rotenone [R8875], 0.5 µM antimycin A [A8674], all from Sigma-Aldrich), and uncouplers (CCCP [C2759] or FCCP [C2920], from Sigma-Aldrich) titrated in 0.5 µM steps until maximal uncoupled respiration was reached.

Intracellular ATP levels were assessed by the CellTiter-Glo kit (Promega, G7570) following the manufacturer's instructions in 96-well format. Data were normalized to the cell number measured by crystal violet staining in a parallel 96-well plate.

Cytochrome C Oxidase-Succinate Dehydrogenase (COX-SDH) activity in situ.

Embedded frozen tissues were sectioned and stained for COX and SDH as described previously [6] Briefly, tissues sections were incubated for 40 min at 37°C with diaminobenzidine (Sigma-Aldrich, D-8001), CYCS/cytochrome c (Sigma-Aldrich, C7752) and CAT (catalase; Sigma-Aldrich, C1345) for COX visualization followed by incubation with nitro blue tetrazolium chloride (Sigma-Aldrich, N6639), sodium succinate (Sigma-Aldrich, 59637), phenazine methosulfate (Sigma-Aldrich, P9625) and sodium azide (Fluka, 71289) for SDH staining. Slides were dehydrated and visualized using the Leica DMIL Led microscope.

Measurements of mitochondrial and cytoplasmic ROS using Orp1-roGFP2 and mitoOrp1-roGFP2.

To measure ROS production using ratiometric genetically encoded sensors, cells expressing roGFP2-Orp1 and mitoOrp1-roGF2 were analyzed as described [1]. Briefly, after washing with PBS, cells were treated with 20 mM of N-ethylmaleimide (Sigma-Aldrich, E3876) in PBS (5 min at RT), detached with trypsin, and fixed with 3% of FA in PBS (7 min at RT). We calculated the ratio of fluorescence signal detected through the 530/30 nm bandpass emission filter upon excitation at 407 and 488 nm using flow cytometry.

RNA-seq data acquisition and analysis.

RNA was isolated using RNAzol (Molecular Research Center, RN190) according to the manufacturer's instructions. RNA was dissolved in the TE buffer (Thermo Fisher Scientific, 12090015), and remaining DNA contamination was removed using DNAse I (Sigma-Aldrich, D4527-10KU) for 30 min. To clean RNA, the same volume of 8 M LiCl (Sigma-Aldrich, L7026) was added and incubated overnight at -20°C. Samples were centrifuged for 30 min at 16,100 x g,

2°C; the supernatant was removed, and the pellet washed twice in 80% ethanol, followed by centrifugation as above. The remaining ethanol was evaporated at 65°C for 10 min, and RNA was dissolved in 20 µl of TE buffer. Concentration of total RNA was measured by Nanodrop 2000. The quality of RNA was verified using a Fragment Analyzer along with the RNA Standard Sensitivity kit (AATI, DNF-471). The RNA-Seq libraries were prepared from 2 ng of Total RNA using the SureSelect Strand-Specific RNA Library Prep kit (Agilent, G9691A), which is targeted for the enrichment of RNA with poly-A tail. The quality of the final libraries was checked using a Fragment Analyzer along with the NGS High Sensitivity kit (AATI, DNF-474). Libraries were pooled and sequenced on the NextSeq500 (Illumina) instrument at high output run with 2 x 80 cycles. The raw sequenced reads were mapped to the human reference transcriptome and genome (build GRCh38) using the Kallisto pipeline [7]. Mapped reads were assigned to ensemble gene IDs by HTSeq. Raw count gene expression data were filtered for genes expressed at a level of at least 1 count per million reads in at least 10% of samples, and normalized using trimmed mean of M-values (TMM) available from the EdgeR package [8]. Differentially expressed genes and their false discovery rate (FDR) corrected p values were identified by the Limma package [9]. We used gene set enrichment analysis (GSEA) as implemented in the clusterProfiler package (version 3.6.0) [10] and gene set variation analysis (GSVA) as implemented in the GSVA R-package (version 1.26.0) [11]. Gene set analysis was performed using KEGG gene sets. GSEA and GSVA scores were calculated for sets with a minimum of 10 detected genes, all other parameters were default. Genes of the hsa04140 Autophagy pathway containing TFEB binding sites within 5000bp upstream of the gene's transcription start site were collected from the Gene Transcription Regulation Database (GTRD) (assess date 21.11.19) [12].

Proteomic analysis.

Cell pellets were lysed in 100 mM TEAB (Sigma-Aldrich, T7408) containing 2% SDC (Sigma-Aldrich, 30970) and boiled at 95°C for 5 min. Protein concentration was determined using BCA protein assay kit and 20 μg of protein per sample was used for MS sample preparation. Cysteine residues were reduced with 5 mM final concentration of TCEP (Thermo Fisher Scientific, 20491) (60°C for 60 min) and blocked with 10 mM final concentration of MMTS (Thermo Fisher Scientific, 64306) (10 min at RT). Samples were digested with trypsin (trypsin:protein ratio 1:30) at 37°C overnight. Next, samples were acidified with TFA (Thermo Fisher Scientific, 28901) to 1% final concentration. SDC was removed by extraction to ethylacetate [13] and peptides were desalted using in-house made stage tips packed with C18 disks (Empore) described previously [14].

Nano Reversed phase columns (EASY-Spray column, 50 cm x 75 μm ID, PepMap C18, 2 μm particles, 100-Å pore size; (Thermo Fisher Scientific, ES80) were used for LC/MS analysis. Mobile phase buffer A was composed of water and 0.1% formic acid (VWR, 84865.180). Mobile phase B was composed of acetonitrile (Fisher Scientific, a955-4) and 0.1% formic acid. Samples were loaded onto the trap column (C18 PepMap100, 5-μm particle size, 300 μm x 5 mm; (Thermo Fisher Scientific, 160454) for 4 min at 18 μl/min, with loading buffer composed of water, 2% acetonitrile and 0.1% trifluoroacetic acid. Peptides were eluted with mobile phase B gradient from 4% to 35% B in 120 min. Eluting peptide cations were converted to gas-phase ions by electrospray ionization and analyzed on a Thermo Orbitrap Fusion (Q-OT- qIT, Thermo Fisher Scientific). Survey scans of peptide precursors from 350 to 1400 m/z were performed in orbitrap at 120K resolution (at 200 m/z) with a 5 × 105 ion count target. Tandem MS was performed by isolation at 1.5 Th with the quadrupole, HCD fragmentation with normalized collision energy of 30, and rapid

scan MS analysis in the ion trap. The MS2 ion count target was set to 104 and the max injection time was 35 ms. Precursors with charge state 2–6 were sampled for MS2. The dynamic exclusion duration was set to 45 s with a 10 ppm tolerance around the selected precursor and its isotopes. Monoisotopic precursor selection was turned on. The instrument was run in top speed mode with 2 s cycles [15].

All data were analyzed and quantified with the MaxQuant software (version 1.6.3.4) [16]. The false discovery rate (FDR) was set to 1% for both proteins and peptides and we specified a minimum peptide length of 7 amino acids. The Andromeda search engine was used for the MS/MS spectra search against the Human database (downloaded from Uniprot in September 2017, containing 20,142 entries). Enzyme specificity was set as C-terminal to Arg and Lys, also allowing cleavage at proline bonds and a maximum of two missed cleavages. Dithiomethylation of cysteine was selected as fixed modification and N- terminal protein acetylation and methionine oxidation as variable modifications. The "match between runs" feature of MaxQuant was used to transfer identifications to other LC-MS/MS runs based on their masses and retention time (maximum deviation 0.7 min) and this was also used in quantification experiments. Quantifications were performed with the label-free algorithm in MaxQuant [17].

Data analysis was performed in R after loading the proteinGroups result files from MaxQuant. Proteins with less than 10% valid values were removed. Differentially expressed proteins and their false discovery rate (FDR) corrected p values were identified by the Limma package [9]. We used gene set enrichment analysis (GSEA) as implemented in the clusterProfiler package (version 3.6.0)[10] and gene set variation analysis (GSVA) as implemented in the GSVA R-package (version 1.26.0) [11]. Gene set analysis was performed using KEGG gene sets. GSEA

and GSVA scores were calculated for sets with a minimum of 5 detected genes, all other parameters were default.

Supplementary references

1. Gutscher M, Sobotta MC, Wabnitz GH *et al.* Proximity-based protein thiol oxidation by H2O2-scavenging peroxidases. J Biol Chem. 2009;284(46):31532-31540. PubMed PMID: 19755417

2. Martinez-Reyes I, Diebold LP, Kong H *et al.* TCA Cycle and Mitochondrial Membrane Potential Are Necessary for Diverse Biological Functions. Mol Cell. 2016;61(2):199-209. PubMed PMID: 26725009

3. Blecha J, Novais SM, Rohlenova K *et al.* Antioxidant defense in quiescent cells determines selectivity of electron transport chain inhibition-induced cell death. Free Radic Biol Med. 2017;112:253-266. PubMed PMID: 28774815

4. Dimri GP, Lee X, Basile G *et al.* A biomarker that identifies senescent human cells in culture and in aging skin in vivo. Proc Natl Acad Sci U S A. 1995;92(20):9363-9367. PubMed PMID: 7568133

5. Weydert CJ, Cullen JJ. Measurement of superoxide dismutase, catalase and glutathione peroxidase in cultured cells and tissue. Nat Protoc. 2010;5(1):51-66. PubMed PMID: 20057381

6. Ross JM. Visualization of mitochondrial respiratory function using cytochrome c oxidase/succinate dehydrogenase (COX/SDH) double-labeling histochemistry. J Vis Exp. 2011;(57):e3266. PubMed PMID: 22143245

7. Bray NL, Pimentel H, Melsted P *et al.* Near-optimal probabilistic RNA-seq quantification. Nat Biotechnol. 2016;34(5):525-527. PubMed PMID: 27043002

8. Robinson MD, McCarthy DJ, Smyth GK. edgeR: a Bioconductor package for differential expression analysis of digital gene expression data. Bioinformatics. 2010;26(1):139-140. PubMed PMID: 19910308

9. Ritchie ME, Phipson B, Wu D *et al.* limma powers differential expression analyses for RNA-sequencing and microarray studies. Nucleic Acids Res. 2015;43(7):e47. PubMed PMID: 25605792

10. Yu G, Wang LG, Han Y *et al.* clusterProfiler: an R package for comparing biological themes among gene clusters. OMICS. 2012;16(5):284-287. PubMed PMID: 22455463

11. Hanzelmann S, Castelo R, Guinney J. GSVA: gene set variation analysis for microarray and RNA-seq data. BMC Bioinformatics. 2013;14:7. PubMed PMID: 23323831

12. Yevshin I, Sharipov R, Kolmykov S *et al*. GTRD: a database on gene transcription regulation-2019 update. Nucleic Acids Res. 2019;47(D1):D100-D105. PubMed PMID: 30445619

13. Masuda T, Tomita M, Ishihama Y. Phase transfer surfactant-aided trypsin digestion for membrane proteome analysis. J Proteome Res. 2008;7(2):731-740. PubMed PMID: 18183947

14. Rappsilber J, Mann M, Ishihama Y. Protocol for micro-purification, enrichment, pre-fractionation and storage of peptides for proteomics using StageTips. Nat Protoc. 2007;2(8):1896-1906. PubMed PMID: 17703201

15. Hebert AS, Richards AL, Bailey DJ *et al*. The one hour yeast proteome. Mol Cell Proteomics. 2014;13(1):339-347. PubMed PMID: 24143002

16. Cox J, Mann M. MaxQuant enables high peptide identification rates, individualized p.p.b.-range mass accuracies and proteome-wide protein quantification. Nat Biotechnol. 2008;26(12):1367-1372. PubMed PMID: 19029910

17. Cox J, Hein MY, Luber CA *et al*. Accurate proteome-wide label-free quantification by delayed normalization and maximal peptide ratio extraction, termed MaxLFQ. Mol Cell Proteomics. 2014;13(9):2513-2526. PubMed PMID: 24942700

Table S1. DNA and protein sequence used for LC3B-PLA2 cloning.

Top: DNA construct used to produce LC3B-PLA2 fusion reporter for measurements of ATG4B activity. Bottom: corresponding protein sequence. Bip secretion signal sequence (red), a twin-Strep tag (blue) and the LC3B-PLA2 sequence (green) are indicated.

Table S2. Primers used for amplification of LC3B-PLA2 fusion.

LC3bPLA_RST_XhoI	attaaCTCGAGttaATCACATTTCGGACTATCCGG
LC3bPLA_F1_BglII	AtAAAAGATCTATGCCGAGCGAAAAAACCTTTAAAC
ATG4b_GWT_F	TCGGAGAACCTGTACTTCCAGGGCGGAGGCACCATGGATGCAGCAACCCTGACCTATG
ATG4b_GWT_R	GGGGACCACTTTGTACAAGAAAGCTGGGTTACAGGCTCAGGATCTCGAAATCTTC

Primers used to obtain LC3B-PLA2 fusion sequence. Restriction sites for cloning into the destination vector are indicated.

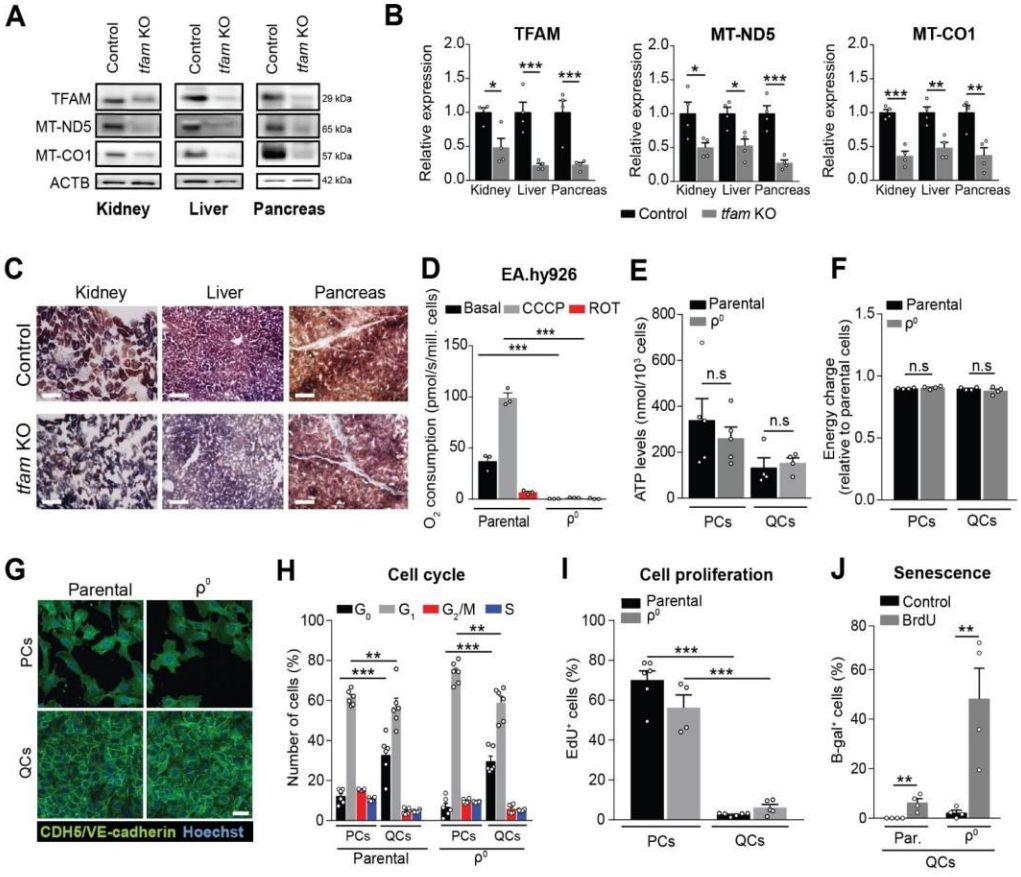
A
Control
tfam KO
TFAM
MT-ND5
MT-CO1
ACTB
29 kDa
65 kDa
57 kDa
42 kDa
Kidney
Liver
Pancreas
B
TFAM
MT-ND5
MT-CO1
Relative expression
Kidney Liver Pancreas
Control
tfam KO
C
Kidney
Liver
Pancreas
Control
tfam KO
D
EA.hy926
Basal
CCCP
ROT
O2 consumption (pmol/s/mill. cells)
Parental
ρ0
E
Parental
ρ0
ATP levels (nmol/10^3 cells)
n.s
PCs
QCs
F
Parental
ρ0
Energy charge (relative to parental cells)
n.s
PCs
QCs
G
Parental
ρ0
PCs
QCs
CDH5/VE-cadherin Hoechst
H
Cell cycle
G0
G1
G2/M
S
Number of cells (%)
PCs
QCs
Parental
ρ0
I
Cell proliferation
Parental
ρ0
EdU+ cells (%)
PCs
QCs
J
Senescence
Control
BrdU
B-gal+ cells (%)
Par.
ρ0
QCs

Figure S1. Characterization of OXPHOS-deficient models. (**A and B**) Representative WB image (A) and densitometric quantification (B) of TFAM, MT-ND5 and MT-CO1 protein expression in kidney, liver and pancreas of control and *tfam* KO mice (mean ± S.E.M, n = 4, *p < 0.05, **p < 0.01, ***p < 0.001, unpaired two-tailed t test). (**C**) Frozen tissues from control and *tfam* KO mice stained for cytochrome c oxidase (brown) and succinyl dehydrogenase (blue) activity. Scale bar: 100 μm. (**D**) Basal and maximal (after CCCP addition) respiration in EA.hy926 parental and OXPHOS-deficient cells (mean ± S.E.M., n = 4, ***p < 0.001, one-way ANOVA with Sidak's multiple comparisons test). (**E**) ATP levels measured using CellTiter-Glo kit in parental and ρ^0 EA.hy926 QCs and PCs (mean ± S.E.M., n ≥ 4, $^{n.s.}$p > 0.05, unpaired two-tailed t test). (**F**) Quantification of mass spectrometry analysis of the energy charge in parental and ρ^0 EA.hy926 QCs and PCs cultivated in the absence of uridine and pyruvate for 24 h (mean ± S.E.M., n = 4, $^{n.s.}$p > 0.05, unpaired two-tailed t test). (**G**) Representative image of adherence junctions in parental and ρ^0 EA.hy926 PCs and QCs visualized by CDH5/VE-cadherin staining. Scale bar: 40 μm (n = 3). (**H**) Cell cycle distribution in parental and ρ^0 EA.hy926 cells evaluated by double staining for Hoechst 33342 and Pyronin Y (mean ± S.E.M., n ≥ 5, **p < 0.01, ***p < 0.001, one-way with Sidak's multiple comparisons test). (**I**) Cell proliferation of parental and ρ^0 EA.hy926 PCs and QCs evaluated by EdU labeling and flow cytometry (mean ± S.E.M., n ≥ 4, ***p < 0.001, one-way ANOVA with Sidak's multiple comparisons test). (**J**) GBA1/β-galactosidase-positive cells in EA.hy926 QCs 5 days after reaching confluence (control). Treatment with 5-BrdU (100 μM) for 9 days (+BrdU) was used as a positive control (mean ± S.E.M., n = 4, **p < 0.01, unpaired two-tailed t test).

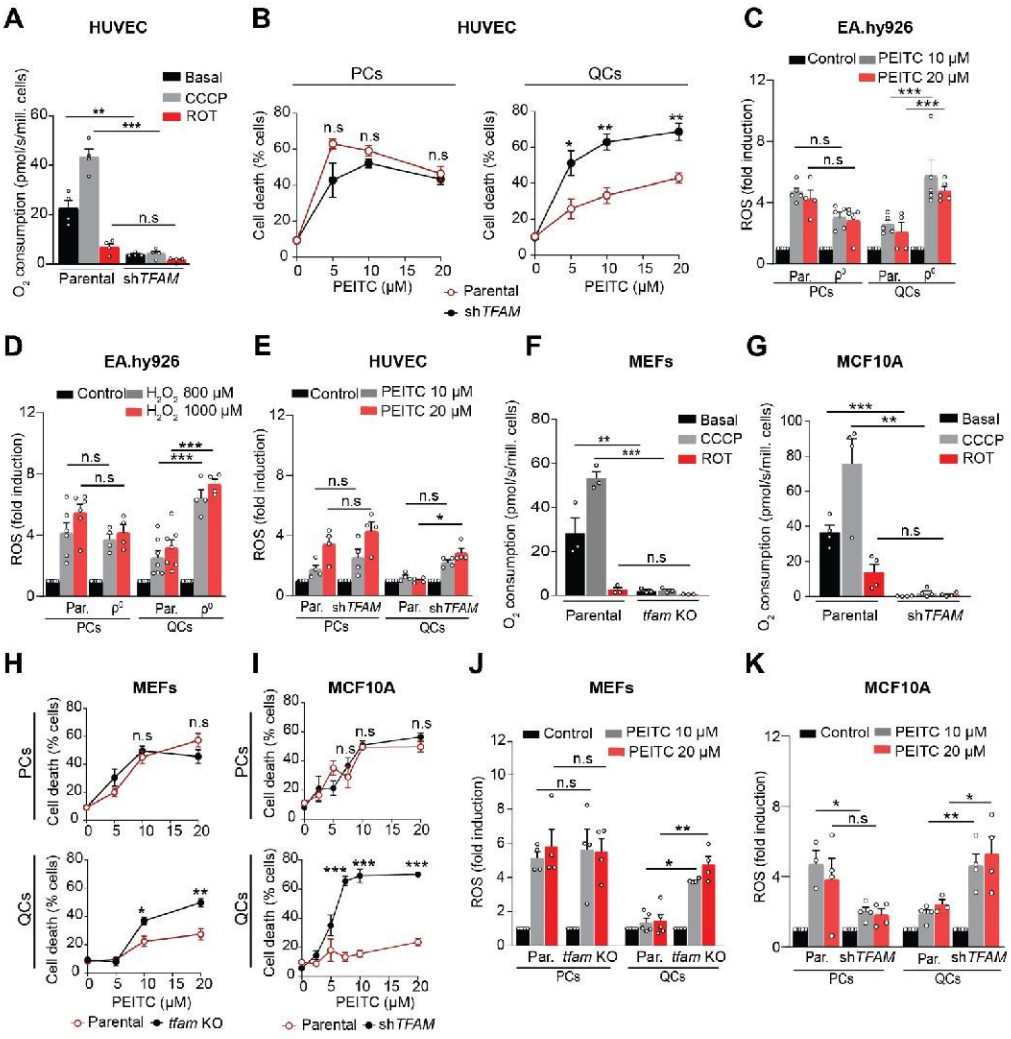
A
HUVEC
Basal
CCCP
ROT
O2 consumption (pmol/s/mill. cells)
Parental
shTFAM
B
HUVEC
PCs
QCs
Cell death (% cells)
PEITC (μM)
Parental
shTFAM
C
EA.hy926
Control
PEITC 10 μM
PEITC 20 μM
ROS (fold induction)
Par.
PCs
QCs
D
EA.hy926
Control
H2O2 800 μM
H2O2 1000 μM
ROS (fold induction)
E
HUVEC
Control
PEITC 10 μM
PEITC 20 μM
ROS (fold induction)
F
MEFs
Basal
CCCP
ROT
O2 consumption (pmol/s/mill. cells)
Parental
tfam KO
G
MCF10A
Basal
CCCP
ROT
O2 consumption (pmol/s/mill. cells)
Parental
shTFAM
H
MEFs
PCs
QCs
Cell death (% cells)
PEITC (μM)
Parental
tfam KO
I
MCF10A
PCs
QCs
Cell death (% cells)
PEITC (μM)
Parental
shTFAM
J
MEFs
Control
PEITC 10 μM
PEITC 20 μM
ROS (fold induction)
Par.
tfam KO
PCs
QCs
K
MCF10A
Control
PEITC 10 μM
PEITC 20 μM
ROS (fold induction)
Par.
shTFAM
PCs
QCs

Figure S2. OXPHOS deficiency sensitizes quiescent cells to oxidative stress in multiple cell types. (**A**) Basal and maximal (after CCCP addition) respiration in parental and sh*TFAM* HUVECs (mean ± S.E.M., n = 4, $^{n.s.}p > 0.05$, $^{**}p < 0.01$, $^{***}p < 0.001$, one-way ANOVA with Sidak's multiple comparisons test). (**B**) Cell death in parental and sh*TFAM* HUVEC PCs and QCs treated with PEITC for 22 h evaluated by ANXA5-FITC and PI (mean ± S.E.M., n ≥ 4, $^{n.s.}p > 0.05$, $^{*}p < 0.05$, $^{**}p < 0.01$, versus parental cells, two-way ANOVA with Tukey's multiple comparisons test). (**C-E**) ROS formation in EA.hy926 (**C and D**) and HUVEC (**E**) PCs and QCs treated with PEITC or H_2O_2 for 1 h measured by DCF-DA (mean ± S.E.M., n ≥ 3, $^{n.s.}p > 0.05$, $^{*}p < 0.05$, $^{***}p < 0.001$ one-way ANOVA with Sidak's multiple comparisons test). (**F and G**) Basal and maximal (after CCCP addition) respiration in parental and *tfam* KO MEFs (**F**) and sh*TFAM* MCF10A (**G**) (mean ± S.E.M., n = 4 for MCF10A, n = 3 for MEFs, $^{n.s.}p > 0.05$, $^{**}p < 0.01$, $^{***}p < 0.001$, one-way ANOVA with Sidak's multiple comparisons test. (**H and I**) Cell death in MEFs (**H**) and MCF10A (**I**) PCs and QCs treated with PEITC for 22 h evaluated by ANXA5-FITC and PI (mean ± S.E.M., n ≥ 4, $^{n.s.}p > 0.05$, $^{*}p < 0.05$, $^{**}p < 0.01$, $^{***}p < 0.001$ versus parental cells, two-way ANOVA with Tukey's multiple comparisons test). (**J and K**) ROS formation in MEFs (**J**) and MCF10A (**K**) PCs and QCs treated with PEITC for 1 h measured by DCF-DA (mean ± S.E.M., n ≥ 3, $^{n.s.}p > 0.05$, $^{*}p < 0.05$, $^{**}p < 0.01$, one-way ANOVA with Sidak's multiple comparisons test).

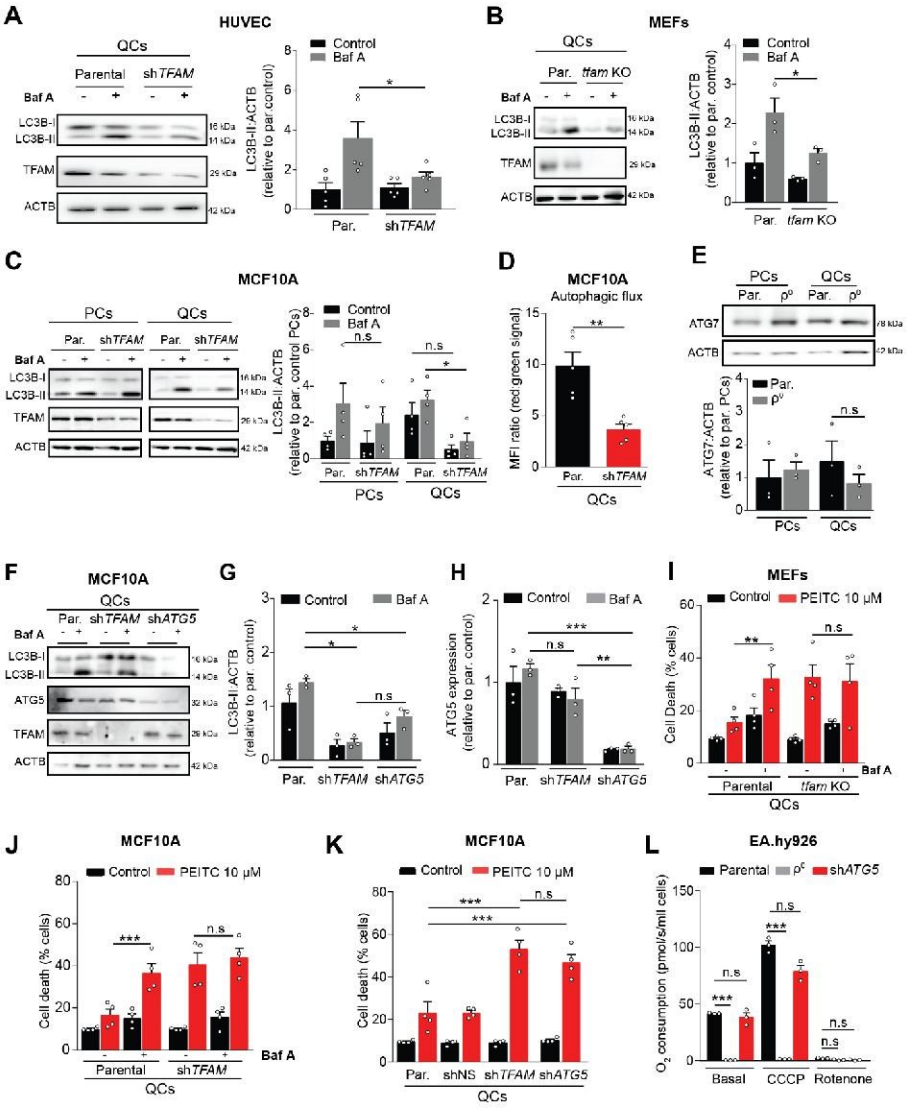
A
HUVEC
QCs
Parental
sh*TFAM*
Baf A
LC3B-I
LC3B-II
TFAM
ACTB
16 kDa
14 kDa
26 kDa
42 kDa
Control
Baf A
LC3B-II:ACTB (relative to par. control)
Par.
sh*TFAM*
B
MEFs
QCs
Par.
tfam KO
C
MCF10A
PCs
QCs
n.s
D
MCF10A
Autophagic flux
MFI ratio (red green signal)
E
ATG7
ACTB
ATG7:ACTB (relative to par. PCs)
F
MCF10A
sh*ATG5*
ATG5
G
H
ATG5 expression (relative to par. control)
I
MEFs
PEITC 10 µM
Cell Death (% cells)
J
MCF10A
Cell death (% cells)
K
MCF10A
shNS
L
EA.hy926
Parental
shATG5
O2 consumption (pmol/s/ml cells)
Basal
CCCP
Rotenone

Figure S3. Autophagy is defective in multiple types of quiescent OPHOS-deficient cells. (**A and B**) Representative WB image (left) and quantification (right) of activated LC3B (LC3B-II) in HUVEC (**A**) and MEFs (**B**) QCs exposed or not to 50 μM Baf A for 4 h (mean ± S.E.M., n = 4, *p < 0.05, one-way ANOVA with Sidak's multiple comparisons test). (**C**) Representative WB image (left) and quantification (right) of activated LC3B (LC3B-II) in MCF10A PCs and QCs exposed or not to 50 μM Baf A for 4 h (mean ± S.E.M., n = 4, n.s p > 0.05, *p < 0.05, one-way ANOVA with Sidak's multiple comparisons test). (**D**) Fluorescent signal of the pHluorin-mKate2-LC3 autophagy reporter in parental and OXPHOS-deficient MCF10A QCs assessed by flow cytometry (mean ± S.E.M., n = 5, **p < 0.01, unpaired two-tailed t test). Note: red/green fluorescence ratio is proportional to the native autophagic flux. (**E**) Representative WB images (top) and quantifications (bottom) of ATG7 in parental and ρ^0 EA.hy926 PCs and QCs, (mean ± S.E.M., n =3, $^{n.s.}$p > 0.05) (**F-H**) Representative WB images (**F**) and quantifications of LC3B-II (**G**), ATG5 (**H**) in MCF10A QCs (mean ± S.E.M., n = 3, $^{n.s.}$p > 0.05, *p < 0.05, **p < 0.01, ***p < 0.001, one-way ANOVA with Sidak's multiple comparisons test). (**I and J**) Cell death in MEFs (**I**) and MCF10A (**J**) QCs with or without OXPHOS deficiency, pre-incubated or not with 50 nM of Baf A for 2 h followed by 10 μM PEITC for 22 h, evaluated by ANXA5-FITC and PI (mean ± S.E.M., n ≥ 4, $^{n.s.}$p > 0.05, **p < 0.01, ***p < 0.001, one-way ANOVA with Sidak's multiple comparisons test). (**K**) Cell death in indicated MCF10A QCs treated with 10 μM of PEITC for 22 h, evaluated by ANXA5-FITC and PI (mean ± S.E.M., n = 4, $^{n.s.}$p > 0.05, ***p < 0.001, one-way ANOVA with Sidak's multiple comparisons test). (**L**) Basal and maximal (after CCCP addition) respiration in parental, ρ^0 and ATG5-silenced (sh*ATG5*) EA.hy926 cells evaluated using Oroboros Oxygraph (mean ± S.E.M., n = 3, $^{n.s.}$p > 0.05, ***p < 0.001, unpaired two-tailed t test).

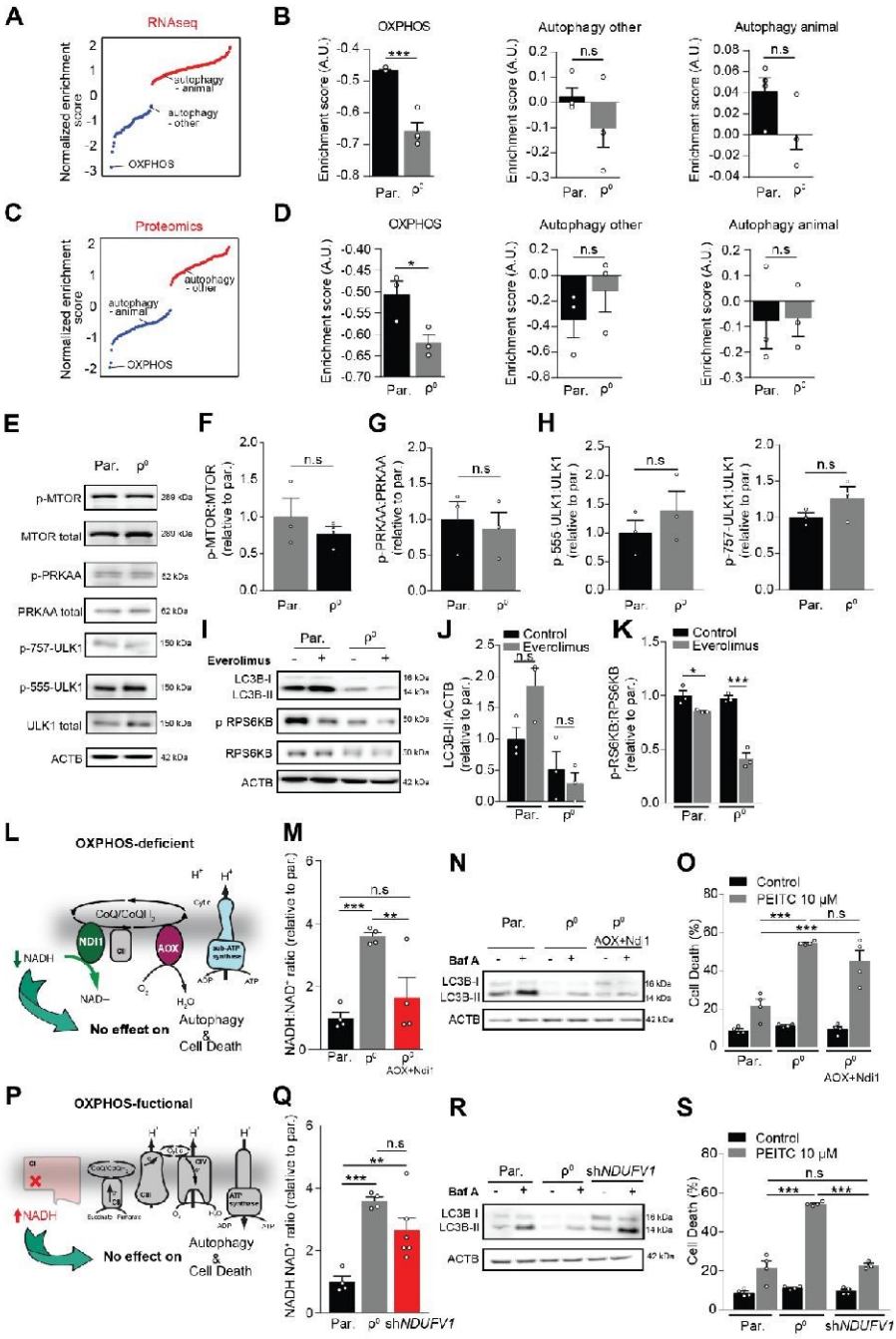
A
RNAseq
Normalized enrichment score
autophagy - animal
autophagy - other
OXPHOS
B
OXPHOS
Autophagy other
Autophagy animal
Enrichment score (A.U.)
n.s
***
Par.
ρ⁰
C
Proteomics
D
*
E
Par.
ρ⁰
p-MTOR
MTOR total
p-PRKAA
PRKAA total
p-757-ULK1
p-555-ULK1
ULK1 total
ACTB
F
p-MTOR:MTOR (relative to par.)
G
p-PRKAA:PRKAA (relative to par.)
H
p-555 ULK1:ULK1 (relative to par.)
p-757-ULK1:ULK1 (relative to par.)
I
Everolimus
LC3B-I
LC3B-II
p RPS6KB
RPS6KB
J
Control
Everolimus
LC3B-II:ACTB (relative to par.)
K
p-RS6KB:RPS6KB (relative to par.)
L
OXPHOS-deficient
NDI1
AOX
NADH
NAD+
No effect on
Autophagy & Cell Death
M
NADH:NAD+ ratio (relative to par.)
AOX+Ndi1
N
Baf A
O
PEITC 10 µM
Cell Death (%)
P
OXPHOS-fuctional
Q
shNDUFV1
R
S

Figure S4. Attenuation of autophagy in OXPHOS-deficient QCs is independent of transcriptional changes, canonical pathways, or NADH:NAD^+ ratio**.** (**A-D**) Independence of transcriptional regulation/protein expression. (**A**) The normalized enrichment scores (NES) of Gene set enrichment analysis (GSEA) for mRNA expression in parental as compared to ρ^0 Ea.hy926 QCs, analyzed as a group on a collection of KEGG pathways. Red and blue, respectively, indicate up- and downregulated pathways in ρ^0 cells. OXPHOS (NES = -2.92, p = 0.0034) is suppressed while autophagy (autophagy-animal, NES = 0.799, p = 0.8705; autophagy-other, NES = -0.42, p = 1.0000, Kolmogorov-Smirnov-like rank test) is unaffected in ρ^0 QCs. (**B**) RNA expression levels of indicated gene sets in parental and ρ^0 EA.hy926 QCs (mean ± S.E.M, n = 4, $^{n.s.}p > 0.05$, ***p < 0.001, unpaired two-tailed t test). (**C**) GSEA analysis on proteomics data in parental and ρ^0 EA.hy926 QCs, determined as in panel A. Red and blue respectively indicate up- and downregulated pathways in ρ^0 cells. OXPHOS in ρ^0 QCs is suppressed on the protein level (NES = -2.66, p = 0.0021), but no effect is observed for the autophagy gene sets (autophagy-animal, NES = -0.99, p = 0.4896; autophagy-other, NES = 1.06, p = 0.4018, Kolmogorov-Smirnov-like rank test). (**D**) Protein expression levels of indicated sets in parental and ρ^0 EA.hy926 QCs (mean ± S.E.M, n = 3, $^{n.s.}p > 0.05$, *p < 0.05, unpaired two-tailed t test). (**E-K**) Independence of the canonical signaling. Representative WB image (**E**) and densitometric quantification of the expression of MTOR (**F**), AMPK (**G**), ULK1 (**H**) and their phosphorylation forms in parental and ρ^0 EA.hy926 QCs (mean ± S.E.M., n = 3, $^{n.s.}p > 0.05$, unpaired two-tailed t test). (**I-K**) Representative WB image (**I**) and quantification of activated LC3B (LC3B-II) (**J**), RPS6KB/p70S6K and its phosphorylated form (p-RPS6KB/p70S6K) (**K**) in parental and ρ^0 EA.hy926 QCs exposed or not to MTORC1 inhibitor everolimus (20 μM) for 4 h (n = 3 mean ± S.E.M., n = 3, $^{n.s.}p > 0.05$, unpaired two-tailed t test). (**L-S**) Independence of the NADH:NAD^+

ratio. (**L**) Restoration of electron transport via coenzyme Q (CoQ) by introducing alternative oxidases Ndi1 and AOX into ρ^0 QCs normalized NADH:NAD ratio but did not restore autophagy/ROS resistance. (**M**) NADH:NAD^+ ratio in EA.hy926 QCs, parental, ρ^0 and ρ^0 expressing AOX+Ndi1 (ρ^0 AOX+Ndi1) (mean ± S.E.M., n = 4, $^{n.s.}p > 0.05$, $^{**}p < 0.01$, $^{***}p < 0.001$, unpaired two-tailed t test). (**N**) Representative WB image of activated LC3B (LC3B-II) in EA.hy926 QCs, parental, ρ^0 and ρ^0 expressing AOX+Ndi1 (n = 3). (**O**) Cell death in EA.hy926 QCs, parental, ρ^0 and ρ^0 expressing AOX+Ndi1, after 22 h treatment with PEITC (10 µM) measured by flow cytometry using ANXA5/annexin V-Dy647/Hoechst33258 (mean ± S.E.M., n = 4, $^{n.s.}p > 0.05$, $^{***}p < 0.001$, one-way ANOVA with Sidak's multiple comparisons test). (**P**) Silencing of CI subunit NDUFV1 in parental QCs disables CI and elevates NADH without affecting autophagy or ROS sensitivity. (**Q**) NADH:NAD^+ ratio in parental, ρ^0 and parental NDUFV1-silenced (sh*NDUFV1*) EA.hy926 QCs (mean ± S.E.M., n ≥ 4, $^{n.s.}p > 0.05$, $^{**}p < 0.01$, $^{***}p < 0.001$, unpaired two-tailed t test). Data for Par. and ρ^0 are identical to those of panel M, as these conditions were tested in the same experiments. (**R**) Representative WB image of PE-conjugated LC3B (LC3B-II) in parental, ρ^0 and sh*NDUFV1* EA.hy926 QCs exposed or not to 50 nM Baf A for 4 h (n = 3). (**S**) Cell death in parental, ρ^0 and sh*NDUFV1* EA.hy926 QCs after 22 h treatment with 10 µM PEITC measured by ANXA5-FITC and PI (mean ± S.E.M., n = 4, $^{n.s.}p > 0.05$, $^{***}p < 0.001$, one-way ANOVA with Sidak's multiple comparisons test).

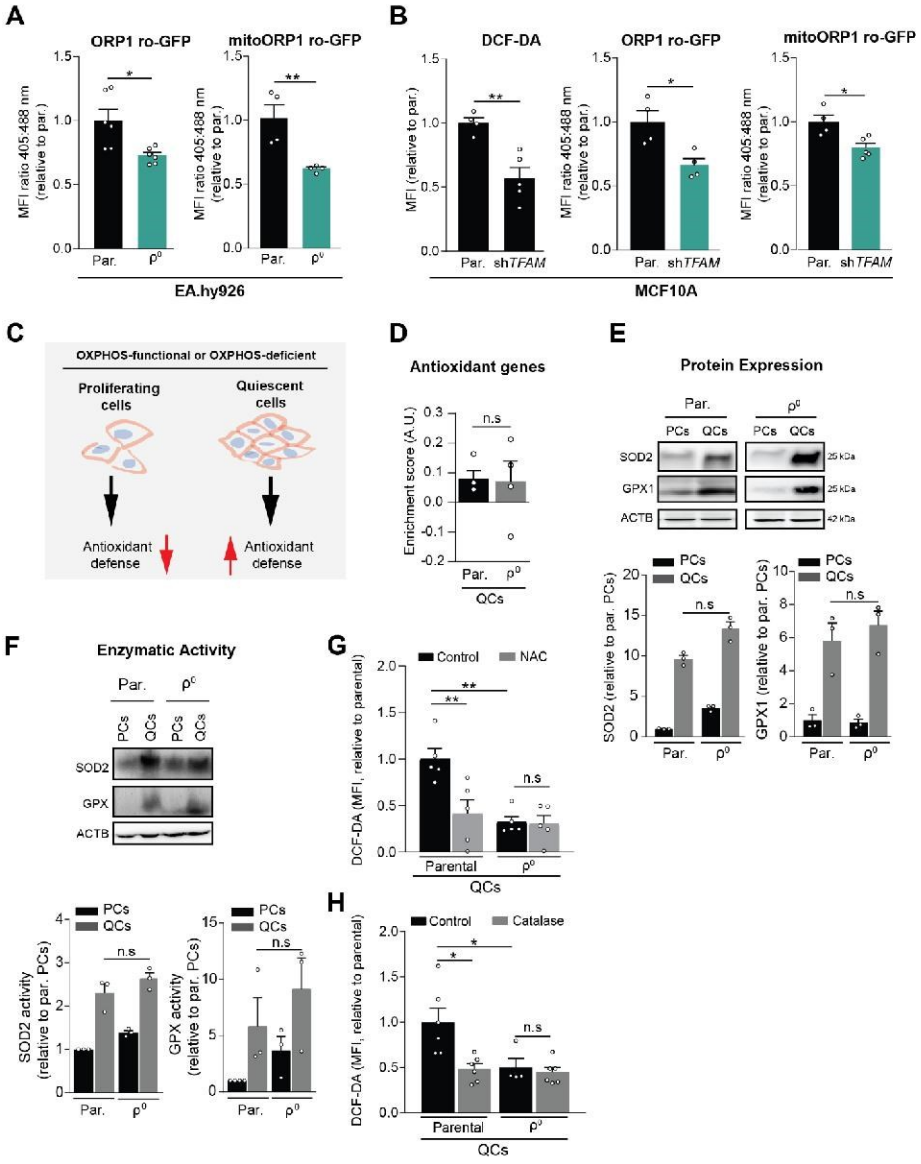
A
ORP1 ro-GFP
mitoORP1 ro-GFP
MFI ratio 405:488 nm (relative to par.)
Par.
ρ⁰
EA.hy926
B
DCF-DA
ORP1 ro-GFP
mitoORP1 ro-GFP
MFI (relative to par.)
MFI ratio 405:488 nm (relative to par.)
Par.
shTFAM
MCF10A
C
OXPHOS-functional or OXPHOS-deficient
Proliferating cells
Quiescent cells
Antioxidant defense
Antioxidant defense
D
Antioxidant genes
Enrichment score (A.U.)
n.s
Par.
ρ⁰
QCs
E
Protein Expression
Par.
ρ⁰
PCs
QCs
SOD2
GPX1
ACTB
25 kDa
25 kDa
42 kDa
SOD2 (relative to par. PCs)
GPX1 (relative to par. PCs)
n.s
F
Enzymatic Activity
SOD2
GPX
ACTB
SOD2 activity (relative to par. PCs)
GPX activity (relative to par. PCs)
G
Control
NAC
DCF-DA (MFI, relative to parental)
Parental
QCs
H
Control
Catalase
DCF-DA (MFI, relative to parental)
Parental
QCs

Figure S5. OXPHOS-derived ROS and antioxidant defense. (**A and B**) Baseline ROS levels in EA.hy926 (**A**) and MCF10A (**B**) QCs treated with DCF-DA or expressing Orp1-roGFP2, a ratiometric fluorescence sensor specific for H_2O_2, or its mitochondrial-targeted variant (mitoOrp1-roGFP2), evaluated by flow cytometry (mean ± S.E.M., n = 4, *p < 0.05, **p < 0.01, unpaired two-tailed t test). The ratio of fluorescence intensity after excitation at 405 and 488 nm reflects the steady state H_2O_2 concentration in the cytoplasm or in mitochondria. (**C**) Antioxidant defense is increased in non-proliferating cells irrespective of OXPHOS function. (**D**) Expression levels of an antioxidant defense gene set in parental and ρ^0 EA.hy926 QCs (mean ± S.E.M, n = 4, $^{n.s.}$p > 0.05, unpaired two-tailed t test). (**E**) Representative WB image (top) and quantification (bottom) of the expression of the indicated antioxidant proteins, SOD2 (superoxide dismutase 2) and GPX1 (glutathione peroxidase 1) in whole cell lysates from parental and ρ^0 EA.hy926 QCs (mean ± S.E.M., n = 3, $^{n.s.}$ p > 0.05, one-way ANOVA with Sidak's multiple comparisons test). (**F**) Representative in-gel activity image (top) and quantification (bottom) of indicated antioxidant enzymes in parental and ρ^0 EA.hy926 QCs and PCs (mean ± S.E.M., n ≥ 3, $^{n.s.}$p > 0.05, one-way ANOVA with Sidak's multiple comparisons test). (**G and H**) ROS levels in parental and ρ^0 EA.hy926 QCs (**G**) treated with NAC and (**H**) with or without overexpression of CAT, evaluated by DCF-DA fluorescence probe (mean ± S.E.M., n ≥ 4, $^{n.s.}$p > 0.05, *p < 0.05, **p < 0.01, one-way ANOVA with Sidak's multiple comparisons test).

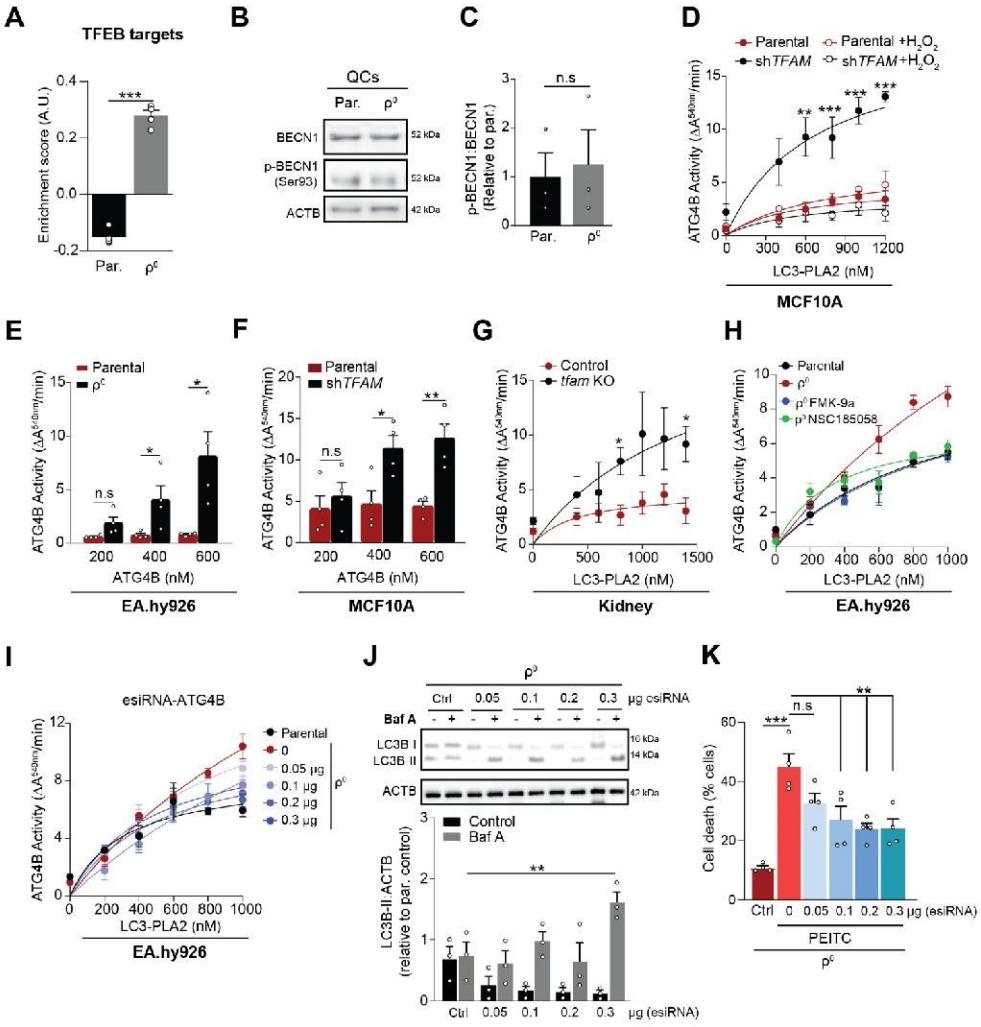
A
TFEB targets
Enrichment score (A.U.)
Par.
ρ⁰
B
QCs
Par.
ρ⁰
BECN1
p-BECN1 (Ser93)
ACTB
C
p-BECN1:BECN1 (Relative to par.)
n.s
D
Parental
Parental +H2O2
shTFAM
shTFAM+H2O2
ATG4B Activity (ΔA540nm/min)
LC3-PLA2 (nM)
MCF10A
E
Parental
ρ⁰
ATG4B (nM)
EA.hy926
F
Parental
shTFAM
MCF10A
G
Control
tfam KO
Kidney
H
Parental
ρ⁰
ρ⁰ FMK-9a
ρ⁰ NSC185058
EA.hy926
I
esiRNA-ATG4B
Parental
0
0.05 µg
0.1 µg
0.2 µg
0.3 µg
ρ⁰
EA.hy926
J
ρ⁰
Ctrl
0.05
0.1
0.2
0.3
µg esiRNA
Baf A
LC3B I
LC3B II
ACTB
Control
Baf A
LC3B-II:ACTB (relative to par. control)
K
Cell death (% cells)
Ctrl
0
0.05
0.1
0.2
0.3 µg (esiRNA)
PEITC
ρ⁰

Figure S6. Regulation of autophagy in QCs by ETC-derived ROS. (**A**) Expression level of TFBE target genes in parental and ρ^0 EA.hy926 QCs (mean ± S.E.M, n = 4, ***p < 0.001, unpaired two-tailed t test) (**B and C**) Representative WB image (**B**) and quantification (**C**) of BECN1 and phospho-BECN1 (Ser93) in parental and ρ^0 EA.hy926 QCs (mean ± S.E.M., n=3, $^{n.s.}$p > 0.05, unpaired two-tailed t test). (**D**) ATG4B activity in cell lysates from MCF10A parental and OXPHOS-deficient QCs treated or not with H_2O_2 (1 mM) for 4 h and incubated with increasing concentrations of LC3B-PLA2 fusion protein substrate (mean ± S.E.M., n ≥ 4, ***p < 0.001, versus parental cells, two-way ANOVA with Tukey's multiple comparisons test). (**E and F**) ATG4B reporter signal in cell lysates from EA.hy926 (**E**) and MCF10A (**F**) QCs incubated with increasing concentrations of recombinant ATG4B (mean ± S.E.M., n ≥ 4, $^{n.s}$, p > 0.05, *p < 0.05, **p < 0.01, one-way ANOVA with Sidak's multiple comparisons test). (**G**) ATG4B activity in cell lysates from the kidney of control or *tfam* KO mice incubated with increasing concentrations of LC3B-PLA2 fusion protein substrate (mean ± S.E.M., n ≥ 4, *p < 0.05, versus parental cells, two-way ANOVA with Tukey's multiple comparisons test). (**H**) ATG4B activity in parental, ρ^0 EA.hy926 and ρ^0 EA.hy926 QCs treated for 4 h with FMK-9a (1 μM) or NSC185058 (0.1 μM) (mean ± S.E.M., n = 4) (**I**) ATG4B activity in parental, ρ^0 EA.hy926 and ρ^0 EA.hy926 QCs transfected with increasing concentrations of esiRNA against *ATG4B* (mean ± S.E.M., n ≥ 3). (**J**) Representative WB images of activated LC3B (LC3B-II) (top) and quantification (bottom) of ρ^0 EA.hy926 QCs transfected with increased concentrations of esiRNA against *ATG4B* in the presence or absence of 50 nM of Baf A for 4 h (mean ± S.E.M., n = 3, **p < 0.01, one-way ANOVA with Sidak's multiple comparisons test). (**K**) PEITC-induced cell death in ρ^0 EA.hy926 QCs transfected with increased concentrations of esiRNA against *ATG4B* evaluated by ANXA5-

FITC and PI (mean ± S.E.M., n = 4, $^{n.s}$, $p > 0.05$, $^{**}p < 0.01$, $^{***}p < 0.001$, one-way ANOVA with Sidak's multiple comparisons test).

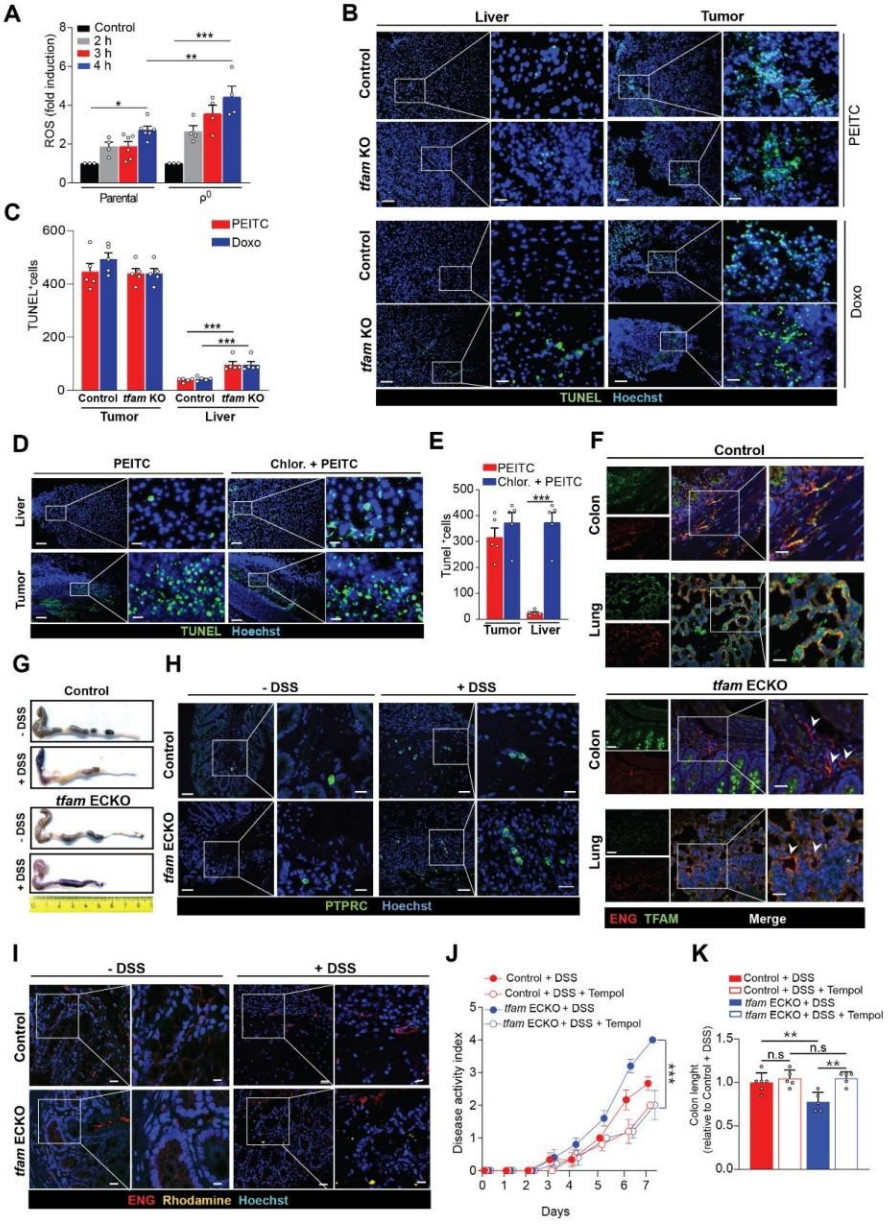
A
Control
2 h
3 h
4 h
ROS (fold induction)
Parental
ρ0
B
Liver
Tumor
Control
tfam KO
PEITC
Doxo
TUNEL Hoechst
C
PEITC
Doxo
TUNEL cells
Control tfam KO Control tfam KO
Tumor
Liver
D
PEITC
Chlor. + PEITC
Liver
Tumor
TUNEL Hoechst
E
PEITC
Chlor. + PEITC
Tunel cells
Tumor Liver
F
Control
Colon
Lung
G
Control
- DSS
+ DSS
tfam ECKO
H
- DSS
+ DSS
Control
tfam ECKO
PTPRC Hoechst
tfam ECKO
ENG TFAM Merge
I
- DSS
+ DSS
Control
tfam ECKO
ENG Rhodamine Hoechst
J
Control + DSS
Control + DSS + Tempol
tfam ECKO + DSS
tfam ECKO + DSS + Tempol
Disease activity index
Days
K
Control + DSS
Control + DSS + Tempol
tfam ECKO + DSS
tfam ECKO + DSS + Tempol
Colon lenght (relative to Control + DSS)
n.s

Figure S7. Pathophysiological relevance of OXPHOS-mediated stress resistance. (**A**) ROS formation in parental and ρ^0 EA.hy926 QCs treated with doxorubicin (1 μM) for 2, 3 and 4 h measured using DCF-DA (mean ± S.E.M., n = 4, *p < 0.05, **p < 0.01, ***p < 0.001, one-way ANOVA with Sidak's multiple comparisons test). (**B**) Representative images of TUNEL staining in liver and B16 cells derived-tumor sections in control and *tfam* KO mice treated or not with PEITC (1.25 mg/25 g mouse) or doxorubicin (0.2 mg / 20 g mouse) for 16 h. Nuclei are counterstained with Hoechst. Right panels are magnifications of the boxed areas on the left. Scale bar, 300 μm (left panels) and 100 μm (right panels). (**C**) Quantification of $TUNEL^+$ cells in B and 4 additional experiments (mean ± S.E.M., n = 5 mice, ***p < 0.001, one-way ANOVA with Sidak's multiple comparisons test. (**D**) Representative images of TUNEL staining in liver and B16 cells derived-tumor sections of control mice after treatment with PEITC (1.25 mg/25 g mouse) or PEITC + chloroquine (1 mg/20 mg of mouse). Nuclei are counterstained with Hoechst. Right panels are magnifications of the boxed areas on the left. Scale bar: 300 μm (left panels) and 100 μm (right panels). (**E**) Quantification of $TUNEL^+$ cells in D and 4 additional experiments (mean ± S.E.M., n = 5 mice, ***p < 0.001, one-way ANOVA with Sidak's multiple comparisons test. (**F**) Representative images of colon and lung tissue from control and *tfam* ECKO mice stained for an endothelial marker ENG/CD105 and for TFAM. Nuclei are counterstained with Hoechst. TFAM deletion in endothelial cells in *tfam* ECKO mice is shown as TFAM negative area in ENG/CD105 positive area (white arrows). Right panels are magnifications of the boxed area of the "Merge" panels. Scale bar: 200 μm (left panels) and 100 μm (right panels). (**G**) Representative images of colons of control and *tfam* ECKO mice (females) treated or not 2.5% DSS. (**H**) Representative images of colon sections of control and *tfam* ECKO mice treated or not with 2.5% DSS, stained with PTPRC/CD45 (green) and Hoechst (blue) Right panels are magnifications of the boxed areas

on the left. Scale bar: 40 μm (left panels) and 20 μm (right panels). (**I**) Representative images of vascular leakiness in colon tissue from control and *tfam* ECKO mice treated or not with 2.5% DSS. Leakages are visualized by dextran-rhodamine staining, blood vessels by ENG/CD105 staining, and nuclei are counterstained with Hoechst. Scale bar: 200 μm (left panels) and 100 μm (right panels). (**J**) Disease activity index of colitis in control and *tfam* ECKO mice treated with 2.5% DSS in the drinking water for 7 consecutive days and co-treated with 15 mg/kg/day of tempol or with solvent control every 12 h ($n \geq 5$ mice, ***$p < 0.001$, two-way ANOVA Tukey's multiple comparisons test). (**K**) Colon length in control and *tfam* ECKO mice after 2.5% DSS treatment co-treated with 15 mg/kg/day of tempol or with solvent control ($n \geq 6$, $^{n.s.}p > 0.05$, **$p < 0.01$, ***$p < 0.001$, one-way ANOVA with Sidak's multiple comparisons test).